Using Inorganic Nanoparticle Surface Passivation as a Tool for New Approaches in Photovoltaics

by

Brian Paul Bloom

B.S., Duquesne University, 2009

Submitted to the Graduate Faculty of the

Dietrich School of Arts and Sciences in partial fulfillment

of the requirements for the degree of

Doctor of Philosophy

University of Pittsburgh

2016

UNIVERSITY OF PITTSBURGH

Dietrich School of Arts and Sciences

This dissertation was presented

by

Brian Paul Bloom

It was defended on

July 29th 2016

and approved by

Dr. Haitao Liu, Assistant Professor, Department of Chemistry

Dr. Jill Millstone, Assistant Professor, Department of Chemistry

Dr. Jung-kun Lee, Associate Professor, Departmental of Mechanical Engineering and Materials Science

Dissertation Advisor: Dr. David Waldeck, Professor, Department of Chemistry

Using Inorganic Nanoparticle Surface Passivation as a Tool for New Approaches in Photovoltaics

Brian Paul Bloom, PhD

University of Pittsburgh, 2016

Using Inorganic Nanoparticle Surface Passivation as a Tool for New Approaches in Photovoltaics

Brian Paul Bloom, PhD

University of Pittsburgh, 2016

Colloidal semiconductor nanoparticles (NPs) are an attractive alternative for optoelectronic devices owing to their low cost, solution processability, and interesting quantum confinement properties. Much progress has been made towards the development of semiconductor NP based devices, however, only recently have researchers begun to understand and utilize the role of the NP surface capping ligands in these systems. The fundamental studies in this dissertation focus on the ligand-NP interaction and the interesting properties that become manifest. The first series of experiments discussed herein explore the influence of the ligand on the size dependent electronic state energies of CdSe NPs. The second study shows how Fermi-level pinning of PbS NPs on a gold substrate inhibits the size and ligand dependent changes in the electronic states. It was found that the insertion of an alumina layer decouples the NPs from the substrate and the size and ligand dependent energy shifts are restored. The third study in this dissertation shows how capping CdSe NPs with chiral ligands can lead to spin specific conduction pathways. The last study investigates charge transport in donor bridge acceptor NP dyads on a microbead template. By changing the size of the acceptor and its ligand length, charge transport could be studied as a function of driving force and bridge length. The findings in these studies elucidate the importance of capping ligand on the physical properties of semiconductor NPs and may guide the development for future advances in optoelectronic devices.

TABLE OF CONTENTS

LIST OF TABLES

LIST OF FIGURES

LIST OF EQUATIONS

LIST OF SCHEMES

PREFACE

I have received a lot of help from many people at the University of Pittsburgh that has truly made all of this work possible. Most importantly I would like to thank my academic advisor Professor David Waldeck for all of the time and energy he has invested in me throughout the years. His teachings and guidance have been invaluable towards my growth not only as a scientist, but also as a person. I would also like to thank my current and former labmates Dr. Prasun Mukherjee, Dr. Emil Wierzbinski, Dr. Kathy Davis, Dr. Yang Wang, Dr. Matthew Kofke, Dr. Mingyan Wu, Dr. Madu Mendis, Daniel Lamont, Dr. Liu-bin Zhao, Brittney Graff, Edward Beal, Jimeng Wei, and Arthur Davis. Working with and beside you has been a privilege.

I would also like to express my appreciation for my other committee members Professor Shigeru Amemiya, Professor Haitao Liu, and Professor Jung-Kun Lee. You have gone above and beyond to help me in my studies and for that I am grateful. I am also thankful for all of the wonderful people I have had the honor of working with outside of the department; Professor Ron Naaman (Weizzman Institute), Professor David Beratan (Duke University), Dr. Vankayala Kiran, Dr. Vaibhav Varade, Dr. Peng Zhang, and Ruibin Liu without your help many of the works in this thesis would not have been possible.

Lastly, I want to thank my family and friends for standing by my side throughout this entire process. I would especially like to thank my father. He has been my biggest supporter, believing in me more than I ever could in myself. His wisdom and advice has been an instrumental part of my success and for that I am forever indebted. Last but not least, I want to thank my fiancée, Suzanne Principe for your love, support, and patience with me all of these years. You mean so much to me and I would not be here today without you.

1.0 Introduction

1.1 Special Properties of Semiconductor Nanoparticles for Photovoltaics

In the past decade, considerable interest has been paid toward the development of next-generation photovoltaics that are both highly efficient and have low manufacturing costs. Colloidal semiconductor nanoparticles (NPs) are attractive candidates for next-generation photovoltaics because of their size-tunable electronic properties and solution processability. These features allow for the appropriate energy alignment and fabrication of bulk heterojunction solar cells, p-n junction solar cells, and quantum dot sensitized solar cells.

Recent progress in the field has focused on the development of hierarchical energy alignment of the electronic states for improved charge separation,[1] as well as, inorganic / organic hybrid passivation for enhanced carrier diffusion.[2-4] Despite these recent advances many substantial challenges remain and are the focus of ongoing research. In this chapter, introductory concepts and theories on nanoparticle synthesis, characterization, and post-synthetic ligand exchange are reviewed. This chapter concludes with an outline of the dissertation and some of the current issues in photovoltaics it aims to address.

1.2 Synthesis and Properties of Semiconductor Nanoparticles

Two main schemes have been employed for the synthesis of semiconductor NPs. In the first method growth and nucleation occur simultaneously over an extended period of time at mild temperatures.[5] This approach leads to a broad range of sizes that can later be separated through size selective precipitation and centrifugation. In the second approach the nucleation phase is separated from the growth phase; a reactant is injected at high temperatures to induce rapid nucleation, after which the temperature is then dropped in order to slow growth.[5] The second method, also known as the hot-injection method, leads to a narrow distribution of sizes for most II-VI nanoparticle materials. The thermodynamic reasoning for why this occurs is provided below.

The nucleation of NPs in the hot injection method is a thermodynamically driven process; for spherical nanoparticles the change in Gibbs free energy (ΔG) can be described by Equation 1-1:

Equation 1-1

$$\Delta G = -3\frac{V_{nuc}}{V_{ppt}}Tk_B\ln(S) + 4\pi r^{2\gamma}$$

where V_{ppt} is the volume of the precipitated species, $V_{nuc} = 4\pi r^3/3$ and is the volume of the nanoparticles nucleus, r is the radius of the nucleus, k_B is the Boltzman constant, T is the temperature in Kelvin, S is the ratio of reactant concentration to the solubility of the precipitant,[6] and γ is the surface free energy density of the nanoparticle.[7] The first term in this equation accounts for the change in bulk free energy and the second term accounts for the surface energy. When S is greater than one, the change in the bulk free energy is negative and the process of nucleation becomes energetically favorable. Whether a newly formed nucleus grows into a stable particle or dissolves back into solution depends on whether a threshold, or critical radius r^*, is reached.[7-9] The value of r^* corresponds to a maximum of the excess free energy and may be found by setting $d\Delta G/dr = 0$:

$$r^* = \frac{2V_{ppt}\gamma}{3k_B T \ln(S)}$$

Equation 1-2

By using this condition and substituting for V_{ppt} in the Gibbs free energy equation we arrive at the following relationship;

$$\Delta G = 4\pi r^2 \gamma \left(1 - \frac{2r}{3r^*}\right)$$

Equation 1-3

When $r > 1.5r^*$, ΔG is negative and the species will grow at a rate dependent upon its size; and when $r < 1.5r^*$, the free energy is positive so the species will dissolve back into solution. After r^* is exceeded, a focusing of the size distribution occurs because small NPs will grow more rapidly than large NPs. As the reactant becomes depleted, S becomes smaller and the critical radius increases. This results in a size dependent shrinking or dissolution of the smaller nanoparticles to enable continual growth of the larger NPs and consequently there is an increase in the nanoparticle size distribution. This phenomenon is known as Ostwald Ripening and can be overcome by additional injections of the reactant.[7-9]

The physical properties of semiconducting NPs change drastically as a function of size. Because of the quantum confinement effect a change in band gap occurs for NPs when the semiconductor's size is below the Bohr exciton radius.[10] This can be observed spectroscopically through steady-state absorbance and photoluminescence measurements. Figure 1-1 shows the evolution of absorbance (solid lines) and photoluminescence (dashed lines) spectra of trioctylphosphine oxide (TOPO) passivated cadmium selenide (CdSe) nanoparticles as a function of the reaction time. As the nanoparticles grow a redshift in the spectrum occurs resulting from a decrease in the semiconductor's bandgap.

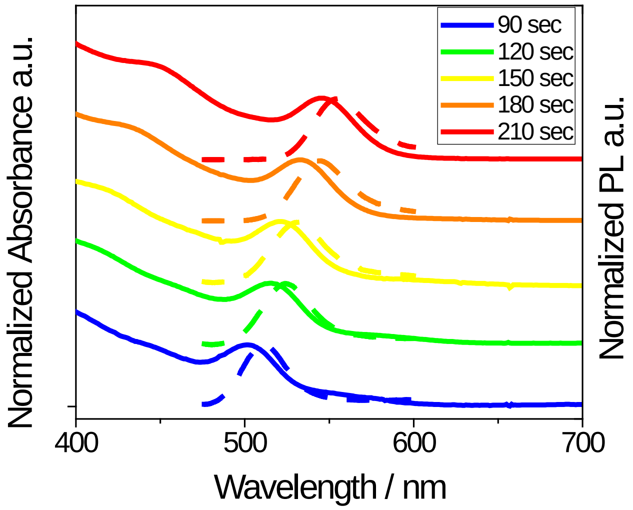

Figure 1-1. Shows the change in absorbance (solid lines) and photoluminescence (dashed lines) spectrum as a function of reaction time for TOPO passivated CdSe NPs. The progressive redshift with time is indicative of larger NP size which coincides with an increase in size.

1.3 Ligand Exchange and Electronic Properties

The organic molecules, referred to as ligands, used to passivate NPs during synthesis play an integral role in the thermodynamic growth process; however, they also impart physical properties onto the inorganic core. Therefore, the functionalization of NPs through post-synthetic modification of the native ligand has been an area of intense interest in the scientific community. Previous experiments have shown that the ligand plays a crucial role in determining the solubility,[11-13] photophysics,[14-16] exciton confinement energies,[17-19] charge transport properties,[20-22] and electronic energies of the NPs.[23,24]

1.3.1 Reaction Mechanism and Characterization

The process of ligand exchange has been described extensively in the works of Owens et al., in which the binding motifs are defined according to the covalent bond classification method.[25] Scheme 1-1 shows the different classes of reactions that nanoparticles of the type ME (where M = Green circle, Cd, Pb, etc. and E = Red Circle, S, Se, Te etc.) can undergo. In this scheme the M atom can either remain on the surface, as is the case in an X-type and L-type ligand exchange, or dissociate with the ligand during exchange, as shown in the Z-type reaction mechanism. Here, the X refers to an anionic binding substituent on the ligand such as a chlorine atom, thiol, or carboxylic acid group and L corresponds to a neutral donor ligand such as a phosphine or amine.

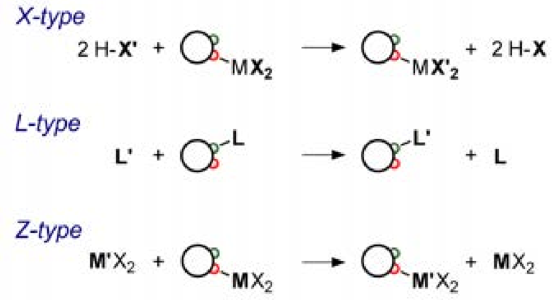

Scheme 1-1. Shows the classification of nanoparticle ligand exchange reactions by type where M = Green circle, Cd, Pb, etc, E = Red Circle, S, Se, Te etc, L is a neutral donor, and X is an anionic ligand.[25]

In order to confirm that the ligand exchange reaction took place, many different analytical techniques are employed. For example, FT-IR experiments have shown that the vibrational mode of a ligand decreases when bound to the surface of a NP and results in a broadening of the spectral peak.[26] Because the ligand orientation can vary when bound to the NP surface, multiple peaks at different frequencies can arise, which may aid in the characterization of the NP - ligand interaction.[27] One caveat of this technique is that it does not discriminate against free ligands in solution and can therefore give misleading results for unpurified samples.

Nuclear magnetic resonance (NMR) is another powerful technique that can be used for studying the surface structure of colloidal semiconductor NPs. Through monitoring a particular nuclear component of the ligand, much can be inferred about mechanistic properties of the nanoparticle synthesis and their change in surface passivation upon ligand exchange. One such example is the series of experiments by Liu et al. in which ^{1}H, ^{13}C, and ^{31}P - NMR spectroscopy determined the ligand's (tri-*n*-octylphosphine oxide and octadecylphosphonic acid) role as a nucleophile to initiate the growth of CdSe nanoparticles.[28,29] Confirmation of ligand exchange via NMR spectroscopy has a similar problem to FTIR; overlap of free ligand signal and ligand bound to the NP. Because the chemical shift arises from the deshielding of protons, the ligand bound to the NP surface often appears overlaps with the resonance of the free ligand. Broadening of the ligand peak because of a decrease in free rotation can imply a strong nanoparticle-ligand interaction; however this conclusion is not foolproof. Indeed, Hassinen et al. showed that ^{1}H NMR was inconclusive at determining the passivation of amine terminated ligands on CdSe nanoparticles, through line-broadening considerations alone.[30]

In order to separate the signal arising from ligands free in solution and those bound to the surface of the nanoparticle, pulsed field gradient NMR spectroscopy, also known as diffusion ordered NMR, is often used. In this technique, a well-defined pulsed magnetic field is used in tandem with the static magnetic field used in regular NMR. In the period between gradient pulses the species in solution diffuse causing a dephasing of the spin polarization, and hence a change in the spin-echo response.[31] The resonance signature of the species can be described using the bipolar Stejskal-Tanner equation;

$$I = I_0 e^{-D*g^2*\gamma^2*\delta^2\left(\Delta-\frac{\tau}{2}-\frac{\delta}{8}\right)} \qquad \textbf{Equation 1-4}$$

where I is the resulting signal intensity, I_0 is the signal intensity prior to the gradient pulse, D is the diffusion coefficient, g is the strength of the gradient pulse, γ is the gyromagnetic ratio, δ is the duration of the gradient pulse, and τ is the time between successive gradient pulses.[31] Because the signal attenuation is exponentially dependent on the diffusion coefficient, signal arising from small molecules, such as undeuterated solvent, water impurities, and free ligands, can be separated from the signal from slower diffusing ligands bound to the surface of a nanoparticle.[32] Figure 1-2A demonstrates how the diffusion coefficient of the different oleic acid (OA) resonances measured through diffusion ordered NMR techniques changes when it is free in solution (red) and bound to the surface of a 2.9 nm CdSe nanoparticle (blue).[33] Ligand exchanging the nanoparticles with octadecylphosphonic acid (ODPA) results in a decrease of the diffusion coefficient for the OA and thus, an attenuation of their peaks under a strong applied gradient pulse (Figure 1-2B). Using this approach, the degree of ligand exchange can be quantified; Figure 1-2C shows that gradual titration of an OA-CdSe sample with ODPA results in a progressive decrease in the ratio of bound OA:ODPA until only ODPA is present.[33]

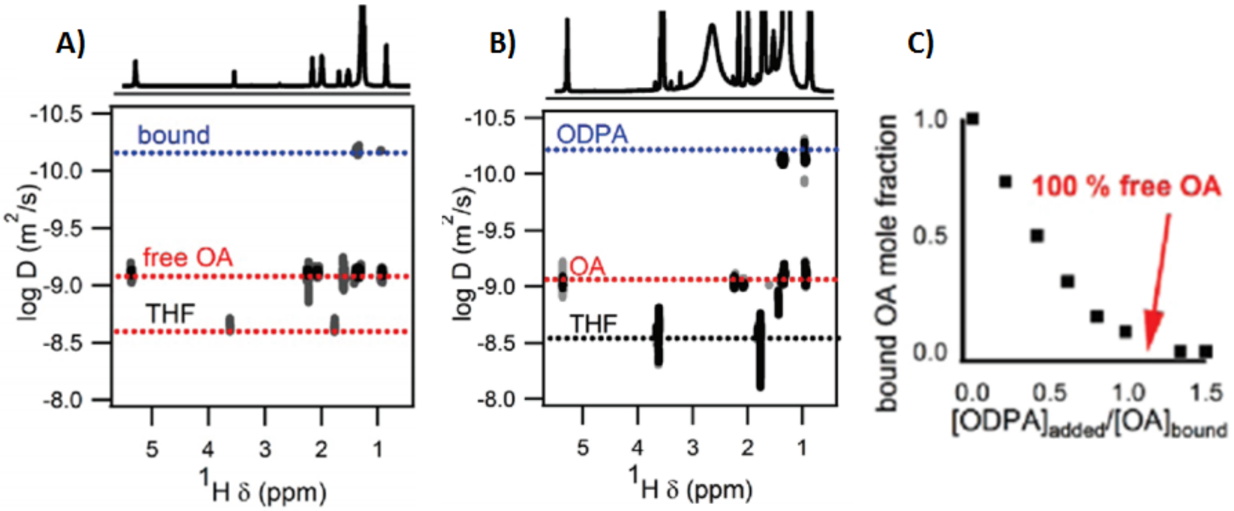

Figure 1-2. Panel A shows the difference in diffusion coefficient, determined through DOSY NMR, for the 1H NMR resonances of OA free in solution (red dashed line) and bound to the surface of a 2.9 nm CdSe nanoparticle (blue dashed line). Panel B shows that complete ligand exchange to ODPA results in the removal of the slowly

diffusing OA peaks. Panel C shows a titration experiment in which OA-CdSe is ligand exchanged with ODPA in a stepwise manner demonstrating the determination of the stoichiometric ratio of ligands on the surface of the nanoparticle for an incomplete ligand exchange.[33]

1.3.2 Role of Ligands on Nanoparticle Electronic State Energies

The ligands used for passivation can also play an integral role in determining the electronic state energies of the NP; experimental studies on PbS NPs have reported up to a 0.9 eV shift in the valence band maximum by chemically modifying the ligands.[23,34-36] As such, the use of different ligands has been shown to increase the efficiency in both photovoltaics[37,38] and fuel cell[39] applications. The origin of the electronic energy shift is attributed to the intrinsic dipole moment of the ligand "$P_{ligand, \perp}$" and the induced dipole moment associated with the NP-ligand bond "$P_{ind, \perp}$".[40] In this model, the energy shift of the electronic states, $\Delta E_{\perp}$, arising from the dipole is given by;

$$\Delta \mathrm{E}_{\perp} = \frac{\mathrm{P}_{\perp} e}{\mathrm{A}\varepsilon\varepsilon_0}$$ **Equation 1-5**

in which A is the surface area per ligand, ε is the dielectric constant of the ligand layer, and $P_{\perp}$ is the sum of the induced and intrinsic ligand dipole moments normal with respect to the nanoparticle surface.[40] Because the $P_{ind, \perp}$ tends to be much larger than the $P_{ligand, \perp}$ changing the surface binding group[23,41] tends to cause a larger change in the electronic state energies than changing the dipole moment of the ligand.[24,35,42]

Although other methods are utilized,[43,44] the two most commonly used techniques for determining the electronic state energies of inorganic nanocrystals are electrochemistry and photoelectron spectroscopy. While these methods are common and straightforward to implement, careful consideration must be paid to the interpretation of the data for appropriate analysis, *vide infra*.

1.3.2.1 Electrochemical Characterization

Electrochemical voltammetry methods, typically involving a three electrode electrochemical cell, are a common technique used for the determination of semiconductor band edges. The system works by varying the potential of a working electrode relative to that of a reference electrode while current flows between the working and counter electrodes. Common voltammetric techniques employed for the use of semiconducting nanoparticles include cyclic voltammetry and differential pulse voltammetry. As the potential is systematically changed, the species of interest can become oxidized, and / or reduced, which corresponds to a change in current. In cyclic voltammetry measurements, the potential is swept in a saw-tooth fashion, at a constant scan rate, for a predetermined number of cycles.[45] Conversely, differential pulse voltammetry is a type of linear sweep method that uses a periodic series of voltage pulses. Current is measured directly before, and at some time τ after each pulse, and the two currents are then subtracted to form a single point.[45,46] This method greatly reduces charging current that is often observed in cyclic voltammetry and thus increases peak resolution.[45]

Initial reports on the size dependent band edge shifts of CdSe NPs are inconsistent; discrepancies in the electronic state energies are on the order of 0.5 eV.[41,47-49] The origins of these differences can be attributed to three principle inconsistencies; improper conversion of the reference electrode to vacuum energy, failure to account for ligand induced electronic energy shifts, and using the peak, opposed to the onset, for the band edge determination. Because solvent type, the supporting electrolyte material and concentration, and potential drift of the reference electrode all influence the reference electrode to vacuum energy conversion it is important to set up an external standard.[50] Indeed, experimental studies show that the electrochemically determined onset for the valence band maximum of CdTe NPs agrees with UPS valence band maximums of the same NPs when appropriately referenced to a ferrocene/ferrocenium redox couple.[51]

1.3.2.2 Photoelectron Spectroscopy Characterization

Photoelectron spectroscopy is another powerful tool used in determining the electronic state energies of nanoparticles. The physical process of photoelectron spectroscopy can be described by a three-step model;[52,53]

1) Photoexcitation of electrons
2) Transport of photoelectrons to the sample-vacuum interface
3) Emission of photoelectrons into the vacuum

The photoelectron spectrum is a plot of the intensity (proportional to the number of electrons collected by the detector per second) as a function of the photoelectron kinetic energy (E_k). The energy spectrum is modeled according to the probability of the three processes as

$$\mathrm{Intensity} = \mathrm{P}(E_k, h\nu) * \mathrm{T}(E_k, h\nu) * \mathrm{D}(E_k) \qquad \textbf{Equation 1-6}$$

where $\mathrm{P}(E_k, \nu)$ corresponds to the energy distribution of the electrons in the sample following photoexcitation, $\mathrm{T}(E_k, \nu)$ is the material dependent transport length, similar to mean free path, for propagation of photoelectrons to the surface, and $\mathrm{D}(E_k)$ is the probability for emission of the photoelectrons.[53] When the transport and emission of photoelectrons is independent of the kinetic energy (within the energy range studied), the electronic states of the sample correspond directly to the first term, $\mathrm{P}(\mathrm{E}_k,\nu)$.[53] Satellite peaks arising from core state excitation and plasmon excitation are a part of the photoelectron spectrum, but occur at lower energies and can be excluded from the $\mathrm{P}(\mathrm{E}_k,\nu)$ term for simplicity.[53] Inelastic scattering during transport can affect the $T(E_k,\nu)$ term, however, this also results in low kinetic energy photoelectrons that do not contribute strongly to the important part of the spectrum.[53] Local vacuum level shifts, caused by a potential difference at the sample-vacuum interface, can change the energy probability term, $D(E_k)$, however, the effect is static and the function remains smooth.[54]

Ultraviolet radiation sources are advantageous for probing valence band or HOMO electronic states because the ionization occurs mostly for outer shell electrons with low binding energies. Although X-ray radiation can be used for valence determination, ultraviolet sources provide higher resolution because the source energy is associated with narrow atomic emission lines. The conduction band (or LUMO) electronic states can be extrapolated from a combination of the optical bandgap and exciton binding energy of the semiconductor.[41] Experimental determination of the conduction band has also been achieved through two photon photoelectron spectroscopy and inverse photoelectron spectroscopy techniques.[51,55]

Figure 1-3 shows a typical ultraviolet photoelectron (UPS) spectrum of a monolayer of PbS nanoparticles on an Au substrate with the different regions of the spectrum labeled. The left image shows a zoomed in portion of the onset region coinciding with the valence band maximum states of the PbS. The right image shows the full spectrum. The red dashed line in both spectra indicates the outer shell orbital contributions and the blue lines indicate the secondary electrons and core state emission processes. The secondary electron cut off, SECO, is the region in which photoelectrons no longer have enough energy to be emitted from the surface of the sample and collected by the detector. A more rigorous interpretation of the analysis is left for the appendix.

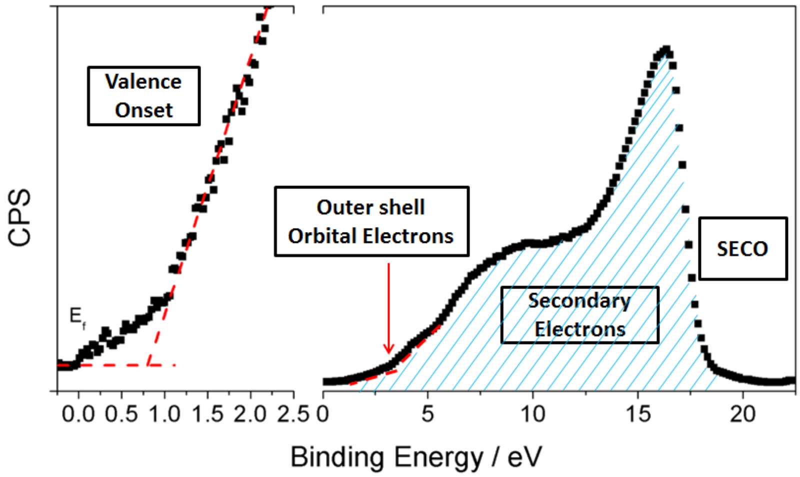

Figure 1-3. shows a UPS spectrum of a monolayer of PbS nanoparticles on an Au surface. The left image shows a zoomed in portion of the spectrum on the onset region and the right image shows the different of the full spectrum. The red dashed lines arise from outer shell electrons of the PbS nanoparticles and are used in the determination of the valence band maximum and the blue lines correspond to secondary electrons. The secondary electron cutoff is labeled “SECO”.

1.4 CHIRAL NANOPARTICLES AND SPIN SELECTIVE CHARGE TRANSPORT

Ligand passivation has also led to the imprinting of chirality onto the surface of semiconducting nanoparticles. Despite L-cysteine being used as a common ligand for the direct aqueous synthesis of CdTe since 2001,[56] the chiroptical properties of inorganic semiconductor NPs were not investigated until Gun’ko et al. in 2007.[57] In this study, CdS nanoparticles were synthesized with L- and D-penicillamine capping ligands through a microwave assisted technique. Circular dichroism spectra of the NPs showed mirror image spectra for the two enantiomers in the first excitonic peak region of the absorbance for the NPs; suggesting chiral imprinting of the ligand shell onto the electronic states of the CdS. Through a combination of density functional theory calculations[58,59] and experimental studies,[58,60] it was found that the origin of the chirality is associated with enantiomeric distortions of surface cadmium atoms by the ligands which translates chirality to the electronic structure of the NP.

More recently the synthesis of different types of chiral inorganic semiconductor NPs (CdSe and CdTe) passivated with different ligands (glutathione, cysteine, n-acetyl-cysteine, homocysteine, cysteine-methylester) has also been shown experimentally.[61-67] Figure 1-4 shows circular dichroism (solid lines) and absorption (dashed lines) spectra of CdSe and CdTe NPs passivated with L-cysteine (red) and D-cysteine (black) ligands. Differences in crystal structure (wurtzite for CdSe and Zinc Blende for CdTe) have been shown to influence the circular dichroism signal orientation and a similar mechanism may be responsible for the differences observed for CdSe and CdTe in Figure 1-4.[66] New synthetic pathways for fabricating chiral NPs have also been realized; Balaz et al. has shown that NPs become chiral through simple post-synthetic ligand exchange when the achiral native ligand is exchanged with something chiral.[65,66] The increasing synthetic flexibility of chiral NPs, in conjunction with their interesting chiroptical properties, open up the possibility for new applications in sensing, enantiomeric separation, catalysis, cell imaging, sources for circularly polarized light, spintronics, and photovoltaics.[68]

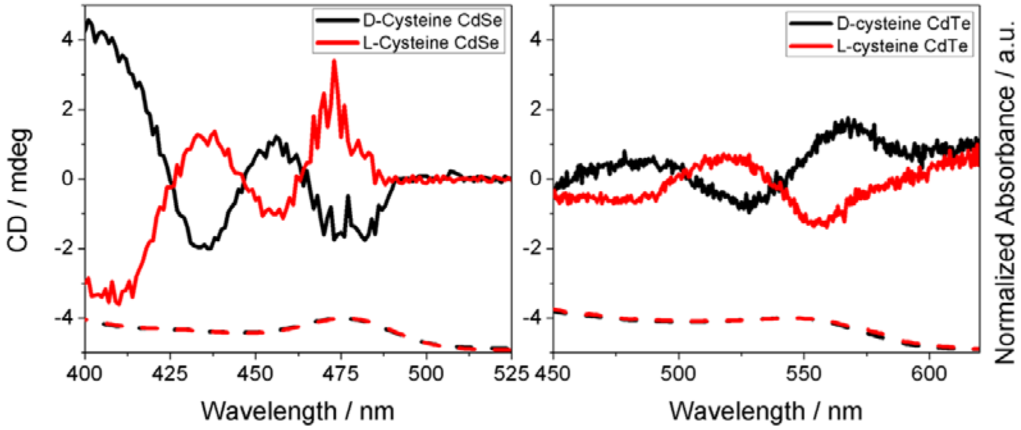

Figure 1-4. shows representative absorbance (dashed lines) and circular dichroism (solid lines) spectra of L-cysteine (red) and D-cysteine (black) passivated 2.1 nm CdSe NPs (left) and 3.2 nm CdTe NPs (right).

1.4.1 Chiral Induced Spin Selectivity

One particular area where chiral NPs hold great potential is for spin selective charge transport applications; through utilization of the chiral induced spin selectivity (CISS) effect.[69,70] The operating principles for the CISS effect are analogous to that of Faraday's law of induction; however, instead of magnetic flux generated through a wire loop around a magnetic core causing an electromotive force, the chiral helix acts as a fixed potential field and the momentum and spin of the electron through the vector-space generates a magnetic field parallel or antiparallel to the electron's momentum. The strength of the magnetic field vector, $\overrightarrow{\beta,}$ can be calculated using Equation 1-7;

$$\vec{\beta} = \frac{\vec{v}}{c^2}\,\mathrm{x}\,\vec{E} \qquad \textbf{Equation 1-7}$$

where $\vec{v}$ is the velocity of the electron, c is the speed of light, and $\vec{E}$ is the electric field vector associated with the chiral molecule acting upon the electron.[69] Because the linear momentum of an electron is coupled to its spin, the efficiency for charge transport becomes strongly dependent upon the spin orientation relative to the magnetization, $\vec{\beta}$.[69] This is often described by a Rashba spin orbit coupling term, equation 1-8, and demonstrates the dependence of the chiral helical field for producing spin selectivity.[69]

$$H_{SO} = \lambda\vec{\sigma}\left(\vec{p}\,\mathrm{x}\,\vec{E}\right) \qquad \textbf{Equation 1-8}$$

H_{so} is the spin orbit coupling Hamiltonian, λ=(e$\hbar$)/(4m^{2}c^2), $\vec{\sigma}$ is the Pauli matrices vector, and $\vec{p}$ is the momentum of the electron. An energy scheme associated with transmission of a freely propagating electron is shown in Figure 1-5.[69] Four different potential states arise as a result of the electron's momentum and spin. The first variable is associated with the momentum, (+) denotes momentum in the positive direction and (-) denotes that the momentum of the electron is in the negative direction. The second variable is associated with the spin of the electron, (+) for spin up and (-) for spin down. For a left handed helix, the transmission of an electron in the positive direction with an up (down) spin is stabilized (destabilized) by the energy associated with the spin orbit coupling. Additionally, the l+,+> state in the energy scheme is degenerate with the l-,-> state; indicating that an electron of the opposite spin propagating in the negative direction is equally stabilized.

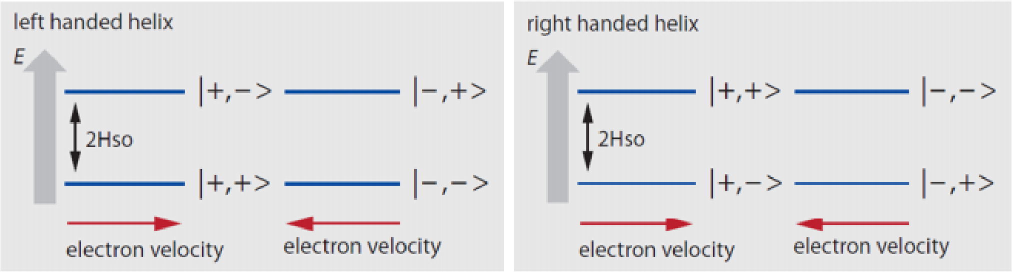

Figure 1-5. shows an energy scheme of the momentum spin states, lmomentum, spin>, for the transmission of an electron through the chiral potential field of a helix.[69]

The first experimental proof for the CISS effect was shown in 1999 by measuring the energy distribution of electrons photoexcited from an Au substrate through chiral monolayer films. When the photoelectrons were emitted using circularly polarized light, the intensity profile was strongly dependent upon the light polarization, clockwise versus counter clockwise, and the chirality of the film.[71] A few years later, spin dependent electron transmission below the vacuum was shown experimentally by measuring the asymmetry in photocurrent produced from porphyrin terminated chiral scaffolds.[72] For scaffolds constructed with the S-enantiomer, a higher photocurrent was observed with counterclockwise circularly polarized light. Conversely, for scaffolds of the R-enantiomer configuration, clockwise circularly polarized light produced the higher photocurrent.

Since these fundamental experiments the CISS effect has been demonstrated for helical DNA,[73-77] α-helical peptides,[78-80] helicenes,[81] amongst other biomolecules.[82,83] Different techniques for observing a change in the spin polarization with chirality has also been established; magnetic conductive probe AFM,[76,79] magnetoresistance within a device,[81] photo induced current changes,[74,77,80] as well as voltammetry techniques.[79,82,83] The underlying principles of these experiments rely on magnetization of a ferromagnetic electrode as a spin source. For example when Ni is under an external magnetic field the spin sub-bands lose their degeneracy and split; aligning the spins in one orientation over the other. Once magnetized, the ferromagnetic electrode can only give (receive) a particular spin. When coupled with a spin filter, this gives rise to an on / off process that depends only on external magnetic field, Figure 1-6. Despite CISS still being a wholly new effect, this phenomenon offers promise for applications in spintronics, water splitting, photovoltaics, and other spin-driven devices.

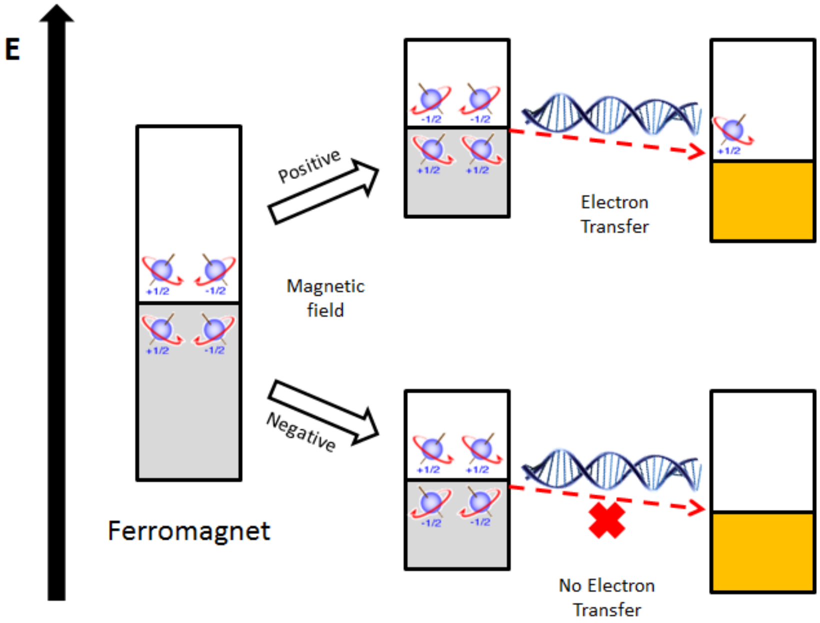

Figure 1-6. shows how the sub-bands of a ferromagnet split under a magnetic field and how that can be used in tandem with a spin filter to generate an on / off process.

1.5 NANOPARTICLE THIN FILMS AND INTERFACIAL PROPERTIES

One of the most advantageous properties of semiconductor NPs remains the simplicity involved with the processing of thin films. Common techniques include layer-by-layer assembly and spin coating of colloidal NP solutions or the direct growth of NP films by chemical bath deposition through successive ionic layer adsorption and reaction (SILAR).[84,85] Spin coating remains the most common, and successful, method for thin film fabrication because of the ability for post-deposition ligand modification; enabling the tuning of energy levels, conductivity, and exciton diffusion lengths.[3] Composite devices consisting of NP-polymeric blends can also be spin coated and allow for the development of alternative hybrid bulk heterojunction devices.[38]

The efficiency of a device remains largely dependent upon the charge separation of the photoexcited NPs. Interfacial regions, such as intralayer grain boundries in the photoactive material, junctions between donor and acceptor species, and contacts between the photoactive material and transport layers or electrodes, all have profound influences on charge transport.[86] While post-deposition ligand exchange has mitigated the intralayer boundaries by increasing conductivity and diffusion length, other interfaces still act as recombination centers and can limit overall efficiency. Progress towards improved charge separation in donor-acceptor systems has also been achieved in solution[22,87] and within devices[88,89] using electric field effects to drive the electron and hole in opposite directions.

When NPs are interfaced with metal contacts or transport layers, a phenomenon known as Fermi-level pinning can occur. In this phenomenon charge exchange creates an electric field that ‘pins’ the semiconductor bandedge to the Fermi level of the adjacent material. The origin of this effect was found to arise from surface state defects on the NP and has been observed experimentally for PbS,[43,90] PbSe,[91] CdSe,[92-95] and CdTe NPs.[51] By minimizing these defects it is thought that the current open-circuit voltage deficit in photovoltaic devices can be overcome.[96] Strategies to eliminate the surface state defects in semiconductor NPs, and subsequently eliminate Fermi-level pinning, have focused on the addition of a wide bandgap oxide or semiconductor which forms a core-shell type nanoparticle.[97,98] While this approach has been shown to improve the open-circuit voltage, the conductivity of the film suffers from the insulating shell.

1.6 DISSERTATION OUTLINE

In order to gain a more fundamental understanding of the role ligands play in the physics of semiconductor NPs this thesis aims to address the following questions; 1) how do the electronic state energies of NPs evolve as a function of size for different ligands? 2) Can a thin insulating film replace the role of an insulating shell on NPs to inhibit Fermi-level pinning? 3) Can chiral ligands on NPs be used as spin selective filters? And 4) what photophysics dictate charge transport in nanoparticle dyad composites? The work in this thesis addresses the influence of ligands in semiconductor NPs and establishes a means to explore their properties in designer systems.

Chapter 2 discusses our work on the ligand induced changes on the size dependent electronic state energies of CdSe NPs. It reveals that the changing surface-to-volume ratio of the NP with size is instrumental in determining the degree of destabilization or stabilization of the electronic state energies. It also suggests that under common passivation the HOMO can be localized on the ligand and not on the NP. The valence band of the NP was determined through differential pulse voltammetry and the findings were corroborated with theoretical simulations on CdSe nanoclusters. This fundamental study is important for determining the correct band structure of CdSe NPs.

Chapter 3 discusses our work on the Fermi-level pinning of PbS NPs on Au substrates with and without a thin alumina interfacial layer. Cyclic voltammetry and ultraviolet photoelectron spectroscopy measurements show that on bare Au substrates the electronic state energies of PbS remain relatively unchanged with size and ligand type. When 3 nm of alumina is inserted between the NPs and the metal substrate Fermi-level pinning is alleviated and the size dependent and ligand dependent properties of the NPs are restored. This work demonstrates a simple methodology for eliminating Fermi-level pinning without changing the inherent properties of the NPs.

Chapter 4 shows our results on the conduction of electrons through chiral imprinted CdSe NPs. Magnetic conductive probe AFM results show that the chirality of the NP and the magnetization of the tip strongly affect the current-voltage curves. These findings were validated by magnetoresistance measurements which demonstrate that electron transport through chiral NP thin films correlate with the chiroptical properties of the NP. The spin selective filtering properties of the NPs are in agreement with the chiral induced spin selectivity effect and may prove useful in spin driven applications.

Chapter 5 discusses our work on charge transport between donor and acceptor NPs templated on a silica microsphere measured using time-resolved fluorescence techniques. Through a change in NP surface passivation, the distance between the donor and acceptor could be modulated, and the electron transfer rate was found to be consistent with an electron tunneling mechanism. Through careful tuning of the acceptor NP size the effect of a change in band offset between donor and acceptor was studied. These results show that the dependence of charge transfer rate on reaction Gibbs energy is consistent with a Marcus theory model. The findings from this study elucidate an appropriate mechanism for describing charge transfer in NP donor-bridge-acceptor systems and introduce a new approach for their assembly.

1.7 REFERENCES

(1) Chuang, C.-H. M.; Brown, P. R.; Bulović, V.; Bawendi, M. G.: Improved performance and stability in quantum dot solar cells through band alignment engineering. *Nat Mater* **2014**, *13*, 796-801.

(2) Zhang, H.; Yang, J.; Chen, J.-R.; Engstrom, J. R.; Hanrath, T.; Wise, F. W.: Tuning of Coupling and Surface Quality of PbS Nanocrystals via a Combined Ammonium Sulfide and Iodine Treatment. *The Journal of Physical Chemistry Letters* **2016**, *7*, 642-646.

(3) Zhitomirsky, D.; Voznyy, O.; Hoogland, S.; Sargent, E. H.: Measuring Charge Carrier Diffusion in Coupled Colloidal Quantum Dot Solids. *ACS Nano* **2013**, *7*, 5282-5290.

(4) Ip, A. H.; Thon, S. M.; Hoogland, S.; Voznyy, O.; Zhitomirsky, D.; Debnath, R.; Levina, L.; Rollny, L. R.; Carey, G. H.; Fischer, A.; Kemp, K. W.; Kramer, I. J.; Ning, Z.; Labelle, A. J.; Chou, K. W.; Amassian, A.; Sargent, E. H.: Hybrid passivated colloidal quantum dot solids. *Nat Nano* **2012**, *7*, 577-582.

(5) Peng, X.; Wickham, J.; Alivisatos, A. P.: Kinetics of II-VI and III-V Colloidal Semiconductor Nanocrystal Growth: "Focusing" of Size Distributions. *J. Am. Chem. Soc* **1998**, *120*, 5343-5344.

(6) Capek, R. K.; Lambert, K.; Dorfs, D.; Smet, P. F.; Poelman, D.; Eychmuı̀ˆller, A.; Hens, Z.: Synthesis of Extremely Small CdSe and Bright Blue Luminescent CdSe/ZnS Nanoparticles by a Prefocused Hot-Injection Approach. *Chem. Mater.* **2009**, *21*, 1743-1749.

(7) Burda, C.; Chen, X.; Narayanan, R.; El-Sayed, M. A.: Chemistry and Properties of Nanocrystals of Different Shapes. *Chem. Rev.* **2005**, *105*, 1025-1102.

(8) Talapin, D. V.; Rogach, A. L.; Haase, M.; Weller, H.: Evolution of an Ensemble of Nanoparticles in a Colloidal Solution:ATheoretical Study. *J. Phys. Chem. B* **2001**, *105*, 12278-12285.

(9) Zeng, J.; Wang, X.; Hou, J. G.: *Colloidal Hybrid Nanocrystals: Synthesis, Properties, and Perspectives*, **2011**.

(10) Brus, L.: Electronic wave functions in semiconductor clusters: experiment and theory. *The Journal of Physical Chemistry* **1986**, *90*, 2555-2560.

(11) Dorokhin, D.; Tomczak, N.; Han, M.; Reinhoudt, D. N.; Velders, A. H.; Vancso, G. J.: Reversible Phase Transfer of (CdSe/ZnS) Quantum Dots between Organic and Aqueous Solutions. *ACS Nano* **2009**, *3*, 661-667.

(12) Zylstra, J.; Amey, J.; Miska, N. J.; Pang, L.; Hine, C. R.; Langer, J.; Doyle, R. P.; Maye, M. M.: A Modular Phase Transfer and Ligand Exchange Protocol for Quantum Dots. *Langmuir* **2011**, *27*, 4371-4379.

(13) Gaponik, N.; Talapin, D. V.; Rogach, A. L.; Eychmüller, A.; Weller, H.: Efficient Phase Transfer of Luminescent Thiol-Capped Nanocrystals: From Water to Nonpolar Organic Solvents. *Nano Letters* **2002**, *2*, 803-806.

(14) Wuister, S. F.; de Mello Donegá, C.; Meijerink, A.: Influence of Thiol Capping on the Exciton Luminescence and Decay Kinetics of CdTe and CdSe Quantum Dots. *The Journal of Physical Chemistry B* **2004**, *108*, 17393-17397.

(15) Bullen, C.; Mulvaney, P.: The Effects of Chemisorption on the Luminescence of CdSe Quantum Dots. *Langmuir* **2006**, *22*, 3007-3013.

(16) Knowles, K. E.; Tice, D. B.; McArthur, E. A.; Solomon, G. C.; Weiss, E. A.: Chemical Control of the Photoluminescence of CdSe Quantum Dot−Organic Complexes with a Series of Para-Substituted Aniline Ligands. *Journal of the American Chemical Society* **2010**, *132*, 1041-1050.

(17) Frederick, M. T.; Weiss, E. A.: Relaxation of Exciton Confinement in CdSe Quantum Dots by Modification with a Conjugated Dithiocarbamate Ligand. *ACS Nano* **2010**, *4*, 3195-3200.

(18) Frederick, M. T.; Amin, V. A.; Swenson, N. K.; Ho, A. Y.; Weiss, E. A.: Control of Exciton Confinement in Quantum Dot–Organic Complexes through Energetic Alignment of Interfacial Orbitals. *Nano Letters* **2013**, *13*, 287-292.

(19) Peterson, M. D.; Cass, L. C.; Harris, R. D.; Edme, K.; Sung, K.; Weiss, E. A.: The Role of Ligands in Determining the Exciton Relaxation Dynamics in Semiconductor Quantum Dots. *Annual Review of Physical Chemistry* **2014**, *65*, 317-339.

(20) Li, X.; Huang, Z.; Zavala, R.; Tang, M. L.: Distance-Dependent Triplet Energy Transfer between CdSe Nanocrystals and Surface Bound Anthracene. *The Journal of Physical Chemistry Letters* **2016**, 1955-1959.

(21) Dibbell, R. S.; Watson, D. F.: Distance-Dependent Electron Transfer in Tethered Assemblies of CdS Quantum Dots and TiO2 Nanoparticles. *The Journal of Physical Chemistry C* **2009**, *113*, 3139-3149.

(22) Wu, M.; Mukherjee, P.; Lamont, D. N.; Waldeck, D. H.: Electron Transfer and Fluorescence Quenching of Nanoparticle Assemblies. *The Journal of Physical Chemistry C* **2010**, *114*, 5751-5759.

(23) Brown, P. R.; Kim, D.; Lunt, R. R.; Zhao, N.; Bawendi, M. G.; Grossman, J. C.; Bulović, V.: Energy Level Modification in Lead Sulfide Quantum Dot Thin Films through Ligand Exchange. *ACS Nano* **2014**, *8*, 5863-5872.

(24) Soreni-Harari, M.; Yaacobi-Gross, N.; Steiner, D.; Aharoni, A.; Banin, U.; Millo, O.; Tessler, N.: Tuning Energetic Levels in Nanocrystal Quantum Dots through Surface Manipulations. *Nano Letters* **2008**, *8*, 678-684.

(25) Anderson, N. C.; Hendricks, M. P.; Choi, J. J.; Owen, J. S.: Ligand Exchange and the Stoichiometry of Metal Chalcogenide Nanocrystals: Spectroscopic Observation of Facile Metal-Carboxylate Displacement and Binding. *Journal of the American Chemical Society* **2013**, *135*, 18536-18548.

(26) Morris-Cohen, A. J.; Malicki, M.; Peterson, M. D.; Slavin, J. W. J.; Weiss, E. A.: Chemical, Structural, and Quantitative Analysis of the Ligand Shells of Colloidal Quantum Dots. *Chemistry of Materials* **2013**, *25*, 1155-1165.

(27) Meulenberg, R. W.; Strouse, G. F.: Chain Packing Analysis of the Passivating Layer on Nanocrystalline Quantum Dot Surfaces. *The Journal of Physical Chemistry B* **2001**, *105*, 7438-7445.

(28) Liu, H.; Owen, J. S.; Alivisatos, A. P.: Mechanistic Study of Precursor Evolution in Colloidal Group II−VI Semiconductor Nanocrystal Synthesis. *Journal of the American Chemical Society* **2007**, *129*, 305-312.

(29) García-Rodríguez, R.; Hendricks, M. P.; Cossairt, B. M.; Liu, H.; Owen, J. S.: Conversion Reactions of Cadmium Chalcogenide Nanocrystal Precursors. *Chemistry of Materials* **2013**, *25*, 1233-1249.

(30) Hassinen, A.; Moreels, I.; de Mello Donegá, C.; Martins, J. C.; Hens, Z.: Nuclear Magnetic Resonance Spectroscopy Demonstrating Dynamic Stabilization of CdSe Quantum Dots by Alkylamines. *The Journal of Physical Chemistry Letters* **2010**, *1*, 2577-2581.

(31) Price, W. S.: Pulsed-field gradient nuclear magnetic resonance as a tool for studying translational diffusion: Part 1. Basic theory. *Concepts in Magnetic Resonance* **1997**, *9*, 299-336.

(32) Hens, Z.; Martins, J. C.: A Solution NMR Toolbox for Characterizing the Surface Chemistry of Colloidal Nanocrystals. *Chemistry of Materials* **2013**, *25*, 1211-1221.

(33) Gomes, R.; Hassinen, A.; Szczygiel, A.; Zhao, Q.; Vantomme, A.; Martins, J. C.; Hens, Z.: Binding of Phosphonic Acids to CdSe Quantum Dots: A Solution NMR Study. *The Journal of Physical Chemistry Letters* **2011**, *2*, 145-152.

(34) Crisp, R. W.; Kroupa, D. M.; Marshall, A. R.; Miller, E. M.; Zhang, J.; Beard, M. C.; Luther, J. M.: Metal Halide Solid-State Surface Treatment for High Efficiency PbS and PbSe QD Solar Cells. *Scientific Reports* **2015**, *5*, 9945.

(35) Santra, P. K.; Palmstrom, A. F.; Tanskanen, J. T.; Yang, N.; Bent, S. F.: Improving Performance in Colloidal Quantum Dot Solar Cells by Tuning Band Alignment through Surface Dipole Moments. *The Journal of Physical Chemistry C* **2015**, *119*, 2996-3005.

(36) Axnanda, S.; Scheele, M.; Crumlin, E.; Mao, B.; Chang, R.; Rani, S.; Faiz, M.; Wang, S.; Alivisatos, A. P.; Liu, Z.: Direct Work Function Measurement by Gas Phase Photoelectron Spectroscopy and Its Application on PbS Nanoparticles. *Nano Letters* **2013**, *13*, 6176-6182.

(37) Albero, J.; Martinez-Ferrero, E.; Iacopino, D.; Vidal-Ferran, A.; Palomares, E.: Interfacial charge transfer dynamics in CdSe/dipole molecules coated quantum dot polymer blends. *Physical Chemistry Chemical Physics* **2010**, *12*, 13047-13051.

(38) Greaney, M. J.; Das, S.; Webber, D. H.; Bradforth, S. E.; Brutchey, R. L.: Improving Open Circuit Potential in Hybrid P3HT:CdSe Bulk Heterojunction Solar Cells via Colloidal tert-Butylthiol Ligand Exchange. *ACS Nano* **2012**, *6*, 4222-4230.

(39) Wang, P.; Zhang, J.; He, H.; Xu, X.; Jin, Y.: The important role of surface ligand on CdSe/CdS core/shell nanocrystals in affecting the efficiency of H2 photogeneration from water. *Nanoscale* **2015**, *7*, 5767-5775.

(40) Yang, S.; Prendergast, D.; Neaton, J. B.: Tuning Semiconductor Band Edge Energies for Solar Photocatalysis via Surface Ligand Passivation. *Nano Letters* **2012**, *12*, 383-388.

(41) Jasieniak, J.; Califano, M.; Watkins, S. E.: Size-Dependent Valence and Conduction Band-Edge Energies of Semiconductor Nanocrystals. *ACS Nano* **2011**, *5*, 5888-5902.

(42) Shalom, M.; Rühle, S.; Hod, I.; Yahav, S.; Zaban, A.: Energy Level Alignment in CdS Quantum Dot Sensitized Solar Cells Using Molecular Dipoles. *Journal of the American Chemical Society* **2009**, *131*, 9876-9877.

(43) Gao, J.; Luther, J. M.; Semonin, O. E.; Ellingson, R. J.; Nozik, A. J.; Beard, M. C.: Quantum Dot Size Dependent J−V Characteristics in Heterojunction ZnO/PbS Quantum Dot Solar Cells. *Nano Letters* **2011**, *11*, 1002-1008.

(44) Kundu, B.; Chakrabarti, S.; Pal, A. J.: Redox Levels of Dithiols in II–VI Quantum Dots vis-à-vis Photoluminescence Quenching: Insight from Scanning Tunneling Spectroscopy. *Chemistry of Materials* **2014**, *26*, 5506-5513.

(45) Bard, A. J.; Ding, Z.; Myung, N.: Electrochemistry and Electrogenerated Chemiluminescence of Semiconductor Nanocrystals in Solutions and in Films. In *Semiconductor Nanocrystals and Silicate Nanoparticles*; Peng, X., Mingos, D. M. P., Eds.; Springer Berlin Heidelberg: Berlin, Heidelberg, **2005**; pp 1-57.

(46) Aoki, K.; Tokuda, K.; Matsuda, H.: Theory of Differential Pulse Voltammetry at Stationary Planar Electrodes. *J Electroanal Chem* **1984**, *175*, 1-13.

(47) Kucur, E.; Riegler, J.; Urban, G. A.; Nann, T.: Determination of quantum confinement in CdSe nanocrystals by cyclic voltammetry. *The Journal of Chemical Physics* **2003**, *119*, 2333-2337.

(48) Querner, C.; Reiss, P.; Sadki, S.; Zagorska, M.; Pron, A.: Size and ligand effects on the electrochemical and spectroelectrochemical responses of CdSe nanocrystals. *Physical Chemistry Chemical Physics* **2005**, *7*, 3204-3209.

(49) Inamdar, S. N.; Ingole, P. P.; Haram, S. K.: Determination of Band Structure Parameters and the Quasi-Particle Gap of CdSe Quantum Dots by Cyclic Voltammetry. *ChemPhysChem* **2008**, *9*, 2574-2579.

(50) Connelly, N. G.; Geiger, W. E.: Chemical Redox Agents for Organometallic Chemistry. *Chemical Reviews* **1996**, *96*, 877-910.

(51) Wang, Y.; Xie, Z.; Gotesman, G.; Wang, L.; Bloom, B. P.; Markus, T. Z.; Oron, D.; Naaman, R.; Waldeck, D. H.: Determination of the Electronic Energetics of CdTe Nanoparticle Assemblies on Au Electrodes by Photoemission, Electrochemical, and Photocurrent Studies. *The Journal of Physical Chemistry C* **2012**, *116*, 17464-17472.

(52) Berglund, C. N.; Spicer, W. E.: Photoemission Studies of Copper and Silver: Theory. *Physical Review* **1964**, *136*, A1030-A1044.

(53) Suga, S.; Sekiyama, A.: Photoelectron Spectroscopy; Bulk and Surface Electronic Structure. *Springer Series in Optical Sciences* **2014**, *176*, 1-396.

(54) Cahen, D.; Kahn, A.: Electron Energetics at Surfaces and Interfaces: Concepts and Experiments. *Advanced Materials* **2003**, *15*, 271-277.

(55) Miller, E. M.; Kroupa, D. M.; Zhang, J.; Schulz, P.; Marshall, A. R.; Kahn, A.; Lany, S.; Luther, J. M.; Beard, M. C.; Perkins, C. L.; van de Lagemaat, J.: Revisiting the Valence and Conduction Band Size Dependence of PbS Quantum Dot Thin Films. *ACS Nano* **2016**, *10*, 3302-3311.

(56) Gaponik, N.; Talapin, D. V.; Rogach, A. L.; Hoppe, K.; Shevchenko, E. V.; Kornowski, A.; Eychmüller, A.; Weller, H.: Thiol-Capping of CdTe Nanocrystals: An Alternative to Organometallic Synthetic Routes. *The Journal of Physical Chemistry B* **2002**, *106*, 7177-7185.

(57) Moloney, M. P.; Gun'ko, Y. K.; Kelly, J. M.: Chiral highly luminescent CdS quantum dots. *Chemical Communications* **2007**, 3900-3902.

(58) Zhou, Y.; Yang, M.; Sun, K.; Tang, Z.; Kotov, N. A.: Similar Topological Origin of Chiral Centers in Organic and Nanoscale Inorganic Structures: Effect of Stabilizer Chirality

on Optical Isomerism and Growth of CdTe Nanocrystals. *Journal of the American Chemical Society* **2010**, *132*, 6006-6013.

(59) Elliott, S. D.; Moloney, M. P.; Gun’ko, Y. K.: Chiral Shells and Achiral Cores in CdS Quantum Dots. *Nano Letters* **2008**, *8*, 2452-2457.

(60) Nakashima, T.; Kobayashi, Y.; Kawai, T.: Optical Activity and Chiral Memory of Thiol-Capped CdTe Nanocrystals. *Journal of the American Chemical Society* **2009**, *131*, 10342-10343.

(61) Li, Y.; Zhou, Y.; Wang, H.-Y.; Perrett, S.; Zhao, Y.; Tang, Z.; Nie, G.: Chirality of Glutathione Surface Coating Affects the Cytotoxicity of Quantum Dots. *Angewandte Chemie International Edition* **2011**, *50*, 5860-5864.

(62) Zhou, Y.; Zhu, Z.; Huang, W.; Liu, W.; Wu, S.; Liu, X.; Gao, Y.; Zhang, W.; Tang, Z.: Optical Coupling Between Chiral Biomolecules and Semiconductor Nanoparticles: Size-Dependent Circular Dichroism Absorption. *Angewandte Chemie* **2011**, *123*, 11658-11661.

(63) Gallagher, S. A.; Moloney, M. P.; Wojdyla, M.; Quinn, S. J.; Kelly, J. M.; Gun'ko, Y. K.: Synthesis and spectroscopic studies of chiral CdSe quantum dots. *Journal of Materials Chemistry* **2010**, *20*, 8350-8355.

(64) Ben Moshe, A.; Szwarcman, D.; Markovich, G.: Size Dependence of Chiroptical Activity in Colloidal Quantum Dots. *ACS Nano* **2011**, *5*, 9034-9043.

(65) Tohgha, U.; Varga, K.; Balaz, M.: Achiral CdSe quantum dots exhibit optical activity in the visible region upon post-synthetic ligand exchange with d- or l-cysteine. *Chemical Communications* **2013**, *49*, 1844-1846.

(66) Tohgha, U.; Deol, K. K.; Porter, A. G.; Bartko, S. G.; Choi, J. K.; Leonard, B. M.; Varga, K.; Kubelka, J.; Muller, G.; Balaz, M.: Ligand Induced Circular Dichroism and Circularly Polarized Luminescence in CdSe Quantum Dots. *ACS Nano* **2013**, *7*, 11094-11102.

(67) Choi, J. K.; Haynie, B. E.; Tohgha, U.; Pap, L.; Elliott, K. W.; Leonard, B. M.; Dzyuba, S. V.; Varga, K.; Kubelka, J.; Balaz, M.: Chirality Inversion of CdSe and CdS Quantum Dots without Changing the Stereochemistry of the Capping Ligand. *ACS Nano* **2016**, *10*, 3809-3815.

(68) Milton, F. P.; Govan, J.; Mukhina, M. V.; Gun'ko, Y. K.: The chiral nano-world: chiroptically active quantum nanostructures. *Nanoscale Horizons* **2016**, *1*, 14-26.

(69) Naaman, R.; Waldeck, D. H.: Chiral-Induced Spin Selectivity Effect. *The Journal of Physical Chemistry Letters* **2012**, *3*, 2178-2187.

(70) Naaman, R.; Waldeck, D. H.: Spintronics and Chirality: Spin Selectivity in Electron Transport Through Chiral Molecules. *Annual Review of Physical Chemistry* **2015**, *66*, 263-281.

(71) Ray, K.; Ananthavel, S. P.; Waldeck, D. H.; Naaman, R.: Asymmetric Scattering of Polarized Electrons by Organized Organic Films of Chiral Molecules. *Science* **1999**, *283*, 814-816.

(72) Wei, J. J.; Schafmeister, C.; Bird, G.; Paul, A.; Naaman, R.; Waldeck, D. H.: Molecular Chirality and Charge Transfer through Self-Assembled Scaffold Monolayers. *The Journal of Physical Chemistry B* **2006**, *110*, 1301-1308.

(73) Göhler, B.; Hamelbeck, V.; Markus, T. Z.; Kettner, M.; Hanne, G. F.; Vager, Z.; Naaman, R.; Zacharias, H.: Spin Selectivity in Electron Transmission Through Self-Assembled Monolayers of Double-Stranded DNA. *Science* **2011**, *331*, 894-897.

(74) Senthil Kumar, K.; Kantor-Uriel, N.; Mathew, S. P.; Guliamov, R.; Naaman, R.: A device for measuring spin selectivity in electron transfer. *Physical Chemistry Chemical Physics* **2013**, *15*, 18357-18362.

(75) Ray, S. G.; Daube, S. S.; Leitus, G.; Vager, Z.; Naaman, R.: Chirality-Induced Spin-Selective Properties of Self-Assembled Monolayers of DNA on Gold. *Physical Review Letters* **2006**, *96*, 036101.

(76) Xie, Z.; Markus, T. Z.; Cohen, S. R.; Vager, Z.; Gutierrez, R.; Naaman, R.: Spin Specific Electron Conduction through DNA Oligomers. *Nano Letters* **2011**, *11*, 4652-4655.

(77) Peer, N.; Dujovne, I.; Yochelis, S.; Paltiel, Y.: Nanoscale Charge Separation Using Chiral Molecules. *ACS Photonics* **2015**, *2*, 1476-1481.

(78) Carmeli, I.; Skakalova, V.; Naaman, R.; Vager, Z.: Magnetization of Chiral Monolayers of Polypeptide: A Possible Source of Magnetism in Some Biological Membranes. *Angewandte Chemie International Edition* **2002**, *41*, 761-764.

(79) Kettner, M.; Göhler, B.; Zacharias, H.; Mishra, D.; Kiran, V.; Naaman, R.; Fontanesi, C.; Waldeck, D. H.; Sęk, S.; Pawłowski, J.; Juhaniewicz, J.: Spin Filtering in Electron Transport Through Chiral Oligopeptides. *The Journal of Physical Chemistry C* **2015**, *119*, 14542-14547.

(80) Mtangi, W.; Kiran, V.; Fontanesi, C.; Naaman, R.: Role of the Electron Spin Polarization in Water Splitting. *The Journal of Physical Chemistry Letters* **2015**, *6*, 4916-4922.

(81) Kiran, V.; Mathew, S. P.; Cohen, S. R.; Hernández Delgado, I.; Lacour, J.; Naaman, R.: Helicenes—A New Class of Organic Spin Filter. *Advanced Materials* **2016**, *28*, 1957-1962.

(82) Mishra, D.; Markus, T. Z.; Naaman, R.; Kettner, M.; Göhler, B.; Zacharias, H.; Friedman, N.; Sheves, M.; Fontanesi, C.: Spin-dependent electron transmission through bacteriorhodopsin embedded in purple membrane. *Proceedings of the National Academy of Sciences* **2013**, *110*, 14872-14876.

(83) Mondal, P. C.; Fontanesi, C.; Waldeck, D. H.; Naaman, R.: Field and Chirality Effects on Electrochemical Charge Transfer Rates: Spin Dependent Electrochemistry. *ACS Nano* **2015**, *9*, 3377-3384.

(84) Choi, Y.; Seol, M.; Kim, W.; Yong, K.: Chemical Bath Deposition of Stoichiometric CdSe Quantum Dots for Efficient Quantum-Dot-Sensitized Solar Cell Application. *The Journal of Physical Chemistry C* **2014**, *118*, 5664-5670.

(85) Becker, M. A.; Radich, J. G.; Bunker, B. A.; Kamat, P. V.: How Does a SILAR CdSe Film Grow? Tuning the Deposition Steps to Suppress Interfacial Charge Recombination in Solar Cells. *The Journal of Physical Chemistry Letters* **2014**, *5*, 1575-1582.

(86) Graetzel, M.; Janssen, R. A. J.; Mitzi, D. B.; Sargent, E. H.: Materials interface engineering for solution-processed photovoltaics. *Nature* **2012**, *488*, 304-312.

(87) Wang, Y.; Liu, K.; Mukherjee, P.; Hines, D. A.; Santra, P.; Shen, H. Y.; Kamat, P.; Waldeck, D. H.: Driving charge separation for hybrid solar cells: photo-induced hole transfer in conjugated copolymer and semiconductor nanoparticle assemblies. *Physical Chemistry Chemical Physics* **2014**, *16*, 5066-5070.

(88) Barea, E. M.; Shalom, M.; Giménez, S.; Hod, I.; Mora-Seró, I.; Zaban, A.; Bisquert, J.: Design of Injection and Recombination in Quantum Dot Sensitized Solar Cells. *Journal of the American Chemical Society* **2010**, *132*, 6834-6839.

(89) Yaacobi-Gross, N.; Soreni-Harari, M.; Zimin, M.; Kababya, S.; Schmidt, A.; Tessler, N.: Molecular control of quantum-dot internal electric field and its application to CdSe-based solar cells. *Nat Mater* **2011**, *10*, 974-979.

(90) Brown, P. R.; Lunt, R. R.; Zhao, N.; Osedach, T. P.; Wanger, D. D.; Chang, L.-Y.; Bawendi, M. G.; Bulović, V.: Improved Current Extraction from ZnO/PbS Quantum Dot Heterojunction Photovoltaics Using a MoO3 Interfacial Layer. *Nano Letters* **2011**, *11*, 2955-2961.

(91) Timp, B. A.; Zhu, X. Y.: Electronic energy alignment at the PbSe quantum dots/ZnO$(10\bar{1}0)$ interface. *Surface Science* **2010**, *604*, 1335-1341.

(92) Markus, T. Z.; Wu, M.; Wang, L.; Waldeck, D. H.; Oron, D.; Naaman, R.: Electronic Structure of CdSe Nanoparticles Adsorbed on Au Electrodes by an Organic Linker: Fermi Level Pinning of the HOMO. *The Journal of Physical Chemistry C* **2009**, *113*, 14200-14206.

(93) Markus, T. Z.; Itzhakov, S.; Alkotzer, Y. I.; Cahen, D.; Hodes, G.; Oron, D.; Naaman, R.: Energetics of CdSe Quantum Dots Adsorbed on TiO2. *The Journal of Physical Chemistry C* **2011**, *115*, 13236-13241.

(94) Xie, Z.; Markus, T. Z.; Gotesman, G.; Deutsch, Z.; Oron, D.; Naaman, R.: How Isolated Are the Electronic States of the Core in Core/Shell Nanoparticles? *ACS Nano* **2011**, *5*, 863-869.

(95) Carlson, B.; Leschkies, K.; Aydil, E. S.; Zhu, X. Y.: Valence Band Alignment at Cadmium Selenide Quantum Dot and Zinc Oxide $(10\bar{1}0)$ Interfaces. *The Journal of Physical Chemistry C* **2008**, *112*, 8419-8423.

(96) Chuang, C.-H. M.; Maurano, A.; Brandt, R. E.; Hwang, G. W.; Jean, J.; Buonassisi, T.; Bulović, V.; Bawendi, M. G.: Open-Circuit Voltage Deficit, Radiative Sub-Bandgap States, and Prospects in Quantum Dot Solar Cells. *Nano Letters* **2015**, *15*, 3286-3294.

(97) Speirs, M. J.; Balazs, D. M.; Fang, H. H.; Lai, L. H.; Protesescu, L.; Kovalenko, M. V.; Loi, M. A.: Origin of the increased open circuit voltage in PbS-CdS core-shell quantum dot solar cells. *Journal of Materials Chemistry A* **2015**, *3*, 1450-1457.

(98) Choi, M.-J.; Oh, J.; Yoo, J.-K.; Choi, J.; Sim, D. M.; Jung, Y. S.: Tailoring of the PbS/metal interface in colloidal quantum dot solar cells for improvements of performance and air stability. *Energy & Environmental Science* **2014**, *7*, 3052-3060.

2.0 LIGAND INDUCED CHANGES IN THE CHARACTERISTIC SIZE DEPENDENT ELECTRONIC ENERGIES OF CDSE

This work has been published as Bloom, B.P.; Zhao, L-B.; Waldeck, D. H.; Liu, R.; Zhang, P.; and Beratan, D. The thesis author performed all of the experimental studies and prepared the manuscript. The supporting information for this chapter is provided in Appendix B.

This work explores the electronic energy of CdSe nanoparticles as a function of nanoparticle (NP) size and capping ligand. Differential pulse voltammetry was used to determine the valence band edge of CdSe NPs that are capped with three different ligands (aniline, thiophenol, and phenylphosphonic acid) and, the experimental values are compared with DFT calculations. These results show how the energy position and the size dependent behavior of CdSe's energy bands can be modulated by the chemical nature of the capping ligand. The computations underscore how the nature of the highest lying filled states of the nanoparticle can change with ligand type and how this can explain differences between previously reported size dependent data on similar systems. The findings show that both the ligand and quantum confinement effects should be accounted for in modeling size dependent effects for different NP-ligand systems.

2.1 INTRODUCTION

Largely because of their tunable electronic properties, semiconducting nanoparticles (NPs) have garnered considerable interest for their use in biological sensing, optoelectronics, and photovoltaics, among others. Of particular importance to the latter two applications are the energy values for the valence band maximum (VBM) and conduction band minimum (CBM); e.g., the energy alignment of NPs within a photovoltaic device is an important factor for charge separation and the corresponding generation of photocurrent.[1] For this reason, a number of electrochemical[2-8] and photoemission[9,10] studies have been performed to quantify the size dependent shift in the electronic energies. A comparison of the data from different studies shows a wide variation in the size dependence, and in part this variation can be rationalized by considering the nanoparticle-ligand interaction.

The surface of a semiconductor NP is typically passivated with organic molecules (ligands), which are known to influence growth dynamics,[11,12] to determine the solubility of the NP,[13-15] to affect photophysical properties,[16-18] and to modulate the confinement of the exciton.[19-21] Over the past decade, a few workers have explored how the capping ligand affects the electronic band energies of CdSe NPs. In 2001, Wang et al. reported that the reduction potential of a 7.0 nm TOPO-capped CdSe was less negative (-0.8 eV) than a 7.0 nm octanethiol-capped CdSe NP (-1.07 eV).[22] Since then, photoemission experiments measuring the VBM were performed on TOPO-capped and pyridine-capped CdSe NPs over a size range of 2.0 to 4.0 nm and showed how the VBM is shifted by the two different capping ligands on the NP.[23] Soreni-

Harari et al. studied this phenomenon in greater depth by using differential pulse voltammetry to study the VBM of 4.4 nm and < 2.0 nm InAs quantum dots that were capped with trioctylphosphine, 4-nitrothiophenol, 4-methoxythiophenol, 4-methylthiophenol, and aniline ligands.[24] The important finding from this study was that the linker group on the ligand plays the most important role in causing a shift in the electronic states of the NP. A similar study was performed by Jasieniak et al. on 4.7 nm CdSe NPs for the linker groups carboxylic acid, phosphine oxide, thiol, and amine, which all contained an alkyl chain.[9] Using photoemission they found a shift in the VBM for each different capping ligand and showed that its effect correlated with the ligand's ability to passivate the NP surface. Despite these efforts, the nature of the ligand induced energy shifts and the ligand's effect on the VBM's size dependence remain elusive. Through experiments that use a similar set of ligands, C_6H_5-X where X is the linker group, and corresponding theoretical calculations, this work explores these matters. The results are compared to previous findings for the size dependence of the VBM of TOPO-capped CdSe,[2,6,8,9] pyridine-capped CdSe,[25] and alkylamine-capped CdSe.[9,26] Note that a number of workers have explored systems in which the NP is covalently linked to an electrode surface,[25,27,28] however, those assemblies display some additional effects from local charge rearrangement and are not considered here.

Differences in the properties of NP-based photovoltaic devices can also be related to the ligand's effect on the NP's electronic energies. Greaney et al. showed differences in the open circuit voltage and solar cell efficiencies of devices comprised of pyridine- and *tert*-butylthiol-capped CdSe NPs which they attributed to changes in their LUMO positions.[29] In a similar study, Albero et al. showed how the open circuit voltage and short circuit current changes of a CdSe NP based device were affected by different substituted thiophenol ligands.[30] Also, Shalom et al.

showed how the efficiency of solar cells which used CdS NPs as a dye sensitizer are affected by the nature of the NP's ligand and concluded that it arose from the ligand's effect on the HOMO and LUMO energy positions.[31] From these studies it is evident that the ligands' effect on the NP energy levels can impact photovoltaic device performance.

The ligand effect on a nanoparticle's energy levels has also been studied computationally. Kuznetsov et al. have reported that NH_3, SH, and PH_3 ligands can cause up to a 1.21 eV shift in the HOMO energy and a 3.26 eV shift of the LUMO energy for CdSe and CdTe nanoclusters.[32] The larger destabilization of the LUMO was rationalized by the ligands coordination to the Cd, which contributes more to the nanocluster's LUMO than its HOMO. Fischer et al. have shown the importance of the density of ligands on a surface by showing how the electronic energies of $Cd_{33}Se_{33}X_{21}$ nanoclusters, where X is NH_2Me, PMe_3, $OPMe_3$, or pyridine, changes upon the removal of a ligand (the cluster becomes $Cd_{33}Se_{33}X_{20}$).[33] Also, a recent study has explained the energy shifts for CdSe NPs as resulting from a sum of the intrinsic dipole of the ligand, P_{ligand}, and the induced dipole that arises from the ligand-NP interaction P_{ind}.[34] In this model, the energy shift, $\Delta E_{\perp}$, arising from the dipole is given by

$$\Delta E_{\perp} = \frac{P_{\perp} e}{A \varepsilon \varepsilon_0} \qquad \textbf{Equation 2-1}$$

in which A is the surface area per ligand, ε is the dielectric constant of the ligand layer, and $P_{\perp}$ is the normal (ligand to NP surface) component of the ligand layer's dipole. $P_{\perp}$ is modeled as a sum of the intrinsic ligand dipole and a ligand-NP contribution

$$P_{\perp} = P_{ligand,\perp} + P_{ind,\perp} \qquad \textbf{Equation 2-2}$$

This latter model coincides with that used to describe the energy shifts that dipolar molecular adsorbates have been reported to cause on bulk substrates.[35,36]

This work describes recent findings on the electronic states of CdSe NPs and how they evolve as a function of size and the capping ligand - aniline (An), thiophenol (TP), and phenylphosphonic acid (PPA); see scheme 2-1. The experimental studies use differential pulse voltammetry to measure the VBM for all three ligand-NP systems. In these studies the nature of the organic ligand (phenyl ring) is held constant and the linker group is varied so that its effect on the energetics can be distinguished from that of the ligand's dipole and solvation. These data are complemented by DFT calculations of the NP capping ligand interaction for Cd_6Se_6 and $Cd_{33}Se_{33}$ clusters with model An, TP, and PPA capping agents. The results demonstrate the strong effect of the chelating group on the VBM of the NP and show that these energies vary with size in a predictable way that is dependent upon the capping ligand's linker group.

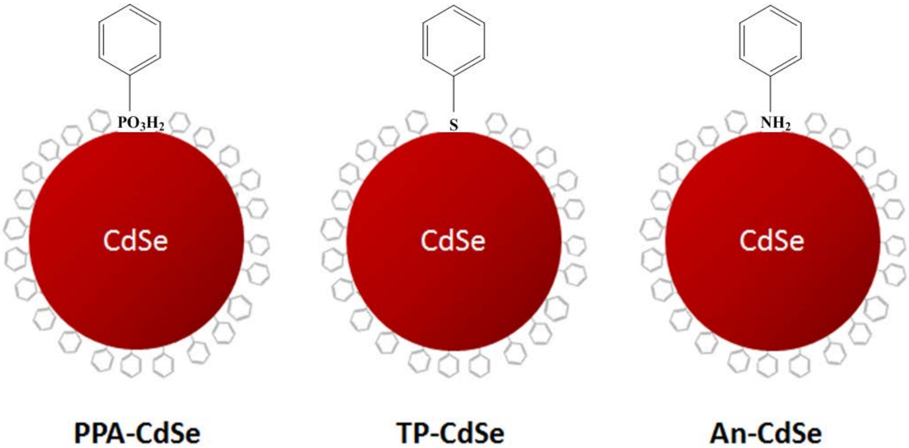

Scheme 2-1. Schematic diagram of the three ligand-NP systems: PPA-CdSe, TP-CdSe, and An-CdSe. Not drawn to scale.

2.2 EXPERIMENTAL METHODS AND MATERIALS

2.2.1 Materials

Selenium and trioctyl phosphine (TOP) were purchased from Strem Chemicals. Octadecylphosphonic acid (ODPA) was purchased from PolyCarbon Industries. Silver Nitrate was purchased from Fisher Scientific. Centrifugal filters were purchased from EMD Millipore. The Agl$AgNO_3$ reference electrode was purchased from CH Instruments, and the Au ball electrodes were made from 99.999% 0.5 mm diameter gold wire, which was purchased from Alfa Aesar. All other chemicals were purchased from Sigma-Aldrich and were used without further purification.

2.2.2 Preparation of PPA-CdSe

Phenlyphosphonic acid capped CdSe was synthesized by modifying a previously reported procedure.[37] Briefly, a three neck round bottom flask was filled with 0.0514 g of CdO (0.4 mmol), 0.126 g of PPA (0.4 mmol), and 4.0 g HDA (16.5 mmol). The flask was heated to 160.0 °C and degassed for 10 min with argon. The solution was then heated to 300 °C under argon until clear and a precursor solution containing 0.119 g of Se (1.5 mmol) and 3.0 ml tri-n-octyl phosphine (6.7 mmol) was injected. The NPs were then purified through precipitation with methanol and dissolved in THF for electrochemical analysis.

2.2.3 Preparation of TP-CdSe

A two-step ligand exchange was used for the synthesis of thiophenol coated CdSe NPs (TP-CdSe). First, ODPA-CdSe was synthesized following protocols published elsewhere.[38] The isolated NPs were then dissolved in 1.4 mMol of MPA in dimethylformamide. This solution was placed under argon, using Schlenk line techniques, and heated at 60 °C for 3 hours in order to exchange the ODPA to MPA. Upon completion the NPs were precipitated out with a DMF potassium *tert*-butoxide solution and dissolved in H_2O. In order to eliminate excess ligand, the NPs were placed in a 10,000 molecular weight cut off Millipore centrifugal filter and centrifuged three times. The MPA-CdSe NPs were then stirred for three days in a solution containing 5.0 mL of H_2O and 1.0 mL of TP. During this process the NPs became insoluble and could be isolated through centrifugation. The NPs were then washed, and dried, three times with hexanes and dissolved in THF for further analysis. For NPs larger than 3 nm a TOPO-CdSe synthesis[39] was used in place of an ODPA-CdSe synthesis.

2.2.4 Preparation of An-CdSe

A two ligand exchange process was used for the preparation of aniline coated CdSe NPs (An-CdSe). First, ODPA-CdSe was synthesized following protocols published elsewhere.[38] Next the isolated NPs were dissolved in 5.0 mL of pyridine and heated under argon at 90 °C for 24 hours. The pyridine exchanged NPs were isolated and washed through precipitation with hexanes and dried with argon. The dried NPs were then suspended in 3.0 mL of chloroform and 0.5 mL of aniline was added to the solution in a glove box. The contents were stirred for 24 hours and isolated through precipitation with methanol. The aniline capped CdSe was dried with argon and dissolved in THF for further analysis. For NPs larger than 3 nm a TOPO-CdSe synthesis[39] was used in place of an ODPA-CdSe synthesis.

2.2.5 Electrochemical Measurements

Differential pulse voltammetry (DPV) experiments were performed in a Faraday cage using a computer-controlled CHI 610D electrochemical workstation (CH Instruments, Austin, Tx). The three electrode system consisted of a platinum counter electrode, a gold ball working electrode, and an AglAgNO$_3$ reference electrode. Experiments were performed in THF with a 0.1 M TBAP supporting electrolyte. DPV experiments were performed using a 5.0 mV step potential, 0.05 s modulation amplitude, 0.05 s pulse width, 0.01 sample width, and 0.2 s pulse period. All of the oxidation potentials were referenced to the formal potential of the ferrocene/ferrocenium redox couple and then converted to the vacuum scale (4.8 eV).[40] The onset of the NP's anodic peak was taken to be the VBM and was found using previously published methods.[40]

2.3 THEORHETICAL METHODS

Density functional theory (DFT) calculations were performed to study the effect of the ligand's binding group on the electronic energies of the CdSe NPs, which were modeled by two different cluster sizes: Cd$_6$Se$_6$ and Cd$_{33}$Se$_{33}$. The capping ligand was modeled in different ways, and this caused some of the model clusters to have excess Cd. The TP ligand was modeled by the thiophenyl radical, $C_6H_5S\cdot$, and by a thiophenylate ion, C_6H_5S-; the PPA was modeled by phenylphosphonic acid, C_6H_5-PO_3H_2, and by phenylphosphonate ion, $C_6H_5PO_3^{2-}$; and the An was modeled with an aniline, $C_6H_5NH_2$. Note that the Cd^{2+} content was changed to ensure that the cluster had a zero overall charge. Full geometric optimization and electronic property analysis were carried out using the Becke's three-parameter exchange functional and Lee-Yang-Parr correlation hybrid functionals (B3LYP)[41,42] associated with the Los Alamos National Lab 2 double-ξ (LANL2DZ)[43,44] effective core potential basis set by Gaussian 09 program.[45]

In agreement with previous studies, the CdSe clusters adopt a wurtzite symmetry with a six-membered ring structure in which the Cd and Se atoms are located at the corners of an equilateral triangle.[46-49] The optimized structures for Cd_6Se_6-$(C_6H_5$-$NH_2)_4$, Cd_6Se_6-$(C_6H_5$-$S)_4$, and Cd_6Se_6-$(C_6H_5$-$PO_3H_2)_4$ are shown in Figure 2-1. The three structures depicted in Figure 2-1 constrain the ligands to be charge neutral in order to compare their effects for a stoichiometrically equivalent, Cd_6Se_6, nanocluster. Because thiols are known to bind as thiolates to surfaces and it has been shown previously that phosphonates, or their corresponding anhydrides, attach in a deprotonated (2-) form,[50-52] these binding motifs were also explored for the smaller clusters. These studies included nonstoichiometric clusters (excess Cd^{2+}) that were capped with anionic ligands to maintain charge neutrality. For the small cluster, the HOMO energy position is not affected strongly, as compared to the energy shifts between ligand types (*vide infra*).

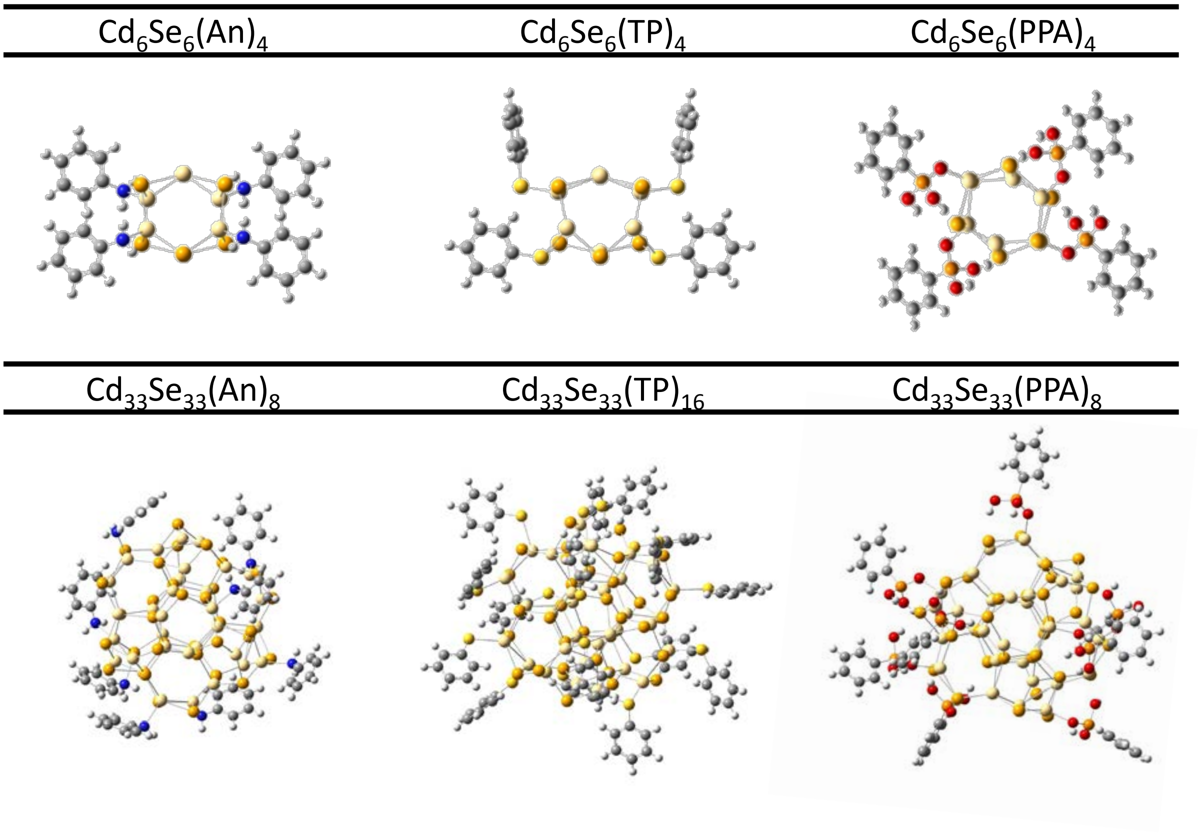

Figure 2-1. Calculated structures, using B3LYP/LANL2DZ level simulations, are shown for each of the systems studied. The top row shows the $Cd_6Se_6An_4$, $Cd_6Se_6TP_4$, and $Cd_6Se_6PPA_4$ structures and the bottom rows show the $Cd_{33}Se_{33}An_8$ $Cd_{33}Se_{33}TP_{16}$, $Cd_{33}Se_{33}PPA_8$ structures.

Because the Cd_6Se_6 clusters are extremely small and all of the atoms exist entirely as surface atoms, the computational studies were extended to $Cd_{33}Se_{33}(An)_8$, $Cd_{33}Se_{33}(PPA)_8$ and $Cd_{33}Se_{33}(TP)_{16}$, in order to examine how strongly the trends were affected by cluster size. These simulations were performed in the same fashion as the Cd_6Se_6 nanoclusters. The optimized structures for the neutral $Cd_{33}Se_{33}X_n$ clusters are shown in the bottom panel of Figure 2-1.

2.4 RESULTS

2.4.1 NP Characterization and Ligand Exchange

The shapes and diameters of the CdSe NP colloids were assessed by transmission electron microscopy (TEM) and electronic absorption spectra. Figure S1 shows representative TEM images for An-CdSe, TP-CdSe, and PPA-CdSe, and Table S1 reports the average size found from the UV-visible λ_{max} of the NP colloid solutions and from the TEM. The assignment of the first absorbance maximum and the use of an empirical model established by Yu et al.[53] shows good agreement with the sizes in the TEM image. Although the capping ligand can affect the exciton confinement (and thus give false size values when using spectral shifts to deduce the size), this effect does not appear to be important for the ligands that are used in this study.[19-21] Only nominal differences in the size, as determined by a comparison of the absorption spectra and the TEM measurements, were seen for the different ligands in this study and their weak effect likely reflects the weak electronic coupling of the ligands with the NP's exciton. Operationally, the CdSe absorption spectra were used to determine the NP sizes.

A two-step process was used to change the ligand coating on the NPs (see schematic diagram in Figure 2-2). Figure 2-2 illustrates the ligand exchange process used to form TP-CdSe, in which the solubility of the CdSe NP is changed from a non-aqueous solution for the ODPA capping, to an aqueous solution for the MPA capping, and then back to a non-aqueous solution for the TP ligand capping. This process ensures that the surface of the NP is coated with the desired TP ligand and aids in the elimination of free ligand in the solvent. For An-CdSe the NP's fluorescence was used to follow the ligand exchange process (see Figure 2-3). The black curve shows the fluorescence emission of the ODPA-CdSe, which exhibits a well-defined excitonic peak and a broad emission to the red that has has been assigned to surface defects.[18] Upon ligand exchange from ODPA to pyridine, the fluorescence signal is quenched (transition from black to red curve) because the pyridine-CdSe interaction gives rise to a recombination center for the photogenerated electron-hole pair in CdSe.[54] Once pyridine is replaced by An in the subsequent step of the process the fluorescence signal recovers (transition from red to blue curve), albeit not completely. Because different ligands have previously been shown to affect the quantum yield of NPs,[16,55] we attribute the majority of the difference in fluorescence signal of ODPA-CdSe and An-CdSe to the effect of the ligands themselves (ODPA and An) on the NP emission and not to any residual pyridine on the NP surface. This assumption was substantiated by performing ^{1}H NMR studies which revealed no pyridine resonances for the An-CdSe colloidal solutions. Pulsed field gradient NMR studies on the CH_2 peak from ODPA were also conducted as further evidence of ligand exchange; see Figure B2 in the supporting information.

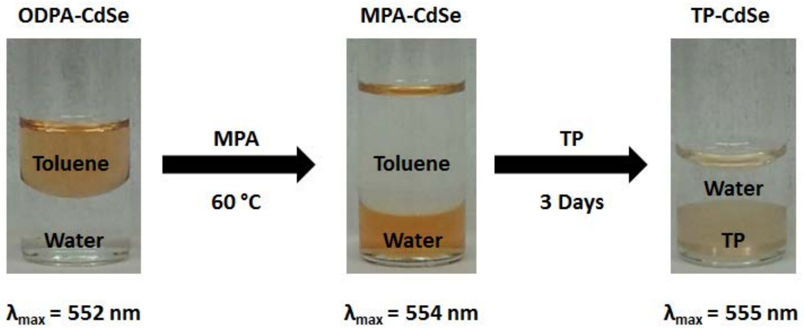

Figure 2-2. The images show the solutions for the ligand exchange from an ODPA coated NP to an MPA coated NP and then to a TP coated NP. The change in solubility of the NP with ligand coating goes from non-aqueous to aqueous and back to non-aqueous. The color differences in the NP solutions arise from a change in concentration and not a change in NP size. Details of the procedure are reported in the experimental section.

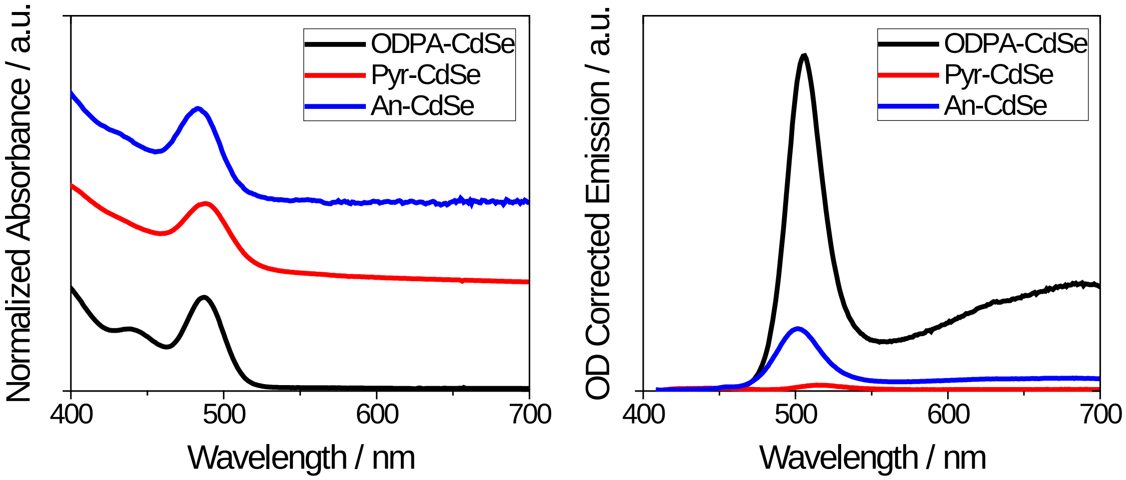

Figure 2-3. Absorbance (left) and fluorescence (right) spectra of the different ligand coated CdSe NPs; ODPA-CdSe (black), Pyr-CdSe (red), and An-CdSe (blue). The recovery in fluorescence signal from pyridine capped to aniline capped indicates a successful ligand exchange (see text).

2.4.2 Voltammetry Studies

Differential pulse voltammetry (DPV) was used to determine the oxidation potential onset of the different ligand coated CdSe NPs as a function of NP size. In contrast to earlier studies by our group, the NPs were not immobilized on the surface, but were freely diffusing in solution. The voltammetry experiments were performed in THF with a tetrabutylammonium perchlorate (TBAP) supporting electrolyte, unless otherwise specified. The voltammetry measurements show that the NP's oxidation potential onset was different for the three ligand systems. For solutions of the TP-CdSe NPs, the voltammogram consisted of three separate anodic peaks; labeled A1, A2, and A3 (Figure 2-4 panel A), with the peak A2 being assigned to the oxidation of the NPs. The peak at A3 is assigned to oxidation of the thiophenol (TP), and was confirmed by the addition of excess thiophenol to the solution (See Figure B3). In order to decipher the origin of the A1 and A2 oxidation peaks, different syntheses of the TP-CdSe NPs with similar size and concentration were compared and are shown in Figure 2-4A. The peak A1 did not appear reliably, whereas the A2 peak always occurred and displayed a similar amount of current density for CdSe NP solutions of similar concentration. Thus the peak A2 is assigned to the oxidation of the TP-CdSe NP's valence band maximum (VBM) and the A1 peak is assigned to surface localized defect states that occur for some sample batches.

For PPA-CdSe NP solutions, the voltammetry revealed two strongly overlapping peaks (B2 and B3 in Figure 2-4B) and a small amplitude broad peak (B1 in Figure 2-4B). Figure 2-4B shows a voltammogram for a solution of 2.8 nm PPA-CdSe NPs and compares it to a voltammogram of the PPA Ligand in solution. From this comparison the peak B3 for the PPA-CdSe NPs is assigned to the oxidation of the NP and the shoulder, B2, is assigned to oxidation of free PPA ligand. The low amplitude and broad oxidation wave, B1, is thought to arise from excess HDA left over following synthesis and/or from surface defect states on the NP.

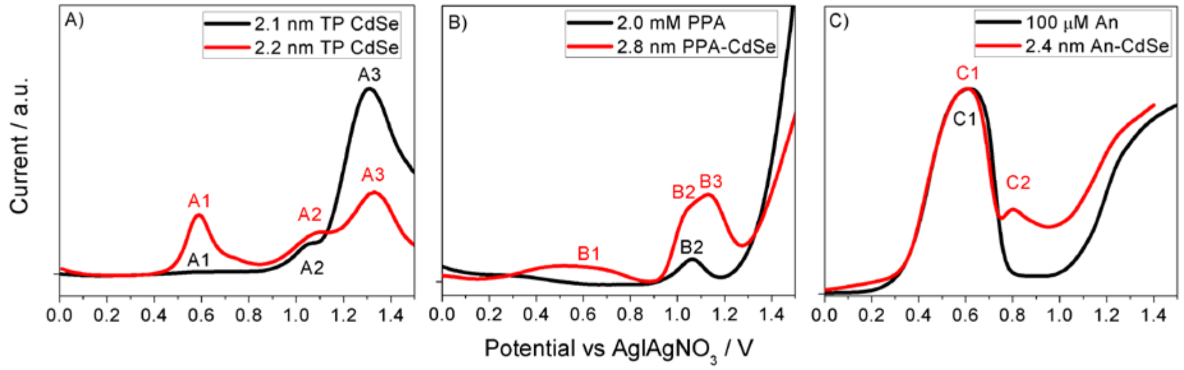

Figure 2-4. Panel A shows background subtracted differential pulse voltammograms (DPV)s for the solutions of 2.1 nm TP-CdSe NPs (black) and of 2.2 nm TP-CdSe NPs (red). Peak A2 is assigned to the oxidation of the NP; see text for details. Panel B shows background subtracted DPVs of a 2.0 mM solution of the PPA ligand (black) and a solution of 2.8 nm PPA-CdSe (red). The NP oxidation was assigned to the peak at B3; see text for details. Panel C shows DPVs of a 2.4 nm An-CdSe solution (red) and a 100 μM solution of aniline (black); the current was normalized to the largest peak. Peak C2 is assigned to the oxidation of the AN-CdSe NP solution; see text for details.

Figure 2-4C shows voltammograms for a 100.0 μM solution of aniline (An) and a solution containing 2.4 nm An-CdSe NPs. Because the amount of free aniline in the NP solution was unknown, the current of the C1 peak was scaled to the same height. The voltammograms in Figure 2-4C indicate that C1 arises from excess aniline in solution. The oxidation wave at C2 is only present for the nanoparticle solutions and is assigned to the VBM of the An-CdSe. Note that control experiments were performed to ensure that electropolymerization of aniline does not contribute to the signal (see Appendix Figure B4).

In each case the assignments of the NP oxidation waves are substantiated by the concentration dependence and the size dependence, as well as other observations. Additional information regarding the peak identification and determination for the different capping ligands are provided in the supporting information.

2.4.3 VBM and Size Dependence

Upon identification of the NP oxidation peak, the VBM was determined by identifying the onset potential of the NPs oxidation wave. Details of this procedure and its rationale are discussed elsewhere.[40] Note that once the VBM is determined, the CBM can be estimated by adding the optical bandgap to it, namely $E_{CBM} \sim E_{VBM} + E_{h\nu}$. For each of the three ligand CdSe NP systems, the dependence of the VBM was studied as a function of the NP size and these data are plotted in Figure 2-5A. The blue diamonds correspond to An-CdSe solutions, the red circles correspond to TP-CdSe solutions, and the green triangles correspond to PPA-CdSe solutions. The reported error bars, which are not much different than the symbol size, were calculated from the experimental resolution in determining the NP size and variations observed in the electrochemical onset potentials between successive voltammetry measurements. From these data it is apparent that the use of different linkers causes a significant (few tenths of an eV) shift in the VBM. Overall, the observed changes of the VBM energy with the capping ligand is qualitatively consistent with previously published photoemission data on thiols and amines[9] and with theoretical calculations (*vide infra*). The change in the VBM with NP size is relatively weak, however; it changes by less than 0.1 eV for the TP-CdSe and the An-CdSe NPs over the range of 2 nm to 4 nm, and it changes by about 0.1 eV for PPA-CdSe over the range of 2 nm to 4 nm. Note that these findings and the observed shift of the CdSe band gap emission with NP size, indicates that the shift of the CBM with NP size is much stronger, on the order of 0.3 eV.

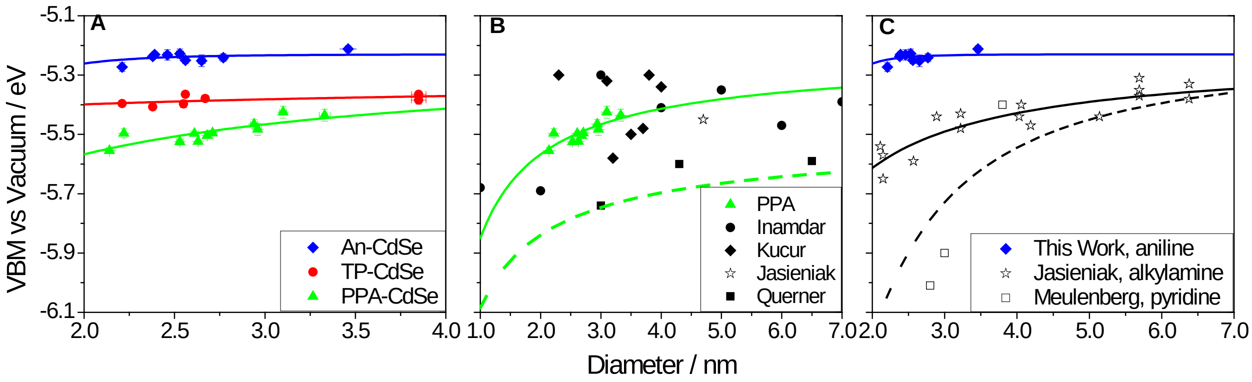

Figure 2-5. Panel A shows the VBM energy positions that are determined in this study for PPA (green triangles), TP (red circles) and An (blue diamonds) capped NPs as a function of the NP diameter. The lines through the data are intended as a guide to the eye and were obtained by fitting the data with a power law functional form. Panel B shows a similar plot (note the change in abscissa scale) for the PPA data (green triangles) with electrochemical (filled black symbols) and photoemission (open symbols) data for TOPO capped CdSe NPs from the literature. The circles correspond to work by Inamdar et al.,[6] the diamonds to Kucur et al.,[8] the star to Jasieniak et al.,[9] and the squares to Querner et al.[2] The dashed green line shows a shift in the VBM position for the PPA data if a peak potential is used in the analysis (see text for details). Panel C shows the VBM positions of aniline (blue diamonds), alkylamine (black stars, solid line)[9], and pyridine (black squares, dashed line)[10] capped NPs as a function of size. Error bars are shown for both the diameter and the VBM, for this work, unless they are smaller than the symbol size. Exact values for the data points in panel A can be found in the supporting information.

Comparison of the size dependent characteristics of PPA-CdSe NPs (green triangles and line) to TOPO-CdSe NPs (Figure 2-5 Panel B) from the literature shows a wide variation. The energies reported by Inamdar et al.[6] (black circles), Kucur et al.[8] (black diamonds), Jasieniak et al.[9] (black star), and Querner et al.[2] (black squares) span an approximately 0.5 eV range for 3 nm diameter nanoparticles. These differences may arise from variability in experimental conditions (e.g., electrolyte choice), methods used to extract the VBM from the voltammetry data, and nanoparticle synthesis. The data of Querner et al.'s TOPO-CdSe appears to be less scattered than the other literature data reported here, and it indicates a size dependence which is similar to that found for the PPA-CdSe but shifted by about 0.2 eV to lower energy. In contrast to the PPA-CdSe results reported here which use the onset potential to calculate the VBM, Querner etal. assigned the voltammogram's peak potential as the VBM position. The dashed green curve in Fig 2-5B shows how the VBM position for the PPA-CdSe data shifts if the peak potential is used to make the assignments rather than the onset potential. Lastly, note that the photoemission data reported for a 4.7 nm TOPO-CdSe NP by Jaseniak et al. lies closer to the VBM values found for the PPA-CdSe from the onset potential than they do to the energy positions reported by Querner et al. The similarity of the PPA-CdSe energies and the TOPO-capped CdSe energies are consistent with the phosphonate linker group making the dominate contribution to the energy position.

In Figure 2-5C, the VBMs for the aniline capped CdSe NPs (blue symbols and line) are compared to results from photoemission studies on the VBMs of alkylamine capped CdSe NPs[9] (black stars and dashed line) and pyridine capped CdSe NPs[10] (black squares and dashed line). Previous work[40] has shown good agreement between photoemission and electrochemical data (also see 2-5B), and the differences between these three nitrogen ligands are significant. Note that the curves through the data are intended as a guide to the eye, and an additional data point for the pyridine capped CdSe NPs (at 1.25 nm) is not shown so that the size dependence trends are clearer. The error bars for the pyridine capped CdSe NPs are also not displayed but were reported to be on the order of ±0.2 eV. The VBM position for the pyridine and alkylamine ligands are shifted significantly from that of the aniline data despite their common use of a nitrogen atom for the ligation to the surface. This comparison shows that the nature of the ligand has a strong influence on how the nitrogen linker affects the position of the VBM and how the VBM changes as a function of size. Note that the trend in the VBM position is consistent with the trend in the reported gas phase ionization potentials of aniline (7.74 eV),[56] butylamine (8.79 eV),[57] and pyridine (9.25 eV),[58] which report primarily on the nitrogen frontier orbital energy.

A caveat that must be considered for the energetics of the amine-coated CdSe is the weak NP-amine interaction. It has been shown previously through NOESY and DOSY measurements that ligands which coordinate through amine groups can undergo facile exchange with the solution; surface desorption rates exceeding 50 s^{-1} at room temperature have been reported.[59] Other experiments show that the adsorption energy of amines on CdSe NPs is more than two times lower than that of their phosphonic acid and thiol counterparts.[60] Furthermore, it has been reported that pyridine desorbs from the surface of CdSe under ultra-high vacuum conditions, [25] an experiment with similar conditions to that of Meulenberg et al.[10] Because the electrochemical measurements with the aniline coated CdSe were performed with excess aniline ligand in solution and assuming that the ligand binding energy is a weak function of NP size (over the size range studied), the size dependent behavior of the VBM for the aniline system is likely not affected by coverage variations. Finally, note that computational studies report that the removal of a ligand from the surface of a nanocluster can cause shifts of the electronic energies and introduce surface states.[33] Thus, the surface coverage of the aniline, alkylamine, and pyridine capped CdSe nanoparticles may vary considerably between the different studies and may impact the observed energy offsets.

2.4.4 Computational Studies

Figure 2-6A shows computational results for the HOMOs and LUMOs of -$(C_6H_5\text{-}NH_2)_4$, $Cd_6Se_6\text{-}(C_6H_5\text{-}S)_4$, $Cd_6Se_6\text{-}(C_6H_5\text{-}PO_3H_2)_4$, and uncapped Cd_6Se_6 nanoclusters; and Figure 2-6B shows similar results for $Cd_{33}Se_{33}\text{-}(C_6H_5\text{-}NH_2)_8$, $Cd_{33}Se_{33}\text{-}(C_6H_5\text{-}S)_{16}$, $Cd_{33}Se_{33}\text{-}(C_6H_5\text{-}PO_3H_2)_8$ and bare $Cd_{33}Se_{33}$ nanoclusters. The choice of four ligands for the Cd_6Se_6 and eight for the $Cd_{33}Se_{33}$ nanoclusters results in a ligand density of approximately 2.9 nm^{-2} and 1.5 nm^{-2} respectively. These ligand densities are consistent with experimental values reported elsewhere for CdSe NPs,[38,61,62] albeit for larger nanoparticles. Although an attempt was made to study the $Cd_{33}Se_{33}$ clusters with sixteen ligands (a 3.0 nm^{-2} coverage) this was only achieved for the TP ligand because of limits on computational time. Although these computational results are in good qualitative agreement with the experimental data on the NPs (namely, the An-coated clusters have the highest lying HOMO, the PPA-clusters have the lowest lying HOMO, and the size dependence is strongest for the PPA ligand), a number of important caveats must be considered. Namely only two cluster sizes have been explored, both of which are significantly smaller than the NPs. Also, the density of surface bound ligands and their binding sites on the cluster can significantly affect the HOMO positions (*vide infra*).

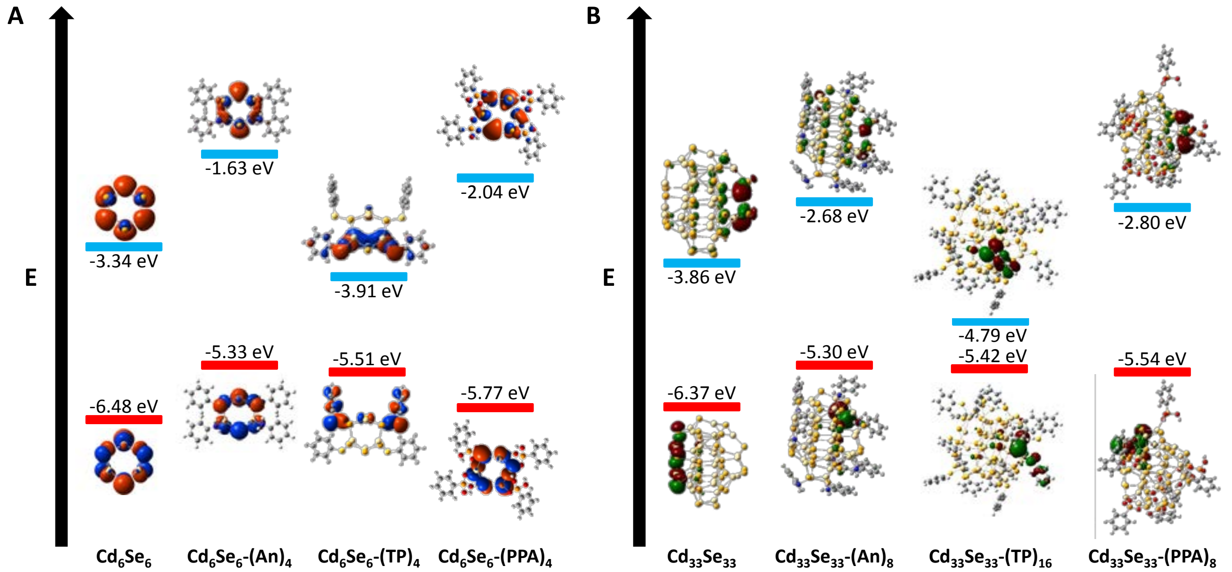

Figure 2-6. This figure shows the calculated HOMOs and LUMOs of bare and capped $Cd_6Se_6X_4$ (A) and $Cd_{33}Se_{33}X_n$ (B) NPs where X is the name of An(n=8), TP(n=16), and PPA(n=8) ligands; calculations were performed at the B3LYP/LANL2DZ level. Note: The energies and orbital contributions were found using the same methodology as Kuznetsov et al.[32] and reproduced their findings for the bare nanocluster.

The data in Table 2-1 report the HOMO energies of Cd_6Se_6 nanoclusters for five different ligation conditions and three different ligand densities. The three ligand densities correspond to two (1.5 nm^{-2}), four (2.9 nm^{-2}), and six (4.4 nm^{-2}) ligands on the Cd_6Se_6 nanocluster. Three of the ligation conditions correspond to neutral ligands binding to Cd sites on the surface; namely aniline (An), the thiophenyl radical (TP·), and phenylphosphonic acid (PPA). Because a number of studies[50,61] indicate that the bonding is likely to occur through a thiolate functionality for TP and a phosphonate functionality for PPA, calculations were also performed using thiolate (TP^-) and phosphonate (PPA^{2-}) linkers; in each case, excess cadmium (as Cd^{2+}) was included in the cluster to maintain overall charge neutrality. While somewhat arbitrary, this choice is consistent with common reports of excess cadmium found on the surface of CdSe nanoparticles.[61,63,64]

Table 2-1. HOMO Energies of Cd_6Se_6 Nanoclusters[*] for Different Ligands and Ligand Densities

Ligand Type	Ligand Density

	1.5 nm^{-2}	**2.9 nm^{-2}**	**4.4 nm^{-2}**
An	-5.82 eV	-5.33 eV	-5.03 eV
TP·	-5.58 eV	-5.55 eV	-5.81 eV
TP $^-$	-5.49 eV	-5.50 eV	-5.48 eV
PPA	-6.05 eV	-5.77 eV	-5.62 eV
PPA^{2-}	-6.28 eV	-6.77 eV	-6.13 eV

*Note that excess Cd^{2+} is included to clusters with TP^- and PPA^{2-} to neutralize the net charge.

An analysis of the data in Table 2-1 shows that the sulfur linker groups (TP· and TP^-) behave differently than do the nitrogen (An) and oxygen linker groups (PPA and PPA^{2-}) as the ligand density increases. With the exception of an anomaly for the $Cd_{10}Se_6$-$(PPA^{2-})_4$ cluster, where an unbalanced number of ligands causes cluster strain and distorts the geometry, the An, PPA, and PPA^{2-} capped Cd_6Se_6 nanoclusters display an increase in HOMO energy of the cluster with an increase in ligand density. The TP· and TP^- ligands do not follow this trend, the HOMO energy does not change significantly as the ligand density ('coverage') changes. An analysis of the frontier molecular orbitals shows that the HOMO for the An and PPA linkers is localized on the nanocluster whereas the HOMO for the model TP linkers is located on the sulfur atoms (see Appendix Figure B6 and its discussion for more detail). Consequently, electrochemical oxidation probably occurs at the S-Cd linkage of the capping ligand and this may be largely responsible for the weak size dependence for the TP-CdSe VBM data; a similar behavior has been observed previously for NPs attached to substrates through disulfide linkers.[27,28,40] Those studies concluded that surface states of the thiolated metal causes Fermi level realignment and a pinning of the NP VBM. The current findings suggest a mechanism for the Fermi level pinning that involves the surface localized S-Cd bonds of the NPs.

The data in Table 2-1 show that the HOMO energies are different for the different ligands. While in some cases the HOMO energy trend is consistent with the experimental observations (see Fig 2-5A), for other cases it is not. For example, only the case of 2.9 nm^{-2} ligand density reproduces the HOMO energy trend between linker types for the charge neutral ligands (see Fig 2-6A). For the case of the anionic linker groups (TP^- and PPA^{2-}) and An, the trend in the calculated HOMO levels agrees with experiment for the two higher ligand densities (2.9 nm^{-2} and 4.4 nm^{-2}). While the sulfur linkers have the HOMO localized on ligand sites, the HOMO is dominated by contributions from the 4p orbitals of the Se atoms for the nitrogen (An) and oxygen (PPA and PPA^{2-}) linkers. Thus, the HOMO energy of the TP-coated nanoparticles is expected to not change much with size, whereas the HOMO energies of the An and PPA coated nanoparticles should show a more significant size dependence; a finding qualitatively in agreement with experiment (see Figure 2-5).

The computations reveal significant energy changes between the smaller uncapped Cd_6Se_6 nanoclusters and the larger uncapped $Cd_{33}Se_{33}$ nanoclusters. In going from the smaller nanocluster to the larger nanocluster the bandgap decreases by about 0.6 eV, and this decrease in bandgap with increasing size is consistent with quantum confinement effects. It was also found that the LUMO energies shift much more as a function of size than the HOMO energies; a phenomenon previously attributed to the difference in effective mass of the charge carriers.[65] Although the energies change somewhat between the different capped cluster sizes, the trend in orbital energies remains robust. This finding may reflect the fact that the frontier molecular orbitals of the larger $Cd_{33}Se_{33}$ structures still reside on the surface of the cluster. As a result, the capping ligands influence the orbitals of the Cd_6Se_6 and $Cd_{33}Se_{33}$ nanoclusters in a similar way. Note that bandgap for the thiophenol capped clusters are unexpectedly small. This finding is consistent with the HOMO (LUMO) being occupied (empty) midgap thiol states bearing little NP orbital contribution.

Charge exchange between the ligand and the nanoparticle creates a dipole layer at the CdSe-ligand interface which could affect the oxidation potential’s observed for the NPs. The magnitude of the dipole layer was determined by analyzing the amount of charge displacement between the ligand and the nanoparticle. The data in Table 2-2 show the outcome of a Mulliken charge analysis for the nanocluster’s Cd and Se atoms and the summation of the Mulliken charges on the surrounding ligands. The values reported are the total net change in the Mullikan charge on the ligands after adsorption to the nanocluster and the net change in Mulliken charge per ligand. A positive value means that the ligands are donating electron density to the NP. Because the phosphonate group is more electronegative than an amine group, the PPA ligands donate less electron density per ligand to the NP. While the net charge displacement per ligand drops with increasing ligand density, the total charge displacement increases as the ligand density is increased and can push the HOMO position higher. This effect can explain the dependence of the HOMO energy on the An and PPA ligand density reported in Table 2-1. As noted above, the thiol and thiolate have the HOMO localized primarily on the ligand nonbonding orbitals and for these ligands the charge displacement per ligand does not change significantly with coverage.

Table 2-2. Ligand and nanocluster excess charge density (in units of e) from Mulliken charges. Note that excess Cd^{2+} is included to clusters with TP^- and PPA^{2-} to neutralize the net charge.

		Small (six Se atoms) CdSe clusters	**Large ($Cd_{33}Se_{33}$) cluster**
Ligand Type		**Ligand Density**	**Ligand density**

		1.5 nm^{-2}	**2.9 nm^{-2}**	**4.4 nm^{-2}**	**1.5 nm^{-2}**
An	total	0.304	0.555	0.757	1.369
	per ligand	0.152	0.139	0.126	0.171
TP·	total	-0.315	-0.642	-0.921	-0.304[a]
	per ligand	-0.158	-0.160	-0.154	-0.019[a]
TP$^-$	total	1.643	3.282	4.859	
	per ligand	0.822	0.820	0.810	
PPA	total	0.158	0.265	0.364	0.581
	per ligand	0.079	0.066	0.061	0.073
PPA^{2-}	total	1.867	2.894	5.048	
	per ligand	0.934	0.724	0.841	

[a] Ligand density here is 2.9 nm^{-2}. Note that the Mulliken charges were found to be a sensitive function of the ligand coverage and placement for this cluster.

2.5 DISCUSSION

The data in Figure 2-5A show that the capping ligand's linker group has a large influence on the HOMO energy of the NPs and its dependence on size. Whereas the VBM for TP-CdSe and An-CdSe change little with the NP size and could be described as independent of size over the range studied, the PPA-CdSe shows a clear size dependence. This size dependence is further exemplified by comparing these results to electrochemical and photoemission data on TOPO capped CdSe NPs in Figure 2-5B. Although the electrochemical data is somewhat scattered between data sets, within a data set (in particular that of Querner et al. and Inamder et al.) a clear trend with size is apparent. In addition, the photoemission data for alykylamine-capped and pyridine-capped CdSe in Figure 2-5C reveal a significant size dependent behavior, which is stronger than that observed for An-CdSe.

To better understand the ligand effect, and its properties on the NP's energetics, data from other works were also considered. PPA-capped CdSe exhibited very similar energies to that found for TOPO-capped CdSe. Since TOPO binds as a phosphonate group these similarities were expected. Aniline- capped CdSe, on the other hand, exhibits different energies from those that have been reported for alkylamine-capped and pyridine-capped CdSe. It is possible, however, that the density of ligands on the surface of the NPs are not the same because of their different adsorption energies.[60] The study on pyridine-capped CdSe is peculiar in that it has a much larger VBM size dependence than the aniline- and alkylamine-capped CdSe NPs. Some of this difference may arise from the measurement of bare CdSe because of ligand desorption under ultra-high vacuum conditions.[25]

A simplified bonding picture suggests a correlation between the ligand binding strength and the NPs HOMO position. The binding strengths reported for the different linkers vary significantly; adsorption free energies for ligands with an amine linkage have been reported in the range of -10.0 to -25.0 kJ/mol,[16,60,66] for alkanethiol ligands on the order of -56.0 kJ/mol,[67] and DFT calculations on phosphonic acid ligands report values exceeding -60.0 kJ/mol.[68-70] In addition, the adsorption energies are affected most by the linker group (thiol versus amine versus phosphonate), and this feature is similar to that found for the VBM data in Figure 2-5B and for the HOMO energies calculated for the two cluster sizes (Cd_6Se_6 and $Cd_{33}Se_{33}$). If such a correlation is to be identified, it will be important to account for variations in ligand density.

Computational results for the HOMO energy trends of Cd_6Se_6 and $Cd_{33}Se_{33}$ nanoclusters show qualitative agreement with experimentally determined trends for VBM position with ligand type, however, only under certain coverage conditions. The ligand density was found to be important for determining the HOMO energies for amine and phosphonate linker groups, whereas the density of ligands is not as significant for the thiol linker because the HOMO is largely localized on the ligand. It is important to point out that the computational studies were done *in vacuo* and solvent contributions, which can vary with capping ligand,[33] are absent. Lastly, even the larger $Cd_{33}Se_{33}$ clusters are dominated by surface atoms and results may change as it becomes possible to perform calculations on larger clusters with more core atoms.

Because the calculations find that the HOMO of An-CdSe and PPA-CdSe are localized on the NP and not on the ligands one might expect that the VBM size-dependent behavior should be very different from that of TP-CdSe, however, the VBM of An-CdSe changes very little with NP size. To explain this apparent dichotomy, we propose that the ligand's effect on the energy partially cancels, and thus masks, the energy shift from the quantum confinement effect; i.e., the ligand effect changes as a function of size. For smaller NPs the surface-to-volume ratio is larger and therefore the ligand's influence on the energy will be larger. In the case of An-CdSe, the destabilization from the ligand strongly counteracts the decrease of the VBM at small sizes. For PPA-CdSe the destabilization of the electronic states is weaker and therefore it does not counteract the NP's size dependent VBM shift. This effect should take place for every capping ligand, in which the electronic states are localized on the NP, and is dependent on 1) how strongly a given ligand destabilizes the NP's HOMO and 2) the density of ligand's on the NP's surface.

In an effort to motivate this explanation, consider a simplified model for the VBM of CdSe NPs as a function of ligand and the NP diameter *d*; namely

$$\mathrm{E}_{\mathrm{VBM}} = (\mathrm{E}_{VBM,bulk} + X) + \frac{h^2}{2m^*d^2} + E_{solv}$$ **Equation 2-3**

The first term accounts for the bulk band edge position of the semiconductor where “X” describes the change in bulk energy arising from the adsorbate; *i.e.*, it describes the band edge position as the NP size exceeds the Bohr exciton radius. In principle, this first term could be determined experimentally from photoemission or electrochemical measurements on the bulk semiconductor, coated with the ligand. The second term is the kinetic energy of localization term for the carrier confinement, in which h is Planck’s constant and $m*$ is the effective mass. The third term accounts for the solvation free energy of the ligand-capped nanoparticle. It is this latter term that has a size dependence and can partially cancel the confinement term. Because the charge rearrangement between the ligand and the nanoparticle changes significantly with ligand type, this term can be different for each ligand-nanoparticle combination and give rise to differences in the distance dependence of the energies.

The accurate modeling of this term requires that we know the change in charge distribution on the nanoparticle for the oxidation reaction in each case; however consideration of an electrostatic model for the solvation energy shows that the extended nature of the charge distribution is important.[71,72] For example, Alavi[71] showed that the solvation energy for an arbitrary charge distribution, represented by N point charges q_i, in a spherical cavity of radius $d/2$, may be written as

$$E_{solv} = \sum_{i=1}^{N}\sum_{j=1}^{N}\sum_{L=0}\sum_{M=-L}^{L} \frac{-2\pi}{2L+1}\frac{q_iq_j}{d}\left(\frac{\varepsilon_s-1}{\varepsilon_s+L/(L+1)}\right)\left(\frac{2r_i}{d}\right)^L\left(2\frac{r_j}{d}\right)^L Y_{LM}^*(\vartheta_i,\varphi_i)Y_{LM}(\vartheta_j,\varphi_j)$$ **Equation 2-4**

in which $(r_i,\vartheta_i,\varphi_i)$ is the position of charge i, ε_s is the solvent dielectric constant, and the Y_{LM} are the spherical harmonics. While this expression should be modified to account for the polarization by the nanoparticle (dielectric constant different from 1) and the charge q_i should be replaced by the change in charge Δq_i, the features of the distance dependence remain the same. For oxidation of a ligand-coated nanoparticle, in which the HOMO is localized near the nanoparticle surface (r/d term in Equation 2-4 is large) the electrostatic solvation energy will be larger than if the HOMO is localized near the core of the nanoparticle (r/d small). Thus, if the HOMO of the aniline-coated NP and the PPA-coated NP move to the core of the nanoparticle differently as the size increases and because their charge displacements can evolve differently with size, then one expects their VBMs to have different distance dependences. Once detailed quantum chemistry calculations become available for larger nanoclusters, it will be possible to test this hypothesis quantitatively.

2.6 CONCLUSION

In this work, electrochemical methods were used to assess the change in energetics of CdSe NPs capped with different ligands as a function of size. By examining both the size dependent band edge shifts of the NPs and the corresponding ligand dependent shift together, this work has allowed us to unveil how these two effects can reinforce or counteract each other. When the ligand destabilizes the electronic states of the NP the size dependent change in energy appears to be weakened for the VBM. Lastly, the rough framework of a model was proposed to describe the combined effects of quantum confinement and ligand induced shifts on semiconducting NPs valence band position.

2.7 REFERENCES

(1) Wang, Y.; Wang, L.; Waldeck, D. H. Electrochemically Guided Photovoltaic Devices: A Photocurrent Study of the Charge Transfer Directionality between CdTe and CdSe Nanoparticles. *J. Phys. Chem. C* **2011**, *115*, 18136.

(2) Querner, C.; Reiss, P.; Sadki, S.; Zagorska, M.; Pron, A. Size and Ligand Effects on the Electrochemical and Spectroelectrochemical Responses of CdSe Nanocrystals. *Phys. Chem. Chem. Phys.* **2005**, *7*, 3204.

(3) Haram, S. K.; Kshirsagar, A.; Gujarathi, Y. D.; Ingole, P. P.; Nene, O. A.; Markad, G. B.; Nanavati, S. P. Quantum Confinement in CdTe Quantum Dots: Investigation through Cyclic Voltammetry Supported by Density Functional Theory (DFT). *J. Phys. Chem. C* **2011**, *115*, 6243.

(4) Poznyak, S. K.; Osipovich, N. P.; Shavel, A.; Talapin, D. V.; Gao, M.; Eychmuller, A.; Gaponik, N. Size-Dependent Electrochemical Behavior of Thiol-Capped CdTe Nanocrystals in Aqueous Solution. *J. Phys. Chem. B* **2005**, *109*, 1094.

(5) Hyun, B. R.; Zhong, Y. W.; Bartnik, A. C.; Sun, L.; Abruna, H. D.; Wise, F. W.; Goodreau, J. D.; Matthews, J. R.; Leslie, T. M.; Borrelli, N. F. Electron Injection from Colloidal PbS Quantum Dots into Titanium Dioxide Nanoparticles. *ACS Nano* **2008**, *2*, 2206.

(6) Inamdar, S. N.; Ingole, P. P.; Haram, S. K. Determination of Band Structure Parameters and the Quasi-Particle Gap of Cdse Quantum Dots by Cyclic Voltammetry. *ChemPhysChem* **2008**, *9*, 2574.

(7) Kucur, E.; Riegler, J. r.; Urban, G. A.; Nann, T. Determination of Quantum Confinement in CdSe Nanocrystals by Cyclic Voltammetry. *J. Chem. Phys.* **2003**, *119*, 2333.

(8) Kuçur, E.; Bücking, W.; Nann, T. Electrochemical Determination of Mesoscopic Phenomena, Defect States in CdSe Nanocrystals and Charge Carrier Manipulability. *Microchim. Acta* **2007**, *160*, 299.

(9) Jasieniak, J.; Califano, M.; Watkins, S. E. Size-Dependent Valence and Conduction Band-Edge Energies of Semiconductor Nanocrystals. *ACS Nano* **2011**, *5*, 5888.

(10) Meulenberg, R. W.; Lee, J. R.; Wolcott, A.; Zhang, J. Z.; Terminello, L. J.; van Buuren, T. Determination of the Exciton Binding Energy in Cdse Quantum Dots. *ACS Nano* **2009**, *3*, 325.

(11) Yu, W. W.; Wang, Y. A.; Peng, X. Formation and Stability of Size-, Shape-, and Structure-Controlled CdTe Nanocrystals: Ligand Effects on Monomers and Nanocrystals. *Chem. Mater.* **2003**, *15*, 4300.

(12) Peng, X.; Manna, L.; Yang, W.; Wickham, J.; Scher, E.; Kadavanich, A.; Alivisatos, A. P. Shape Control of CdSe Nanocrystals. *Nature* **2000**, *404*, 59.

(13) Zylstra, J.; Amey, J.; Miska, N. J.; Pang, L.; Hine, C. R.; Langer, J.; Doyle, R. P.; Maye, M. M. A Modular Phase Transfer and Ligand Exchange Protocol for Quantum Dots. *Langmuir* **2011**, *27*, 4371.

(14) Dong, A.; Ye, X.; Chen, J.; Kang, Y.; Gordon, T.; Kikkawa, J. M.; Murray, C. B. A Generalized Ligand-Exchange Strategy Enabling Sequential Surface Functionalization of Colloidal Nanocrystals. *J. Am. Chem. Soc.* **2011**, *133*, 998.

(15) Gaponik, N.; Talapin, D. V.; Rogach, A. L.; Eychmüller, A.; Weller, H. Efficient Phase Transfer of Luminescent Thiol-Capped Nanocrystals: From Water to Nonpolar Organic Solvents. *Nano Lett.* **2002**, *2*, 803.

(16) Bullen, C.; Mulvaney, P. The Effects of Chemisorption on the Luminescence of Cdse Quantum Dots. *Langmuir* **2006**, *22*, 3007.

(17) Liu, I. S.; Lo, H.-H.; Chien, C.-T.; Lin, Y.-Y.; Chen, C.-W.; Chen, Y.-F.; Su, W.-F.; Liou, S.-C. Enhancing Photoluminescence Quenching and Photoelectric Properties of CdSe Quantum Dots with Hole Accepting Ligands. *J. Mater. Chem.* **2008**, *18*, 675.

(18) Baker, D. R.; Kamat, P. V. Tuning the Emission of CdSe Quantum Dots by Controlled Trap Enhancement. *Langmuir* **2010**, *26*, 11272.

(19) Frederick, M. T.; Weiss, E. A. Relaxation of Exciton Confinement in CdSe Quantum Dots by Modification with a Conjugated Dithiocarbamate Ligand. *ACS Nano* **2010**, *4*, 3195.

(20) Frederick, M. T.; Amin, V. A.; Swenson, N. K.; Ho, A. Y.; Weiss, E. A. Control of Exciton Confinement in Quantum Dot-Organic Complexes through Energetic Alignment of Interfacial Orbitals. *Nano Lett.* **2013**, *13*, 287.

(21) Frederick, M. T.; Amin, V. A.; Weiss, E. A. Optical Properties of Strongly Coupled Quantum Dot–Ligand Systems. *J. Phys. Chem. Lett.* **2013**, *4*, 634.

(22) Wang, C.; Shim, M.; Guyot-Sionnest, P. Electrochromic Nanocrystal Quantum Dots. *Science* **2001**, *291*, 2390.

(23) Wu, P.-J.; Tsuei, K.-D.; Hsieh, M.-T.; Wei, K.-H.; Liang, K. S. Dependence of the Final-State Effect on the Coupling between a CdSe Nanoparticle and Its Neighbors Studied with Photoemission Spectroscopy. *Phys. Rev. B.* **2007**, *75*, 115402.

(24) Soreni-Harari, M.; Yaacobi-Gross, N.; Steiner, D.; Aharoni, A.; Banin, U.; Millo, O.; Tessler, N. Tuning Energetic Levels in Nanocrystal Quantum Dots through Surface Manipulations. *Nano Lett.* **2008**, *8*, 678.

(25) Munro, A. M.; Zacher, B.; Graham, A.; Armstrong, N. R. Photoemission Spectroscopy of Tethered CdSe Nanocrystals: Shifts in Ionization Potential and Local Vacuum Level as a Function of Nanocrystal Capping Ligand. *ACS Appl. Mater. Inter.* **2010**, *2*, 863.

(26) The exact chain length of the alkylamine is unspecified within the referenced text, however the author's state that they tested butylamine to octylamine and there was not large variations to the VBM position.

(27) Carlson, B.; Leschkies, K.; Aydil, E. S.; Zhu, X. Y. Valence Band Alignment at Cadmium Selenide Quantum Dot and Zinc Oxide $(10\bar{1}0)$ Interfaces. *J. Phys. Chem. C* **2008**, *112*, 8419.

(28) Markus, T. Z.; Wu, M.; Wang, L.; Waldeck, D. H.; Oron, D.; Naaman, R. Electronic Structure of CdSe Nanoparticles Adsorbed on Au Electrodes by an Organic Linker: Fermi Level Pinning of the Homo. *J. Phys. Chem. C* **2009**, *113*, 14200.

(29) Greaney, M. J.; Das, S.; Webber, D. H.; Bradforth, S. E.; Brutchey, R. L. Improving Open Circuit Potential in Hybrid P3HT:CdSe Bulk Heterojunction Solar Cells Via Colloidal Tert-Butylthiol Ligand Exchange. *ACS Nano* **2012**, *6*, 4222.

(30) Albero, J.; Martinez-Ferrero, E.; Iacopino, D.; Vidal-Ferran, A.; Palomares, E. Interfacial Charge Transfer Dynamics in CdSe/Dipole Molecules Coated Quantum Dot Polymer Blends. *Phys. Chem. Chem. Phys.* **2010**, *12*, 13047.

(31) Shalom, M.; Ruhle, S.; Hod, I.; Yahav, S.; Zaban, A. Energy Level Alignment in CdS Quantum Dot Sensitized Solar Cells Using Molecular Dipoles. *J. Am. Chem. Soc.* **2009**, *131*, 9876.

(32) Kuznetsov, A. E.; Balamurugan, D.; Skourtis, S. S.; Beratan, D. N. Structural and Electronic Properties of Bare and Capped Cd_NSe_N/Cd_NTe_N Nanoparticles (N= 6, 9). *J. Phys. Chem. C* **2012**, *116*, 6817.

(33) Fischer, S. A.; Crotty, A. M.; Kilina, S. V.; Ivanov, S. A.; Tretiak, S. Passivating Ligand and Solvent Contributions to the Electronic Properties of Semiconductor Nanocrystals. *Nanoscale* **2012**, *4*, 904.

(34) Yang, S.; Prendergast, D.; Neaton, J. B. Tuning Semiconductor Band Edge Energies for Solar Photocatalysis Via Surface Ligand Passivation. *Nano Lett.* **2012**, *12*, 383.

(35) Bruening, M.; Moons, E.; Yaron-Marcovich, D.; Cahen, D.; Libman, J.; Shanzer, A. Polar Ligand Adsorption Controls Semiconductor Surface Potentials. *J. Am. Chem. Soc.* **1994**, *116*, 2972.

(36) Ray, S. G.; Cohen, H.; Naaman, R.; Liu, H.; Waldeck, D. H. Organization-Induced Charge Redistribution in Self-Assembled Organic Monolayers on Gold. *J. Phys. Chem. B* **2005**, *109*, 14064.

(37) Schreuder, M. A.; McBride, J. R.; Dukes, A. D.; Sammons, J. A.; Rosenthal, S. J. Control of Surface State Emission Via Phosphonic Acid Modulation in Ultrasmall CdSe Nanocrystals: The Role of Ligand Electronegativity. *J. Phys. Chem. C* **2009**, *113*, 8169.

(38) Kalyuzhny, G.; Murray, R. W. Ligand Effects on Optical Properties of Cdse Nanocrystals. *J. Phys. Chem. B* **2005**, *109*, 7012.

(39) Peng, Z. A.; Peng, X. Formation of High-Quality CdTe, CdSe, and CdS Nanocrystals Using CdO as Precursor. *J. Am. Chem. Soc.* **2001**, *123*, 183.

(40) Wang, Y.; Xie, Z.; Gotesman, G.; Wang, L.; Bloom, B. P.; Markus, T. Z.; Oron, D.; Naaman, R.; Waldeck, D. H. Determination of the Electronic Energetics of CdTe Nanoparticle Assemblies on Au Electrodes by Photoemission, Electrochemical, and Photocurrent Studies. *J. Phys. Chem. C* **2012**, *116*, 17464.

(41) Lee, C.; Yang, W.; Parr, R. G. Development of the Colle-Salvetti Correlation-Energy Formula into a Functional of the Electron Density. *Phys. Rev. B* **1988**, *37*, 785.

(42) Becke, A. D. Density-Functional Thermochemistry. III. The Role of Exact Exchange. *J. Chem. Phys.* **1993**, *98*, 5648.

(43) Hay, P. J.; Wadt, W. R. Ab Initio Effective Core Potentials for Molecular Calculations. Potentials for the Transition Metal Atoms Scandium to Mercury. *J. Chem. Phys.* **1985**, *82*, 270.

(44) Wadt, W. R.; Hay, P. J. Ab Initio Effective Core Potentials for Molecular Calculations. Potentials for Main Group Elements Sodium to Bismuth. *J. Chem. Phys.* **1985**, *82*, 284.

(45) Frisch, M. J.; Trucks, G. W.; Schlegel, H. B.; Scuseria, G. E.; Robb, M. A.; Cheeseman, J. A.; Scalmani, G.; Barone, V.; Mennucci, B.; Petersson, G. A.*et al.* Dft. *Gaussian 09, Revision A.02, Gaussian, Inc.: Wallingford, CT* **2009**.

(46) Jose, R.; Zhanpeisov, N. U.; Fukumura, H.; Baba, Y.; Ishikawa, M. Structure-Property Correlation of CdSe Clusters Using Experimental Results and First-Principles DFT Calculations. *J. Am. Chem. Soc.* **2006**, *128*, 629.

(47) Nguyen, K. A.; Day, P. N.; Pachter, R. Understanding Structural and Optical Properties of Nanoscale Cdse Magic-Size Quantum Dots: Insight from Computational Prediction. *J. Phys. Chem. C* **2010**, *114*, 16197.

(48) Puzder, A.; Williamson, A. J.; Gygi, F.; Galli, G. Self-Healing of CdSe Nanocrystals: First-Principles Calculations. *Phys. Rev. Lett.* **2004**, *92*, 217401.

(49) Troparevsky, M. C.; Kronik, L.; Chelikowsky, J. R. Optical Properties of CdSe Quantum Dots. *J. Chem. Phys.* **2003**, *119*, 2284.

(50) Owen, J. S.; Park, J.; Trudeau, P.-E.; Alivisatos, A. P. Reaction Chemistry and Ligand Exchange at Cadmium−Selenide Nanocrystal Surfaces. *J. Am. Chem. Soc.* **2008**, *130*, 12279.

(51) Kopping, J. T.; Patten, T. E. Identification of Acidic Phosphorus-Containing Ligands Involved in the Surface Chemistry of CdSe Nanoparticles Prepared in Tri-N-Octylphosphine Oxide Solvents. *J. Am. Chem. Soc.* **2008**, *130*, 5689.

(52) Liu, H.; Owen, J. S.; Alivisatos, A. P. Mechanistic Study of Precursor Evolution in Colloidal Group II−VI Semiconductor Nanocrystal Synthesis. *J. Am. Chem. Soc.* **2006**, *129*, 305.

(53) Yu, W. W.; Qu, L.; Guo, W.; Peng, X. Experimental Determination of the Extinction Coefficient of CdTe, CdSe, and CdS Nanocrystals. *Chem. Mater*. **2003**, *15*, 2854.

(54) Kloepfer, J. A.; Bradforth, S. E.; Nadeau, J. L. Photophysical Properties of Biologically Compatible CdSe Quantum Dot Structures. *J. Phys. Chem. B* **2005**, *109*, 9996.

(55) Knowles, K. E.; Tice, D. B.; McArthur, E. A.; Solomon, G. C.; Weiss, E. A. Chemical Control of the Photoluminescence of CdSe Quantum Dot-Organic Complexes with a Series of Para-Substituted Aniline Ligands. *J. Am. Chem. Soc.* **2010**, *132*, 1041.

(56) Meek, J. T.; Sekreta, E.; Wilson, W.; Viswanathan, K. S.; Reilly, J. P. The Laser Photoelectron Spectrum of Gas Phase Aniline. *J. Chem. Phys.* **1985**, *82*, 1741.

(57) Al-Joboury, M. I.; Turner, D. W. 851. Molecular Photoelectron Spectroscopy. Part Ii. A Summary of Ionization Potentials. *J. Chem. Soc. (Resumed)* **1964**, *0*, 4434.

(58) Lifshitz, C. Time-Dependent Mass Spectra and Breakdown Graphs. 2. The Kinetic Shift in Pyridine. *J. Phys. Chem* **1982**, *86*, 606.

(59) Hassinen, A.; Moreels, I.; de Mello Donegá, C.; Martins, J. C.; Hens, Z. Nuclear Magnetic Resonance Spectroscopy Demonstrating Dynamic Stabilization of CdSe Quantum Dots by Alkylamines. *J. Phys. Chem. Lett.* **2010**, *1*, 2577.

(60) Donakowski, M. D.; Godbe, J. M.; Sknepnek, R.; Knowles, K. E.; Olvera de la Cruz, M.; Weiss, E. A. A Quantitative Description of the Binding Equilibria of Para-Substituted Aniline Ligands and CdSe Quantum Dots. *J. Phys. Chem. C* **2010**, *114*, 22526.

(61) Fritzinger, B.; Capek, R. K.; Lambert, K.; Martins, J. C.; Hens, Z. Utilizing Self-Exchange to Address the Binding of Carboxylic Acid Ligands to CdSe Quantum Dots. *J. Am. Chem. Soc.* **2010**, *132*, 10195.

(62) Gomes, R.; Hassinen, A.; Szczygiel, A.; Zhao, Q.; Vantomme, A.; Martins, J. C.; Hens, Z. Binding of Phosphonic Acids to CdSe Quantum Dots: A Solution NMR Study. *J. Phys. Chem. Lett.* **2011**, *2*, 145.

(63) Morris-Cohen, A. J.; Frederick, M. T.; Lilly, G. D.; McArthur, E. A.; Weiss, E. A. Organic Surfactant-Controlled Composition of the Surfaces of CdSe Quantum Dots. *J. Phys. Chem. Lett.* **2010**, *1*, 1078.

(64) Jasieniak, J.; Mulvaney, P. From Cd-Rich to Se-Rich − the Manipulation of CdSe Nanocrystal Surface Stoichiometry. *J. Am. Chem. Soc.* **2007**, *129*, 2841.

(65) Brus, L. E. Electron–Electron and Electron-Hole Interactions in Small Semiconductor Crystallites: The Size Dependence of the Lowest Excited Electronic State. *J. Chem. Phys.* **1984**, *80*, 4403.

(66) Ji, X.; Copenhaver, D.; Sichmeller, C.; Peng, X. Ligand Bonding and Dynamics on Colloidal Nanocrystals at Room Temperature: The Case of Alkylamines on CdSe Nanocrystals. *J. Am. Chem. Soc.* **2008**, *130*, 5726.

(67) Munro, A. M.; Jen-La Plante, I.; Ng, M. S.; Ginger, D. S. Quantitative Study of the Effects of Surface Ligand Concentration on CdSe Nanocrystal Photoluminescence. *J. Phys. Chem. C* **2007**, *111*, 6220.

(68) Rempel, J. Y.; Trout, B. L.; Bawendi, M. G.; Jensen, K. F. Density Functional Theory Study of Ligand Binding on CdSe (0001), $(000\bar{1})$, and $(11\bar{2}0)$ Single Crystal Relaxed and Reconstructed Surfaces: Implications for Nanocrystalline Growth. *J. Phys. Chem. B* **2006**, *110*, 18007.

(69) Puzder, A.; Williamson, A. J.; Zaitseva, N.; Galli, G.; Manna, L.; Alivisatos, A. P. The Effect of Organic Ligand Binding on the Growth of CdSe Nanoparticles Probed by Ab Initio Calculations. *Nano Lett.* **2004**, *4*, 2361.

(70) Liu, H. Tuning the Binding Energy of Surfactant to CdSe Nanocrystal: A Theoretical Study. *J. Phys. Chem. C* **2009**, *113,* 3116.

(71) Alavi, D.; Waldeck, D. In *Ultrafast Dynamics of Chemical Systems*; Simon, J., Ed.; Springer Netherlands: 1994; Vol. 7, p 249.

(72) Still, W. C.; Tempczyk, A.; Hawley, R. C.; Hendrickson, T. Semianalytical Treatment of Solvation for Molecular Mechanics and Dynamics. *J. Am. Chem. Soc.* **1990**, *112*, 6127.

3.0 ELIMINATING FERMI-LEVEL PINNING IN PBS QUANTUM DOTS USING AN ALUMINA INTERFACIAL LAYER

This work has been published as Bloom, B.P.; Mendis, M. N.; Wierzbinski, E.; and Waldeck, D. H. The thesis author aided in the experimental design of the project, did all of the UPS experiments and participated in writing the manuscript. The supporting information for this chapter is provided in Appendix C.

Through a systematic approach, we show that the insertion of a thin alumina layer in between a PbS QD layer and an Au substrate can eliminate Fermi level pinning. In this study, band edge energies of different sized PbS QD monolayers with different cross-linkers were measured by using ultraviolet photoelectron spectroscopy and electrochemistry. When PbS QDs were immobilized directly on the Au, the measured valence band maximum was found to be insensitive to changes in the QD size or cross-linker indicating Fermi level pinning of the QD valence band to the Au Fermi level. After insertion of a thin film of alumina in between the PbS quantum dot monolayer film and the Au substrate, the measured valence band position revealed a shift that depended on ligand and QD size. These results identify a general method for eliminating Fermi level pinning in QDs and an approach for predictably controlling the energetics at the QD - metal interfaces which is beneficial for improving the performance of QD based solar cells.

3.1 INTRODUCTION

Third generation solar cells are aimed at overcoming the thermodynamic limit set for the power conversion efficiency calculated by Shockley and Queisser in 1961 for a single junction and to do so at low-cost.[1,2] Several approaches have been proposed to exceed this limit and one of the most promising schemes is the multi exciton generation by semiconductor quantum dots (QDs). Compared to organic bulk heterojunction solar cells that suffer from lower carrier diffusion lengths and large offsets in the donor and acceptor levels, QD based solar cells have important advantages that mitigate these constraints. The optical band gap in the QDs can be adjusted by changing their size, shape, surface passivation, and composition. Moreover, QDs allow for easy inexpensive solution based synthesis and processing, making them cost effective for large scale fabrication. In addition to these attributes, the organic ligand shell on a QD can be used to fine tune the electronic properties and the solvation characteristics.

In photovoltaic devices, QD films are commonly sandwiched between a cathode and an anode, which may be a metal (Schottky junction cells) or another semiconductor (p-n heterojunction solar cells), to form a complete functional device. Upon illumination by photons with sufficient energy, an electron-hole pair is formed in the QDs and they must be separated and extracted to opposing electrodes to produce a current. In a conventional p-n junction solar cell the charge carriers are driven by an electric field at the interface of the two semiconductors. One common strategy for enhancing charge separation is to alter the band positions within the QD films so that they form a staggered type-II alignment, creating a favorable energy cascade for both electron and hole transport.[3-5] Using arrays of different sized CdSe QDs, Weiss et al. have demonstrated that the photocurrent produced by each sized QD is largely dependent on the relative spatial arrangement and the band offset between them.[6] Similarly, El-Ballouli et al. have shown that favorable charge transfer from PbS QDs to PCBM[7] and cationic porphyrins[8] is determined by the size of the nanoparticle. In a previous study by Wang et al, donor- acceptor assemblies of CdSe-CdTe QD layers were shown to facilitate unidirectional charge transfer as long as proper energy band alignment is maintained in the photovoltaic device.[5] In a recent implementation of this strategy Chuang et al., used ligand induced band energy shifts to create a QD energy gradient that led to a photovoltaic efficiency over 8%.[3] Furthermore, an efficiency as high as 10.7% has been achieved by tuning the energy alignment at the rectifying interface, a new record for QD based solar cells.[9]

Surface ligands have been shown to shift the absolute energy positions of the valence band maximum (VBM) and conduction minimum (CBM) of QDs, and a growing body of evidence suggests that the magnitude of the energy shift can be characterized as a function of the dipole moment between the surface and linking group and the intrinsic dipole moment of the ligand itself. [10-12] By changing the capping ligand one can shift band energies of CdSe[10,13-15], CdS[16], PbS[4,11,17,18], as well as other nanocrystals[19]. Most recently, researchers have been using ligands to shift the absolute energy levels of QDs and to form an energy level gradient for efficient charge separation. However, the magnitudes of the ligand’s influence on the band energies can be affected by the electronic and chemical properties of a QD photovoltaic device at interfaces. When QDs are adsorbed onto a metal, charge equilibrium between the metal and the QD occurs; and it can ‘pin’ the electronic states of the QD to the Fermi level of the metal substrate. Often times the electronic energies of QDs determined in solution or under flat band conditions are used in determining a photovoltaic device architecture. When Fermi level pinning occurs in QD based solar cell devices, the QD size and ligand induced effects over the energy position may no longer persist. In a study on CdSe QDs immobilized onto Au substrates by a decanedithiol linker, Markus et al. have shown that the absolute energy position of the VBM of the QDs larger than 2.8 nm does not change.[20] Depending upon the relationship of the QDs electronic states to that of the substrate, the CBM can also be pinned.[21] Previous electrochemical and UPS measurements on CdTe QD monolayers attached to an Au substrate through dithiol linkers showed no shift in VBM over the size range of 3.7 to 6.0 nm.[22] In Schottky junction solar cells, Fermi level pinning reduces the interfacial barrier height for charge injection and can reduce overall device efficiency. In some cases the pinning between the QDs and a can persist for significant distances, e.g. 25 nm thick MO_3 layers.[23] Because the photoinduced free carriers must transfer through interfaces to be collected, control over the electronic properties of the QD-metal junction are important for improving the photoconversion efficiency of QD based solar cells.

3.2 BACKGROUND OF LIGAND EFFECTS ON PBS QD ENERGETICS

In photovoltaic devices, QDs are usually coated with short ligands to achieve better electronic coupling by changing the inter-QD tunneling distance and the effective dielectric constant. In a study by Liu et al, the dependence of ligand length and QD size on carrier mobility were reported for PbSe QDs field effect transistors.[24] The degree of QD surface passivation is also important for minimizing trap induced charge recombination. Wanger et al. showed that the effective density of trapped carriers has a strong dependence on ligand treatment in PbS QD films.[25] Zhitomirsky et al. measured the effect that QD films treated with organic (mercaptoproponoic acid) or a mixture of hybrid organic-inorganic (tetrabutylammonium iodide) ligand types have on charge mobility, trap density, and exciton diffusion length in QD films.[26] They have found that films with such organic-inorganic passivation exhibit the largest charge diffusion lengths. These findings have led to the use of organic-inorganic hybrid passivation of PbS QDs to make a photovoltaic device with 7% power conversion efficiency.[27] Control of energetics at the rectifying interface of the PbS QD solar cells has allowed further improvement in photoconversion efficiency up to 10.7 %.

Axnanda et al. used photoelectron spectroscopy to measure the work function of 30 nm thick PbS QD films as a function of the capping ligand and observed a ligand effect on the energetics.[17] This work showed that methoxide, mercaptopropionic acid, and ethanedithiol (EDT) ligands could shift the VBM over a range of 0.3 eV. The resulting deeper work function VBM energy position has been explained by incomplete surface passivation and the presence of hole trap states. In a more comprehensive study, Brown et al. examined the band energies of PbS QD films (~100 nm) modified with 12 different ligands and reported that the VBM shifts over a range of 0.9 eV with ligand.[11] The same group has used the VBM energy offset between tetrabutylammonium iodide (TBAI) and 1, 2-ethanedithiol (EDT) capping ligands to alter the band energy positions and produce favorable charge transport in a photovoltaic device, achieving a power conversion efficiency of 8.5 %.[3] In another study by Crisp et al. it was shown that inorganic metal halide ligands in thick films of PbS (~ 300 -750 nm) leads to high efficiency photovoltaic devices.[18] They have used four different metal halides and attributed the improved device efficiency to better carrier transport in the film with halide passivation. Their XPS studies performed on the films of PbS treated with iodide ligands suggest a deeper work function, as compared to sulfur containing ligands. Santra et al. used three different para-substituted thiophenols with different dipole moments as capping ligands for PbS QD films (350 nm) to fabricate type-II heterojunction solar cells and reported a systematic shift in the VBM in PbS QDs.[4] Again type-II VBM alignment was shown to facilitate favorable unidirectional charge transport, however, when the bands edges are aligned in a way that the electron and hole encounter a potential barrier to reach the respective electrodes, a lower efficiency results.

Taken together, all the above studies affirm the role of capping ligand in manipulating the electronic band energies of PbS QDs and subsequently, the band alignment in solar cells. Control over the carrier mobility, trap state density, and charge diffusion has been achieved by tuning the cross-linker. Major advances in photoconversion efficiency have been obtained using this strategy in QD solar cell devices. Moreover, photovoltaic devices of PbS QD-polymer blends (oly((4,8-bis(octyloxy)benzo(1,2-b:4,5-b′)-dithiophene-2,6diyl)(2((dodecyloxy)carbonyl)thieno(3,4-b)-thiophenediyl)) have reported a dependence of the open circuit voltage and overall device performance on the PbS QD ligand treatment which has been credited to the ligands influence over the carrier lifetime.[28] Despite these advances, the overall power conversion efficiencies of the QD based solar cells still remain below their expected performance largely because of low open circuit voltage.[29-32] Generally this limitation has been understood to originate from the presence of sub-bandgap states or midgap states that are formed by a large number of surface states associated with the defects on the QD surface. Such midgap states drive Fermi level pinning at the QD/metal interface in Schottky junction solar cells; as a result, the open circuit voltage is controlled by the pinning rather than the metal’s work function or the QD’s band edge.[31] This work is substantiated by the work of Yoon et al.

who showed that insertion of an LiF layer between the top Al contact and PbS QDs improved the open circuit voltage in PbS QD solar cells.[33] Furthermore, oxidized interfacial layers on PbS QDs,[34] as well as insertion of a CdS shell on PbS QDs,[35] have been shown to increase the open circuit voltage in Schottky junction solar cell. A general approach to passivate these gap states and eliminate Fermi pinning at the QD – metal interfaces is not available.

PbS quantum dots (QDs) are promising candidates for third generation photovoltaics because the elements are earth abundant[36], the bandgap is tunable over a wavelength range that can best exploit the solar spectrum[37], and they offer the potential for multiple exciton generation[38,39]. This work examines the band edge energetics in PbS QD films and demonstrates the conditions for Fermi level pinning versus ligand control over the energetics. More specifically, this work shows that a thin alumina film (circa 1 to 3 nm) can be used to eliminate Fermi level pinning effects. The energy band positions of PbS QD monolayers on Au substrates, with and without an alumina layer, were measured using electrochemistry and ultraviolet photoelectron spectroscopy. When a monolayer of PbS QDs was deposited on top of an Au substrate, valence band positions were independent of known trends with QD size and surface ligand type, indicating strong Fermi level pinning. Introduction of a thin alumina interfacial layer between the Au and PbS inhibits Fermi level pinning so that the QD size and ligand can be used to manipulate the band edge positions. These findings highlight the importance of interfacial states in photovoltaic devices and enable precise control over QD properties for charge injection.

3.3 EXPERIMENTAL

3.3.1 Substrate preparation

Substrates (12.5 mm × 25.0 mm) for these experiments were prepared by e-beam evaporation (AJA Deposition System) of 100 nm thick films of Au on glass substrates supported by a 5.0 nm Ti adhesion layer. For bare Au experiments the samples were plasma cleaned and used immediately. For experiments with an alumina layer, half of the substrate was covered with a wafer tape and poly-methyl-methacrylate (950k A11 PMMA, Micro Chem) was spun on it at a speed of 1500 rpm for 1 min using a spin processor (Laurell WS-400-6NPP-LITE). The wafer tape was removed, and the substrates were baked on a hot plate at 180 ^{o}C for 5 min. Thin films of Al_2O_3 were then deposited using atomic layer deposition (Cambridge Nanotech Fiji). The samples were then kept overnight in acetone to remove the PMMA and to expose the underlying Au substrate on half of the electrode.

3.3.2 PbS QD Synthesis and Characterization

The synthesis of PbS QDs followed a general procedure described elsewhere.[40] All of the materials, such as; $PbCl_2$ (Stern Chemicals), oleylamine (OLA, Sigma Aldrich), oleic acid (OA, Sigma Aldrich), and bis(trimethylsilyl) sulfide (TMS, Sigma Aldrich) were purchased in the highest purity grade available and used without further purification. In a typical synthesis, 3.0 mmol $PbCl_2$ (0.834 g) was mixed with 10 ml of OLA and degassed at 80.0 C, followed by heating to 140.0 C under argon. The suspension was maintained at this temperature for 30 min and then cooled to 30.0 C. Then 210.0 µl of TMS mixed in 2.0 ml of OLA was injected into the reaction mixture. The mixture was then rapidly elevated to a high temperature while stirring and subsequently quenched in a water bath once the desired QD size was obtained. The PbS QDs were precipitated from solution through the addition of acetone and centrifugation. The purified QDs were then dissolved in octane with 500 µl of OA, for ligand exchange, for 12 hours. The subsequent solution was then filtered using a 0.2 µm syringe filter, purified again, and then dissolved in 4.0 ml of octane.

Absorption spectra of the PbS QDs were recorded in octane using a spectrometer (Model 8453 Agilent Spectrometer). PbS QD emission spectra were obtained after exciting at 500 nm wavelength using a spectrofluorometer (Nanolog, Hobira).

3.3.3 PbS Thin Film Preparation and Ligand Exchange

All of the QD films were prepared by spin-casting. For each QD size, the PbS QD concentration was determined by evaluating the absorption spectrum. 10 µl of the PbS QD solution was spun onto Au substrates at a speed of 2500 rpm for 15 s. The resulting QD film was then cross-linked (vide infra) and thickness was determined using AFM (Agilent Technologies) under tapping mode. This thickness was then used to determine a dilution factor of the QD solution to obtain a submonolayer thickness. The sample was prepared again and AFM was used to confirm submonolayer formation.

Ligands used for solid state ligand exchange, 1,4-benzedithiol (BDT, Alpha Aesar), 1,2-ethanedithiol (EDT, Sigma Aldrich), and ethylenediamine (EDA, Sigma Aldrich) were used as purchased. All ligands were dissolved in acetonitrile at varying concentrations; 1.7 mM BDT and one volume percent for both EDT and EDA. In a typical ligand exchange procedure, ~ 0.3 ml of ligand solution was dispersed onto the PbS monolayer film and allowed to sit for 1 min. The film was flushed with acetonitrile and spun dry two times to remove any unbound ligand. The samples were immediately transferred to a glove bag and stored under argon until electrochemical or UPS analysis.

3.3.4 Atomic Force Microscopy Characterization

AFM measurements were performed with an Agilent 5500 atomic force microscopy system using silicon cantilevers with resonance frequency of 96-175 kHz and spring constant of 5-37 N/m (PPP-SEIHR, Nanosensors). Precise values of the spring constants were determined using a thermal oscillation technique.[41] The film thickness was determined from the difference in the average height of the substrate covered with the PbS nanoparticle film and the bare gold substrate. The gold surface was exposed by scraping off the film in a 500 nm by 500 nm square area by performing a single AFM scan in a contact mode with an applied load force of ca. 500 nN. Following this procedure, a larger 4 micrometer by 4 micrometer square area was imaged in acoustic AFM mode to capture the original nanoparticle film together with the exposed gold substrate area. Switching between AFM operating modes was performed with a fully contracted z-axis piezoelement (the tip and the substrate were out of contact).

3.3.5 Electrochemical Characterization

Cyclic voltammetry on PbS films was performed in deoxygenated acetonitrile (99.9%, Sigma Aldrich) in a three electrode configuration on a CH Instruments 618B potentiostat. A Pt wire was used for the counter electrode, and Ag/$AgNO_3$ was used as the reference electrode. A 0.1 M solution of tetrabutylammonium hexafluorophosphate (Sigma Aldrich) was used as the supporting electrolyte. Voltammograms were obtained by scanning from 0 V to -1.2 V at a scan rate of 200 mV/s. The onset of the reduction peak for the QD was determined after subtraction of the background charging current, through an exponential fit. The formal potential of ferrocene / ferrocenium was used to calibrate the $Ag/AgNO_3$ reference electrode and convert the CBM of the PbS QDs to the vacuum energy scale.[22] The VBM was determined through addition of the optical band gap and exciton binding energy to the CBM.

3.3.6 Photoelectron Spectroscopy Characterization

UPS measurements were performed using an ESCALAB 250XI XPS at a base pressure of $\sim 10^{-10}$ millibar. Electrical contact to the stage was made using copper tape on the edge of the Au substrate. Experiments were performed to ensure that no Cu photoemission signal contributed to the spectra. A bias of -5.0 eV was applied to the stage so that 1) the secondary electron cut off of the sample is distinguishable from that of the detector and 2) to ensure that the local vacuum level of the sample is more negative than that of the detector. A pass energy of 1.0 eV and a dwell time of >50 s were used to increase resolution and eliminate charging. A He (I) discharge lamp, 21.22 eV, was used as the ultraviolet source. The onset region and subsequent determination of the valence states were fit using previously published protocols.[20] In all experiments the Fermi edge of the underlying Au substrate is monitored to accurately reference the data.

3.4 RESULTS

Absorbance and emission spectra of the three different sized PbS quantum dots (QDs) used in this study are shown in Figure 3-1 (A). The sizes of these QDs were estimated from the empirical model developed by Moreels et al.[42] Note that the Stokes shift observed for the PbS QDs changes with size in a manner consistent with previous literature.[43,44] The PbS QDs were then spin-coated onto an Au substrate and AFM measurements were performed. Figure 3-1 (B) and (C) show an example AFM image and measured thickness used to characterize each QD film for the determination of average thickness.

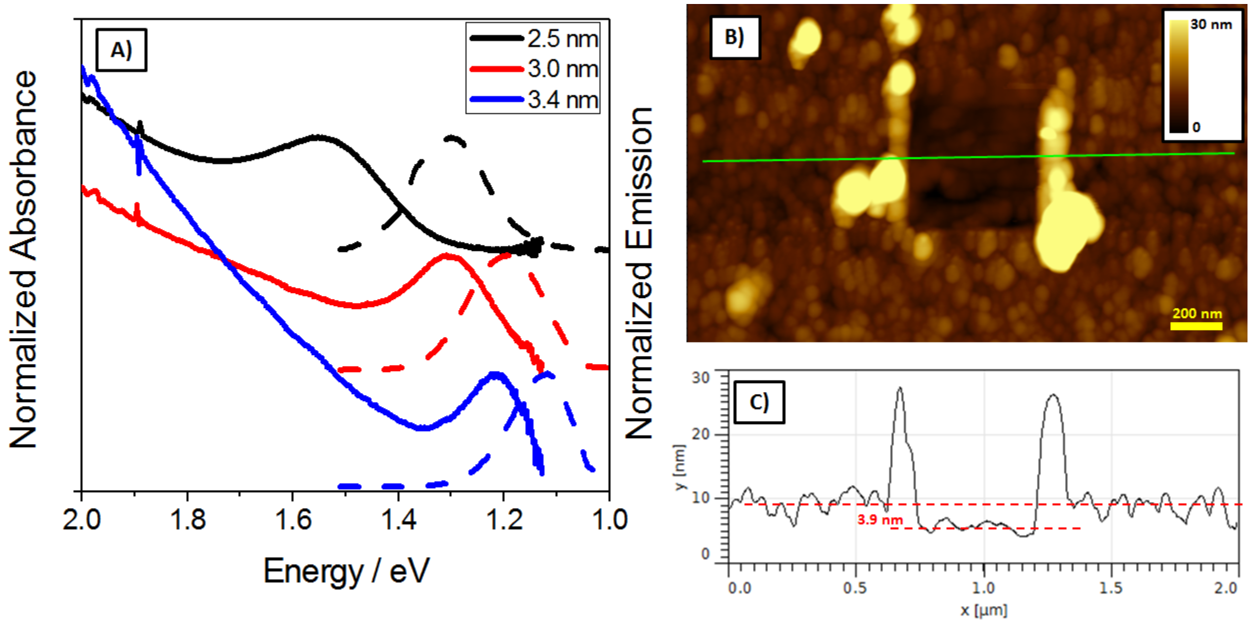

Figure 3-1. A) Normalized absorbance (solid line) and emission (dashed line) spectra of 2.5, 3.0, and 3.4 nm QDs in octane; B) AFM image of 3.0 nm PbS QDs that are cross-linked with EDT on Au; and C) height profile of the scratched QD film.

Figure 3-2 shows representative data from UPS (A) and electrochemistry (B) for 3.0 nm PbS with an EDA cross-linker. For UPS measurements, the VBM is determined by measuring the onset of the photoelectron spectra relative to the Fermi edge of Au (E_f). The work function of a bare Au substrate (4.8 eV) was then used to reference these data to absolute electrode potential found in the electrochemical measurements. Cyclic voltammetry measurements on the CBM of PbS were performed in a manner similar to that reported previously.[22] Briefly, the PbS QDs exhibited a cathodic peak in the potential range of -0.9 to -0.5 volts versus AglAgNO$_3$, similar to those reported by Hyun et al.[45] Because the range overlaps with the limit of the solvent's potential window it was necessary to perform background subtraction. The voltammogram, excluding the peak region, was fit to an exponential (green) and then subtracted from the data to give a background subtracted (blue) curve, Figure 3-2B. This procedure minimizes the effect of the capacitive current and allows for more accurate determination of the onset potential. Using the known absolute electrode potential for ferrocene, the onset potential can then be related to the vacuum energy scale by referencing to the ferrocene / ferrocenium redox couple.

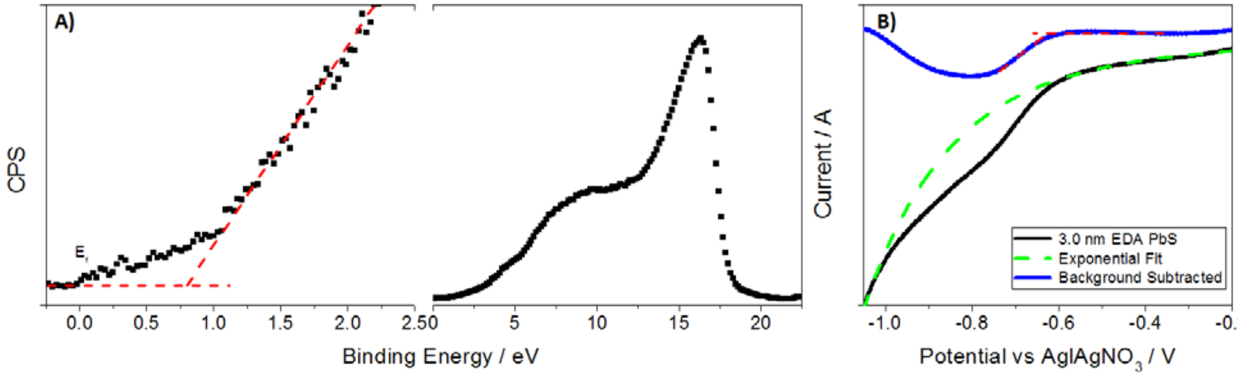

Figure 3-2. UPS spectra (A) and cyclic voltammogram (B) of 3.0 nm PbS QDs that are cross-linked by EDA to determine the VBM and CBM respectively. UPS of the onset region (A, left) and the full spectra (A, right) are shown. The red dashed line in both the UPS spectra and voltammogram show the onset potential associated with the corresponding electronic states.

Figure 3-3 summarizes the VBM and the CBM positions that were determined for thin films of the three different sized QDs that are capped with three different ligands: EDT, BDT, and EDA. The VBM was experimentally determined by UPS (Figure 3-3B, stars) and the CBM was experimentally determined using cyclic voltammetry (Figure 3-3A, stars). The optical bandgap and exciton binding energy were then used to determine the other bandedge. The measurements were performed on the same sample which was divided into two separate pieces using a glass cutter following the thin film fabrication. Each symbol represents the average of three independent measurements (an example of each is included in the supporting information). The standard deviation of the measurement is used for the error bars in the electrochemistry measurements and the resolution of the instrument, 0.1 eV, is used for the error bars in the UPS measurements. Slight differences in the electronic state positions obtained through the UPS and voltammetry methods exist and are attributed to environmental differences during measurement. Note that each of the experimental methods has limitations that affect the accuracy. The voltammetry is performed in an electrolyte solution where dielectric and double layer, as well as solvation, effects can influence the measured reduction potential. The UPS measurements are performed in vacuum and can be affected by local vacuum level shifts.[46] Despite the differences in energy found for the VBM from the two different techniques the experimental data are in reasonable agreement. Moreover, the two methods independently demonstrate that the VBM of the PbS QD monolayer films does not change significantly over the size range and cross-linker types studied. In both experiments the CBM shifts systematically to higher energies with a decrease in QD size. For UPS measurements on medium and large sized QDs the CBM is reported below the bulk band energy of PbS (4.35 eV),[15] providing further evidence that Fermi-level realignment occurs at the metal-NP interface.

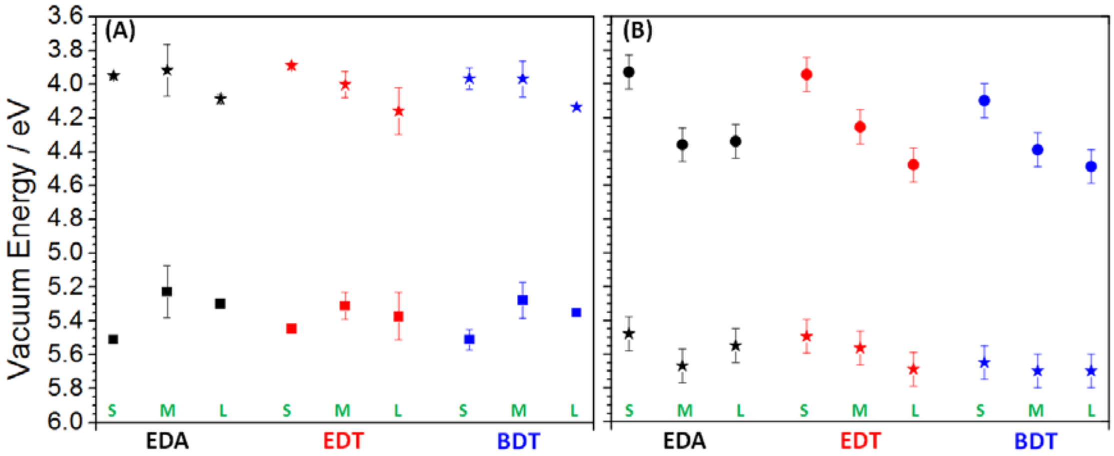

Figure 3-3. Electronic states of PbS monolayers determined by cyclic voltammetry (A) and photoelectron spectroscopy (B) are plotted versus the three different ligands used for cross-linking: EDA (black), EDT (red), and BDT (blue). Stars are representative of the experimentally determined values and a combination of the optical band gap and exciton binding energy was used to calculate the other bandedge. The S, M, and L represent the three different QD diameters 2.5 nm, 3.0 nm, and 3.4 nm, respectively. The dashed black line corresponds to the bulk CBM of PbS and the gray bar illustrates that all of the experimental UPS data fall within the error associated with the UPS measurement 5.6 +/- 0.1 eV. The error bars in the UPS measurement are a result of instrument resolution and the error bars in the electrochemistry data are representative of the standard deviation of multiple measurements.

When a thin interfacial layer of alumina is placed between the PbS monolayer film and the Au substrate, a trend different from that shown in Figure 3 was observed. The Au substrate used for these studies contained Al_2O_3 on one half of the substrate while the other half was bare Au (see Figure 3-4(A)). This procedure enabled a direct comparison of the two systems under identical conditions. UPS was employed to deduce the VBM for EDT cross-linked monolayer films of 2.5 nm and 3.0 nm diameter PbS QDs with 1 and 3 nm alumina layers (supporting information Figure C4). Figure 3-4(B) shows the bandedge values obtained, as relative shifts from the Fermi level of Au (E_f), from these measurements. The plot shows that when no alumina is present (0 nm), no relative shift in VBM from the Fermi level of Au is found as a function of QD size. When alumina is present, however, the two different sized QDs have distinctly different electronic energy positions. Furthermore this shift depends on the thickness of the interfacial alumina, indicating that the PbS VBM is being decoupled from the Au Fermi level and the expected size dependent VBM shift is becoming manifest. Namely, the larger nanoparticles (in the 1 and 3 nm alumina thickness) have the VBM slightly higher, closer to that of bulk PbS. Note that a different cleaning procedure (see experimental section) was used here than in the previous measurements (Figure 3-3) in order to maintain the integrity of the film. As a result the work function of Au can shift slightly, however, both are internally consistent.

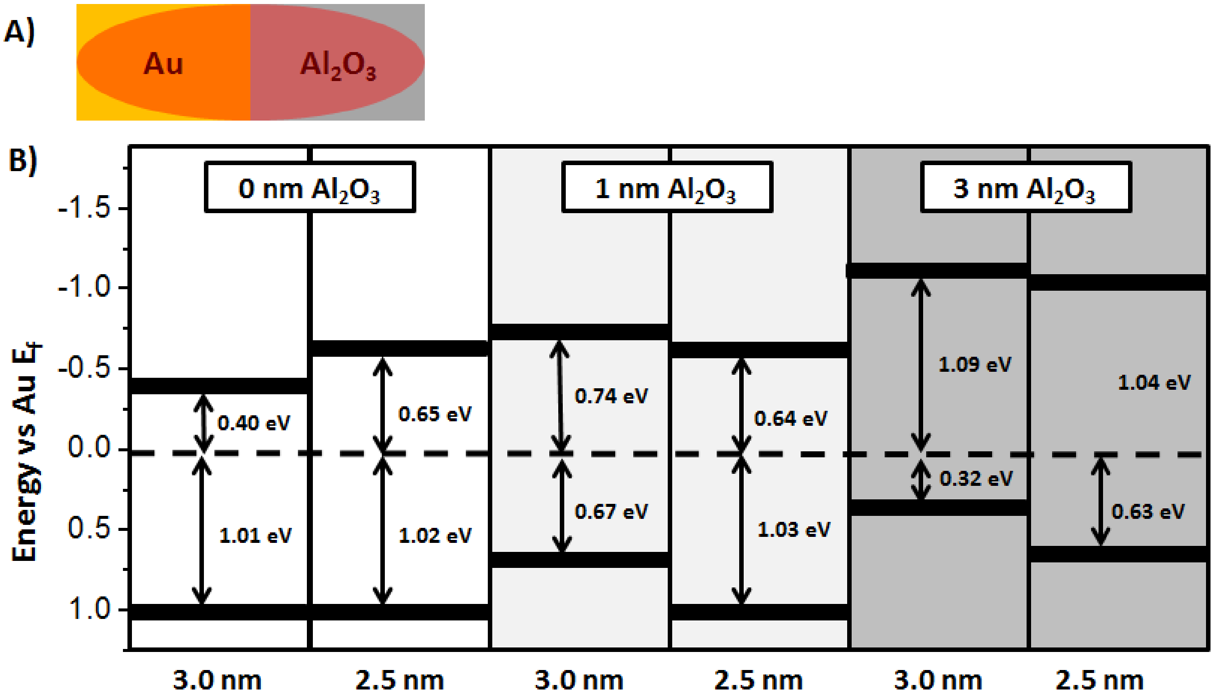

Figure 3-4. Diagram (A) shows a schematic of the substrate configuration used in this part of the study and diagram (B) shows the UPS determined energy band positions of the PbS monolayers. In B) the VBM and CBM are presented as relative shifts from the Au Fermi level (E_f = 0 eV) for two different size QDs and three different thicknesses of alumina. The black boxes correspond to the band edge positions and their shift from E_f is provided next to the double headed arrow.

Figure 3-5 shows the VBM and CBM of PbS QD monolayers on 100 nm Au substrates and their energies obtained by UPS for 2.5 nm QDs (open symbol) and 3.0 nm QDs (closed symbol) without (A) and with (B) a 3 nm alumina interfacial layer. The NPs are cross-linked in the same manner that was used in the Fermi level pinning study: BDT, EDT, and EDA. The energy of the VBM (black symbols) and CBM (red symbols) are reported with respect to the Au Fermi edge in the UPS spectra (supporting information Figure C5). On the Au substrate without alumina, it is clear that there is no variation in the VBM with QD diameter and cross-linker type. When alumina is present the VBM changes in a manner consistent with earlier reports: 1) the shift in VBM is correlated with the ligand identity for QDs of the same size and 2) the VBM shifts more strongly for QDs with a larger surface-to-volume ratio.

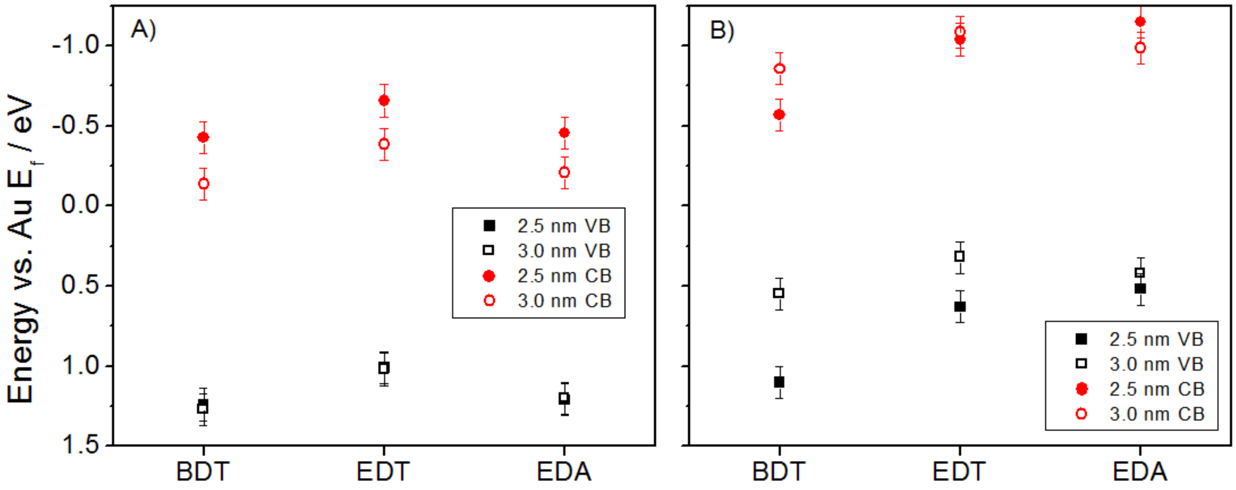

Figure 3-5. VBM (black symbols) and CBM (red symbols) of PbS monolayers with 2.5 nm (open symbols) and 3 nm (closed symbols) size QDs, as determined by UPS. Diagram A) is on the bare Au part of the substrate and diagram B) is for the part of the substrate covered with 3.0 nm of alumina. Three different cross-linkers were studied: BDT, EDT and EDA. Energy level positions are reported with respect to the Au Fermi edge in the UPS spectra.

3.5 DISCUSSION

When a semiconductor QD is in physical and electrical contact with a metal, charge equilibration occurs and the semiconductor's electronic states couple to those of the metal. If these interactions are caused by localized interfacial states,[47] then the charge exchange creates an electric field that 'pins' the semiconductor bandedge to the metal Fermi level. Which bandedge is pinned depends on the details of the orbitals that contribute to the electronic coupling and the surface state energy, with respect to the bandedge. Fermi level pinning results in different sizes of QDs exhibiting similar barrier heights for charge injection upon photoexcitation. This phenomenon has been demonstrated for quantum dots at the interface with either a metal, or metal oxide, through electrochemical,[20,22] photoemission,[20-22,48-50] and Kelvin probe techniques.[51] The data in Figure 3-2 show that this pinning behavior is observed for monolayers of three differently sized PbS QDs on Au. Interestingly, the pinning effect persists for different cross-linkers (EDT, EDA, and BDT) despite recent studies which indicate that a change in the surface passivation changes bandedge positions of the QDs.

It is important to appreciate the difference between the monolayer films studied herein and the thicker films reported on by a number of other workers.[4,11,17] As the film thickness increases, the outer layers which are no longer directly coupled to the substrate, should have their energetics affected by the coupling between QDs, rather than by the asymmetric QD to metal coupling. In this limit, strong ligand dipolar effects are expected to determine the VBM and CBM of the PbS NPs. Thus one expects that the profile of bandedge energy with thickness will change through a thick film, from the Fermi level pinning value at the metal electrode surface to the QD-QD coupling value for thick films.

This study shows how the Fermi level pinning, caused by electronic coupling between the QDs surface states and the underlying metal electrode, can be eliminated by inserting a thin Al_2O_3 layer. The presence of this layer acts to reduce the metal-QD coupling and charge exchange. As Figure 3-3 illustrates, an increase in the thickness of Al_2O_3 from 0 nm to 3 nm between Au and an EDT cross-linked PbS monolayer causes a shift in the VBM energy from a size independent pinned value to a size dependent value. These data provide direct evidence that strong coupling and charge displacement between the NPs and the Au electrode cause the Fermi level pinning, and ligand control is returned when this coupling is weakened enough. A different type of oxide film could be used to modulate the magnitude of the effect observed here; for example Beard et al. have examined how the open circuit voltage of a PbS QD film changes with thickness of a MoO_3 layer (up to 25 nm) between it and a metal electrode.[23] As such, it is expected that the barrier height for charge injection would be weakly dependent or even independent of cross-linker type or NP size when the thickness of MoO_3 is less than this amount. The large thicknesses needed to reduce the pinning effect in their study likely arises because the electronic states of the MoO_3 are energetically close to the electronic states of PbS; ie. enhancing their mixing.

The system under investigation in Figure 3-4 is in agreement with the explanation given by Choi et al. in which a PbS film was annealed in air to passivate the NPs with a thin oxide layer prior to deposition of the top contact (LiF/Al/Ag).[34] The PbO passivates the surface state defects on the QDs that are assumed to participate in charge equilibration and therefore inhibits Fermi level pinning. In this situation, the Schottky barrier height for hole injection is expected to increase and the surface recombination is minimized, thus leading to an improvement in device photoconversion efficiency. Using a core-shell QD consisting of a CdS shell and PbS core has also been shown as a way to increase open circuit voltage compared to core only devices of the same size, presumably for the same reason.[35] Deposition of a thin alumina film accomplishes the same goal as oxidation of the PbS and passivation with a CdS shell; namely, it inhibits charge equilibration at the interface, but unlike the other methods it also preserves the QD's chemical composition.

Shifts in the electronic state energies of the PbS QDs as a function of cross linker are also expected to return in the presence of an alumina tunneling barrier. Figure 3-5 shows how the VBM of 2.5 and 3.0 nm PbS QDs transition from ligand independent behavior on Au (a) to ligand dependent characteristic shifts, similar to those reported by Brown et al.[11], when alumina is present (b). Previous studies on CdSe have shown that small QDs exhibit larger ligand effects than large QDs because of their larger surface-to-volume ratio.[10] Figure 3-5(B) shows that BDT, EDT, and EDA cross-linkers shift the VBM much more for 2.5 nm PbS QDs than for 3.0 nm PbS QDs, in agreement with this claim. These ligand dependent shifts in electronic energies further corroborate the conclusion that the thin alumina layer acts to decouple the electronic states of QDs from Au. Operating under these conditions it should now be possible to tune the PbS QD properties at the interface and overcome charge injection and separation issues that have plagued previous architectures.

3.6 CONCLUSION

This work demonstrates that Fermi level pinning persists in monolayer PbS QD films on Au substrates with different cross-linkers. Introduction of a thin alumina layer between the PbS QDs and the Au substrate was shown to weaken Fermi level pinning enough that size- and ligand-dependent properties are manifest. These findings point to a procedure for using ligand tuning of QD energetics to enhance charge injection and separation to overcome the open circuit voltage deficit reported for PbS.

3.7 REFERENCES

(1) Brown, G. F.; Wu, J.: Third generation photovoltaics. *Laser & Photonics Reviews* **2009**, *3*, 394-405.

(2) Nozik, A. J.; Beard, M. C.; Luther, J. M.; Law, M.; Ellingson, R. J.; Johnson, J. C.: Semiconductor Quantum Dots and Quantum Dot Arrays and Applications of Multiple Exciton Generation to Third-Generation Photovoltaic Solar Cells. *Chemical Reviews* **2010**, *110*, 6873-6890.

(3) Chuang, C.-H. M.; Brown, P. R.; Bulović, V.; Bawendi, M. G.: Improved performance and stability in quantum dot solar cells through band alignment engineering. *Nat Mater* **2014**, *13*, 796-801.

(4) Santra, P. K.; Palmstrom, A. F.; Tanskanen, J. T.; Yang, N.; Bent, S. F.: Improving Performance in Colloidal Quantum Dot Solar Cells by Tuning Band Alignment through Surface Dipole Moments. *The Journal of Physical Chemistry C* **2015**, *119*, 2996-3005.

(5) Wang, Y.; Wang, L.; Waldeck, D. H.: Electrochemically Guided Photovoltaic Devices: A Photocurrent Study of the Charge Transfer Directionality between CdTe and CdSe Nanoparticles. *The Journal of Physical Chemistry C* **2011**, *115*, 18136-18141.

(6) Weiss, E. A.; Porter, V. J.; Chiechi, R. C.; Geyer, S. M.; Bell, D. C.; Bawendi, M. G.; Whitesides, G. M.: The Use of Size-Selective Excitation To Study Photocurrent through Junctions Containing Single-Size and Multi-Size Arrays of Colloidal CdSe Quantum Dots. *Journal of the American Chemical Society* **2008**, *130*, 83-92.

(7) El-Ballouli, A. a. O.; Alarousu, E.; Bernardi, M.; Aly, S. M.; Lagrow, A. P.; Bakr, O. M.; Mohammed, O. F.: Quantum Confinement-Tunable Ultrafast Charge Transfer at the PbS Quantum Dot and Phenyl-C61-butyric Acid Methyl Ester Interface. *Journal of the American Chemical Society* **2014**, *136*, 6952-6959.

(8) El-Ballouli, A. a. O.; Alarousu, E.; Kirmani, A. R.; Amassian, A.; Bakr, O. M.; Mohammed, O. F.: Overcoming the Cut-Off Charge Transfer Bandgaps at the PbS Quantum Dot Interface. *Advanced Functional Materials* **2015**, n/a-n/a.

(9) Kim, G.-H.; García de Arquer, F. P.; Yoon, Y. J.; Lan, X.; Liu, M.; Voznyy, O.; Yang, Z.; Fan, F.; Ip, A. H.; Kanjanaboos, P.; Hoogland, S.; Kim, J. Y.; Sargent, E. H.: High-Efficiency Colloidal Quantum Dot Photovoltaics via Robust Self-Assembled Monolayers. *Nano Letters* **2015**.

(10) Bloom, B. P.; Zhao, L.-B.; Wang, Y.; Waldeck, D. H.; Liu, R.; Zhang, P.; Beratan, D. N.: Ligand-Induced Changes in the Characteristic Size-Dependent Electronic Energies of CdSe Nanocrystals. *The Journal of Physical Chemistry C* **2013**, *117*, 22401-22411.

(11) Brown, P. R.; Kim, D.; Lunt, R. R.; Zhao, N.; Bawendi, M. G.; Grossman, J. C.; Bulović, V.: Energy Level Modification in Lead Sulfide Quantum Dot Thin Films through Ligand Exchange. *ACS Nano* **2014**, *8*, 5863-5872.

(12) Yang, S.; Prendergast, D.; Neaton, J. B.: Tuning Semiconductor Band Edge Energies for Solar Photocatalysis via Surface Ligand Passivation. *Nano Letters* **2012**, *12*, 383-388.

(13) Wang, C.; Shim, M.; Guyot-Sionnest, P.: Electrochromic Nanocrystal Quantum Dots. *Science* **2001**, *291*, 2390-2392.

(14) Wu, P.-J.; Tsuei, K.-D.; Hsieh, M.-T.; Wei, K.-H.; Liang, K. S.: Dependence of the final-state effect on the coupling between a CdSe nanoparticle and its neighbors studied with photoemission spectroscopy. *Physical Review B* **2007**, *75*, 115402.

(15) Jasieniak, J.; Califano, M.; Watkins, S. E.: Size-Dependent Valence and Conduction Band-Edge Energies of Semiconductor Nanocrystals. *ACS Nano* **2011**, *5*, 5888-5902.

(16) Shalom, M.; Rühle, S.; Hod, I.; Yahav, S.; Zaban, A.: Energy Level Alignment in CdS Quantum Dot Sensitized Solar Cells Using Molecular Dipoles. *Journal of the American Chemical Society* **2009**, *131*, 9876-9877.

(17) Axnanda, S.; Scheele, M.; Crumlin, E.; Mao, B.; Chang, R.; Rani, S.; Faiz, M.; Wang, S.; Alivisatos, A. P.; Liu, Z.: Direct Work Function Measurement by Gas Phase Photoelectron Spectroscopy and Its Application on PbS Nanoparticles. *Nano Letters* **2013**, *13*, 6176-6182.

(18) Crisp, R. W.; Kroupa, D. M.; Marshall, A. R.; Miller, E. M.; Zhang, J.; Beard, M. C.; Luther, J. M.: Metal Halide Solid-State Surface Treatment for High Efficiency PbS and PbSe QD Solar Cells. *Scientific Reports* **2015**, *5*, 9945.

(19) Soreni-Harari, M.; Yaacobi-Gross, N.; Steiner, D.; Aharoni, A.; Banin, U.; Millo, O.; Tessler, N.: Tuning Energetic Levels in Nanocrystal Quantum Dots through Surface Manipulations. *Nano Letters* **2008**, *8*, 678-684.

(20) Markus, T. Z.; Wu, M.; Wang, L.; Waldeck, D. H.; Oron, D.; Naaman, R.: Electronic Structure of CdSe Nanoparticles Adsorbed on Au Electrodes by an Organic Linker: Fermi Level Pinning of the HOMO. *The Journal of Physical Chemistry C* **2009**, *113*, 14200-14206.

(21) Markus, T. Z.; Itzhakov, S.; Alkotzer, Y. I.; Cahen, D.; Hodes, G.; Oron, D.; Naaman, R.: Energetics of CdSe Quantum Dots Adsorbed on TiO2. *The Journal of Physical Chemistry C* **2011**, *115*, 13236-13241.

(22) Wang, Y.; Xie, Z.; Gotesman, G.; Wang, L.; Bloom, B. P.; Markus, T. Z.; Oron, D.; Naaman, R.; Waldeck, D. H.: Determination of the Electronic Energetics of CdTe Nanoparticle Assemblies on Au Electrodes by Photoemission, Electrochemical, and Photocurrent Studies. *The Journal of Physical Chemistry C* **2012**, *116*, 17464-17472.

(23) Brown, P. R.; Lunt, R. R.; Zhao, N.; Osedach, T. P.; Wanger, D. D.; Chang, L.-Y.; Bawendi, M. G.; Bulović, V.: Improved Current Extraction from ZnO/PbS Quantum Dot Heterojunction Photovoltaics Using a MoO3 Interfacial Layer. *Nano Letters* **2011**, *11*, 2955-2961.

(24) Liu, Y.; Gibbs, M.; Puthussery, J.; Gaik, S.; Ihly, R.; Hillhouse, H. W.; Law, M.: Dependence of Carrier Mobility on Nanocrystal Size and Ligand Length in PbSe Nanocrystal Solids. *Nano Letters* **2010**, *10*, 1960-1969.

(25) Wanger, D. D.; Correa, R. E.; Dauler, E. A.; Bawendi, M. G.: The Dominant Role of Exciton Quenching in PbS Quantum-Dot-Based Photovoltaic Devices. *Nano Letters* **2013**, *13*, 5907-5912.

(26) Zhitomirsky, D.; Voznyy, O.; Hoogland, S.; Sargent, E. H.: Measuring Charge Carrier Diffusion in Coupled Colloidal Quantum Dot Solids. *ACS Nano* **2013**, *7*, 5282-5290.

(27) Ip, A. H.; Thon, S. M.; Hoogland, S.; Voznyy, O.; Zhitomirsky, D.; Debnath, R.; Levina, L.; Rollny, L. R.; Carey, G. H.; Fischer, A.; Kemp, K. W.; Kramer, I. J.; Ning, Z.; Labelle, A. J.; Chou, K. W.; Amassian, A.; Sargent, E. H.: Hybrid passivated colloidal quantum dot solids. *Nat Nano* **2012**, *7*, 577-582.

(28) Colbert, A. E.; Wu, W.; Janke, E. M.; Ma, F.; Ginger, D. S.: Effects of Ligands on Charge Generation and Recombination in Hybrid Polymer/Quantum Dot Solar Cells. *The Journal of Physical Chemistry C* **2015**, *119*, 24733-24739.

(29) Lan, X.; Masala, S.; Sargent, E. H.: Charge-extraction strategies for colloidal quantum dot photovoltaics. *Nat Mater* **2014**, *13*, 233-240.

(30) Gao, J.; Perkins, C. L.; Luther, J. M.; Hanna, M. C.; Chen, H.-Y.; Semonin, O. E.; Nozik, A. J.; Ellingson, R. J.; Beard, M. C.: n-Type Transition Metal Oxide as a Hole Extraction Layer in PbS Quantum Dot Solar Cells. *Nano Letters* **2011**, *11*, 3263-3266.

(31) Luther, J. M.; Law, M.; Beard, M. C.; Song, Q.; Reese, M. O.; Ellingson, R. J.; Nozik, A. J.: Schottky Solar Cells Based on Colloidal Nanocrystal Films. *Nano Letters* **2008**, *8*, 3488-3492.

(32) Chuang, C.-H. M.; Maurano, A.; Brandt, R. E.; Hwang, G. W.; Jean, J.; Buonassisi, T.; Bulović, V.; Bawendi, M. G.: Open-Circuit Voltage Deficit, Radiative Sub-Bandgap States, and Prospects in Quantum Dot Solar Cells. *Nano Letters* **2015**, *15*, 3286-3294.

(33) Yoon, W.; Boercker, J. E.; Lumb, M. P.; Placencia, D.; Foos, E. E.; Tischler, J. G.: Enhanced Open-Circuit Voltage of PbS Nanocrystal Quantum Dot Solar Cells. *Scientific Reports* **2013**, *3*, 2225.

(34) Choi, M.-J.; Oh, J.; Yoo, J.-K.; Choi, J.; Sim, D. M.; Jung, Y. S.: Tailoring of the PbS/metal interface in colloidal quantum dot solar cells for improvements of performance and air stability. *Energy & Environmental Science* **2014**, *7*, 3052-3060.

(35) Speirs, M. J.; Balazs, D. M.; Fang, H. H.; Lai, L. H.; Protesescu, L.; Kovalenko, M. V.; Loi, M. A.: Origin of the increased open circuit voltage in PbS-CdS core-shell quantum dot solar cells. *Journal of Materials Chemistry A* **2015**, *3*, 1450-1457.

(36) Wadia, C.; Alivisatos, A. P.; Kammen, D. M.: Materials Availability Expands the Opportunity for Large-Scale Photovoltaics Deployment. *Environmental Science & Technology* **2009**, *43*, 2072-2077.

(37) Graetzel, M.; Janssen, R. A. J.; Mitzi, D. B.; Sargent, E. H.: Materials interface engineering for solution-processed photovoltaics. *Nature* **2012**, *488*, 304-312.

(38) Ellingson, R. J.; Beard, M. C.; Johnson, J. C.; Yu, P.; Micic, O. I.; Nozik, A. J.; Shabaev, A.; Efros, A. L.: Highly Efficient Multiple Exciton Generation in Colloidal PbSe and PbS Quantum Dots. *Nano Letters* **2005**, *5*, 865-871.

(39) Yang, Y.; Rodríguez-Córdoba, W.; Lian, T.: Multiple Exciton Generation and Dissociation in PbS Quantum Dot-Electron Acceptor Complexes. *Nano Letters* **2012**, *12*, 4235-4241.

(40) Zhang, J.; Gao, J.; Miller, E. M.; Luther, J. M.; Beard, M. C.: Diffusion-Controlled Synthesis of PbS and PbSe Quantum Dots with in Situ Halide Passivation for Quantum Dot Solar Cells. *ACS Nano* **2014**, *8*, 614-622.

(41) Hutter, J. L.; Bechhoefer, J.: Calibration of atomic-force microscope tips. *Review of Scientific Instruments* **1993**, *64*, 1868-1873.

(42) Moreels, I.; Lambert, K.; Smeets, D.; De Muynck, D.; Nollet, T.; Martins, J. C.; Vanhaecke, F.; Vantomme, A.; Delerue, C.; Allan, G.; Hens, Z.: Size-Dependent Optical Properties of Colloidal PbS Quantum Dots. *ACS Nano* **2009**, *3*, 3023-3030.

(43) Peterson, J. J.; Krauss, T. D.: Photobrightening and photodarkening in PbS quantum dots. *Physical Chemistry Chemical Physics* **2006**, *8*, 3851-3856.

(44) Zhang, J.; Jiang, X.: Confinement-Dependent Below-Gap State in PbS Quantum Dot Films Probed by Continuous-Wave Photoinduced Absorption. *The Journal of Physical Chemistry B* **2008**, *112*, 9557-9560.

(45) Hyun, B.-R.; Zhong, Y.-W.; Bartnik, A. C.; Sun, L.; Abruña, H. D.; Wise, F. W.; Goodreau, J. D.; Matthews, J. R.; Leslie, T. M.; Borrelli, N. F.: Electron Injection from Colloidal PbS Quantum Dots into Titanium Dioxide Nanoparticles. *ACS Nano* **2008**, *2*, 2206-2212.

(46) Munro, A. M.; Zacher, B.; Graham, A.; Armstrong, N. R.: Photoemission Spectroscopy of Tethered CdSe Nanocrystals: Shifts in Ionization Potential and Local Vacuum Level As a Function of Nanocrystal Capping Ligand. *ACS Applied Materials & Interfaces* **2010**, *2*, 863-869.

(47) Tung, R. T.: Formation of an electric dipole at metal-semiconductor interfaces. *Physical Review B* **2001**, *64*, 205310.

(48) Xie, Z.; Markus, T. Z.; Gotesman, G.; Deutsch, Z.; Oron, D.; Naaman, R.: How Isolated Are the Electronic States of the Core in Core/Shell Nanoparticles? *ACS Nano* **2011**, *5*, 863-869.

(49) Carlson, B.; Leschkies, K.; Aydil, E. S.; Zhu, X. Y.: Valence Band Alignment at Cadmium Selenide Quantum Dot and Zinc Oxide $(10\bar{1}0)$ Interfaces. *The Journal of Physical Chemistry C* **2008**, *112*, 8419-8423.

(50) Timp, B. A.; Zhu, X. Y.: Electronic energy alignment at the PbSe quantum dots/ZnO$(10\bar{1}0)$ interface. *Surface Science* **2010**, *604*, 1335-1341.

(51) Gao, J.; Luther, J. M.; Semonin, O. E.; Ellingson, R. J.; Nozik, A. J.; Beard, M. C.: Quantum Dot Size Dependent J−V Characteristics in Heterojunction ZnO/PbS Quantum Dot Solar Cells. *Nano Letters* **2011**, *11*, 1002-1008.

4.0 CHIRAL INDUCED SPIN SELECTIVE CHARGE TRANSPORT IN CYSTEINE PASSIVATED CDSE QUANTUM DOTS

This work has been published as Bloom, B.P.; Kiran, V.; Varade, V.; Naaman, R. and Waldeck, D. H. The thesis author aided in the project design, collaborated in the experiments, and wrote the document. The supporting information for this chapter is provided in Appendix D.

This work demonstrates that chiral imprinted CdSe quantum dots (QDs) can act as spin selective filters for charge transport. The spin filtering properties of chiral nanoparticles were investigated by magnetic conductive-probe atomic force microscopy (mCP-AFM) measurements and magnetoresistance measurements. The mCP-AFM measurements show that the chirality of the quantum dots and the magnetic orientation of the tip affect the current-voltage curves. Similarly, magnetoresistance measurements demonstrate that the electrical transport through films of chiral quantum dots correlates with the chiroptical properties of the QD. The spin filtering properties of chiral quantum dots may prove useful in future applications; e.g., photovoltaics, spintronics, and other spin-driven devices.

4.1 INTRODUCTION

Semiconductor quantum dots remain an attractive material for photovoltaics because of their solution processability and potential for multiple exciton generation; enabling a promising route for the realization of low cost, high efficiency solar cells. Much of the recent progress in device efficiency has been focused on increasing the exciton diffusion length through surface passivation[1] and band alignment engineering of multiple semiconductor quantum dot layers.[2] However, Fermi-level pinning and interfacial recombination continues to limit device efficiency and often necessitate the use of additional tunneling barriers[3] and charge transport layers4 to mitigate them. Previous experiments have shown that spin selective charge transport, achieved through the addition of galvinoxyl radicals[5,6] or paramagnetic nanoparticles,[7] can enhance the photoconversion efficiencies of organic bulk heterojunctions. The present work explores whether chiral induced spin selectivity (CISS),[8,9] which has been demonstrated for helical DNA,[10-13] α-helical peptides,[14-16] helicenes,[17] and other biomolecules,[18,19] can be used as an alternative approach to affect charge transport through quantum dot films. The present work demonstrates that quantum dot thin films composed of chiral semiconductors preferentially transmit electrons with a particular spin orientation.

While semiconducting QDs have been used in spin selective charge transport devices in other works,[20-22] those studies consisted of achiral quantum dot assemblies on chiral molecular films acting as a spin filter. The idea of imprinting chirality onto semiconductor QDs was first introduced by Gun’ko and Kelly et al. for CdS QDs stabilized by D- and L- enantiomers of penicillamine, synthesized through a microwave assisted technique.[23] The D- and L- stabilized QDs showed mirror image circular dichroism spectra, whereas the rac- stabilized QDs showed only a weak signal. In a series of theoretical[24,25] and experimental[25,26] reports the origin of the chirality was found to arise from the interaction of the ligand with the QD surface. Since then, the chiroptical behavior of QDs has been demonstrated for different ligand stabilizers (cysteine, glutathione), other semiconductors (CdSe and CdTe), different synthetic routes (solution phase techniques and ligand exchanged from its native achiral ligand to a chiral one), and different QD shapes (tetrapods, rods).[25,27-33]

Here, chiral cysteine passivated CdSe QDs are synthesized and their spin dependent charge transport properties are measured using magnetic conductive probe atomic force microscopy (mCP-AFM) and magnetoresistance (MR) measurements. The findings from this study show that the individual QDs and the QD films act as spin filters. Such QD assemblies may prove useful for creating spin selective conduction pathways and for spin driven quantum dot sensitized photovoltaic devices.

4.2 CHIRALITY IN QUANTUM DOTS

Mirror image circular dichroism (CD) spectra of L- and D-cysteine in solution and those bound to the CdSe are shown in Figures 4-1A and 4-1B, respectively. The CD transitions for cysteine arise from disulphide bond formation and its helical geometry.[34,35] The CD spectrum in Fig. 1B results from the cysteine ligand binding to the nanoparticle surface; hence the original disulphide CD signal is not present and a new bisignate peak is apparent. A similar red shifted signal response has been reported for cysteine-silver metal complexes[36] and cadmium-cysteine complexes.[23,25] We assign the signal in this case to a charge transfer band between the metal and the cysteine ligand.[37] Interestingly, a change in the sign of the Cotton effect is also observed for the most intense peak when the free ligand is bound to the surface of the CdSe QDs. While the

CD signal is positive for L-cysteine and negative for D-cysteine when they exist as disulfides in solution, it is negative for L-cysteine CdSe and positive for D-cysteine CdSe quantum dots. Such a change in signal response is not unusual and can result from the geometry of the coordination motif arising from the interaction of the cysteine with Cd atoms at the surface.[25]

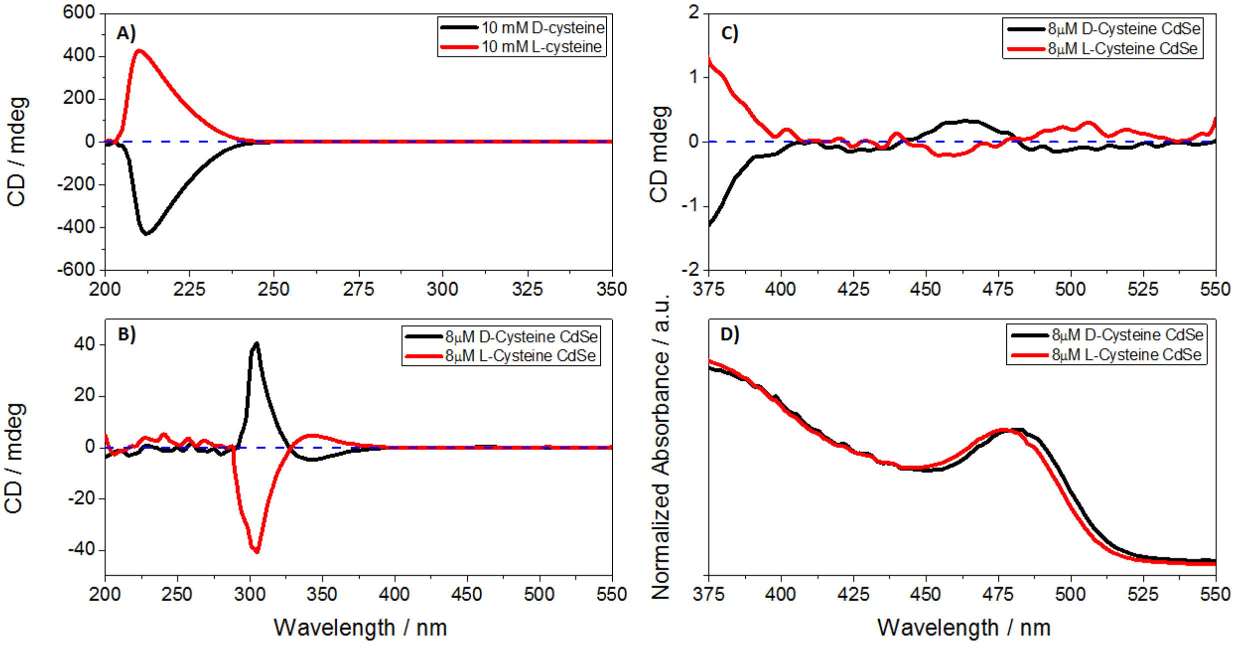

Figure 4-1 Circular Dichroism and Absorbance Spectra. Panel A) shows the CD spectrum for cysteine in solution, which arises from the disulphide structure that they form;[35,36] panel B shows the CD spectrum for the cysteine coordinated on the CdSe QD, which agrees with similar spectra found for Cd-cysteine adducts,[23,25] and panel C shows the CD spectrum for the QD in the region of its exciton transitions. Panel D shows the absorption spectra of the cysteine coated QDs.

Panels C and D of Figure 4-1 plot the CD spectrum (4-1C) and the absorbance spectrum (4-1D) of the D- and L-cysteine coated CdSe quantum dots over an expanded wavelength range of 375 nm to 550 nm. The CD spectrum (4-1C) shows a weak bisignate peak centered on the absorbance maximum of the first excitonic peak of CdSe; suggesting chiral imprinting of the ligand shell onto the electronic states of the CdSe. The absorbance spectrum shows an exciton peak at 480 nm which is consistent with a quantum dot size of about 2.2 nm for both chiralities.

4.3 MAGNETIC CONDUCTIVE PROBE AFM (MCP-AFM) MEASUREMENTS

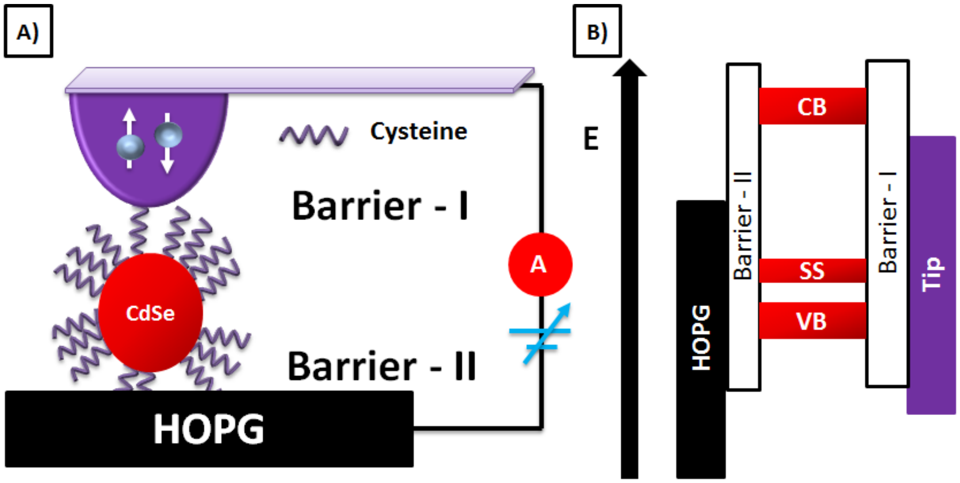

Scheme 4-1. Experimental framework and double barrier tunnel junction. Panel A) shows a schematic of the tunnel junction under investigation in the mCP-AFM experiments and its corresponding energy diagram is sketched in panel B). Barrier - I indicates the tunnel barrier between the CdSe QD and tip, and Barrier - II indicates the tunnel barrier between the QD and the HOPG substrate. In Panel B, the red bars indicate the QD electronic states: CB for conduction band, SS for surface states, and VB for valence band.

The mCP-AFM measurements were performed on CdSe QDs coated with L- and D-cysteine, using a magnetized tip; see methods section. The films were prepared by drop-casting a solution of the cysteine coated QDs onto a freshly cleaved highly oriented pyrolytic graphite (HOPG) substrate. A bias potential was applied with respect to the substrate; note that a negative bias indicates the transfer of electrons from the substrate to the tip; Scheme 4-1 illustrates the measurement design. The VB to CB energy gap (of Scheme 4-1B) corresponds to the first exciton transition at 480 nm, and the near UV charge transfer band is assumed to originate from the SS state (only the SS state is shown in diagram).

Figure 4-2 shows the average current versus voltage (I-V) curves that were measured for each magnetization and chirality of the QDs. The curves represent the average over all measurements conducted with a given sample, circa 100 individual curves (see Supplemental

Information for the raw data), and the shaded region about each curve marks the 95% confidence limits. For the L-cysteine coated CdSe QDs, a larger current is observed when the tip is magnetized in the "up" direction; namely magnetization vector of the tip is pointing away from the substrate. This difference indicates that the L-cysteine/CdSe preferentially transfers electrons with their spin oriented anti-parallel with respect to their flow from the HOPG to the magnetized tip. When current flows in the opposite direction, the preferred spin is pointing to the opposite direction in the laboratory frame, but it is again aligned anti-parallel to the electron propagation. The data in panel B show that the behavior is reversed for QDs of opposite chirality.

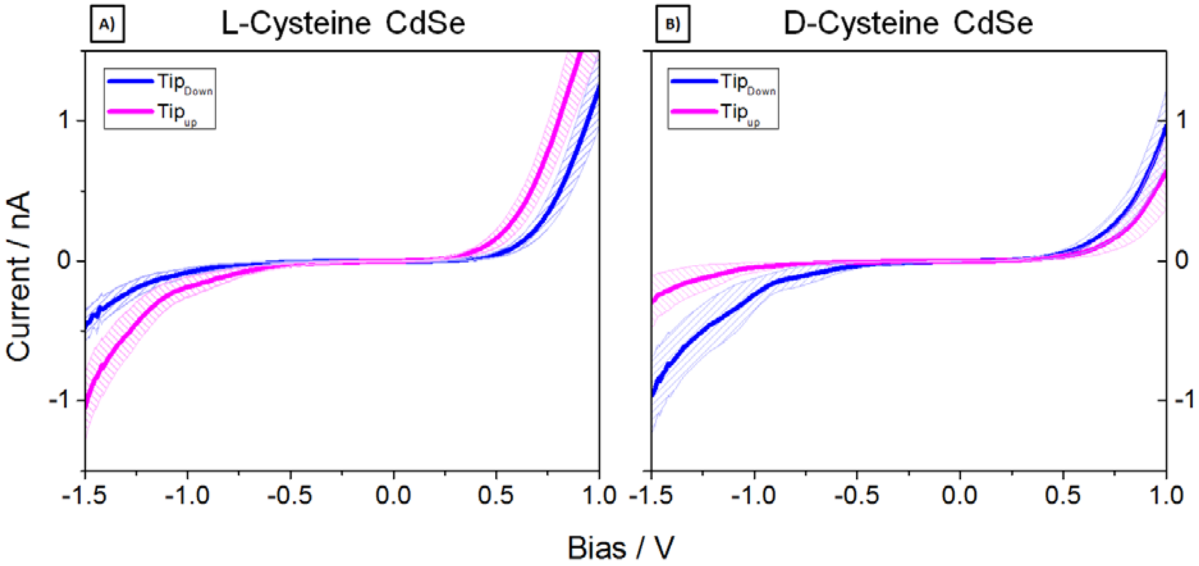

Figure 4-2 QD chirality effect on conductance. The figure shows results from the mCP-AFM studies of 2.2 nm L-cysteine (A) and D-cysteine (B) passivated CdSe QD films that are drop cast on HOPG substrates. The tip was magnetized in the up (magenta) and down (blue) direction and over 100 current-voltage curves were collected for each sample. The dashed lines mark the 95% confidence limits for the current-voltage (solid lines) curves which are an average of all the measurements.

Note that the current-voltage (I-V) curves are consistently asymmetric with respect to zero bias. This asymmetry in the I-V curves is consistent with a double barrier tunnel junction (Scheme 4-1, panel B). In addition, the gap in the conductance is shifted towards negative bias (see Fig. 3), indicative of a shift in the Fermi level towards the upper region of the CdSe band gap. Similar observations were reported previously for STM measurements on achiral CdS QDs.[38]

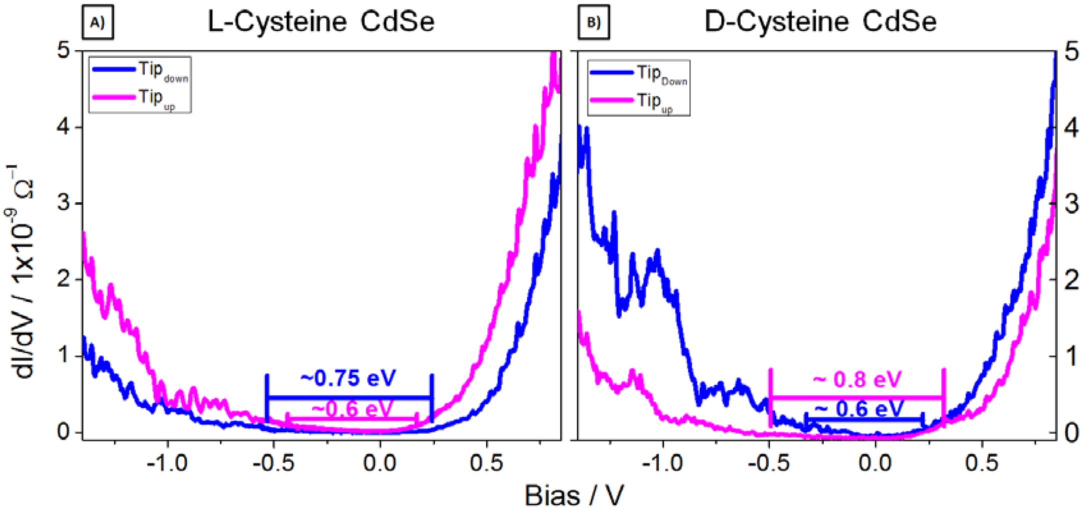

Figure 4-3 partial density of states of chiral QDs. This figure shows a plot of the dI/dV data, representing the partial density of states, for 2.2 nm L-cysteine (A) and D-cysteine (B) passivated CdSe QDs at different tip magnetizations. Note that this gap is different from the bandgap of the quantum dot (see text).

The dI/dV data in Figure 4-3 can be used to estimate the density of the electronic states involved in the tunneling and extract an effective barrier height for the spin transport. Note that the gap in the density of states shown here does not correspond to the optical bandgap of the nanoparticle; rather it is a conductance gap and likely indicates the energy difference between the defect states found within the bandgap of the QD[39,40] and the conduction band of the nanoparticle. These results are consistent with previous reports on dithiol modified CdSe nanoparticle films.[41] As indicated in the figure, the difference in the effective barrier heights for the two spins is about 0.2 eV. Figure S2 in the supporting information shows the determination of the onset energies used in calculating the barrier height.

The circular dichroism response of CdSe QDs decreases with increasing QD size because the contributions of the ligand to the QD's electronic states are 'diluted' as the QD size increases.[42] Figure D3 shows plots of the I-V data for 6.0 nm L-cysteine coated CdSe QDs and they do not show a magnetization dependence. This result demonstrates that the spin selectivity is controlled by the semiconductor nanoparticle's electronic chirality and not by the ligand chirality, which is not affected by the QD size.

4.4 MAGNETORESISTANCE MEASUREMENTS

Figure 4-4 shows magnetoresistance (MR) measurements recorded as a function of applied external magnetic field for three different devices, composed of L-cysteine (A), mercaptopropionic acid (MPA, B), and D-cysteine (C) passivated CdSe QD layers (see Figure S4 for molecular structures). Note that mercaptopropionic acid differs from cysteine by the replacement of the amine group on the cysteine with a hydrogen, which makes it achiral; however its surface binding thiolate group and its length are similar to cysteine. The insets show the device structure, and a more illustrative side-view of the device is shown at the top of Figure 4-4. An SEM image for the top down view of the device is shown in Figure D5. Resistance was measured at a constant current (of 1 mA) through the sample. An external magnetic field was varied from – 1 T to 1T to generate the magnetoresistance (MR) plot, and the MR is calculated as a percentage; namely

$$MR = \frac{R(H) - R(0)}{R(0)} \times 100\% \qquad \textbf{Equation 4-1}$$

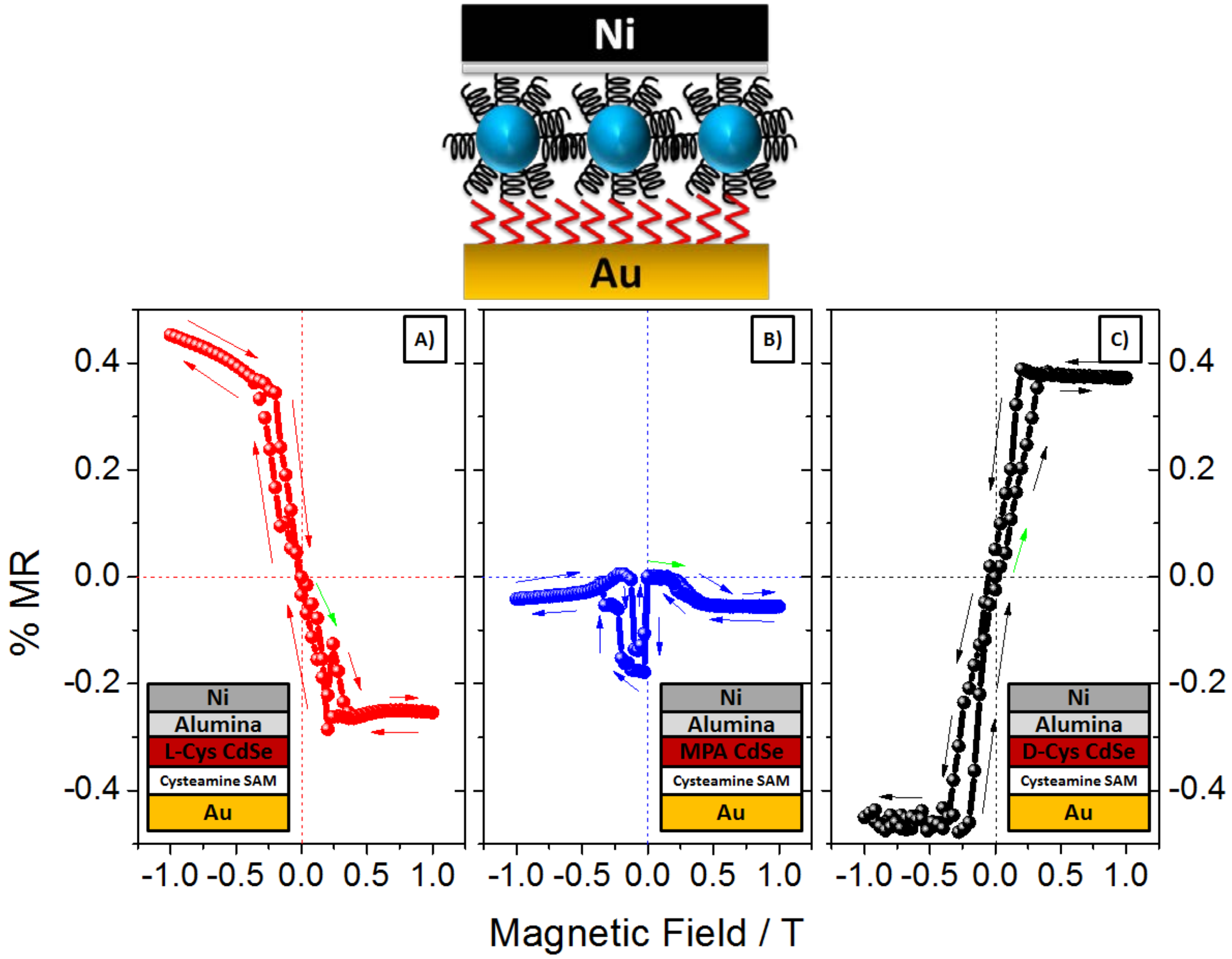

Figure 4-4. **Magnetoresistance of Chiral QD thin films.** (Top) Schematic illustration of the cross-section of the magnetoresistance (MR) device structure. (Bottom) MR data are shown for thin films composed of L-Cysteine (A), MPA (B), and D-Cysteine (C) passivated CdSe QDs at 20 K, recorded as a function of external magnetic field up to 1T at a fixed current of 1 mA. The arrows indicate the scan direction, and the green arrow indicates the origin of the scan.

The MR curves, as a function of the external magnetic field, show that the devices with chiral ligand passivated QDs and the device with the achiral MPA capped QD are qualitatively different. Each experiment was repeated for separate QD syntheses and device constructions and the same behavior was observed. The L-cysteine and D-cysteine CdSe QDs show opposite behaviors for the magnetoresistance. The MR plots are not entirely anti-symmetric about zero magnetic field. For example, L-cysteine QDs have a positive MR that saturates at approximately

0.4 % and a negative MR that saturates at approximately -0.3%. This behavior may arise because of the asymmetric tunnel barrier for the device, namely Au as the bottom contact and Ni as the top contact influencing the spin injection properties (see ref 43 to for a more detailed discussion).

The chiral QD devices show an anti-symmetric MR response whereas the achiral QDs show a symmetric MR response. The symmetric response for CdSe/CdS core-shell nanoparticles has been reported previously,[44,45] and the shape of the response has been attributed to a spin blockade mechanism which depends on field magnitude but is not dependent on the field orientation. The small deviation of the dip from zero field is assumed to arise from hysteresis. The anti-symmetric MR response for the chiral QDs can be understood from their spin filtering properties. Consider the D-cysteine QD device, for which the MR is negative under a negative magnetic field and positive under a positive magnetic field. Under a negative magnetic field the resistance is lower because the spin sub-bands of the Ni are split so that the spin 'up' states are less populated than under zero field; hence the spin 'up' electron which is preferentially transmitted by the D-cysteine QD (electron spin aligned parallel to propagation direction) finds more accepting levels in the Ni; a lower resistance.[10] Under a positive magnetic field, the spin sub-levels of Ni are split in the opposite direction, so that the spin 'up' states are more populated than under zero field, hence the spin 'up' electron which is preferentially transmitted by the D-cysteine QDs finds fewer accepting levels in the Ni; a higher resistance. To account for the case of current flow in the opposite direction, one can consider the transport of holes for which the preferred spin alignment is opposite to that of electrons, and the same antisymmetric shape of the MR curve is predicted. A similar logic can be used to understand the opposite behavior found for the L-cysteine QDs as long as one assumes it filters preferentially for the opposite spin orientation than that the D-cysteine QDs select.

Interestingly, the magnetoresistance results in this study are opposite in direction to previous measurements that have been reported for self-assembled monolayers (SAMs) composed of cysteine molecules.[42] In order to validate the measurement method used here, magnetoresistance devices like that reported earlier for cysteine SAMs were constructed and the behavior reported earlier in the literature was confirmed. Figure D6 shows the reproduction of these results and they confirm that the MR behavior in the cysteine SAMs are opposite to that found for the cysteine coated QD films. This difference correlates with the inversion in the Cotton effect observed for cysteine bound to the CdSe QD surface as compared to free cysteine. This substantiates the claim that the asymmetry in the MR signal is associated with the chirality of the system and that the charge transport through the QDs occurs through a chiral pathway.

The MR response (Figure 4-5) was measured for a number of different temperatures (from 20K to 300K). Although some variation in the MR response with temperature exists, the differences are relatively minor (typical variations are only 0.1 to 0.2%). The mostly temperature independent MR is consistent with former works,[17,42] suggesting that a high degree of spatial confinement in the QD inhibits electron motion in the lattice and therefore minimizes the D’yakonov-Perel’ (DP) scattering.[46]

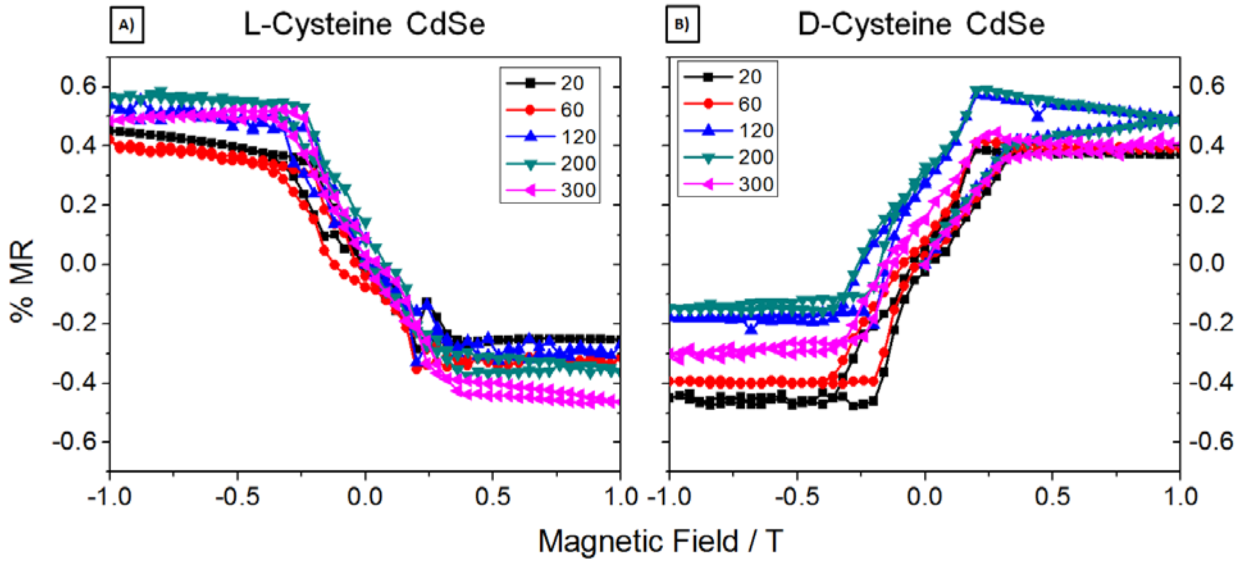

Figure 4-5 Temperature dependent MR of chiral QDs. Temperature dependent magnetoresistance data on L-cysteine CdSe QD films (A) and D-cysteine CdSe QD films (B). The orientation and magnitude of the magnetoresistance remains relatively unchanged with a change in temperature.

4.5 CONCLUSION

These studies demonstrate that the charge transport through L- and D-cysteine passivated CdSe QDs is spin selective; i.e., they act as spin filters. Magnetic conductive probe AFM studies showed that the current-voltage characteristics of the QDs depend on the induced magnetization of the conducting probe tip and on the chirality of the QD. For achiral QDs, no spin filtering was found. Magnetoresistance measurements further corroborate these findings, demonstrating a lower resistivity for one spin orientation over the other and the spin filtering properties of the QD correlates with their circular dichroism spectra. While the spin filtering properties of chiral functionalized quantum dots is wholly new, this behavior can be rationalized in terms of the CISS effect.[9] Chiral QDs offer promise as active materials for devices in which spin selective charge transport is desirable; e.g., spintronics applications and vectorial charge transport in energy transduction schemes.

4.6 METHODS

4.6.1 QD Ligand Exchange and Characterization

Chiral cysteine passivated CdSe QDs were synthesized following a modified procedure described by Balaz et al.[33] Briefly, octadecylamine capped CdSe QDs (M.K. Nano) were precipitated out of toluene and re-dissolved in 3.0 mL of chloroform. A solution of cysteine at a 1000x excess to that of the QDs was dissolved in 3.0 mL of water and the pH was adjusted to 11.5 using sodium hydroxide. The solutions of the cysteine and the QDs were then combined, deoxygenated, and vigorously stirred overnight. Upon ligand exchange, the QDs switched to the aqueous phase and were passed through syringe (0.2 μm, Millipore) and centrifugal (30,000 MWCO, Millipore) filters for purification. Absorption spectra of the cysteine passivated CdSe QDs were recorded using a Model 8453 Agilent Spectrometer. Circular dichroism measurements were conducted with an Olis DSM 17 CD spectrophotometer in a 3 mL quartz cuvette. The average of two scans was acquired with a 5 sec integration time and a 2 nm bandwidth at 20°C.

4.6.2 Magnetic Conductive Probe Atomic Force Microscopy

Samples for the mCP-AFM measurements were prepared by drop-casting of aqueous dispersions of chiral CdSe colloids onto freshly cleaved highly oriented pyrolytic graphite (HOPG) substrates and dried under a controlled humidity. Current-voltage measurements were carried out using a Multimode AFM with a Nanoscope V controller (Bruker-Nano, Santa Barbara, CA, U.S.A.). In these measurements, a Co-Cr tip (MESP, Bruker) was magnetized by placing it on the pole of a permanent magnetic for 30 min, and it was subsequently used in measurements for up to 60 min; this procedure is similar to that used by others.[47,48] In order to ensure that the AFM tip did not demagnetize or oxidize during the duration of the experiment magnetic force microscopy (MFM) studies on a hard drive were conducted at a lift height of 30 nm. Figure S7 shows that there was not a noticeable change in the measurement over the course of 120 min. The topography of the QD modified samples was obtained using the peak force mode. I-V spectroscopic measurements were performed by recording voltage ramps at an applied force of 10 nN. For each measurement, the tip was placed in a new position, and it was lifted up when moving from one point to another point in order to prevent damage to the sample. Approximately 5% of the traces shorted and 5-8% of the traces showed insulating behavior, which were excluded during analysis. Around 100-150 I-V traces were recorded and averaged for each magnetic field orientation (magnet up and down). A magnetic Co-Cr tip (MESP, Bruker) with a nominal spring constant of 2.8 N/m was used to acquire the I-V curves. The force constant of each probe used was calibrated using the thermal tune procedure of the software.

4.6.3 Device Fabrication and Magnetoresistance Measurements

The devices were fabricated using optical lithography by a laser writer, followed by e-beam evaporation (to deposit metal lines) on pre-cleaned glass substrates in a cross-bridge geometry. Gold lines of dimensions 2 µm width, 2 mm length, and 120 nm thick were evaporated onto an 8 nm Ti layer (adhesion layer) deposited on top of the glass substrate. Chiral CdSe QDs (3 h. incubation from aqueous CdSe colloid) were adsorbed on the Au lines via amino ethanethiol SAMs (12 h. incubation from 1 mM ethanolic solution), which acts as a linker. The adsorption of linker molecules on the Au substrate is confirmed using polarization modulated infrared absorption spectroscopy (PMIRRAS) (Figure S8). In order to verify that the QDs were attached onto the surface of the Au film in the magnetoresistance experiments, ellipsometry and electrochemistry measurements on a similar system were investigated. Figure D9 shows a photocurrent experiment of L-cysteine coated CdSe quantum dots that are electrostatically attached to an 8-mercaptooctylamine SAM immobilized on an Au working electrode. The coverage of the monolayer increased with incubation time, from 30% after 1 hour to 50% after 3 hours. An Al2O3 layer with thickness around ~2 nm was then deposited on the QD modified Au via atomic layer deposition at 100oC. The top Ni electrode was then evaporated using a shadow mask with a line width of ~50 µm and thickness of ~120 nm, without an adhesion layer. Subsequently, macro contact gold pads of dimensions 500 x 500 µm^2 and thickness of 150 nm were deposited for wire bonding. For MR measurements, the solid state device was attached to a chip carrier and electrically connected to the measuring unit. The sample was placed in-between poles of a superconducting magnet that can be cooled down to 1.5 K (Cryogenics Ltd). A magnetic field of up to 1 T was applied perpendicular to the plane of the sample. The temperature of the sample was controlled precisely using a PID controller procured from

Lakeshore with a stability of 0.02% at 300 K and 0.2 % at 1.5 K. The resistance of the device was measured using a standard four-probe method in a cross-bridge geometry. Typically, a DC current of 1 mA was applied using a Keithley current source (Model 2400), and the voltage across the junction was measured using a Keithley nanovoltmeter (Model 2182A).

4.7 REFERENCES

(1) Zhitomirsky, D.; Voznyy, O.; Hoogland, S.; Sargent, E. H. *ACS Nano* 7, 5282 (**2013**).

(2) Chuang, C.-H. M.; Brown, P. R.; Bulovic, V.; Bawendi, M. G. *Nat. Mater.* 13, 796 (**2014**).

(3) Bloom, B. P.; Mendis, M. N.; Wierzbinski, E.; Waldeck, D. H. *J. Mater. Chem. C* 4, 704 (**2016**).

(4) Yoon, W.; Boercker, J. E.; Lumb, M. P.; Placencia, D.; Foos, E. E.; Tischler, J. G. *Scientific Reports* 3, 2225 (**2013**).

(5) Zhang, Y.; Hukic-Markosian, G.; Mascaro, D.; Vardeny, Z. V. *Synthetic Metals* 160, 262 (**2010**).

(6) Zhang, Y.; Basel, T. P.; Gautam, B. R.; Yang, X.; Mascaro, D. J.; Liu, F.; Vardeny, Z. V. *Nat. Commun.* 3, 1043 (**2012**).

(7) Jaramillo, J.; Boudouris, B. W.; Barrero, C. A.; Jaramillo, F. *ACS Appl. Mater. & Interfaces* 7, 25061 (**2015**).

(8) Naaman, R.; Waldeck, D. H. Annu. *Rev. Phys. Chem.* 66, 263 (**2015**).

(9) Naaman, R.; Waldeck, D. H. *J. Phys. Chem. Lett.* 3, 2178 (**2012**).

(10) Göhler, B.; Hamelbeck, V.; Markus, T. Z.; Kettner, M.; Hanne, G. F.; Vager, Z.; Naaman, R.; Zacharias, H. *Science* 331, 894 (**2011**).

(11) Senthil Kumar, K.; Kantor-Uriel, N.; Mathew, S. P.; Guliamov, R; Naaman, R; *Phys. Chem. Chem . Phys.* 15, 18357 (**2013**).

(12) Ray, S. G.; Daube, S. S.; Leitus, G.; Vager, Z.; Naaman, R. *Phys. Rev. Lett.* 96, 036101 (**2006**).

(13) Xie, Z.; Markus, T. Z.; Cohen, S. R.; Vager, Z.; Gutierrez, R.; Naaman, R. *Nano Lett.* 11, 4652 (**2011**).

(14) Wei, J. J.; Schafmeister, C.; Bird, G.; Paul, A.; Naaman, R.; Waldeck, D. H. *J. Phys. Chem. B.* 110, 1301 (**2006**).

(15) Carmeli, I.; Skakalova, V.; Naaman, R.; Vager, Z. Angew. *Chem. Int. Ed.* 41, 761 (**2002**).

(16) Kettner, M.; Göhler, B.; Zacharias, H.; Mishra, D.; Kiran, V.; Naaman, R.; Fontanesi, C.; Waldeck, D. H.; Sęk, S.; Pawłowski, J.; Juhaniewicz, J. *J. Phys. Chem. C.* 119, 14542 (**2015**).

(17) Kiran, V.; Mathew, S. P.; Cohen, S. R.; Hernández Delgado, I.; Lacour, J.; Naaman, R. *Adv. Mater.* 28, 1957 (**2016**).

(18) Mishra, D.; Markus, T. Z.; Naaman, R.; Kettner, M.; Göhler, B.; Zacharias, H.; Friedman, N.; Sheves, M.; Fontanesi, C. *Proc. Natl. Acad. Sci.* 110, 14872 (**2013**).

(19) Mondal, P. C.; Fontanesi, C.; Waldeck, D. H.; Naaman, R. *ACS Nano* 9, 3377 (**2015**).

(20) Mtangi, W.; Kiran, V.; Fontanesi, C.; Naaman, R., *J. Phys. Chem. Lett.* 6, 4916 (**2015**).

(21) Ben Dor, O.; Morali, N.; Yochelis, S.; Baczewski, L. T.; Paltiel, Y. *Nano Lett.* 14, 6042 (**2014**).

(22) Peer, N.; Dujovne, I.; Yochelis, S.; Paltiel, Y. *ACS Photonics* 2, 1476 (**2015**).

(23) Moloney, M. P.; Gun'ko, Y. K.; Kelly, J. M., *Chem. Commun.* 3900 (**2007**).

(24) Elliott, S. D.; Moloney, M. P.; Gun'ko, Y. K. *Nano Lett.* 8, 2452 (**2008**).

(25) Zhou, Y.; Yang, M.; Sun, K.; Tang, Z.; Kotov, N. A. *J. Am. Chem. Soc.* 132, 6006 (**2010**).

(26) Nakashima, T.; Kobayashi, Y.; Kawai, T. *J. Am. Chem. Soc.* 131, 10342 (**2009**).

(27) Gallagher, S. A.; Moloney, M. P.; Wojdyla, M.; Quinn, S. J.; Kelly, J. M.; Gun'ko, Y. K. *J. Mater. Chem*. 20, 8350 (**2010**).

(28) Zhou, Y.; Zhu, Z.; Huang, W.; Liu, W.; Wu, S.; Liu, X.; Gao, Y.; Zhang, W.; Tang Z. *Angew. Chem. Int. Ed.* 50, 11456 (**2011**).

(29) Tohgha, U.; Varga, K.; Balaz, M. *Chem. Commun.* 49, 1844 (**2013**).

(30) Mukhina, M. V.; Maslov, V. G.; Baranov, A. V.; Fedorov, A. V.; Orlova, A. O.; Purcell-Milton, F.; Govan, J.; Gun'ko, Y. K. *Nano Lett.* 15, 2844 (**2015**).

(31) Govan, J. E.; Jan, E.; Querejeta, A.; Kotov, N. A.; Gun'ko, Y. K. *Chem. Commun.* 46, 6072 (**2010**).

(32) Li, Y.; Zhou, Y.; Wang, H.-Y.; Perrett, S.; Zhao, Y.; Tang, Z.; Nie, G. *Angew. Chem. Int. Ed*. 50, 5860 (**2011**).

(33) Tohgha, U.; Deol, K. K.; Porter, A. G.; Bartko, S. G.; Choi, J. K.; Leonard, B. M.; Varga, K.; Kubelka, J.; Muller, G.; Balaz, M. *ACS Nano* 7, 11094 (**2013**).

(34) Malon, P.; Bendnarova, L.; Straka, M.; Krejci, L.; Kraus, T.; Kubanova M.; Baumruk, V. *Chirality* 22 E47 (**2010**).

(35) Beychok, S. P *Proc. Natl. Acad. Sci.* 53, 999 (**1965**).

(36) Nan, J.; Yan, X.-P. *Chem. Eur. J.* 16, 423 (**2010**).

(37) a) Stillman, M. J. Coord Chem. Rev. 144 461 (1995); b) Frisinger, E; Vasak, M. *Cadmium: From Toxicity to Essentiality* A. Sigel, H. Sigel, and RKO Sigel eds. (Springer, **2013**, NY) 345.

(38) Svit, K. A.; Zhuravlev, K. S. *J. Phys. Chem. C.* 119, 19496 (**2015**).

(39) Bloom, B. P.; Zhao, L-B.; Wang, Y. Waldeck, D.H.; Liu, R.; Zhang, P.; Beratan, D. N. *J. Phys. Chem. C.* 117 22401 (**2013**).

(40) Wuister, S. F.; Donega, C.; Meijerink, A. *J. Phys. Chem. B.* 108 17393 (**2004**)

(41) Kundu, B.; Chakrabarti, S.; Pal, A. *J. Chem. Mater*. 26, 5506 (**2014**).

(42) Ben Moshe, A.; Szwarcman, D.; Markovich, G. *ACS Nano* 5, 9034 (**2011**).

(43) Mathew, S. P.; Mondal, P. C.; Moshe, H.; Mastai, Y.; Naaman, R. *Appl. Phys. Lett*. 105, 242408 (**2014**).

(44) Pourret, A.; Ramirez, A.; Guyot-Sionnest, P. *Appl. Phys. Lett.* 95, 142105 (**2009**).

(45) Liu, H.; Guyot-Sionnest, P. *J.Phys. Chem. C.* 119, 14797 (**2015**).

(46) Li, C. H.; Kioseoglou, G.; van 't Erve, O. M. J.; Ware, M. E.; Gammon, D.; Stroud, R. M.; Jonker, B. T.; Mallory, R.; Yasar, M.; Petrou, A. *Appl. Phy. Lett.* 86, 132503 (**2005**).

(47) Chakrabarti, S.; & Pal A. *J. Appl. Phys. Lett.* 104, 013305 (**2014**).

(48) Aragonès, A. C.; Aravena, D.; Cerdá, J. I.; Acís-Castillo, Z.; Li, H.; Real, J. A.; Sanz, F.; Hihath, J.; Ruiz, E.; Díez-Pérez, I *Nano Lett.* 16, 218 (**2016**).

5.0 ELECTRON TRANSFER IN NANOPARTICLE DYADS ASSEMBLED ON A COLLOIDAL TEMPLATE

This work has been submitted as Graff, B.M.; Bloom, B.P.; Wierzbinski, E.; and Waldeck, D. H. The thesis author developed the nanoparticle syntheses and ligand exchange procedures and performed the electrochemical experiments. The supporting information for this chapter is provided in Appendix E.

This work shows how to create covalently bound nanoparticle dyad assemblies on a colloidal template and studies photoinduced charge transfer in them. New results are reported for how the electron transfer rate changes with the inter-nanoparticle distance and the energy band offset of the nanoparticles (reaction Gibbs energy). The experimental findings show that the distance dependence is consistent with an electron tunneling mechanism. The dependence of the rate on the energy band offset is found to be consistent with Marcus theory, as long as one performs a sum over final electronic states. These results indicate that our understanding of electron transfer in molecular donor-bridge-acceptor assemblies can be translated to describe nanoparticle-bridge-nanoparticle assemblies.

5.1 INTRODUCATION

Electron transfer reactions are ubiquitous in nature, and their control is important for many technologies. This work explores fundamental aspects of photoinduced electron transfer between semiconductor nanoparticles, which are one promising material for use in new types of solar cells and solid-state lighting technologies.[1] In particular, bulk heterojunction solar cells are a low-cost photovoltaic technology,[2-4] however, the best bulk heterojunction solar cells currently have an efficiency of 8-10%, which is less than their predicted maximum efficiency of 15-18%.[5] Organic-inorganic nanoparticle composites offer one strategy for improving the performance of such inexpensive self-assembling photovoltaic structures but better control over the optical properties and the charge separation and recombination kinetics is required for its realization. This work develops our understanding of how to manipulate semiconductor nanoparticle properties, in particular their charge transfer and recombination kinetics, to yield efficient charge separation.

Over the past few decades, the study of electron transfer in donor-bridge-acceptor (DBA) supermolecules has provided a platform for examining fundamental features of electron transfer between molecular units.[6-9] Experimental electron transfer studies in molecular DBA systems have allowed for the detailed and rigorous examination of the predictions made by the Marcus electron transfer model and its extensions. These studies have elucidated the dependence of electron transfer on reaction Gibbs energy and reorganization energy, as well as their dependence on molecular and solvent structure. Through the examination of different bridging units, the importance of bridge architecture, electronic structure, and connectivity have been revealed.[10-16] This understanding has allowed for the extension of these models to examine the role of solvent polarization[17] and solvent mediated electron tunneling.[18,19] The current study introduces an analogous platform with the aim of examining electron transfer between nanoparticles; i.e., donor and acceptor molecular units are replaced by semiconductor nanoparticles. The ability to vary the optical and electronic properties of semiconductor nanoparticles by varying their size[20] provides a strategy for examining whether or not Marcus theory and our understanding of electron transfer in molecules can be directly translated to nanostructures or whether they need to be modified.[21,22] This work provides a novel protocol for preparing donor-bridge-acceptor nanoparticle structures and examining electron transfer rates in them.

Charge transfer at semiconductor heterojunctions and interfaces has been studied since the middle of the twentieth century and it is well known that a staggered, or Type II, band alignment facilitates charge transfer.[23-25] The same energy level structure is important for charge transfer in semiconductor nanoparticles and a number of earlier works have demonstrated charge transfer for such nanomaterials. A recent review provides an up-to-date and comprehensive discussion for charge transfer involving nanoparticles,[26] including the importance of how donor-acceptor ratios, donor-acceptor distance, and environmental factors can affect observed electron transfer rates. As the current study examines charge transfer in cadmium selenide/cadmium telluride (CdSe/CdTe) heterojunctions this discussion focuses on the earlier work for these materials. Scholes and coworkers have examined charge transfer in CdTe/CdSe heterostructure nanorods and core/shell nanoparticles.[27,28] They confirmed the presence of a charge transfer band from which they were able to quantify the reorganization energy and reaction Gibbs free energy ($\Delta_r G$). They found a very small reorganization energy which is consistent with the nanoscale size of the donor and acceptor. Several groups have studied charge transfer in CdSe and CdTe nanoparticle aggregates that are linked together electrostatically or covalently, and charge transfer rates in these systems range from picoseconds to nanoseconds.[29,30] It is likely that these assemblies contain a large variation in charge transfer rates because of their distribution of sizes, interparticle distance, and band energy differences. Additionally, because the nanoparticle aggregates that have been studied are not uniform (the ratio of donor to acceptor can vary greatly), there can be large variations in the measured charge transfer rate.[29,31] While nanoparticle aggregates of this sort are highly relevant for understanding charge transfer in bulk heterojunction materials, more precise assemblies are needed to understand how the structural features impact charge separation and recombination kinetics, enabling the design of better bulk heterojunction materials.

This work describes electron transport kinetics of nanoparticle assemblies, approximately nanoparticle dyads, defined better than randomly formed aggregates of nanoparticles in solution. Preparation of such assemblies was accomplished by utilization of a colloidal template and step wise formation of a designed nanoparticle composite architecture. Figure 5-1 shows a general scheme for the nanoparticle assembly formation and their anticipated structure.

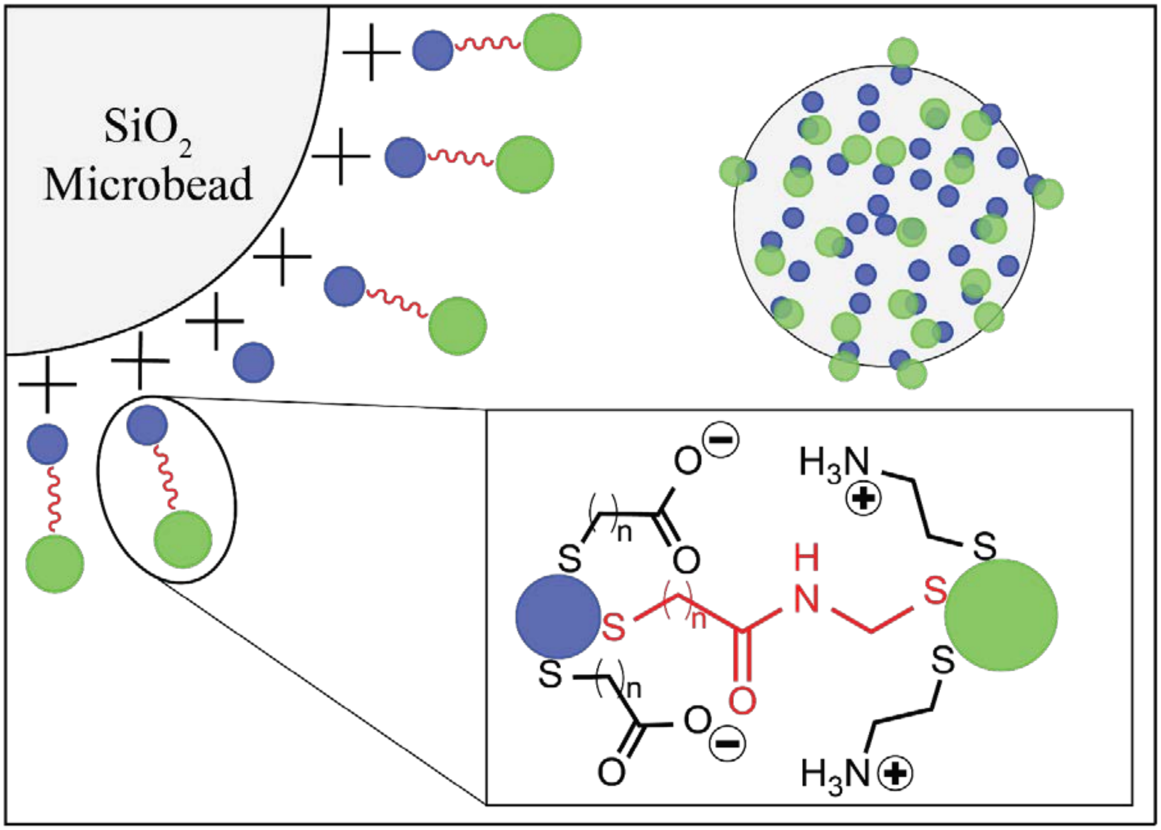

Figure 5-1. Cartoon describing the attachment of the nanoparticles on a microbead. The acceptor nanoparticle (blue) is electrostatically attached to a SiO_2 template and covalently linked (red) to a donor nanoparticle (green) yielding a nanoparticle dyad on the microbead (2NPA). The upper left corner of the image depicts a cartoon of a single microbead with many nanoparticles on the surface. The upper left hand corner zooms in on one section of the microbead containing many nanoparticle dyads and the lower right hand corner zooms in on a single dyad. The capping ligand on the donor nanoparticles were always cysteamine (CA), but the acceptor nanoparticles had a variety of different surface ligands. The number of methylene units, *n*, in the cartoon indicate the various ligands utilized in these experiments (*n*=1 TGA, *n*=3 MBA, *n*=5 MHA, *n*=7 MOA, *n*=10 MUA). Note that in the zoomed in image, ligand sizes are dramatically exaggerated with respect to the size of the nanoparticle.

Covalent linkage of the nanoparticles by way of organic capping ligands on the nanoparticles provides good control over the interparticle distance and enables independent manipulation of the nanoparticle size. By studying the relationship between the electron transfer rate and the interparticle distance, changed by a variation of the number of methylene groups in an amide linker chain, we demonstrate that the natural log of the electron transfer rate falls off exponentially with the length of the interparticle bridge. By studying the electron transfer rate as a function of the reaction driving force (Gibbs free energy, $\Delta_r G$) we demonstrate that the electron transfer rate increases as $\Delta_r G$ becomes more negative, and this dependence can be modeled using semi-classical Marcus theory. These findings imply that our understanding of electron transfer in molecular systems can be translated to describe electron transfer in inorganic semiconductor nanoparticle systems.

5.2 RESULTS

5.2.1 Demonstration of Nanoparticle Dyad Assemblies

The formation of nanoparticle assemblies on a 500 nm diameter silicon dioxide (SiO_2) sphere has been confirmed by fluorescence, zeta potential, and electron microscopy measurements. An excess of thioglycolic acid coated cadmium telluride nanoparticles (TGA-CdTe) were added to a solution of amine coated SiO_2 microspheres, and it was left to shake for one hour. After one hour, the assembly was purified by filtration through a 100 nm porous filter, see Supplemental Information for a more detailed description of the purification protocol. The assembly is driven by the electrostatic interaction of the negatively charged nanoparticle and the positively charged microsphere.

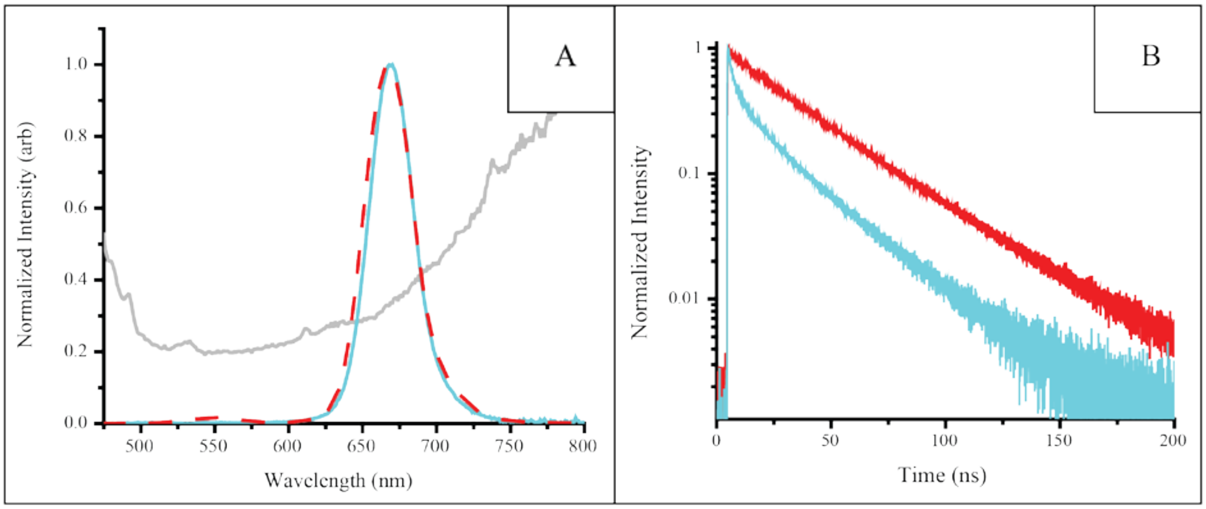

Figure 5-2. Panel A shows normalized steady state fluorescence spectra of the TGA-CdTe in solution (red dashed) and assembled on the colloidal microspheres (1NPA) in solution (blue) (λ_{ex}: 440 nm, 0.7 x 0.7 nm slits, 0.1 s integration time). Note that the microsphere scattering is subtracted from the 1NPA spectrum. The scattering from the microsphere (grey) is shown and is amplified by 25 times compared to that of the 1NPA spectrum. Panel B shows photoluminescence decays of the TGA-CdTe in solution (red) and the 1NPA (blue) in solution.

Figure 5-2 panels A and B show spectral data confirming the loading of negatively charged CdTe nanoparticles onto the silica beads, 1NPA assemblies. The spectra in Figure 5-2A show the characteristic emission peak from the TGA-CdTe (red dashed) in solution and when it is bound onto the microbead (blue). Figure 5-2B shows the photoluminescence decay for the nanoparticle on the microbead (blue) and compares it to that of the nanoparticle in solution (red). Note that the fluorescence decay for the 1NPA is more nonexponential than that of the free nanoparticle in solution. The electron transfer analysis accounts for this effect (*vida infra*); however, its origin will be reported on elsewhere. When the nanoparticle is removed from the microsphere, however, the photoluminescence decay recovers to that obtained before bead loading (see Figure E5).

After the first nanoparticle layer was successfully assembled, a second nanoparticle could be attached to the first one, either through electrostatic interactions or by covalent bonding.

These two nanoparticle assemblies (2NPA) on the microsphere were confirmed by zeta potential and fluorescence energy transfer measurements. After the addition of each oppositely charged layer a zeta potential measurement was taken. A change in the sign of the zeta potential indicated the presence of an oppositely charged layer on the surface of the microbead. The fluorescence of the filtrate, 1NPA, and 2NPA were monitored. The decrease in the filtrate emission intensity after each successive filtration indicated that no free nanoparticle was left in solution. Additionally, the existence of an emission peak from each nanoparticle in the 2NPA was indicative of their attachment. In the studies reported herein, a positively charged cysteamine-coated CdTe (CA-CdTe) nanoparticle was covalently attached to a TGA-CdTe through the formation of an amide bond, facilitated by the catalyst 1-ethyl-3-(3-dimethylaminopropyl)carbodiimide (EDC). The purification of the reaction mixture was the same as that used for the 1NPA. Throughout this series of experiments, the ratio between the donor and acceptor nanoparticles was maintained at 3 donor: 4 acceptor. We refer to these assemblies as nanoparticle dyads.

Formation of the 1NPA and 2NPA was further confirmed by electron microscopy. Because of instrumental limitations it was necessary to change the relative sizes of the particles in the assemblies and to increase the microbead loading so that they could be imaged; however, the chemistry and procedures were kept the same. For the images shown in Figure 5-3 the microspheres were approximately 150 nm, the CdSe nanoparticle was 5.5 nm, and the CdTe nanoparticle was 4.0 nm. Note that the smaller microsphere reduced charging effects in the scanning transmission electron microscopy (STEM) measurement, but it caused the filtration procedure to be less effective. Figure 5-3A shows an example STEM image of a colloidal silica template with a nominal diameter of 150 nm. The beads composed of the template are characterized by a spherical shape with a surface that is devoid of any distinguishable features. The 1NPAs (Figure 5-3B) show distinguishable features (ca. 5 nm) that are uniformly distributed on the template's surface. These dark spots in Figure 3B are assigned to the 4.0 nm CdTe nanoparticles and they show a typical separation of several nanometers along the surface. Presumably, the nanoparticles form a sparse monolayer rather than a compact film because of their electrostatic repulsion. The 2NPA (see Figure 5-3C) is less evenly distributed than the 1NPA, nevertheless, a bi-layer type surface film is formed in certain parts of the template surface, rather than large aggregates of the nanoparticles. Please note that while there are acceptor nanoparticles (inner layer) that do not have any donor nanoparticles (outer layer) attached to them, only the donor nanoparticles are photoexcited. Details in the structures of 1NPA and 2NPA are somewhat more distinguishable on the images digitally processed with an FFT bandpass filter,[32] which improves the image contrast at the edges of the beads (see insets in Figures 5-3A-C). Additional examples of STEM images of 1NPA and 2NPA and particles size analysis based on microscopic data are provided in the Supplemental Information. Additional data that confirm the 1NPAs and the 2NPAs are provided in the Supplemental Information.

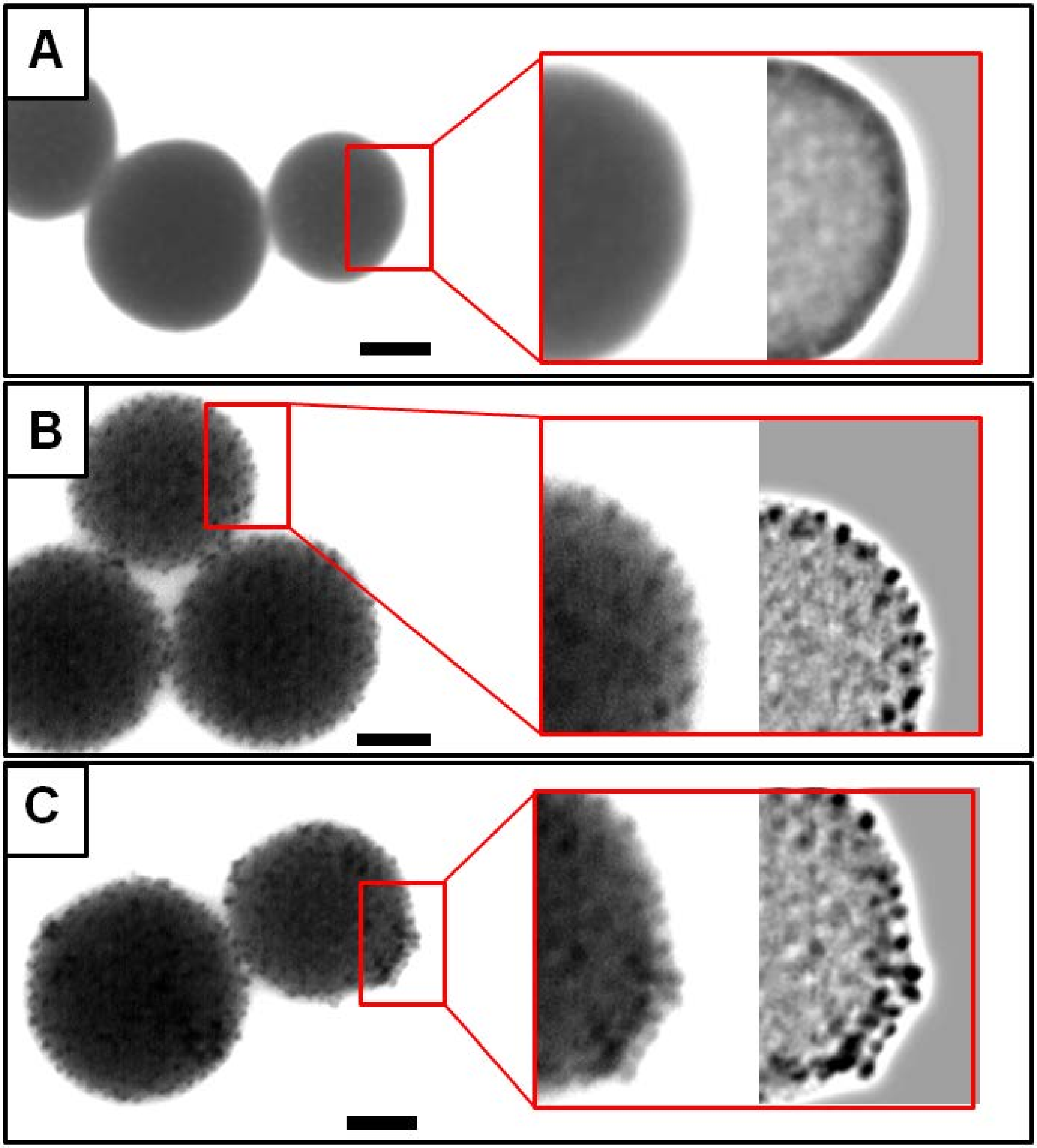

Figure 5-3 Electron Microscopy Characterization. Panel A shows the micrograph of the silica sphere used as a template for the nanoparticle assembly. Panel B shows an example of the 1NPA composed of CA-CdTe on silica beads. Panel C presents an image for 2NPA assemblies obtained after further modification of the 1NPA with MPA-CdSe. The scale bar on each image represents 50 nm. Insets in A-C show digitally two-fold magnified fragments of the original micrographs together with images processed with an FFT bandpass filter. Contrast of the features outside of the c.a. 1.5 - 7 nm diameter range was suppressed by the bandpass filter (right panels in the insets). Note

that the diameter of the silica spheres template and the size of the nanoparticles differs significantly from the parameters used in electron transfer studies. See text for details.

5.2.2 Mechanism of Fluorescence Quenching

The mechanism of fluorescence quenching in the nanoparticle dyads can be controlled by manipulating the energy bands of the individual nanoparticles. Figure 5-4A shows a Type I system which has an energy level structure that allows both charge transfer and energy transfer if the wider bandgap nanoparticle is excited; it maximizes the spectral overlap integral between the donor (green, CA-CdTe) and the acceptor (red, TGA-CdTe) (Figure 5-4C). In contrast, if the smaller bandgap nanoparticle, TGA-CdTe, is excited, then both charge transfer and energy transfer are blocked. Figure 5-4B shows a Type II, or staggered, energy band offset. In this case, if only the wider bandgap semiconductor (TGA-CdSe) is excited both energy transfer and hole transfer to the smaller band gap nanoparticle (CA-CdTe) is allowed. In contrast, excitation of the smaller bandgap nanoparticle allows only electron transfer from the smaller bandgap CA-CdTe to the larger bandgap TGA-CdSe.

The electronic state energies of the CdSe and CdTe nanoparticles reported in Figures 5-4 and 5-5 are inferred from previous experimental measurements. For CdSe nanoparticles functionalized with a thiol linker it was shown that the valence band maximum does not shift greatly with size.[33] The conduction band minimum was then determined by using the optical band gap and exciton binding energy of the nanoparticle.[34] For CdTe nanoparticles the valence and conduction band energies reported by Jasieniak et. al. were utilized.[35] Although a different passivating ligand was used in their experiments than in the nanoparticle assemblies studied here, electrochemical measurements were performed on a 4.1 nm CA-CdTe nanoparticle, and they showed that the valence band maxima are in good agreement with Jasieniak et. al. (Supplemental Information Figure E6). [35]

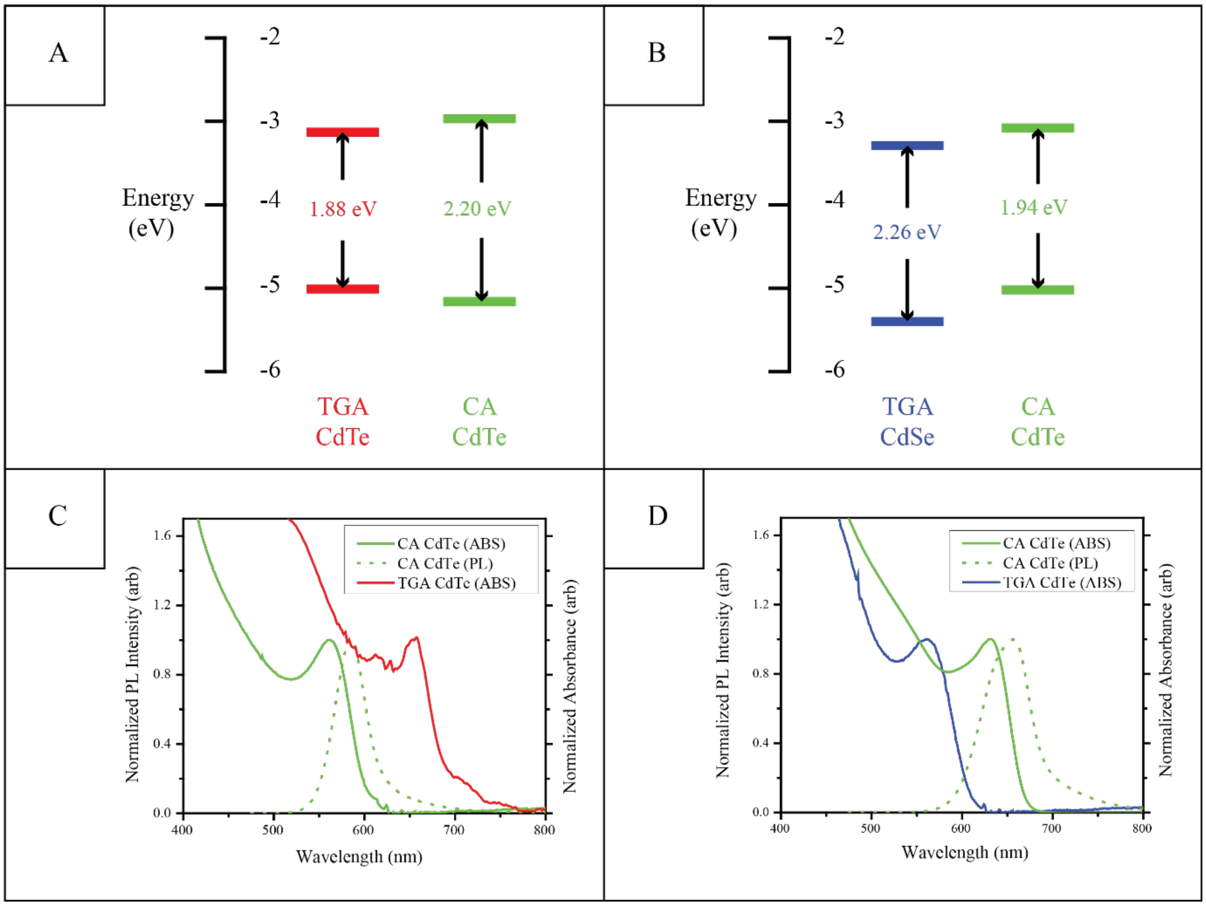

Figure 5-4. Energy schemes and optical spectra are shown for the nanoparticle assemblies under investigation. Panels A and B show the donor (green) and acceptor (red/blue) energy levels for the case of energy transfer (A) and electron transfer (B). Panels C and D show the normalized absorbance (solid) and photoluminescence (dashed) in the energy transfer (C) and electron transfer case (D).

Time-resolved photoluminescence (PL) measurements were used to monitor the quenching rate of the donor, CA-CdTe, for the two assemblies shown in Figure 5-4. In each case the fluorescence decay profiles were non-exponential, but could be well characterized by a distribution of lifetime components. To ensure a consistent analysis the nanoparticle assemblies were also fit to a sum of exponentials. Examples of the fluorescence decay data and the fitting are provided in Figure E7 of the SI. For this survey study, the fluorescence decay rate of the CA-CdTe free in aqueous solution was used as a reference system for extracting the quenching rate constants.

Two interparticle distances, obtained by changing the number of methylene groups in the capping ligand for the acceptor nanoparticle, were studied for the Type I and Type II nanoparticle assemblies (see Table 5-1). For the short linker, thioglycolic acid (TGA) was used; and for the long linker, mercaptoundecanoic acid (MUA) was used. For the Type I assemblies both distances were found to have a quenching rate of about 1.65×10^9 s^{-1}, and for the Type II assemblies the donor nanoparticle was quenched nine times more strongly for the shorter interparticle distance than for the longer distance case (See Table 5-1). The difference in fluorescence quenching rate is consistent with the difference in distance dependences that are expected for energy transfer and electron transfer, and it substantiates the nanoparticle dyad energy band alignments of Figure 5-4. If one approximates the nanoparticles as dipole absorbers, the Förster energy transfer model gives a Förster radius of 50 Å which is consistent with the weak distance dependence. Electron transfer rates are expected to decay more rapidly than energy transfer rates as a function of distance, which indicates that the Type II heterojunction assemblies undergo electron transfer.[29]

Table 5-1. The dyad assemblies (2NPA) and their corresponding quenching rate, k_{quench}. Type I assemblies are Microsphere-X CdTe-CA CdTe and the Type II assemblies are Microsphere-X CdSe-CA CdTe.

Type	**I**	**I**	**II**	**II**
Distance (Å)	6.2	12.2	6.2	12.2
$\boldsymbol{k_{quench}}$ **(ns^{-1})**	1.7 ± 0.1	1.6 ± 0.1	3.6 ± 0.08	0.4 ± 0.08
X	TGA	MUA	TGA	MUA

a - X is the capping ligand on the acceptor QD; TGA is thioglycolic acid and MUA is mercaptoundecanoic acid
b - The error in k_{quench} was calculated from the width of the lifetime distribution peak; see SI for more detail.

Note that the rate constants in Table 5-1 overestimate the actual electron transfer rate, because this analysis does not account for the fact that the nanoparticles experience some intrinsic quenching on the microbead assembly (see Figure 5-2B). In order to provide a more realistic reference system for the quantitative studies of the electron transfer rate that are described below, a Type I system for which energy transfer and electron transfer are blocked was used as the reference system (*vide infra*).

5.2.3 Distance Dependent Electron Transfer Study

The electron transfer rate was examined as a function of the inter-nanoparticle distance by using five acceptor ligand lengths, differing by the number of methylene groups. Because the nanoparticle's proximity to the microsphere causes some quenching (Figure 5-2B), a Type I nanoparticle assembly, in which a larger bandgap nanoparticle replaces the electron acceptor nanoparticle, was used as a reference system (see Figure 5-5A). The Type I system was chosen as the reference because it maintains the same assembly structure, just with a larger bandgap (smaller in size) CdSe acceptor nanoparticle. In every case, the donor CA-CdTe has a smaller band gap so that energy transfer is not significant. Additionally, only the donor nanoparticle is excited to ensure that electron transfer rather than hole transfer is observed.[36] The relative conduction and valence bands for the Type I and Type II systems utilized in this distance dependent study were calculated in a manner similar to that described above.

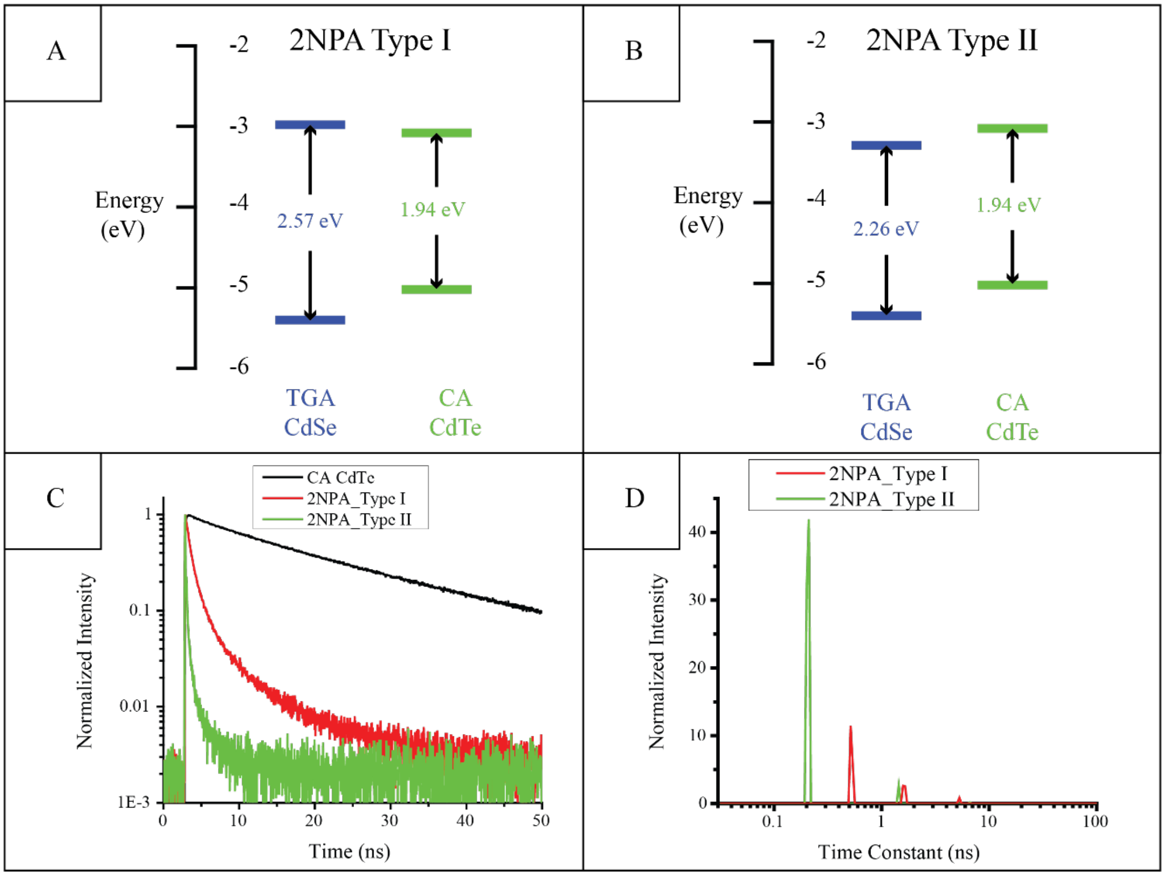

Figure 5-5. Band diagrams are shown for the nanoparticle assemblies used in the electron transfer rate measurements; in each case the smaller band gap nanoparticle, CA-CdTe, is photoexcited. The energy scheme in panel A depicts the band edges for the Type I reference system, and the scheme in panel B depicts the band edges for the photoinduced electron transfer. Photoluminescence decays are shown in panel C and the lifetime distribution fitting results are shown in panel D; for the CA-CdTe free in solution (black), the Type I 2NPA (red), and the Type II 2NPA (green). The donor emission is quenched most dramatically in the Type II nanoparticle dyad assembly.

Figure 5-5 provides an example of the fluorescence decay data and the lifetime distribution analysis for the two different types of assemblies. Panel 5-5C shows fluorescence decays for the free donor nanoparticle in solution (black), the Type I 2NPA (red), and the Type II 2NPA (green). Comparison of the free donor in solution to the Type I system shows that the microsphere assembly introduces some quenching; however, a significant increase in the quenching of the donor occurs when the Type II acceptor is present. Figure 5D shows the lifetime distributions that are obtained by fitting the fluorescence decays of the Type I and Type II assemblies in Figure 5-5C. These distributions show that the long lifetime components (τ_{long}) have low amplitude and do not change significantly in shape or position between the two assemblies; however, the short lifetime components change dramatically. Thus, it was assumed that the short lifetime component (τ_{short}) provides an accurate measure of the electron transfer. The electron transfer rate was determined from the difference in the two short lifetime rate constants ($k = \frac{1}{\tau_{short}}$); namely

$$k_{Type\ II} - k_{Type\ I} = k_{et} \qquad \textbf{Equation 5-1}$$

The error in the rate constant was estimated from the full-width-at-half maximum of the short-lived lifetime components from the two distribution fits. In order to ensure that the method of analysis utilized was not falsely depicting any relationships observed in this study, the average lifetime of the decay was compared to the short time constant of each decay and it was found that there is a linear relationship between the short time constant and the average lifetime. In addition, another control (a dendrimer) was utilized. It was found that the dendrimer control mimics the results found for the Type I TGA-CdSe system, however, it fails to do so for the longer ligands studied. Thus, a Type I reference system was used throughout. For more discussion of these analyses and detailed k_{et} evaluation see the Supplemental Information.

Figure 5-6 shows a plot of the natural log of the electron transfer rate constants versus the number of methylene units in the nanoparticle linker. These data show the results from multiple trials involving different batches of both donor (CA-CdTe) and acceptor (CdSe) nanoparticles as well as different nanoparticle coverages on the microsphere. Note that k_{et} does not change significantly with coverage, for the range studied. The ratio of donor to acceptor nanoparticles was kept consistent; even when the coverage of nanoparticle dyads on the surface of the microsphere was varied over a factor of three. The data in Figure 5-6 are well described by an exponential dependence on the number of methylene groups (n) in the ligand, namely

$$k_{et} = k_{et}\,(n = 0) \cdot \exp(-\beta n) \qquad \text{or} \qquad \ln(k_{et}) = -\beta n + \ln(k_{et}(n = 0))$$

Equation 5-2

where k_{et} is the electron transfer rate constant and β is the tunneling decay constant per methylene unit. Note that for the number of methylene groups, n, it has been assumed that all of the linkages between the donor and acceptor (from thiol to thiol) behave akin to a methylene group. For tunneling through a self-assembled monolayer of alkanes, workers[37,38] have reported β values ranging from 0.9 to 1.1 per methylene, however a β of 0.68 was observed in this study. A couple of explanations for rationalizing this 'softer' distance dependence are described in the discussion section.

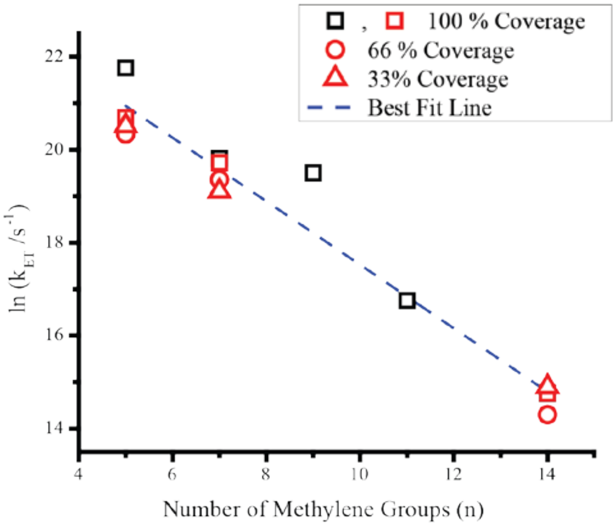

Figure 5-6 The natural log of the electron transfer rate constant is plotted against the number of methylene groups. The blue dashed line shows a best fit by Equation 5-2 and it has a slope of 0.68 ± 0.04 (error determined via least-squares fitting). The black and red symbols indicate different batches of donor and acceptor nanoparticles. Various coverages for the same batch of nanoparticles were studied and are distinguished by their symbol: maximum

coverage is a square (□), two-thirds maximum coverage is a circle (○), and one-third maximum coverage is a triangle (△). In all cases the donor to acceptor ratio was maintained.

5.2.4 Dependence of $\Delta_r G$

The electron transfer rate in the nanoparticle dyad systems was studied as a function of the reaction Gibbs energy, $\Delta_r G$, by changing the size of the acceptor nanoparticle (CdSe) which changes the conduction band offsets. In all cases the interparticle distance was fixed by using cysteamine (CA) as the ligand shell for the donor nanoparticle and mercaptohexanoic acid (MHA) as the ligand shell for the acceptor nanoparticle, ~ 14.8 Å. Experimentally it is observed that as the reaction free energy becomes more favorable, the electron transfer rate increases in a monotonic manner (Figure 5-7).

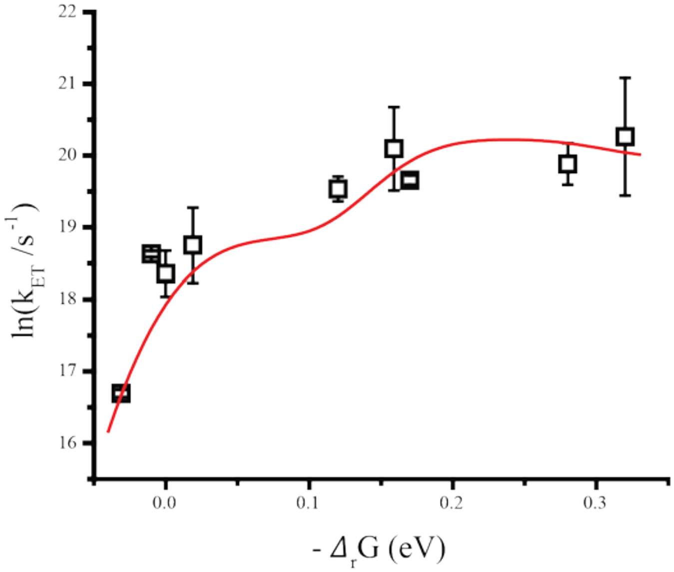

Figure 5-7 The natural log of the electron transfer rate constant is plotted against the negative $\Delta_r G$ for the experimental data (black squares). The red curve shows a fit by the semiclassical Marcus equation with a sum over electronic final states (see text for details).

The experimental data are well described by the traditional semi-classical Marcus equation (Equation 5-3), as long as one includes the two possible final electronic states; the S_e and P_e that reside in the acceptor's conduction band. The S_e state of CdSe is taken to be the conduction band edge and the difference in energy between the S_e and P_e state was previously reported for CdSe of this size.[39] The energy offset of these two discrete electronic states are what cause the Marcus curve to display a second rise at approximately -0.15 eV. For $\Delta_r G$ near zero the S_e state dominates, but as $\Delta_r G$ becomes more negative the P_e state contributes more to the reaction rate. Equation 5-3 shows the explicit form of the semiclassical equation[17]

k_{ET} **Equation 5-3**

$$= \frac{2\pi}{\hbar}|V|^2 \frac{1}{\sqrt{4\pi\lambda_s k_B T}} \left[\sum_{n=0}^{\infty} e^{-S} \left(\frac{S^n}{n!}\right) \exp\left(-\frac{(\lambda_s + \Delta_r G(S_e) + nhv)^2}{4\,\lambda_s k_B T}\right) \right.$$

$$\left. + 3\sum_{n=0}^{\infty} e^{-S} \left(\frac{S^n}{n!}\right) \exp\left(-\frac{(\lambda_s + \Delta_r G(P_e) + nhv)^2}{4\,\lambda_s k_B T}\right) \right]$$

where k_B is Boltzmann's constant, $|V|$is the electronic coupling matrix element, $\Delta_r G$ is the reaction free-energy, λ_s is the outer-sphere or solvent reorganization energy, ν is the frequency of the effective quantized vibrational mode, and S is the Huang-Rhys factor given as the ratio of the inner-sphere reorganization energy, λ_v, to the quantized mode energy spacing, $\frac{\lambda_v}{h\nu}$. The $h\nu$ term refers to the energy of a single effective quantized mode associated with the electron transfer reaction, and in this analysis it was taken to correspond to the longitudinal optical phonon frequency of the acceptor (207 cm^{-1} for CdSe).[40] The solvent reorganization energy was approximated by using a two-sphere model in a dielectric continuum; namely[17]

$$\lambda_S = \frac{e^2}{4\pi\varepsilon_0}\left(\frac{1}{D_{OP}} - \frac{1}{D_S}\right)\left(\frac{1}{2r_D} + \frac{1}{2r_A} - \frac{1}{R}\right)$$

Equation 5-4

where D_{OP} is the optical dielectric constant, D_S is the static dielectric constant, $r_D$is the donor nanoparticle radius, r_A is the acceptor nanoparticle radius (which is changing in this system), and R is the interparticle distance. The two sphere model predicts that the value of the solvent reorganization energy,λ_s, should lie between 0.018 eV and 0.023 eV; thus, the best fit to the experimental data was constrained to have a λ_s over this range. In addition to λ_s , the electronic coupling parameter and the inner-sphere reorganization energy, λ_v, were floated to minimize the residuals. The best fit curve is indicated by the red line in Figure 7. The best fit parameters were found to be $\lambda_s = 0.022$ eV, $\lambda_v = 0.009$ eV, and $|V| = 2.8$ cm^{-1}.

Note that Equation 5-3 assumes that the quantized vibrational mode is significantly larger than kT; however this assumption is not strictly valid. A more rigorous model is available for cases in which $h\nu \approx kT$ [41] and it gives a similarly good fit to the data, however the best fit value of the electronic coupling is 0.4 cm^{-1} rather than 2.8 cm^{-1}. See the discussion and Supplemental Information for more details.

5.3 DISCUSSION

5.3.1 Electron Transfer Kinetics

These studies improve on the earlier work of Wu et. al.,[29] that investigated electrostatically bound semiconductor nanoparticle aggregates of variable size, by studying covalently bound semiconductor nanoparticle donor-acceptor dyads. The donor nanoparticle was photoexcited at the first excitonic peak maximum (635 nm); and to minimize the effect from scattering by the microspheres, the nanoparticle fluorescence was collected at the red edge of the emission spectrum. The photoluminescence decays were fit using a lifetime distribution analysis. The difference in quenching between the Type II system which promotes electron transfer and the Type I control system was used to determine the electron transfer rate (Equation 5-1). Comparison of the lifetime distributions show that the dominate change in the lifetime distribution is a shift in the value of the shortest lifetime component, and it was used to calculate an electron transfer rate (See Equation 5-1).

The ability to focus on a single lifetime component differs significantly from what other groups have observed.[42-45] Frequently, electron transfer rates are calculated as a difference between the average lifetime of a control system (where electron transfer is not favored) and the investigated system (where electron transfer is favored). However, this process provides an effective electron transfer rate that is an average over a nanoparticle distribution that is not necessarily known or well defined. In the absence of a charge transfer band it has been difficult to attribute electron transfer as arising from a single time constant in these complex assemblies.[46] For example, if we mimic the type of system designed by Wu et. al.[29] and fabricate covalently bound nanoparticle aggregates in solution, the photoluminescence decays are significantly less controlled. Figure 5-8 shows data from such a system in which it can be seen that the long lived lifetime components are not fixed in shape and position in the presence of the acceptor nanoparticle. Additionally, the amplitude of the long-lived lifetime components are much larger than that which is reported in Figure 5-4D. Thus, the nanoparticle dyad assemblies studied here represent an advancement toward the sort of system homogeneity found in molecular dyads.

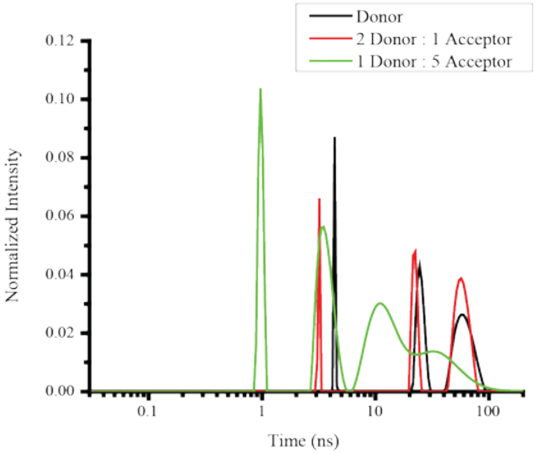

Figure 5-8. Sample of the PL distribution fitting for the Type II covalently bound nanoparticle assemblies. The free donor in solution, MPA CdTe, (black) 2 Donor: 1 Acceptor (red), and 1 Donor : 5 Acceptor (green) are depicted here. The prefactors before donor and acceptor are molar ratios.

5.3.2 Electron Transfer Rate as a Function of Interparticle Distance

The data in Figure 5-6 report how charge transfer changes with the distance between two semiconductor nanoparticles that form a dyad. Over the last two decades a number of closely related studies have been performed; other research groups have investigated how electron transfer rates in semiconductor nanoparticles attached to either molecular/polymer[47] or metal/metal oxide[46,48] systems change as a function of donor-acceptor distance. In the metal and metal oxide systems, the semiconductor quantum dots have been linked through a molecular bridge, and electron transfer between a semiconductor quantum dot and a metal oxide[46] was studied as a function of interparticle distance yielding a decay parameter of 0.94 per methylene. This is similar, but is somewhat larger than the β value of 0.68 per methylene found for the 2NPAs. Tagliazucchi et. al.,[47] studied electron transfer between CdSe nanoparticles and poly(viologen) for varying viologen units, and found β to be 0.8 per Å, and if one assumes the length of a methylene unit is 1.26 Å,[49] then the value of β for this work is determined to be 0.86 per Å. Thus, the decay parameter for the CdSe-polymer system[47] is comparable to the value for the CdTe-CdSe dyad systems.

For traditional alkane self-assembled monolayers the distance dependence for alkane chains is reported to range from 0.9 to 1.1 per methylene.[37,38] There are a few explanations for why the distance dependence for this system would be less than the value of 1.0 per methylene. The current system has an amide linkage, and others report that amide groups can enhance the electron transfer efficiency and yield a β that is less than 1.0.[48,50,51] Additionally, when the molecules in a SAM are not oriented normal to the surface, both ‘through bond’ superexchange and ‘through space’ superexchange can contribute to the electron tunneling. For example, alkanethiol SAMs on indium phosphide with a 55 degree tilt angle were shown to have a β value of 0.49 per methylene.[38,52] Since it is unlikely that the ligands on the nanoparticle surface are entirely perpendicular to the surface and they contain an amide group in the middle of the chain, the β value reported for the dyads seems reasonable.

In complex nanoscale systems, the electron transfer distance relationships are frequently reported to have slopes that are much less than one.[12,53-57] Gilbert et. al.[12] describes molecular wires in which electrons can hop along the bridge, as well as tunnel through it, yielding smaller β values. In complex two nanoparticle systems separated by “alkane-like” linkers β values have been reported to be 0.42 and 0.08 per Å. [56,57] For the current system, very shallow slopes are not observed, which is consistent with an electron tunneling mechanism by way of a covalent pathway of saturated C-C bonds. Lastly, we note that the magnitude of the electron transfer rate for the shortest linker, TGA, falls within the regime of reported electron transfer rates in the literature for dyes directly attached to a nanoparticle.[46,47,58,59]

5.3.3 Free Energy Dependence of the Electron Transfer

Figure 5-9 shows plots of the electron transfer rates versus $-\Delta_r G$. Because of the number of free parameters in Equation 5-3, $h\nu$ was fixed at 207 cm^{-1} [40] and λ_s was restricted to lie in the range of 0.018 eV to 0.023 eV found by using the two sphere model. The longitudinal optical (LO) phonon of the acceptor, CdSe, used for the quantized mode, ν, is known to be important for the carrier relaxation in the CdSe conduction band. It is reported in the literature to be 207 cm^{-1} over the size regime studied.[40] As a caveat, it should be noted the value of the LO phonon does change as a function of nanoparticle size, particularly for very small nanoparticle diameters; however, the change is small ~ 5 cm^{-1} and does not affect the fit quality. An appropriate range for the solvent reorganization energy, λ_s, was chosen by using a two-sphere model in a dielectric continuum. The two-sphere model predicts that the value of λ_s should be between 0.018 eV and 0.023 eV and is in good agreement with experiment.[60] In a CdSe-CdTe nanorod heterostructure reported on by Scholes et. al.[60], a charge transfer band was present and the reorganization energy of 0.02 eV was calculated directly using the shape of the free energy curves. Thus, the best fit value of 0.022 eV seems quite reasonable.

Other groups have observed an increase in electron transfer rate with an increase in driving force, even in locations where the inverted regime is expected.[21,61-64] The lowest energy state, S_e, in the conduction band was used to define the driving force, $\Delta_r G$, and model the experimental system (Figure 5-9A, green). Using S_e only, the semi-classical Marcus theory matches the experimental data fairly well for the more positive $\Delta_r G$ values, but it does not fit the entire experimental data set. Note that the top of the Marcus curve for the S_e only case is less round than may be anticipated; this results from the summation of vibrionic final states yielding a much broader curve. Similarly, the second excited state alone (Figure 5-9A, blue) does not match the experimental findings. However, summing over the first two electronic states of the acceptor was able to represent the experimental data accurately (Figure 5-8, red). The energy spacing between S_e and P_e was fixed at 0.15 eV in keeping with earlier reports.[39] The ledge that exists in the best fit line (Figure 5-9A, red) to the experimental data results from the fact that the model includes a sum over two electronic states and that the λ_s value is quite small. Given that the nanoparticles have a distribution of sizes and have a distribution of $\Delta_r G$ values, this feature is likely to be masked in the data.

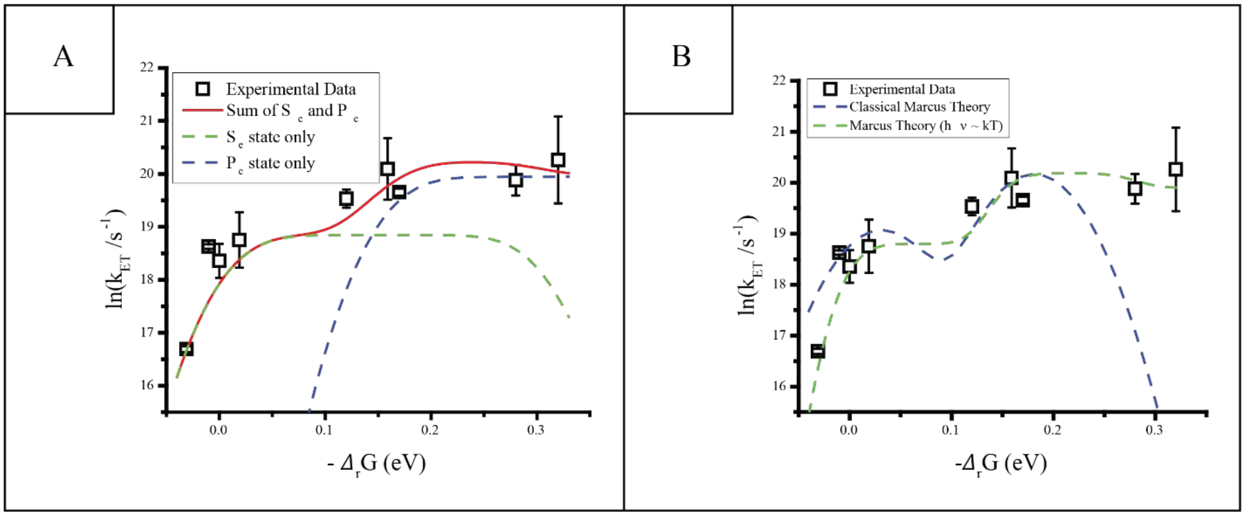

Figure 5-9. The natural log of the electron transfer rate constant is plotted against the reaction Gibbs energy, - $\boldsymbol{\Delta_r G}$, for the experimental data (black squares). The red curve shows a fit by the semi-classical Marcus equation with a sum over electronic final states for the first two energetic states of the acceptor (solid red) the dashed lines indicate using only the first excited sate (green) or the second excited state (blue) (A). Experimental data best fit to a variety of models including classical Marcus theory (blue) and a semi-classical Marcus theory at intermediate temperature (green) (B).

Figure 5-9B compares the predictions of different models for describing the experimental data for the $\Delta_r G$ trend. The classical Marcus theory, without quantized nuclear modes, describes the data until the driving force becomes too large; although the inclusion of more than two product energy levels improves the fit, it does not adequately describe the data. The incorporation of the vibrational states (i.e., longitudinal optical phonon mode) in the semi-classical Marcus theory ($kT > h\nu$) helps to broaden the Marcus curve and describes the system well over the $\Delta_r G$ regime investigated (Figure 5-9A, red). If we incorporate the fact that $h\nu \approx kT$, however, we can utilize a more rigorous model and a fit by this model is shown by the dashed green line in Figure 5-9B. While it gives a similarly good fit to the data, the best fit model parameters change somewhat; most notably the value of the electronic coupling is 0.4 cm^{-1} rather than 2.8 cm^{-1}.Note that the model used here to describe the charge transfer is fundamentally related to the multiphonon emission model for charge carrier trapping in deep traps of a semiconductor.[65] We note that an Auger-assisted electron transfer mechanism, which has been used to describe hole transfer in the deeply inverted Marcus regime, does not need to be invoked to generate a good fit to the data. Thus, the best fit, with the most realistic physical parameters, is found by using the semi-classical Marcus equation, (aka, multiphonon emission model), either at high or intermediate temperature, over a sum of the two final states.

In an effort to assess whether the high frequency limit or the intermediate frequency model more accurately describes the data, the value of the electronic coupling at contact between the nanoparticles was obtained by extrapolating to a zero distance, using the distance dependence from Figure 5-6. Two limits were considered for contact, direct contact between nanoparticle atoms, as in a core-shell material, and a disulfide bond linkage.[66] For the fit by Equation 5-3 (red curve) we obtain a 202 meV electronic coupling for direct contact and an 82 meV electronic coupling for the disulfide linkage; whereas for the fit by Equation E5 (green curve) we find $|V|$ = 30 meV at direct contact and 12 meV for a disulfide linker. For CdSe-CdTe nanorod heterostructures Scholes et. al.[60] reports 50 meV, for CdTe-CdTe aggregates (via a quantum mechanical calculation) a value of 40 meV[67] is reported, and for dye molecules directly bound to a semiconductor nanoparticle electronic couplings in the range of 10 to 10^3 meV have been reported. Although both models give reasonable coupling strengths, the intermediate frequency limit is more consistent with the known phonon properties of the nanoparticle.

5.4 CONCLUSION

A controlled covalently linked nanoparticle dyad system on a template was fabricated. The band edges of the nanoparticles in these systems were designed in a manner such that electron transfer could be studied. Electron transfer was studied as a function of interparticle distance and driving force. The semi-classical Marcus theory using the appropriate summation over states was able to accurately describe the relationship between electron transfer and $\Delta_r G$ These findings imply that much of the knowledge gained from studies in molecular systems can be readily translated to the case of nanoparticle quantum dots and should prove useful for understanding, controlling, and designing bulk heterojunction solar cells that transfer charge using semiconductor nanoparticles.

5.5 EXPERIMENTAL DETAILS, MATERIALS, AND METHODS

Selenium powder (99.999%), tellurium powder (99.999%), cadmium chloride ($CdCl_2$; 99%) sodium borohydride ($NaBH_4$; 98%), CdO (99.999%), thioglycolic acid (TGA), 4-mercaptobutyric acid (MBA), 6-mercaptohexanoic acid (MHA), 8-mercaptooctanoic acid (MOA), 11-mercaptoundecanoic acid (MUA), 1-ethyl-3-(3-dimethylaminopropyl)carbodiimide (EDC), *N*-hydroxysulfosuccinimide (S-NHS), and phosphate buffered saline tablets (PBS), Oleic Acid (OA), trioctylphosphine oxide (99%) were purchased from Sigma-Aldrich. trioctylphospine was purchased from Strem Chemicals. Octadecylphosphonic acid (ODPA, >99%) and tetradecylphosphonic acid (TDPA, >99%) were purchased from PCI Synthesis. Silica microbeads, both amine coated and bare, 150 nm and 500 nm diameter were purchased from Polysciences, Inc. All reagents and solvents were used as received. Water used in all experiments was purified by a Barnstead Nanopure system, and its resistance was 18.2 MΩ-cm at 25 °C.

5.5.1 Carboxylic acid terminated cadmium selenide (CdSe)

Octadecylphosponic acid (ODPA) CdSe nanoparticles, < 2.5 nm, as well as oleic acid (OA) CdSe nanoparticles, > 2.5 nm, were synthesized following previously published methodologies.[68,69] The purified nanoparticles were ligand exchanged to TGA, MBA, MHA, MOA, or MUA by stirring the ligand in a solution whose concentration was 1000 times in excess to that of the nanoparticle. The mixture was stirred overnight in a 4.0 mL 50% water (pH=11) 50% chloroform solution. The exchanged nanoparticles were then isolated from the water phase and purified through syringe and centrifugal filtration. For synthesis of larger, 5.5 nm, OA CdSe nanoparticles a multiple injection of the selenium precursor was utilized.

5.5.2 Amine terminated CdSe

ODPA-CdSe, 2.2 nm, and OA-CdSe, 3.1 nm, stock solutions were ligand exchanged to cysteamine (CA) through a precipitation process, demonstrated previously by Strekal et. al. for CdSe/ZnS core-shell nanoparticles.[70] The precipitation was performed through the addition of 200 μL of a 20 mg/mL concentration cysteamine/methanol solution to a 2.0 mL NP stock solution. The nanoparticle solutions were isolated through centrifugation and dried. The nanoparticles could then be dissolved in water and purified through syringe and centrifugal filtration.

5.5.3 Amine terminated cadmium telluride (CdTe)

CA-CdTe nanoparticles, 3.3 nm, 4.0 nm, and 4.1 nm were synthesized by an adaptation of a procedure by Wang et. al.[71] Briefly, 1.145 g $CdCl_2$ and 0.8521 g CA were dissolved in 20.0 mL of water and the pH was adjusted to be approximately 5.75. This solution was then heated to 90.0 °C and deoxygenated for approximately 20 min. Reduced tellurium was made by dissolving 127.5 mg Te and 94.5 mg $NaBH_4$ in 5.0 mL of water and heated under argon to 70.0 °C. The reduced tellurium precursor (2.5 mL) was injected into the cadmium solution and refluxed until the desired size was reached. The nanoparticles were purified through syringe and centrifugal filtration.

5.5.4 Carboxylic acid terminated CdTe

Carboxylic acid terminated CdTe nanoparticles, 4.1 and 4.4 nm, were synthesized through a two part process. First, large tetradecylphosphonic acid (TDPA) capped CdTe nanoparticles were synthesized following a multiple injection approach using the synthesis developed by Peng et al.[72] Next, the TDPA-CdTe nanoparticles were ligand exchanged to either TGA or MUA following a procedure similar to that published by Wang et al.[36] A 10.0 mL solution of water containing 0.1 mmol $CdCl_2$ and 0.2 mmol TGA or MUA at pH 11.5 was degassed with argon at 80°C for 10 min. Then, 0.5 mL of the TDPA-CdTe nanoparticle chloroform solution was injected and. the heating was continued until all the chloroform was boiled off. The solution was then brought to 100 °C and refluxed for 3 hours. The resulting solution was purified by centrifugation and syringe filters to remove any non-soluble nanoparticles and unreacted precursors.

5.5.5 Assembly Formation

Nanoparticle dyads were formed by templating on a SiO_2 microsphere. The first step in a one nanoparticle assembly (1NPA) was to attach a nanoparticle to an amine coated SiO_2 microsphere, approximately 500 nm in diameter. Approximately 30 mg of SiO_2 microspheres (zeta potential = 41.91 ± 0.60 mV) were dispersed in 1 mL of water. An excess of oppositely charged (carboxylic acid terminated) nanoparticles was added to the microsphere solution and the total volume was adjusted to equal 3 mL. Then, it was shaken for one hour. During this process, nanoparticles bind electrostatically to the surface of the microsphere. The assembly was purified using a stirred ultrafiltration cell with a 100 nm pore size cellulose nitrate membrane filter (Whatman). The “free” nanoparticles (< 5 nm) go through the filter, but those that are attached to the SiO_2 template do not and are captured by the filter. The pressure used in the filtration was 50 psi and filtrate samples were collected. After filtration, the solid on the filter paper was suspended in 4 mL of water. An additional two to three rounds of filtrations were performed on this sample and the 1NPA was suspended in 3 mL of water. The zeta potential for a sample 1NPA was -19.66 ± 2.49 mV.

The nanoparticle dyads (2NPA) were assembled by forming an amide bond between the exposed carboxylic acid group of the 1NPA and the solvent exposed terminus of an amine terminated nanoparticle (Figure 1). The catalyst 1-ethyl-3-(3-dimethylaminopropyl)carbodiimide (EDC) was used to promote this reaction. By choosing the second nanoparticle to be larger than that in the 1NPA the reaction is biased to create dyads. The 1NPA and EDC were added to a 500 mM PBS buffer solution in a 1:1000 ratio,[73] and stirred for 15 minutes. Then the amine terminated nanoparticles were added to the solution and it was stirred overnight. The sample was cooled to 4 ^{o}C to quench the excess EDC and then purified using the same methodology as described above for the 1NPA. The zeta potential for a resulting 2NPA was 9.35 ± 1.45 mV. A more detailed description of this procedure can be found in the SI.

5.5.6 Steady State Spectroscopy

Steady-state absorption spectra were measured on an Agilent 8453 spectrometer, and the steady-state emission spectra were measured on a Horiba J-Y Fluoromax 3 fluorescence spectrophotometer.

5.5.7 Time-Dependent Fluorescence Spectroscopy

Time resolved fluorescence measurements of the nanoparticle assemblies were measured using the time correlated single photon counting (TSCPC) technique with a PicoHarp 300 TCSPC module (PicoQuant GmbH).[74] The samples were excited at 635 nm using a synchronously pumped dye laser. All measurements were made at the magic angle. Measurements were collected using a 1 MHz repetition rate, 32 ps resolution, and until a maximum count of 10,000 was observed at the peak channel. The instrument response function was measured using colloidal $BaSO_4$ and in every case the instrument response function had a full-width-at-half-maximum of $\leq$96 ps. The decay curves were fit to a distribution of lifetime components by a convolution and compare method using Edinburgh Instruments fluorescence analysis software technology (FAST)[75] namely (Equation 5-5)[76]

$$I(t) = \int_{\tau=0}^{\infty} \alpha(\tau) \cdot \exp\left({-t}/{\tau}\right) \mathrm{d}\tau$$

Equation 5-5

5.5.8 Zeta Potential Measurements

Zeta potential measurements were performed at room temperature in a 90° geometry with a 532 nm laser (Brookhaven Instrument Co.). The electrophoretic mobility measurements were performed on the same instrument at room temperature with an electrical field strength of 16 V/cm and a field frequency of 2.00 Hz by using a Zeta Plus zeta potential analyzer.

5.5.9 Scanning Transmission Electron Microscopy (STEM)

Samples for electron microscopy characterization were drop casted on a carbon film on a copper transmission microscopy grid (Ted Pella Inc.). The measurements were performed using a ZEISS Sigma 500 VP Scanning Electron Microscope equipped with a STEM detector. The images were collected in bright field mode, with an electron beam acceleration voltage of 24-28 keV, 10 μm aperture, and working distance of about 2.5 mm.

5.6 REFERENCES

(1) Shami, S.; Is Solar Power The Best Energy Option To Meet Our Future Demands? *IJSTR*, **2015**, 4, 165.

(2) Yu, G.; Gao, J.; Hemmelen, J. C.; Wudl, F.; Heeger, A. J.; Polymer Photovolatic Cells: Enhanced Efficencies via a Network of Internal Donor-Acceptor Heterojunctions. *Science*, **1995**, 270, 1789-1791.

(3) Huynh, W. U.; Dittmer, J. K.; Alivisatos, A. P.; Hybrid Nanorod-Polymer Solar Cells. *Science*, **2002**, 295, 2425-2427.

(4) Park, S. H.; Roy, A.; Beaupre´, S.; Cho, S.; Coates, N.; Moon, J. S.; Moses, D.; Leclerc, M.; Lee, K.; Heeger, A.; Bulk heterojunction solar cells with internal quantum efficiency approaching 100%. *J. Nat. Photon*, **2009**, 3, 297-302.

(5) You, J.; Dou, L.; Yoshimura, K.; Takehito, K.; Ohya, K.; Moriarty, T.; Emery, K.; Chen, C.; Gao, J.; Gang, L.; Yang, Y.; A polymer tandem solar cell with 10.6% power conversion efficiency. *Nat. Commun.*, **2013**, 4, 1446.

(6) Marcus, R. A.; Sutin, N.; Electron transfers in chemistry and biology. *Biochim. Biophys. Acta.*, **1985**, 811, 265-322.

(7) Sanders, A. M.; Magnanelli, T. J.; Bragg, A. E.; Tovar, D. J.; Photoinduced Electron Transfer within Supramolecular Donor-Acceptor Peptide Nanostructures under Aqueous Conditions. *J. Am. Chem. Soc.*, **2016**, 138, 3362-3370.

(8) Chen, P.; Meyer, T. J.; Medium Effects on Charge Transfer in Metal Complexes. *Chem. Rev.*, **1998**, 98, 1439-1478.

(9) Jortner J; Bixon, M. *Electron Transfer-From Isolated Molecules to Biomolecules, Part 1 and Part 2*; John Wiley & Sons, Inc. New York, **1999**.

(10) a) Paddon-Row, M.N.; Orbital interactions and long-range electron transfer. Adv. *Phys Org. Chem*. **2003**, 38, 1-85; b) Oevering, H.; Paddon-Row, M. N.; Heppener, M.; Oliver, A. M.; Cotsaris, E.; Verhoeven, J. W.; Hush, N. S.; Long-Range Photoinduced Through-Bond Electron Transfer and Radiative Recombination via Rigid Nonconjugated Bridges: Distance and Solvent Dependence. *J. Am. Chem. Soc.*, **1987**, 109, 3258-3269.

(11) Lawson, J. M.; Paddon-Row, M. N.; Schuddeboom, W.; Warman, J. M.; Clayton, A. H. A.; Ghiggino, K. P.; Photoinduced giant charge-separated states in a new series of completely rigid covalently linked triads. *J. Phys. Chem.* **1993**, 97, 13099-13106.

(12) Gilbert M, Albinsson B.; Photoinduced charge and energy transfer in molecular wires. *Chem. Soc. Rev.*, **2015**, 44, 845-886.

(13) Bixon, M.; Jortner, J.; Electron transfer via bridges. *J. Chem. Phys.* **1997**, 107, 5154-5170.

(14) Natali M., Campagna S., Scandola, F. *Chem. Soc. Rev.* **2014**, 43, 4005-4018.

(15) Weiss, E.A., Wasielewski, M. R., Ratner, M.A.; Photoinduced charge and energy transfer in molecular wires. *Curr Chem.* **2005**, 257, 10-3-133.

(16) Gu, Y.; Kumar, K.; Lin, Z.; Read, I.; Zimmt, M. B.; Waldeck, D. H.; Studies into the character of electronic coupling in electron transfer reactions. J. *Photochem. Photobio. A: Chem.* **1997**, 105, 189 - 196.

(17) Liu, M.; Waldeck, D. H.; Oliver, A. M.; Head, N. J.; Paddon-Row, M. N.; Observation of Dynamic Solvent Effect for Electron Tunneling in U-Shaped Molecules. *J Am. Chem Soc.* **2004**, 126, 10778-10786.

(18) Chakrabarti, S.; Parker, M. F. L.; Morgan, C. W.; Schafmeister, C. E.; Waldeck D. H.; Experimental Evidence for Water Mediated Electron Transfer Through Bis-Amino Acid Donor-Bridge-Acceptor Oligomers. *J. Am. Chem. Soc.* **2009**, 131, 2044-2045.

(19) Zimmt, M. B. and Waldeck, D. H.; Exposing Solvent's Roles in Electron Transfer Reactions:? Tunneling Pathway and Solvation. *J. Phys. Chem. A* **2003**, 107, 3580-3597.

(20) Smith, A. M.; Nie, S.; Semiconductor Nanocrystals: Structure, Properties, and Band Gap Engineering. *Acc. Chem. Res.,* **2010**, 43, 190-200.

(21) Zhu, H.; Yang, Y.; Hyeon-Deuk, K.; Califano, M.; Song, N.; Wang, Y.; Zhang, W.; Prezhado, O. V.; Lian T.; Auger-Assisted Electron Transfer from Photoexcited Semiconductor Quantum Dots. *Nano. Lett.*, **2014**, 14, 1263-1263-1269.

(22) Olshansky, J. H.; Ding, T. X.; Lee, Y. V.; Leone, S. R.; Alivisatos, A. P.; Hole Transfer from Photoexcited Quantum Dots: The Relationship Between Driving Force and Rate. *J. Am. Chem. Soc.*¸ **2015**, 137, 15567-15575.

(23) Sze, S. M.; Kwok, N. K.; *Physics of Semiconductor Devices Nanomaterials: 2nd Edition*; John Wiley & Sons Inc. Publishing: Hoboken, New Jersey, **2007**.

(24) Komsa, H.; Krasheninnikov, A.; Electronic structures and optical properties of realistic transition metal dichalcogenide heterostructures from first principles. *Phys. Rev. B*, **2013**, 88 1-7.

(25) Kang, J.; Tongay, S.; Zhou, J.; Li, J.; Wu, J.; Band offsets and heterostructures of two-dimensional semiconductors. *Appl. Phys. Lett.*, **2013**, 012111, 22-25.

(26) Vokhmintcev, K. V.; Samokhvalov, P. S.; Nabiev, I.; Charge transfer and separation in photoexcited quantum dot-based systems. *Nanotoday*, **2016**, 11, 189-211.

(27) Chuang, C-H.; Doane, T. L.; Lo, S. S.; Scholes, G. D.; Burda, C.; Measuring Electron and Hole Transfer in Core/Shell Nanoheterostructures. *ACS Nano*, **2011**, 5, 6016.

(28) a) Scholes, G. D.; Controlling the Optical properties of Inorganic Nanoparticles. *Adv. Funt. Mater.*, **2008**, 18, 1157-1172; b) Lo, S. S.; Mirkovic, T.; Chaung, C-H.; Burda, C.; Scholes, G. D.; Emergent properties resulting from type-II band alignment in semiconductor nanoheterostructures. *Adv. Mater.*, **2011**, 23, 180-197.

(29) Wu, M.; Mukherjee, P.; Lamont, D. N.; Waldeck, D. H.; Electron Transfer and Fluorescence Quenching of Nanoparticle Assemblies. *J. Phys. Chem. C*, **2010**, 114, 5751-5759.

(30) a) Sellers, D. G.; Button, A. A.; Nasca, J. N.; Wolfe, G. E.; Chauhan S.; Watson, D. F.; Excited-State Charge Transfer within Covalently Linked Quantum Dot Heterostructures. *J. Phys. Chem. C*, **2015**, 119, 27737-27748; b) Gross, D.; Susha, A. S.; Klar, T. A.; Da Como, E.; Rogach, A. L.; Feldmann, J.; Charge Separation in Type II Tunneling Structures of Close-packed CdTe Nanocrystals. *Nano Lett.*, **2008**, 8, 1482-1485.

(31) Wang, D.; Zhao, H.; Wu, N.; Khakani, M. A. E.; Ma, D.; Tuning the Charge-Transfer Property of PbS-Quantum-Dot/TiO2-Nanobelt Nanohybrids via Quantum Confinement. *J. Phys. Chem. Lett.* **2010**, 1, 1030-1035.

(32) Rasband, W.S., ImageJ, U. S. National Institutes of Health, Bethesda, Maryland, USA, http://imagej.nih.gov/ij/, **1997-2016**

(33) Bloom, B. P.; Zhao, L.-B.; Wang, Y.; Waldeck, D. H.; Liu, R. ; Zhang, P.; Beratan, D. N. Ligand-Induced Changes in the Characteristic Size-Dependent Electronic Energies of CdSe Nanocrystals. *J. Phys. Chem. C*, **2013**, 117, 22401-22411.

(34) Meulenberg, R. W.; Lee, J. I. R.; Wolcott, A.; Zhang, J. Z.; Terminello, L. J.; van Buuren, T.; Determination of the Exciton Binding Energy in CdSe Quantum Dots. *ACS Nano*, **2009**, 3, 325-330.

(35) Jasieniak, J.; Califano, M.; Watkins, S. E.; Size Dependent Valence and Conduction Band-Edge Energies of Semiconductor Nanocrystals. *ACS Nano*, **2011**, 5, 5888-5902.

(36) Wang, Y.; Liu, K.; Mukherjee, P.; Hines, D. A.; Santra, P.; Shen, H. Y.; Kamat, P.; Waldeck, D. H.: Driving charge separation for hybrid solar cells: photo-induced hole transfer in conjugated copolymer and semiconductor nanoparticle assemblies. *Phys. Chem. Chem. Phys.* **2014**, 16, 5066-5070.

(37) Smalley, J. F.; Feldberg, S. W.; Chidsey, C. E. D.; Linford, M. R.; Newton, M. D.; Liu, Y.-P.; The Kinetics of Electron Transfer through Ferrocene-Terminated Alkanethiol Monolayers on Gold. *J. Phys. Chem.*, **1995**, 99,, 13141-13149.

(38) Slowinski, K.; Chamberlain, R. V.; Miller, C. J.; Majda M.; Through-Bond and Chain-to-Chain Coupling. Two Pathways in Electron Tunneling through Liquid Alkanethiol Monolayers on Mercury Electrodes. *J. Am. Chem. Soc.*, **1997**, 119, 11910-11919.

(39) Norris, D. J.; Bawendi, M. G.; Measurement and assignment of the size-dependent optical spectrum in CdSe quantum dots. *Phys. Rev. B.*, **1996**, 53, 16338-16346.

(40) Lin, C.; Gong, K.; Kelley, D. F.; Kelley, A. M. Electron-Phonon Coupling in CdSe/CdS Core/Shell Quantum Dots. *ACS Nano*, **2015**, 9, 8131-8141.

(41) Jortner, J.; Temperature dependent activation energy for electron transfer between biological molecules. *J. Chem. Phys.*, **1976**, 64, 4860-4867.

(42) Robel, I.; Kuno, M.; Kamat, P. V.; Size Dependent Electron Injection from Excited CdSe Quantum Dots into TiO2 Nanoparticles. *J. Am. Chem. Soc.*, **2007**, 129, 4136-4137.

(43) Yang, J.; Oshima, T.; Yindeesuk, W.; Pan, Z.; Zhong, X.; Shen Q.; Influence of linker molecules on interfacial electron transfer and photovoltaic performance of quantum dot sensitized solar cells. *J. Mater. Chem. A*, **2014**, 2, 20882-20888.

(44) Xu, Z.; Cotlet, M.; Quantum Dot-Bridge-Fullerene Heterodimers with Controlled Photoinduced Electron Transfer. *Agnew. Chem. Int. Ed.*, **2011**, 50, 6079-6083.

(45) Dibbell, R. S.; Watson, D. F.; Distance-Dependent Electron Transfer in Tethered Assemblies of CdS Quantum Dots and TiO2 Nanoparticles. *J. Phys. Chem. C*, **2009**, 113, 3139-3149.

(46) Morris-Cohen, A. J.; Frederick, M. T.; Cass, L. C.; Weiss, E. A.; Simultaneous Determination of the Adsorption Constant and the Photoinduced Electron Transfer Rate for CdS Quantum Dot-Viologen Complex. *J. Am. Chem. Soc.*, **2011**, 133, 10146-10154.

(47) Tagliazucchi, M.; Tice, D. B.; Sweeny, C. M.; Morris-Cohen, A. J.; Weiss, E. A.; Ligand-Controlled Rates of Photoinduced Electron Transfer in Hybrid CdSe Nanocrystal/Poly(viologen) Films. *ACS Nano*, **2011**, 5, 9907-9917.

(48) Wang, H.; McNellis, E. R.; Kinge, S.; Bonn, M.; Canovas, E.; Tuning Electron Transfer Rates through Molecular Bridges in Quantum Dot Sensitized Oxides. Nano. Lett., **2013**, 13, 5311-5315.

(49) Wasserman, S. R.; Tao, Y.-T.; Whitesides, G. M.; Structure and Reactivity of Alkylsiloxane Monolayers Formed by Reacion of Alkyltrichlorosilanes on Silicon Substrates. *Langmuir*, **1989**, 5, 1074-1087.

(50) a)Slowinski, K.; Majda, M.; Mercury-mercury tunneling junctions: Part II. Structure and stability of symmetric alkanethiolate bilayers and their effect on the rate of electron tunneling. *J. Electroanal. Chem.*, **2000**, 491, 139-147; b) Sek, S.; Misicka, A.; Bilewicz, R.; Effect of Interchain Hydrogen Bond on Electron Transfer through Alkanethiol Monolayers Containing Amide Bonds. *J. Phys. Chem. B*, **2000**, 104, 5399-5402; c) Sek, S.; Palys, B.; Bilewicz, R.; Contribution of Intermolecular Interactions to Electron Transfer through Monolayers of Alkanethiols Containing Amide Groups. *J. Phys. Chem. B*, **2002**, 106, 5907-5914; d) Slowinski, K.; Fong, H. K. Y.; Majda, M.; Mercury-Mercury Tunneling Junctions 1. Electron Tunneling Across Symmetric and Asymmetric Alkanethiolate Bilayers. *J. Am. Chem. Soc.,* **1999**, 121, 7257-7261.

(51) Kai, M.; Takeda, K.; Morita, T.; Kimura, S.; Distance dependence of long-range electron transfer through helical peptides. *J. Pept. Sci.,* **2008**, 14, 192-202.

(52) Yamamoto, H. and Waldeck, D. H.; Effect of Tilt-Angle on Electron Tunneling through Organic Monolayer Films. *J. Phys. Chem. B*, **2002**, 106, 7469-7473.

(53) Bradbury, C. R.; Zhao, J.; Fermin, D. J.; Distance-Independent Charge-Transfer Resistance at Gold Electrodes Modified by Thiol Monolayers and Metal Nanoparticles. *J. Phys. Chem. C*, **2008**, 112, 10153-10160.

(54) Shein, J. B.; Lai, L. M. H.; Eggers, P. K.; Paddon-Row, M. N.; Gooding, J. J.; Formation of Efficient Electron Transfer Pathways by Adsorbing Gold Nanoparticles to Self-Assembled Monolayer Modified Electrodes. *Langmuir*, **2009**, 25, 11121-11128.

(55) Gotesman, G.; Guliamov, R.; Naaman, R.; Horizontal Versus Vertical Charge and Energy Transfer in Hybrid Assemblies of Nanoparticles. Beilstein. *J. Nanotechnol.*, **2012**, 3, 629-636.

(56) Hines, D. A.; Forrest, R. P.; Corcelli, S. A.; Kamat, P. V.; Predicting the Rate Constant of Electron Tunneling Reactions at the CdSe-TiO2 Interface. *J. Phys. Chem. B,*. **2015**, 119, 7439-7446.

(57) Ji, X.; Wang, W.; Mattoussi, H.; Effects of separation distance on the charge transfer interactions in quantum dot-dopamine assemblies. *Phys. Chem. Chem. Phys.*, **2015**, 17, 10108-10117.

(58) Haung, J.; Haung, Z.; Yang, Y; Zhu, H.; Lian, T.; Multiple Exciton Dissociation in CdSe Quantum Dots by Ultrafast Electron Transfer to Adsorbed Methylene Blue *J. Am. Chem. Soc.*, **2010**, 132, 4858-4864.

(59) Haung, J.; Stockwell, D.; Haung, Z.; Mohler, D.; Lian, T.; Photoinduced Ultrafast Electron Transfer from CdSe Quantum Dots to Rebipyridyl Complexes. *J. Am. Chem. Soc.*, **2008**, 130, 5632-5633.

(60) Scholes, G. D.; Jones, M.; Kumar, S.; Electron-Transfer Reactions Decided by Quantum Confinement. *J. Phys. Chem. C,* **2007**, 111, 13777-13785.

(61) Chakrapani, V.; Tvrdy, K.; Kamat, P. V.; Modulation of Electron Injection in CdSe-TiO2 System through Medium Alkalinity. *J. Am. Chem. Soc.*, **2010**, 132, 1228-1229.

(62) Sellers, D. G.; Watson, D. F.; Probing the Energetic Distribution of Injection Electrons at Quantum Dot-Linker-TiO2 Interfaces. *J. Phys. Chem. C*, **2012**, 116, 19215-19225.

(63) Heyon-Deuk, K.; Kim, J.; Prezhdo, O. V.; Ab Initio Analysis of Auger-Assisted Electron Transfer. *J. Phys. Chem. Lett.,* **2015**, 6, 244-249.

(64) Olshansky, J. H.; Ding, T. X.; Lee, Y. V.; Leone, S. R.; Alivisatos, A. P.; Hole Transfer from Photoexcited Quantum Dots: The Relationship between Driving Force and Rate. *J. Am. Chem. Soc.,* **2015**, 137, 15567-15575.

(65) a) Krasikov,D.N.; Scherbinin, A. V.; Knizhnik, A. A.; Vasiliev, A. N.; Potapkin, B. V.; Sommerer, T. J. ; Theoretical analysis of non-radiative multiphonon recombination activity of intrinsic defects in CdTe *J. Appl. Phys.,* **2016**, 119, 085706 ; b) Henry, C. H. ; Lang, D. V.; Nonradiative capture and recombination by multiphonon emission in GaAs and GaP *Phys. Re.v B,* **1977**, 15, 989.

(66) a) Boles, M. A.; Ling, D.; Hyeon, T.; Talapin, D. V.; The surface science of nanocrystals. *Nat. Mater.*, **2016**, 15, 141-356.; b) Dubois, L. H.; Nuzzo, R. G.; Synthesis, Structure, and Properties of Model Organic Surfaces. *Annu. Rev. Phys. Chem.*, **1992**, 43, 437-463.

(67) Koole, R.; Liljeroth, P.; Donega, C. d. M.; Vanmaekelbergh, D.; Meikjerink, A.; Electronic Coupling and Exciton Energy Transfer in CdTe Quantum-Dot Molecules. *J. Am. Chem. Soc.*, **2006**, 128, 10436-10441.

(68) Kalyuzhuy, G.; Murray, R. W. Ligand Effects on Optical Properties of CdSe Nanoparticles. *J. Phys. Chem. B*, **2005**, 109, 7012-7021.

(69) Yu. W. W.; Peng, X.; Formation of High-Quality CdS and Other II-VI Semiconductor Nanocrystals in Noncoordinating Solvents: Tunable Reactivity of Monomers. *Agnew. Chem. Int. Ed.,* **2002**, 41, 2368-2371.

(70) Strekal, N.; Kulakovich, O.; Belyaev, A.; Stsiapura, V.; Maskevich, S.; Photoluminescence of water-soluble CdSe/ZnS nanoparticles in complexes with cationic and anionic polyelectrolytes. *Optics and Spectroscopy*, **2011**, 104, 50-56.

(71) Wang, R.; Wang, Y.; Feng, Q.; Zhou, L.; Gong, F.; Lan, Y.; Synthesis and characterization of cysteamine-CdTe quantum dots via a one-step method. *Mater. Lett.*, **2012**, 66, 261-263.

(72) Yu, W. W.; Wang, Y. A.; Peng, X.: Formation and Stability of Size-, Shape-, and Structure-Controlled CdTe Nanocrystals: Ligand Effects on Monomers and Nanocrystals. *Chem. Mater*. **2003**, 15, 4300-4308.

(73) Hoppe, K.; Geidel, E.; Weller, H.; Eychmuller, A. Covalently bound CdTe nanocrystals. *Phys. Chem. Chem. Phys.*, **2002**, 4, 1704-1706.

(74) Yin X.; Kong, J.; De Leon, A.; Li Y.; Ma Z.; Wierzbinski, E.; Achim, C.; Waldeck, D. H. Luminesence Quenching by Photoinduced Charge Transfer between Metal Complexes in Peptide Nucleic Acids. *J. Phys. Chem. B*, **2014**, 118, 9037-9047

(75) McGuinness, C. D.; Nishimura, M. K. Y.; Keszenman-Pereyra, D.; Dickinson, P.; Campbell, C. J.; Bachmann, T. T.; Ghazalb, P.; Crainac, J. Detection of single nucleotide polymorphisms using DNA Holliday junction nanoswitch – a high-throughput fluorescence lifetime assay. *Mol. BioSyst.*, **2010**, 6, 386-390.

(76) Lakowicz, J. R. *Principles of Fluorescence Spectroscopy*, 3rd ed. Springer: **2006**; p. 1-61, 97-155, 331-382, 443-475.

6.0 CONCLUDING REMARKS

This dissertation has explored the fundamental role that is played by surface ligands on the physical properties of semiconductor NPs is discussed. Chapter 2 describes the electrochemical measurements of CdSe NPs of different sizes and passivated by three different ligand types. It was found that the ligand's connecting group has a strong influence over the electronic state energy of the valence band and that the magnitude of this effect can depend greatly on the surface-to-volume ratio of the NP. By examining both of these effects in tandem, we were able to unveil how these effects may reinforce or counteract each other. These findings were further corroborated by theoretical studies on $Cd_{33}Se_{33}$ and Cd_6Se_6 nanoclusters passivated with similar ligands to those used experimentally. Lastly, the framework of a model was proposed in an effort to simultaneously account for both the quantum confinement and ligand induced shifts on the valence band position. With a more thorough understanding of the electronic state energies of nanoparticles, the fabrication of devices with band engineered alignment at heterojunction interfaces for the improvement of charge carrier directionality is possible.

Chapter 3 demonstrates the importance of interfacial phenomenon when determining the energy band offset between semiconductor nanoparticles and other materials. Electrochemical and photoelectron spectroscopy measurements showed that the valence band maximum of PbS monolayers on Au substrates does not change substantially with nanoparticle size or ligand type. The Fermi-level pinning was shown to arise from the coupling of the electronic states of the nanoparticle to the states of the Au substrate. When an insulating alumina layer was inserted between the nanoparticles and the substrate, Fermi-level pinning was weakened enough that size- and ligand-dependent properties become manifest. The findings from this study point to a procedure for tuning the energies of semiconductor nanoparticles in the solid state without the detrimental effects caused by interfacial coupling that may limit charge transfer and injection efficiencies. Despite a rigorous investigation of the effects that occur at the nanoparticle – substrate interface, further exploration is required for other interfacial regions in a photovoltaic device such as; NP – NP and NP – Polymer heterojunctions.

Chapter 4 demonstrates how the ligand chirality of chiral imprinted nanoparticles influences spin dependent charge transport. Through a series of magnetic conductive probe AFM and magnetoresistance measurements it was found that conduction through chiral imprinted nanoparticles is spin specific in a manner consistent with that describe by the chiral induced spin selectivity effect. These effects were found to coincide with the observed chiroptical properties of the nanoparticles and represent the development of a wholly new type of spin filter. Ongoing efforts are placed on quantifying the chiroptical properties of the nanoparticles and relating that to the magnitude of spin selectivity. For future directions there is much interest in determining the role of the nanoparticle composition, crystal structure, and ligand type in spin dependent charge transport.

Chapter 5 investigates the charge transport properties of a donor-bridge-acceptor semiconductor nanoparticle ensemble. Here, a modular assembly approach was developed on a silica microbead template in an effort to have a well-defined architecture. By changing the surface passivation of the acceptor NP, the bridge length, or interparticle distance between donor and acceptor nanoparticles, could be varied. The experimentally determined electron transfer rates calculated from these systems were found to be consistent with an electron tunneling mechanism. The dependence of charge transfer rate on driving force was also investigated by controlling the size of the acceptor NP. Interestingly, the complex photophysics of the nanoparticle assembly could be well described by semiclassical Marcus theory if all of the contributing electronic states on the acceptor are included. The findings from this study illustrate that the same physical properties that dictate electron transfer in molecular systems are fully transferable to those in semiconductor nanoparticle assemblies.

While the effects of the surface chemistry on the NP properties that presented in this thesis may seem distinct, in many applications these effects exist together and it will be interesting to explore in future works the interconnectedness of some of these phenomena. Chapter 3 touches upon this by examining how the ligand induced electronic state shifts reported in Chapter 2 are influenced by the surface of an Au substrate. Another area of current interest is combining the works of Chapters 4 and 5 to investigate how spin dependent charge transport is facilitated in chiral acceptor-donor nanoparticle assemblies. It is hoped that the findings in this thesis help future researchers to better understand the role of surface chemistry on the physics of semiconductor nanoparticles.

APPENDIX A

ULTRAVIOLET PHOTOELECTRON SPECTROSCOPY ANALYSIS

This appendix discusses the analysis and interpretation of ultraviolet photoelectron spectroscopy (UPS) spectra for metals and semiconductors. The work function of a metal, Φ_m, is defined as the energy required to take an electron from the Fermi-level, E_f^m, to vacuum, E_{vac}^m. In a UPS spectrum the work function is defined as;

$$\Phi_\mathrm{m} = h\nu - W \qquad \textbf{Equation A1}$$

where $h\nu$ is the energy of the incident ultraviolet radiation and W is the width of the photoelectron spectrum (from the Fermi edge to the secondary electron cutoff). Panel A of Figure A1 shows the photoemission of electrons from a bare metal surface, and the resulting spectrum, used in determining the work function.[1] The photoelectron spectrum is a representation of the energy distribution of electrons that are photoexcited from the substrate. The onset of the photoelectron spectrum, the high kinetic energy region often referred to as the Fermi-edge, corresponds to primary electrons which do not experience any inelastic collisions. Energy loss from collisions or scattering to the primary electrons results in a secondary electron energy distribution that is superimposed onto the primary electrons. As the energy loss of the photoelectrons becomes greater than the energy required to reach the detector of the instrument, a cut off region of the spectrum, known as the secondary electron cut off, forms. In Panel A of Figure A1 the energy associated with the secondary electron cut off region is labeled as E_{vac}^{m}.

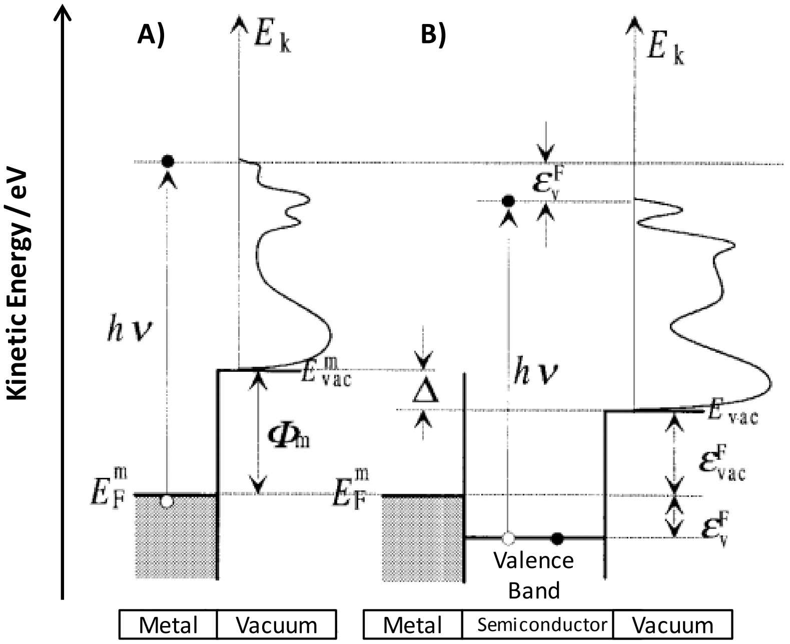

Figure A1. Panel A shows the photoemission of electrons from a metal substrate and Panel B shows the photoemission arising from a semiconductor on the surface of a metal. This figure is an adaptation from reference (1). See text for more details.

The photoelectron spectrum of a semiconductor differs greatly from that of a pure metal; unlike a metal where electrons are photoexcited from the Fermi level, photoelectrons in semiconductors originate from the valence band. Panel B of Figure A1 shows an energy diagram and UPS spectrum associated with a semiconductor on a metal substrate. Here, the primary electrons in the spectrum correspond to binding energies of different occupied electronic states in the semiconductor and secondary electrons have a similar meaning to those for a metal. For thin films, in which the underlying substrate's photoelectrons are observed, the energy of the semiconductor valence band can be reported relative to the Fermi-level of the substrate, ε^{f}_{v}. This is reflected in the photoelectron spectrum as the difference in Fermi-edge of the substrate to the onset of the photoelectrons in the semiconductor.

It is important to note that in these systems the traditional definition of a vacuum level is no longer applicable and instead a local vacuum level is needed to correctly interpret electronic states of the system.[2,3] When a charge or dipole resides on the surface of a metal substrate, an energy shift occurs that is associated with photoemission of an electron into the vacuum. A new term, Δ, is used to describe the energy shift, ε_{vac}^{f}, from the original vacuum level, E_{vac}^{m}, to the local vacuum level that arises, E_{vac}. In Figure A1 Panel A it is assumed that the substrate is pristine and no charges or dipoles exist, however, when a semiconductor is immobilized on the substrate, a dipole moment can form that produces this energy shift, Figure A1 Panel B. The magnitude of Δ is related to the dipole moment density relative to the surface;

$$\Delta = \frac{\mu N \cos\vartheta}{\varepsilon\varepsilon_0} \qquad \textbf{Equation A2}$$

where μ is the effective dipole moment, N is the density of dipoles, ϑ is the angle at which the dipole moment is projected relative to the surface, ε is the dielectric constant of the dipole layer, and ε_0 is the vacuum permittivity.[4] This effect is readily observed experimentally by monitoring the change in work function of a bare metal substrate and a metal substrate in contact with an organic SAM e.g. normalizing the Fermi-edge of the two samples and then taking the difference in the secondary electron cutoffs for the two samples.[4-7] Because the magnitude of Δ can vary by more than ∓2.0 eV it is necessary to account for the change in local vacuum level when reporting the electronic state energies of the semiconductor in units of vacuum energy.[7] A difference of up to 0.3 eV was previously reported for 6.0 nm and 3.6 nm CdSe nanoparticles with the same capping ligand.[3]

For thick films, where the Fermi edge of the substrate is not apparent, the difference in secondary electron cut off energy no longer accurately describes the change in local vacuum level. Because charging of the surface can shift the entire photoelectron spectrum, it is unknown whether the secondary electron cut off is associated with charging or a change in local vacuum level. Instead, only the ionization potential, IP, of the semiconductor can be reported. IP is calculated as shown in Equation A3 as;

$$IP = h\nu - W \qquad \textbf{Equation A3}$$

where W represents the width of the semiconductor's photoelectron spectrum.[3] Here, charging effects may shift the entire spectrum but do not change the magnitude of the ionization potential.

REFERENCES

(1) Ishii, H.; Seki, K.: Energy level alignment at organic/metal interfaces studied by UV photoemission: breakdown of traditional assumption of a common vacuum level at the interface. *IEEE Transactions on Electron Devices* **1997**, 44, 1295-1301.

(2) Cahen, D.; Kahn, A.: Electron Energetics at Surfaces and Interfaces: Concepts and Experiments. *Adv. Mater.* **2003**, 15, 271-277.

(3) Munro, A. M.; Zacher, B.; Graham, A.; Armstrong, N. R.: Photoemission Spectroscopy of Tethered CdSe Nanocrystals: Shifts in Ionization Potential and Local Vacuum Level As a Function of Nanocrystal Capping Ligand. *ACS Appl. Mater. & Inter.* **2010**, 2, 863-869.

(4) Ray, S. G.; Cohen, H.; Naaman, R.; Liu, H.; Waldeck, D. H.: Organization-Induced Charge Redistribution in Self-Assembled Organic Monolayers on Gold. *J.Phys.Chem.B* **2005**, 109, 14064-14073.

(5) Alloway, D. M.; Hofmann, M.; Smith, D. L.; Gruhn, N. E.; Graham, A. L.; Colorado, R.; Wysocki, V. H.; Lee, T. R.; Lee, P. A.; Armstrong, N. R.: Interface Dipoles Arising from Self-Assembled Monolayers on Gold: UV−Photoemission Studies of Alkanethiols and Partially Fluorinated Alkanethiols. *J. Phys. Chem. B.* **2003**, 107, 11690-11699.

(6) Zehner, R. W.; Parsons, B. F.; Hsung, R. P.; Sita, L. R.: Tuning the Work Function of Gold with Self-Assembled Monolayers Derived from X−[C6H4−C⁝C−]nC6H4−SH (n = 0, 1, 2; X = H, F, CH3, CF3, and OCH3). *Langmuir* **1999**, 15, 1121-1127.

(7) Alloway, D. M.; Graham, A. L.; Yang, X.; Mudalige, A.; Colorado, R.; Wysocki, V. H.; Pemberton, J. E.; Randall Lee, T.; Wysocki, R. J.; Armstrong, N. R.: Tuning the Effective Work Function of Gold and Silver Using ω-Functionalized Alkanethiols: Varying Surface Composition through Dilution and Choice of Terminal Groups. *J. Phys. Chem. C.* **2009**, 113, 20328-20334.

APPENDIX B

SUPPORTING INFORMATION FOR CHAPTER 2

In order to confirm that the exciton confinement of the NPs was not changing as a function of capping ligand, and therefore influencing the sizes that were extracted through the empirical model,[1] TEM data were compared with absorbance data for each NP/capping ligand combination. Figure B1 shows TEM images of An-CdSe, PPA-CdSe, and TP-CdSe, and Table B1 reports the TEM determined sizes and compares them to the sizes found from the UV-visible spectra.

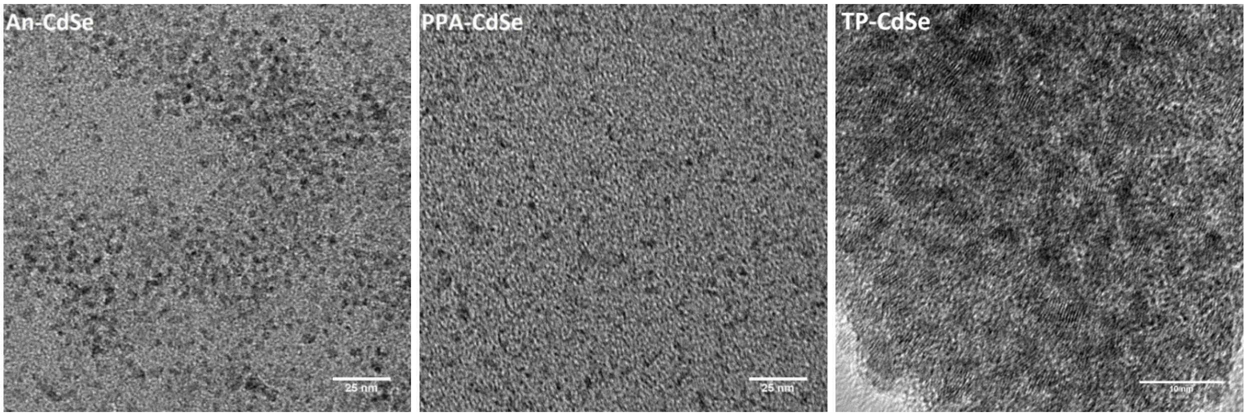

Figure B1. The figure shows TEM images of An-CdSe PPA-CdSe and TP-CdSe NPs.

Table B1. TEM derived sizes and sizes from the use of UV-Visible spectra and an empirical model are reported for An-CdSe, PPA-CdSe, and TP-CdSe.

	Absorption determined size	TEM determined size
An-CdSe	2.7 nm	3.11 +/- 0.55 nm
PPA-CdSe	2.9 nm	2.86 +/- 0.37 nm
TP-CdSe	3.4 nm	3.67 +/- 0.65 nm

Further validation of ligand exchange was pursued using pulsed field gradient (PFG) NMR spectroscopy on a Bruker Avance III 500MHz spectrometer with a Bruker 500 MHz BBFO probe (5.0 G/cmA). Spectra were collected using a delay time of 0.2 ms, diffusion time of 50.0 ms, and a gradient strength of 65% with a 4.0 ms duration and sinusoidal shaped pulse. Other parameters were chosen based on standard operating procedures. PFG-NMR was performed using similar sample concentrations and the intensities were O.D. corrected. Under these conditions, signal arising from freely diffusing ligands are attenuated. Unfortunately, direct measurement of aniline and thiophenol resonances under these conditions is not possible because of the limited mobility of the ligands, in tandem with the gradient, leading to broadening of the peak below the S/N. However, monitoring the CH_2 resonance of ODPA enables the determination of the amount of ligand displaced during the ligand exchange processes. Figure B2 shows these results. Integration of the CH_2 peak at approximately 1.2 ppm indicates that 86% of ODPA is exchanged in the case of An-CdSe and 99% in the case of TP-CdSe. Pyridine and MPA peaks were not observed for An-CdSe and TP-CdSe respectively, indicating complete exchange.

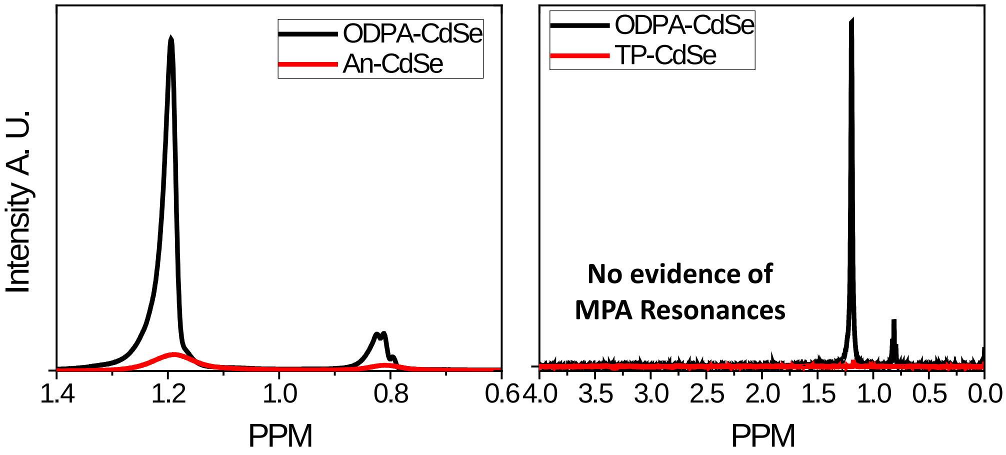

Figure B2. Pulsed Field Gradient NMR of ODPA-CdSe (black) and ligand exchanged CdSe to aniline (red, left) or thiophenol (red, right).

Figure B3 shows the effect that of excess thiophenol on the DPV peaks of a 2.38 nm TP-CdSe solution (the current was normalized to peak A2, the oxidation of the nanoparticle). Upon increasing the concentration of thiophenol by 1μM, a corresponding increase in the current of A3 ensues. The decrease in current of peak A1 may arise from better passivation of the NPs with an increase in thiophenol concentration.

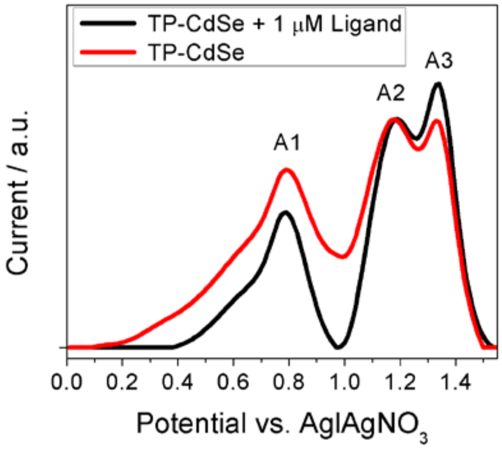

Figure B3. DPVs are shown for a 2.38 nm TP-CdSe solution and the same solution with an increase in the concentration of TP by 1μM. The increase in current of peak A3 with concentration implies that it arises from the thiophenol rather than the CdSe NPs.

In order to confirm which anodic peak arose from the oxidation of CdSe and not electropolymerization of aniline, studies comparing the voltammograms of 4-methylaniline-CdSe to An-CdSe were performed. The methylation of aniline in the para position prevents the electropolymerization process and therefore can resolve this issue. Figure B4 shows voltammograms for a solution of 2.4 nm CdSe NPs with the two different capping ligands. The position of C2 for the two systems is at the same potential and therefore confirms that it arises from the oxidation of the NP and not electropolymerization. Slight differences found in C1 most likely arise from the methyl group.

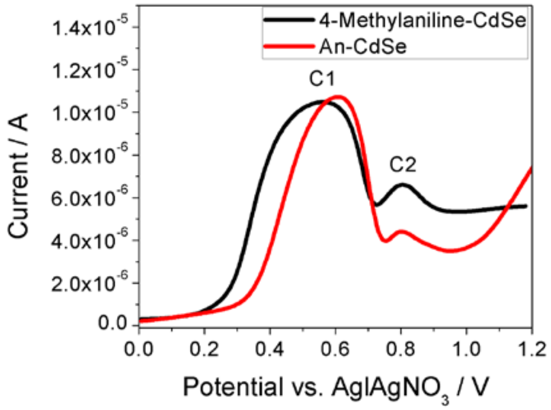

Figure B4. DPVs are shown for solutions of 4-methylaniline-CdSe (black) and An-CdSe (red). The similar position of C2 in both voltammograms shows that it is not based in a process involving electrochemical polymerization of aniline

Table B2. Displays the data points used in Figure 2-5.

PPA-CdSe			TP-CdSe			An-CdSe		
Size /nm	VBM /eV	CBM /eV	Size /nm	VBM /eV	CBM /eV	Size /nm	VBM /eV	CBM /eV
2.14	-5.555	-2.955	2.21	-5.396	-2.836	2.21	-5.273	-2.713
2.22	-5.496	-2.946	2.38	-5.407	-2.944	2.38	-5.237	-2.774
2.53	-5.525	-3.128	2.55	-5.397	-3.005	2.39	-5.231	-2.773
2.61	-5.497	-3.128	2.56	-5.365	-2.977	2.46	-5.232	-2.802
2.63	-5.524	-3.159	2.67	-5.379	-3.028	2.53	-5.228	-2.831
2.68	-5.504	-3.157	3.85	-5.365	-3.228	2.56	-5.250	-2.862
2.71	-5.495	-3.157	3.85	-5.384	-3.247	2.65	-5.252	-2.892
2.94	-5.465	-3.187				2.77	-5.241	-2.920
2.96	-5.483	-3.209				3.46	-5.212	-3.026
3.10	-5.425	-3.180						
3.33	-5.435	-3.230						

Values for the VBM were calculated by taking the onset potential of the oxidation peak of the NP and referencing it to the ferrocene / ferrocenium formal potential. This value was then converted to the vacuum energy scale through the conversion factor 4.8 eV. Error for the VBM measurements never exceeded 20 meV and in the majority of circumstances did not exceed 10 meV.

Previous studies on TOPO capped CdSe[2-4] found that the binding geometry to the surface of the NPs can be a combination of phosphonate and pyrophosphonate. To ensure that their variations do not have a large effect on the simulations, the HOMO and LUMOs of the smallest CdSe clusters were calculated to evaluate their effect (see Figure B5). The change in energy for the HOMO is minimal (0.25 eV) however the LUMO changes by almost 0.5 eV. The larger shift in the LUMO most likely arises from the anionic ligands donating electron density to the Cd^{2+} orbitals leading to greater stabilization

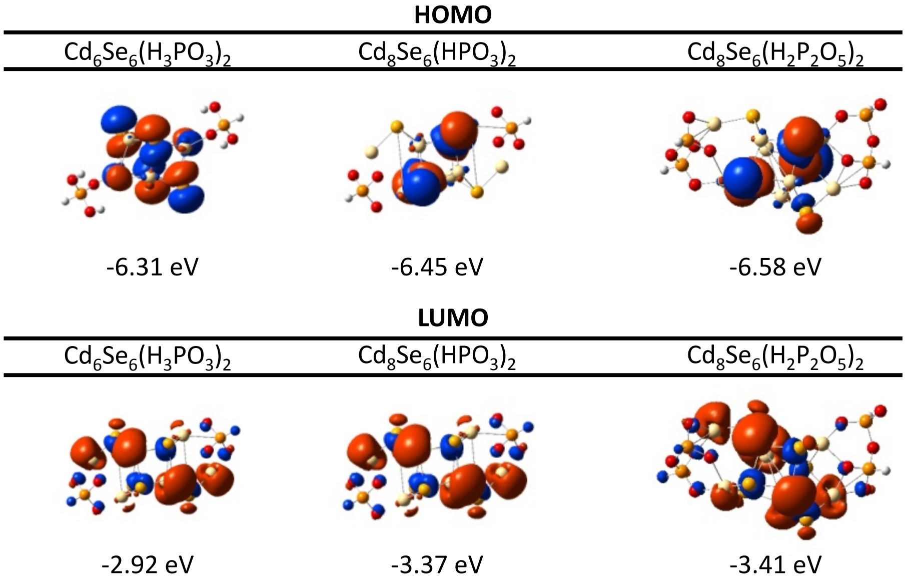

Figure B5. HOMO (top row) and LUMO (bottom row) of phosphonate, anionic phosphonate, and anionic pyrophosphonate capped CdSe NPs. Note, excess Cd^{2+} was included to clusters with anionic ligands to neutralize the net charge.

It was found that the thiophenol ligands insert into the bridge site of the Cd-Se bond causing a slight deformation in the NP crystal structure. This deformation leads to a stabilization of the HOMO and LUMO energies of the NP (β states), however the additional non-bonding 3p orbitals of the S atom (α states) lie in the NP's bandgap. As a result the HOMO and LUMO are localized on the α states. Figure B6 shows the energy alignment of the α and β states of a $Cd_6Se_6TP_4$ nanocluster. As a result, the HOMO and the LUMO orbitals are localized on the sulfurs' 3p orbitals (see Figure B6) and would have energies independent of the density of ligands. These findings are consistent with that reported earlier by Kuznetsov et al. on Cd6Se6-(SCH3)6 nanoclusters,[5] and it implies that the thiol will act as a recombination center for the photoexcited electron hole pair in CdSe, something which has been demonstrated in various experimental studies.[6-8]

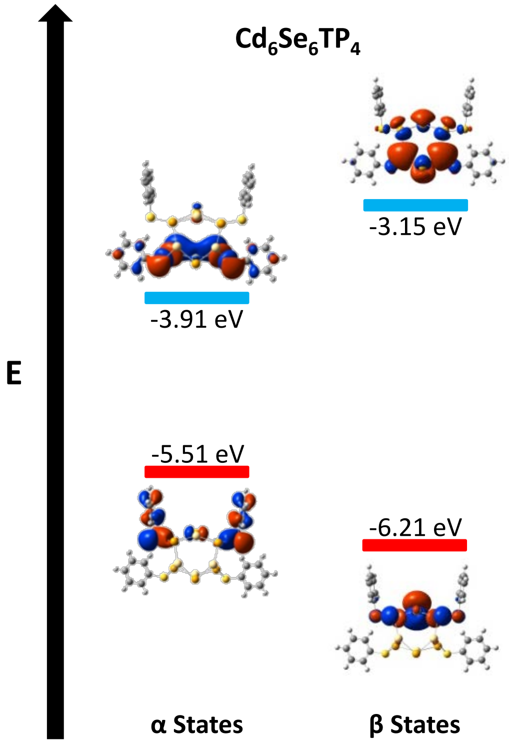

Figure B6. Displays the different electronic energies of $Cd_6Se_6TP_4$ nanoclusters. The α states correspond to the TP's 3p orbitals and act as the HOMO and LUMO of the cluster. The β states correspond to the HOMO and LUMO energy coming from the NP are destabilized in comparison to an uncapped NP.

REFERENCES

(1) Yu, W. W.; Qu, L.; Guo, W.; Peng, X. Experimental Determination of the Extinction Coefficient of CdTe, CdSe, and CdS Nanocrystals. *Chem. Mater*. **2003**, *15*, 2854.

(2) Liu, H.; Owen, J. S.; Alivisatos, A. P. Mechanistic Study of Precursor Evolution in Colloidal Group II−VI Semiconductor Nanocrystal Synthesis. *J. Am. Chem. Soc*. **2006**, *129*, 305.

(3) Owen, J. S.; Park, J.; Trudeau, P.-E.; Alivisatos, A. P. Reaction Chemistry and Ligand Exchange at Cadmium−Selenide Nanocrystal Surfaces. *J. Am. Chem. Soc*. **2008**, *130*, 12279.

(4) Kopping, J. T.; Patten, T. E. Identification of Acidic Phosphorus-Containing Ligands Involved in the Surface Chemistry of CdSe Nanoparticles Prepared in Tri-N-Octylphosphine Oxide Solvents. *J. Am. Chem. Soc.* **2008**, *130*, 5689.

(5) Kuznetsov, A. E.; Balamurugan, D.; Skourtis, S. S.; Beratan, D. N. Structural and Electronic Properties of Bare and Capped Cd_NSe_N/Cd_NTe_N nanoparticles (N= 6, 9). *J. Phys. Chem. C* **2012**, *116*, 6817.

(6) Wuister, S. F.; de Mello Donegá, C.; Meijerink, A. Influence of Thiol Capping on the Exciton Luminescence and Decay Kinetics of CdTe and CdSe Quantum Dots. *J. Phys. Chem. B* **2004**, *108*, 17393.

(7) Sarkar, S.; Patra, B. K.; Guria, A. K.; Pradhan, N. The Redox Chemistry at the Interface for Retrieving and Brightening the Emission of Doped Semiconductor Nanocrystals. *J. Phys. Chem. Lett.* **2013**, *4*, 2084.

(8) Aldana, J.; Wang, Y. A.; Peng, X. Photochemical Instability of CdSe Nanocrystals Coated by Hydrophilic Thiols. *J. Am. Chem. Soc.* **2001**, *123*, 8844.

APPENDIX C

SUPPORTING INFORMATION FOR CHAPTER 3

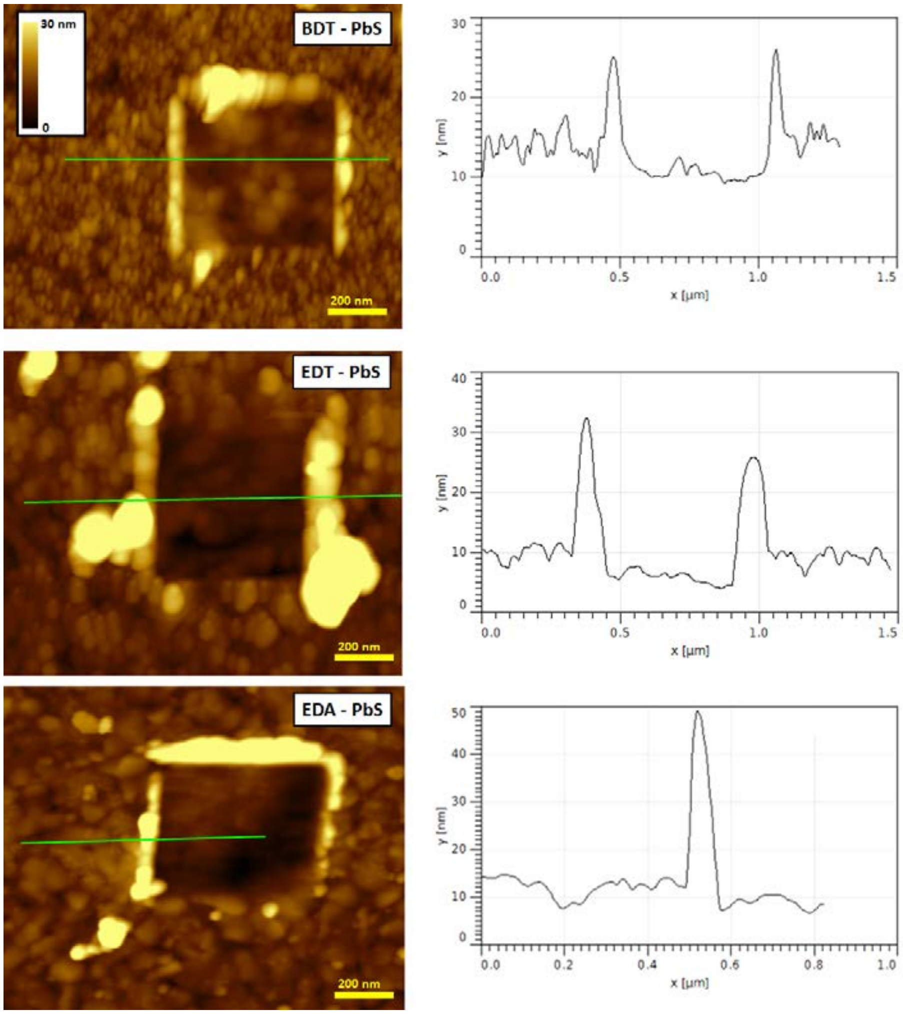

Figure C1. Shows representative AFM images of BDT, EDT, and EDA cross-linked 3.0 nm PbS and their respective thickness profiles. BDT, EDT and EDA had an average thickness of 4.0 nm, 3.9 nm, and 4.24 nm respectively.

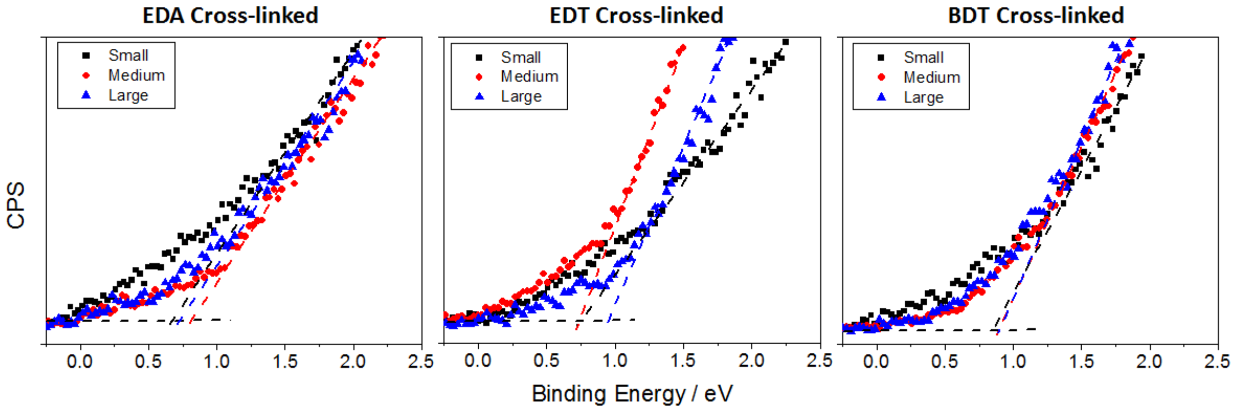

Figure C2. Shows representative UPS spectra for 2.5 nm (black), 3.0 nm (red), and 3.4 nm (blue) PbS QDs cross-linked with EDA (left), EDT (middle), and BDT ligands. The onset energy derived from these spectra, along with those determined from three additional sets of spectra for each ligand and size, were averaged to form the data points in Figure3-1.

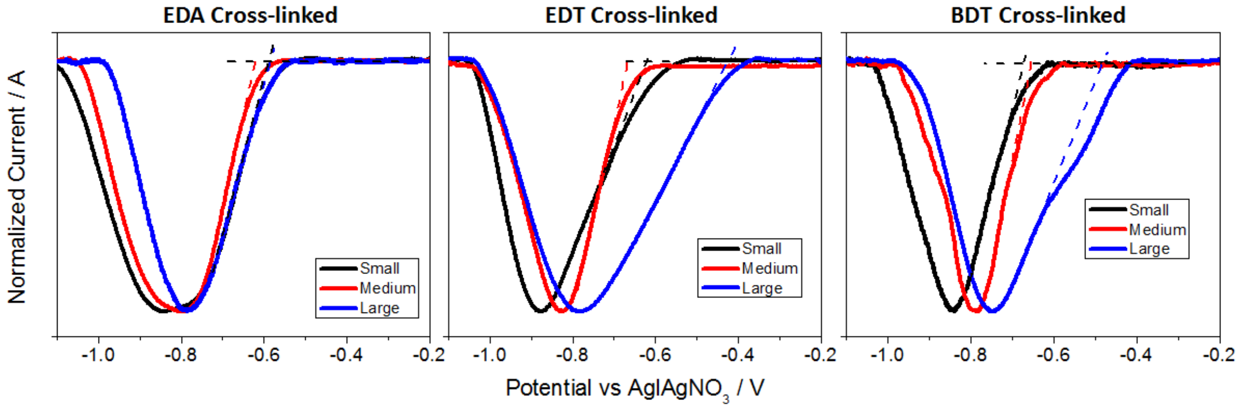

Figure C0-3. Shows representative background subtracted voltammograms for 2.5 nm (black), 3.0 nm (red), and 3.4 nm (blue) PbS QDs cross-linked with EDA (left), EDT (middle), and BDT ligands. The onset energy derived from these voltammograms, along with those determined from three additional sets of spectra for each ligand and size, were averaged to form the data points in Figure 3-3.

Table C1. Average electronic state energies in electron volts of the 2.5, 3.0, and 3.4 nm PbS QDs cross-linked with EDA, EDT, and BDT ligands. The CBMs were determined experimentally in the electrochemistry studies and the optical bandgap and exciton binding energy were used to calculate the VBMs. The VBMs were determined experimentally in the UPS studies and the optical band gap and exciton binding energy were used to calculate the CBMs. These values correspond to the data points in Figure 3-3.

Electronic States of PbS NPs of with Different Sizes and Ligands on Au						
Electrochemistry Data						
	EDA VBM	EDA CBM	EDT VBM	EDT CBM	BDT VBM	BDT CBM
2.5 nm	5.51	3.95	5.45	3.89	5.51	3.97
3.0 nm	5.23	3.92	5.31	4.00	5.28	3.97
3.4 nm	5.30	4.09	5.37	4.16	5.35	4.14
Ultraviolet Photoelectron Spectroscopy Data						
	EDA VBM	EDA CBM	EDT VBM	EDT CBM	BDT VBM	BDT CBM
2.5 nm	5.48	3.93	5.50	3.95	5.65	4.10
3.0 nm	5.67	4.36	5.57	4.26	5.70	4.39
3.4 nm	5.55	4.34	5.69	4.48	5.70	4.49

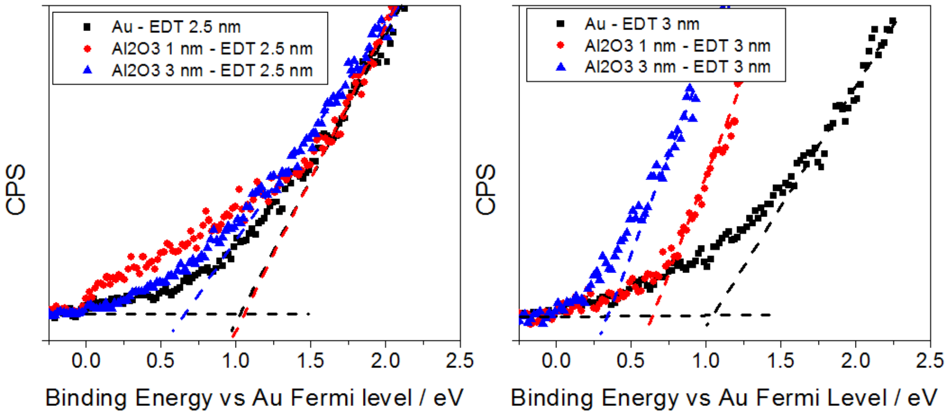

Figure C4. Shows the UPS spectra used for determining the VBM of EDT cross-linked 2.5 nm (left) and 3.0 nm (right) PbS QDs deposited on Au (black), 1.0 nm alumina (red), and 3.0 nm of alumina (blue). The shift in the onset energy as a function of alumina thickness is plotted in Figure 3-4.

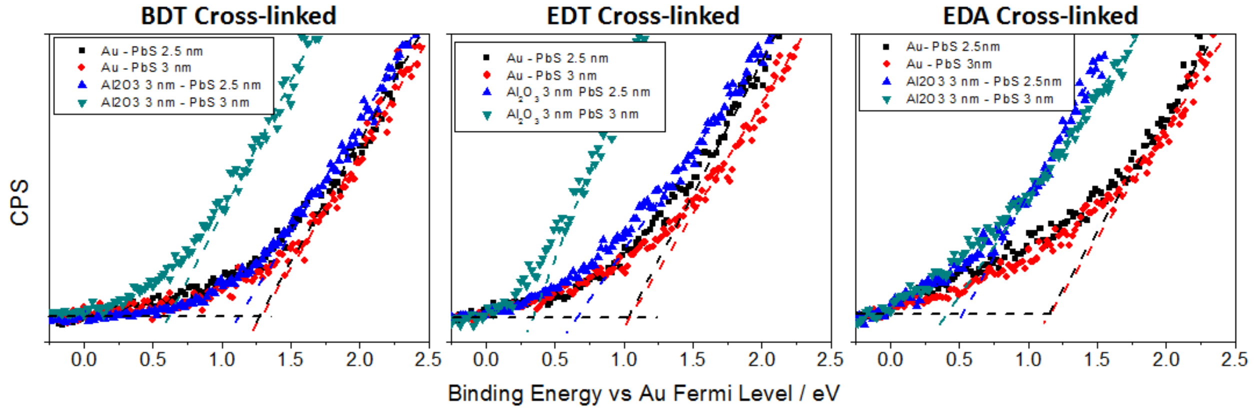

Figure C5. Shows UPS spectra of 2.5 nm (black) and 3.0 nm (red) PbS on Au substrates and 2.5 nm PbS (blue) and 3.0 nm PbS (teal) on 3.0 nm thick alumina substrates. The cross-linkers used in the experiments were BDT (left), EDT (middle), and EDA (right). These data correspond to the data points of Figure 3-5.

Table C2. Average electronic state energies in electron volts of 2.5 and 3.0 nm PbS QDs cross-linked with EDA, EDT, and BDT ligands reported against the Fermi edge of Au. The VBM were determined by UPS and the CBM was found by adding the optical band gap and the exciton binding energy. These values correspond to the data points in Figure 3-5

Comparison of Electronic States of PbS on Au and Alumina						
Measured on Gold						
	EDA VBM	EDA CBM	EDT VBM	EDT CBM	BDT VBM	BDT CBM
2.5 nm	1.21	-0.46	1.01	-0.657	1.21	-0.43
3.0 nm	1.20	-0.21	1.02	-0.387	1.27	-0.14
Measured on 3.0 nm of Alumina						
	EDA VBM	EDA CBM	EDT VBM	EDT CBM	BDT VBM	BDT CBM
2.5 nm	0.52	-1.15	0.63	-1.04	1.1	-0.57
3.0 nm	0.42	-0.99	0.32	-1.09	0.55	-0.86

APPENDIX D

SUPPORTING INFORMATION FOR CHAPTER 4

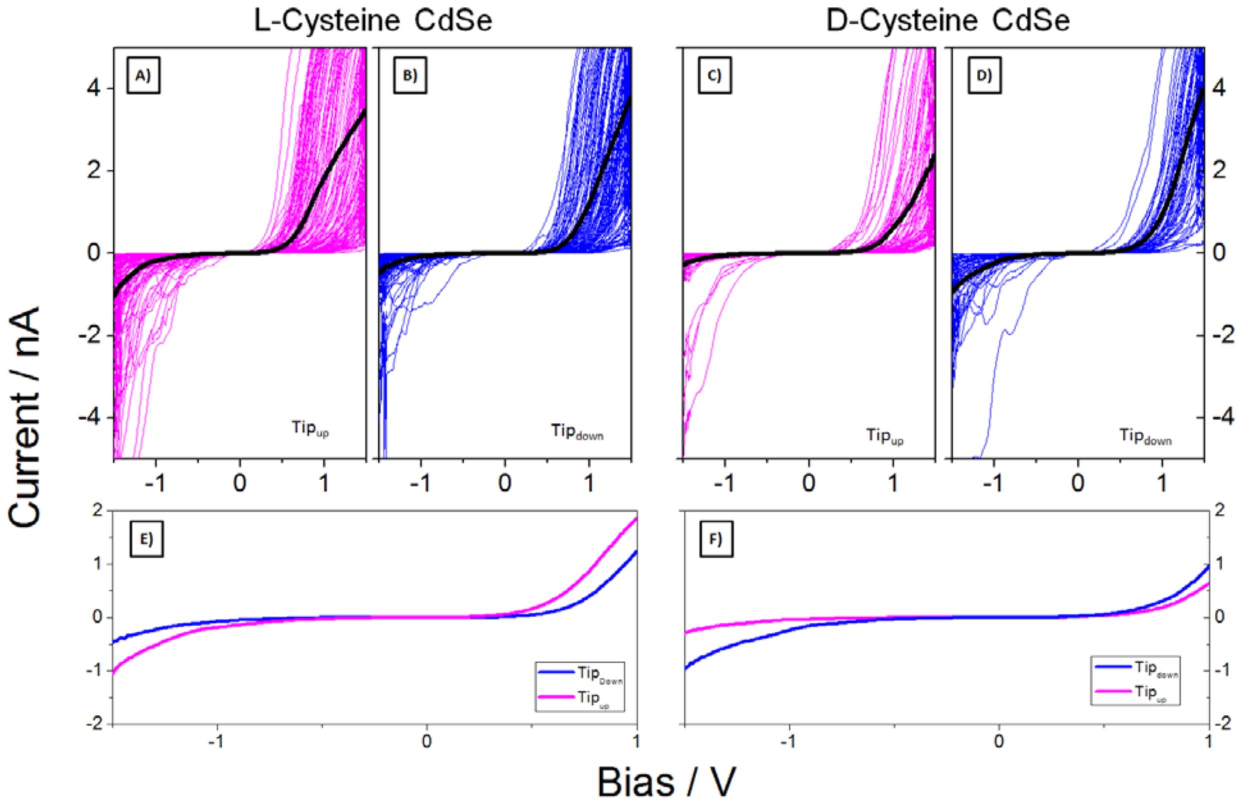

Figure D1. mCP-AFM studies of 2.2 nm L-cysteine (A, B, E) and D-cysteine (C, D, F) passivated CdSe QD films that are drop cast on HOPG substrates. The tip was magnetized in the up (magenta) and down (blue) direction and over 100 current-voltage curves were collected for each sample. The black line in (A-D) represents the average of all measurements for this data set. The effect of magnetization and chirality on the I-V curves are shown in E and F. For L-cysteine CdSe (D-cysteine CdSe) a higher current was observed when the tip was magnetized in the up (down) direction.

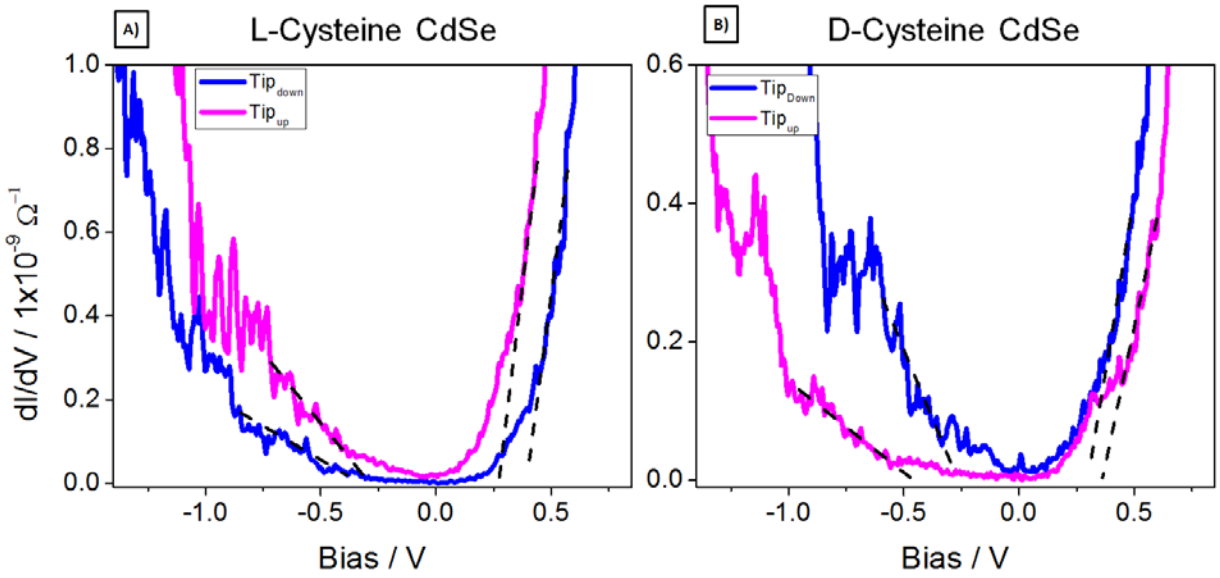

Figure D2. The dI/dV plots of the average mCP-AFM measurements for 2.2 nm L- cysteine (A) and D-cysteine (B) passivated CdSe quantum dots. The black dashed lines correspond to the onset energy values for the two different electronic states; the conduction band at a positive bias and surface state defects at a negative bias.

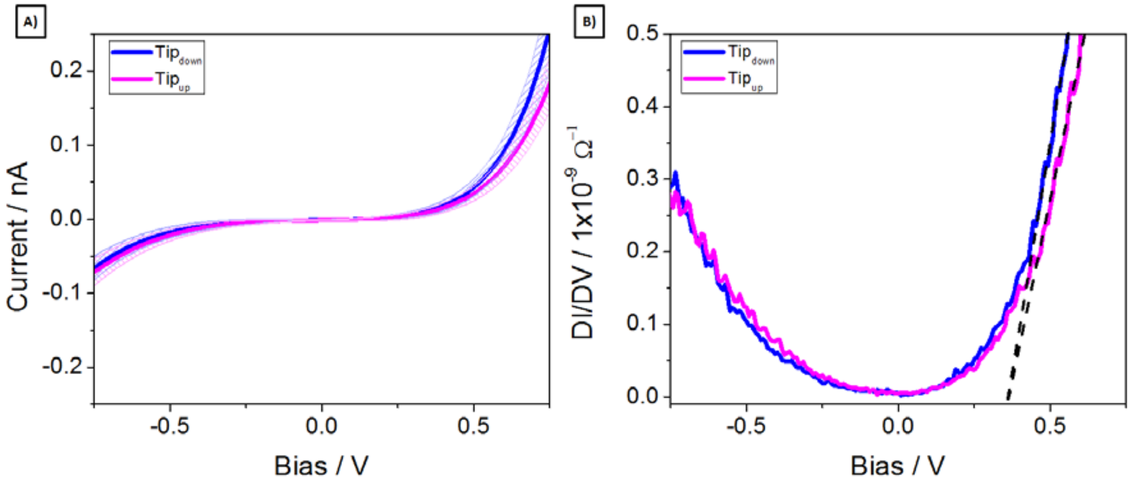

Figure D3. The current-voltage (A) and dI/dV (B) plots for 6.0 nm L-cysteine capped quantum dots drop cast on HOPG substrates. The black lines in panel B correspond to the onset region of the conduction band of the quantum dots. For this size of quantum dots very little difference in the conduction and density of states is observed when the tip is magnetized in the down (blue) and up (magenta) orientations. These data should be contrasted with Figures 2 and 3 for the 2.2 nm quantum dots.

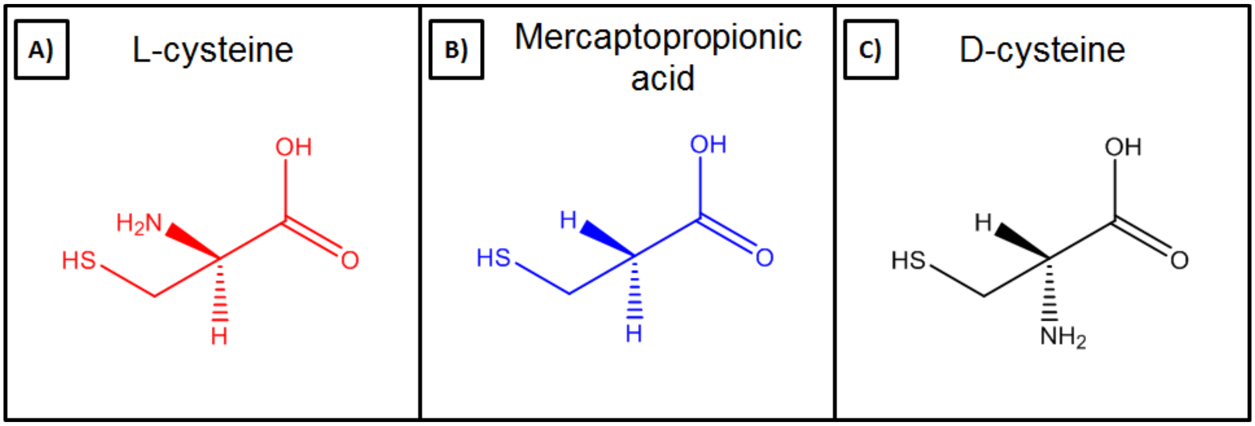

Figure D4. The molecular structures of the 3 ligands used in the magnetoresistance measurements; A) L-cysteine, B) 3-mercaptopropionic acid, and C) D-cysteine

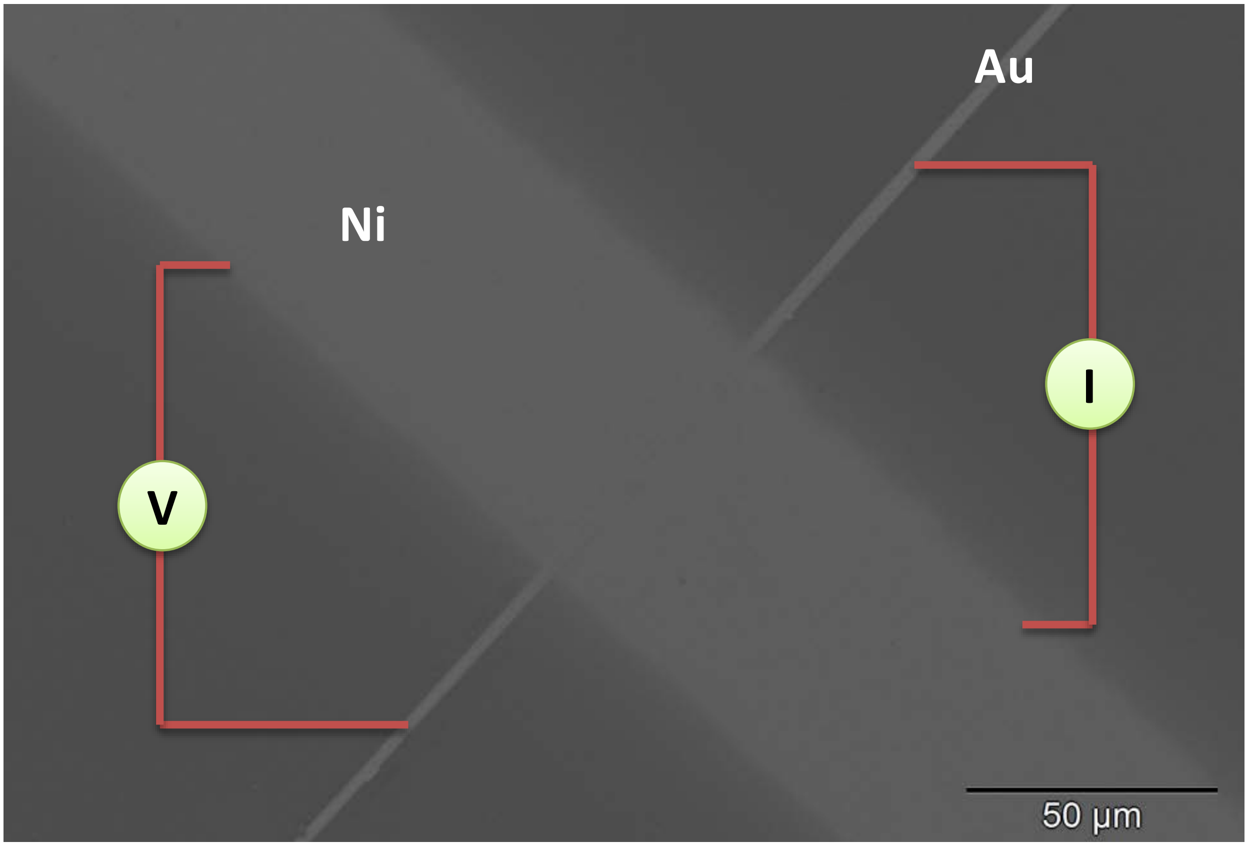

Figure D5. SEM image of the top view of the magnetoresistance device.

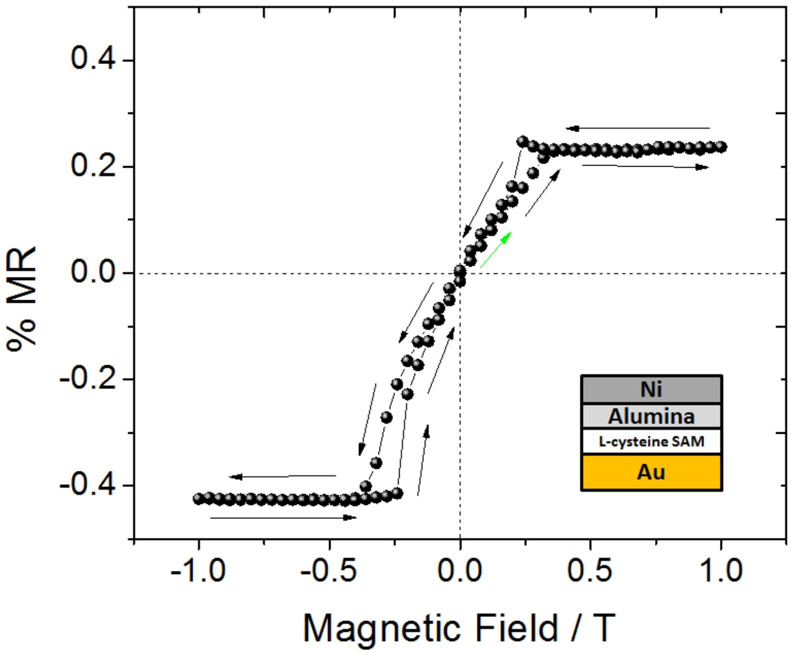

Figure D6. The magnetoresistance (MR) measured with a device which includes a L-cysteine SAM at 20 K. It is important to note that the orientation of the asymmetric response is opposite to that of the devices made with L-cysteine coated CdSe Nanoparticles.

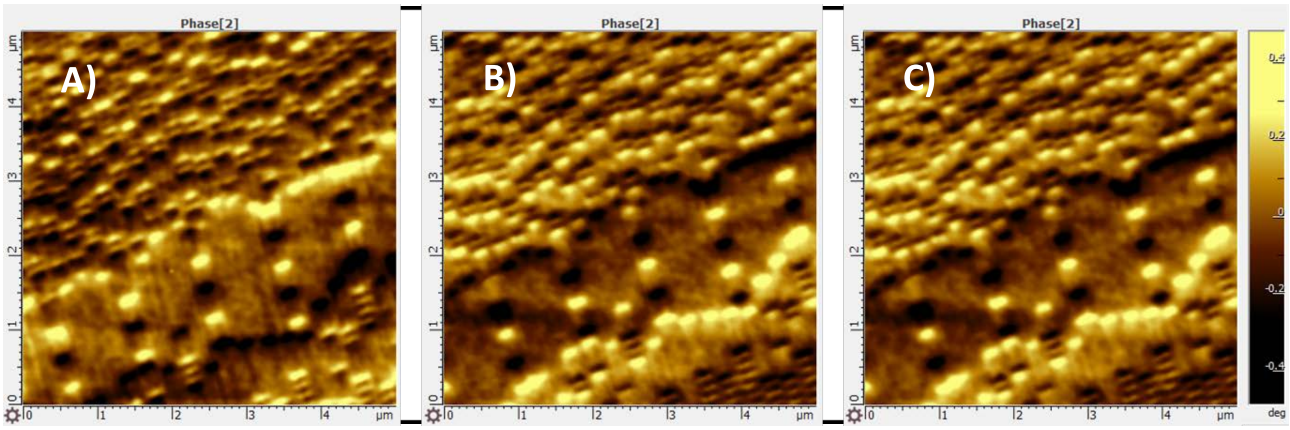

Figure D7. Shows MFM images recorded using a Co-Cr tip magnetized in (A) DOWN, (B) UP and (C) UP after 2 hours. The domains in (A) and (B) are opposite to each other, confirming the reversal of magnetic polarity of the tip between DOWN and UP orientations. The fidelity of the two MFM images (middle & right) shows that the tip does not undergo oxidation or demagnetization over the course of the 2 hours.

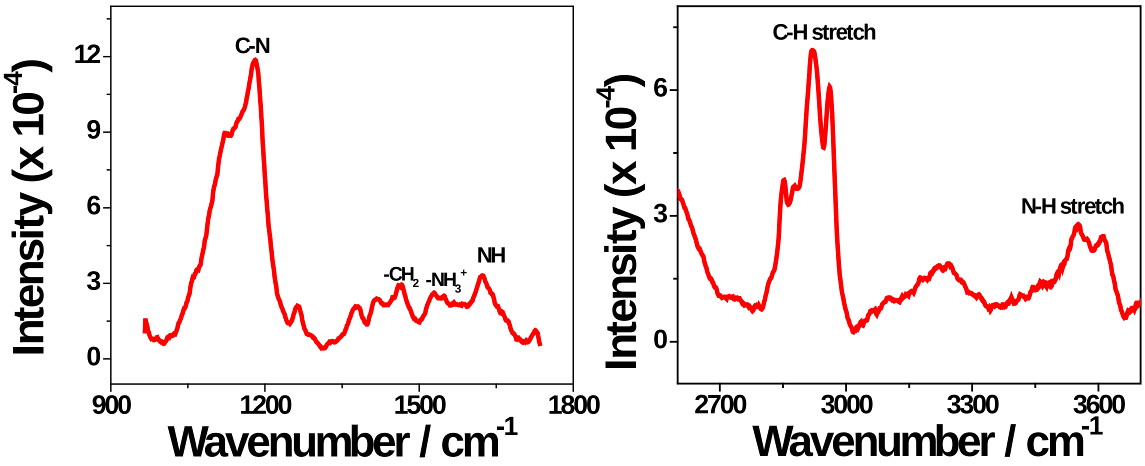

Figure D8. PMIRRAS of 2-aminoethanethiol monolayers adsorbed on Au recorded in two different regions.

Adsorption of the self-assembled monolayer (cysteamine) used in the MR devices were confirmed using PMIRRAS spectra figureS7. The spectra's peaks are labeled C-N, N-H and C-H corresponding to the different stretches of the cysteamine monolayer. The peaks located at 1175 cm^{-1} and 1625 cm^{-1} correspond to the C-N stretch and the deformation asymmetric vibration (-NH) of primary ammonium functions respectively. The peaks located around 3400-3600 cm^{-1} represents N-H stretching modes of the amine group. Also, the vibrations corresponding to C-H modes are also seen in the spectra around 2800-3000 cm^{-1}.

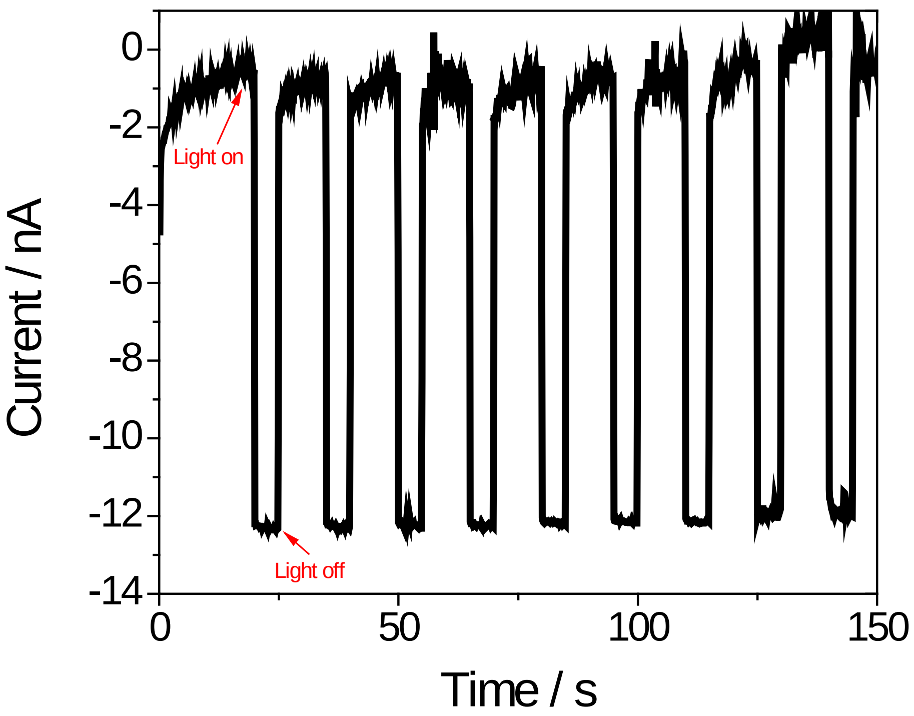

Figure D9. Shows photocurrent measurements made on L-cys CdSe QDs electrostatically attached to an Au electrode – 8-mercaptooctylamine SAM. The counter electrode was a platinum mesh and the auxiliary electrode was Ag/AgCl (CHInstruments). The supporting electrolyte was a 0.1 M NaS solution and measurements were performed under a 0V bias potential.

APPENDIX E

SUPPORTING INFORMATION FOR CHAPTER 5

E1. Assembly Formation

The formation of nanoparticle assemblies on a 500 nm diameter SiO_2 sphere has been confirmed by fluorescence, zeta potential, and scanning electron microscopy measurements. Figure E1A indicates the first fabrication step. An amine coated SiO_2 microsphere, approximately 500 nm in diameter, was the template for this assembly. Using sonication, 30 mg of the SiO_2 microspheres were dispersed in 2 mL of water. Thioglycolic acid passivated cadmium telluride, TGA-CdTe, was added in excess to the solution and the charged microsphere and nanoparticle in water were left to shake for one hour. After one hour, the assembly was purified using a stirred ultrafiltration cell. A cellulose nitrate membrane filter (Whatman), 100 nm pore size, was used in the ultrafiltration cell. Therefore, the “free” TGA-CdTe nanoparticles (4.1 nm) should go through the filter, but the SiO_2 microbead and anything attached to it, would not go through the filter. The pressure used in the filtration was 50 psi and filtrate samples were collected. After filtration, the solid on the filter paper was resuspended in 4 mL of water. An additional 2-3 filtrations were performed on this sample and the assembly was resuspended in 3 mL of water.

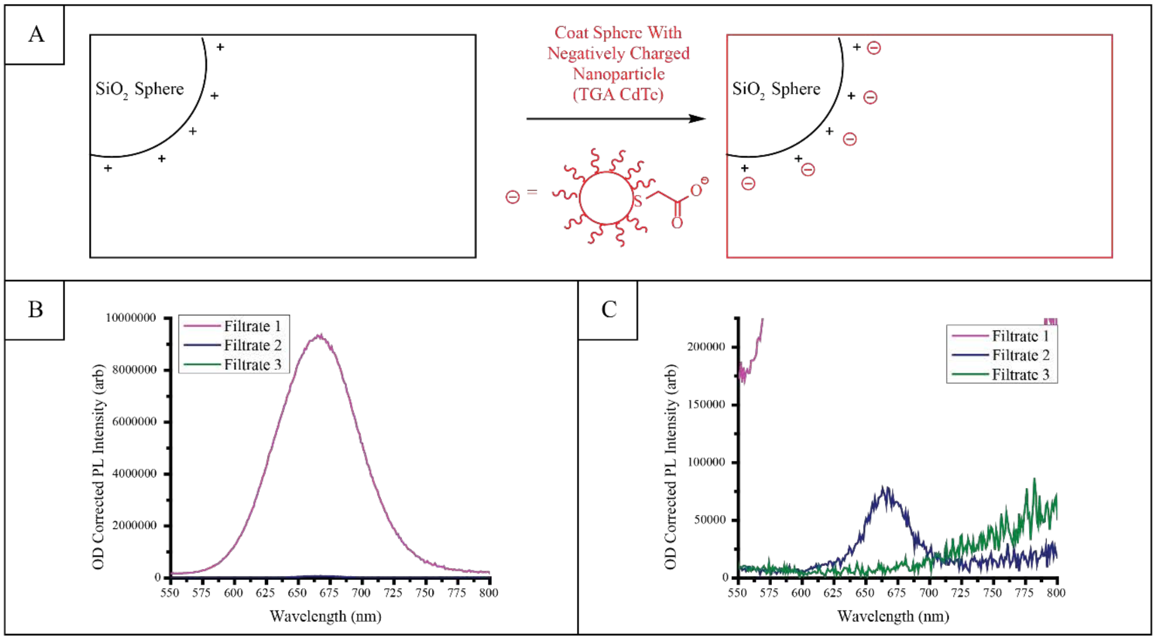

Figure E1. Cartoon describing the experimental procedure used for attaching a TGA-CdTe to SiO_2 template (A). Steady state fluorescence spectra of collected filtrates Ex: 440 nm, 0.7 x 0.7 nm slits, 0.1 s integration time (B) and 1B after zooming in on the data from Filter 2 and Filter 3 (C).

A positively charged SiO_2 template was placed in the presence of a negatively charged TGA-CdTe nanoparticle in water; the TGA-CdTe was electrostatically attached to the surface of the template. Figures E1B and C show photoluminescence spectra depicting the emission intensity of the nanoparticle in the filtrate after successive filtrations. Because the assembly was resuspended in the same volume of water before each filtration, the photoluminescence intensity should be related to the concentration of free nanoparticles that are removed from the assembly solution. After each filtration the nanoparticle emission found in the filtrate decreases in intensity indicating that fewer nanoparticles are removed from solution (Figure E1B). In fact, after the second filtration there is no nanoparticle emission peak that is discernible from the noise (Figure E1C). For all of the experiments reported in this work at least two filtrations were performed to ensure that the fluorescence from the 1NPA came from nanoparticles attached to the surface of the microsphere rather than any residual free unbound nanoparticles.

The assembly of nanoparticles on the microsphere could also be monitored by zeta potential measurements after each filtration step. Initially, the microspheres are positively charged in water and the TGA-CdTe is negatively charged; however, after the microsphere is coated with the negatively charged nanoparticle it becomes negatively charged as well. Note that the charged surface prevents aggregation of these particles.

Table E1. Zeta potential measurements for microsphere, TGA CdTe, and nanoparticle assembly in water.

Sample	**Zeta Potential (mV)**
Microsphere (MS)	41.91 ± 0.60
Free Nanoparticle	-42.95 ± 4.13
1NPA	-19.66 ± 2.49

The surface of the acceptor nanoparticle (blue circle) can be covalently bonded to the donor nanoparticle (green circle) using an EDC and sulfo-NHS reaction. MS-Acceptor nanoparticle, EDC, and sulfo-NHS were added to a 100 mM PBS buffer solution in a 1:1000:2500 ratio, respectively.[1] The solution was stirred for 15 minutes, then donor nanoparticle (in a 1 donor:1.33 acceptor ratio) was added to the solution, and the solution was stirred overnight. The sample was cooled to 4 ^{o}C to quench the excess EDC and then purified using the same methodology as described for the assembly of the first nanoparticle. Figure E2 depicts the two nanoparticle assembly (MS-Acceptor Nanopartice-Donor Nanoparticle).

Figure E2. Cartoon describing the experimental procedure for attaching a second nanoparticle covalently to first nanoparticle on the SiO_2 microsphere template.

Formation of the nanoparticle assemblies on the surface of the microbeads template was further monitored with Scanning Transmission Electron Microscopy (STEM). Figure E3 shows several examples of original micrographs of the 1 NPA (Figure E3A, top row) and 2 NPA (Figure E3B, top row), together with the images processed with a FFT bandpass filter using ImageJ software (bottom rows in Figure E3A and B).[2] Image processing suppressed heavy contrast between the microbeads and the carbon support background, thus enhancing the contrast associated with the nanoparticles themselves (dark spots in the images). The average diameter of the particles visible in the images c.a. 5 nm is close to the average size of the particles used to form the nanoparticles assembly i.e. 4.0 nm and 5.5 nm for the first and second nanoparticle layer, respectively.

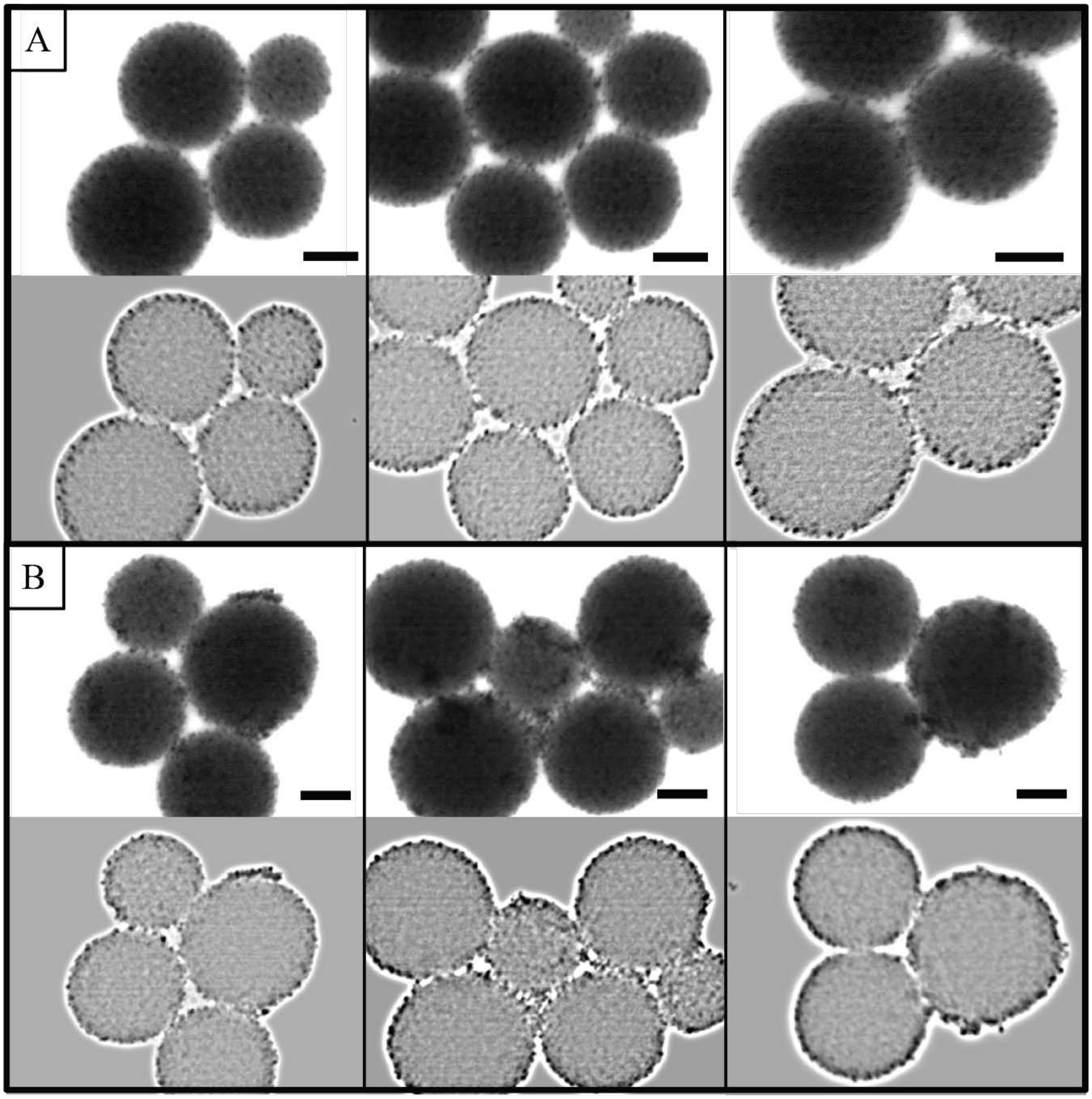

Figure E3. Panels A and B show examples of STEM micrographs of 1NPA and 2NPA samples, respectively (top rows) together with data digitally processed with FFT bandpass filter (bottom rows). Images obtained for 1NPA and 2NPA are shown in A and B, respectively. Scale bars in all micrographs represent 50 nm. Note that the diameter of the silica spheres template and the size of the nanoparticles differs significantly from the parameters used in electron transfer studies. See main text for details.

Figure E4 shows more detailed analysis of the dimensions of the nanoparticles and nanoparticle clusters in the assemblies. In 1 NPA the nanoparticles are typically separated from each other by several nanometers on the surface of individual template beads, nevertheless in some cases they are perceived in the image processing as the nanoparticle clusters due to the curvature of the bead template (separated along the electron beam axis but in the projection plane) or because of the close proximity of the particles assembled on different beads that aggregated when drop casted on the substrate. The left image in Figure E4A shows the size distribution of the nanoparticles (expressed as area) combined from the STEM data presented in Figure E3 and Figure 5-3 of the main text. The majority of particle areas vary over a broad range, which indicates that the above circumstances clearly play a role in the particle size analysis. As a result the mean particle size value of 19.0 nm^2 calculated from the distribution is somewhat higher than that deduced from the average size of the particles used for 1NPA i.e. 12.6 nm^2. The right panel in Figure E4 Panel A shows an analgous size distribution for the 2NPA. The average size of the particles of 28.4 nm^2 is about fifty percent larger than that calculated for 1NPA. The larger size of the particle are as expected because of (i) larger size of the nanoparticles used to form second layer c.a. 19.6 nm^2, and (ii) the 2NPA should contain by design nanoparticle dyads of total area of 32.5 nm^2 (12.6 nm^2 + 19.6 nm^2). Both distributions in Figure E4 Panel A are affected by the presence of individual nanoparticles and nanoparticle clusters i.e. the distribution for 1NPA shows higher than expected average size values due to the ‘presence’ of the nanoparticle clusters, and distribution for 2NPA is affected by large number of individual nanoparticles, which did not form the nanoparticle dyads. In order to bias the particle analysis towards the dyads, the analysis of particle size approximated by the ellipsoids with the aspect ratio ranging from 1.7:1 to 2.5:1 was performed. Obtained results are shown in Figure E4 Panel B. The average size of the particles calculated for 1NPA was 30.7 nm^2, while for 2NPA 38.7 nm^2. These values are about twenty percent larger than estimated 25.4 nm^2 (two particles with area of 12.6 nm^2 each) for 1NPA and 32.5 nm^2 for 2NPA. Several factors such as non-ideal spherical shape of individual nanoparticles, ligand shells around nanoparticles, and larger than two nanoparticles agglomerates, can contribute to a larger than the expected size of the dimer of the nanoparticles in addition to mentioned earlier factors. The protocol of STEM image processing and the outlines (ellipsoids) used for the particle size analysis are shown in Figures E4C and D, respectively.

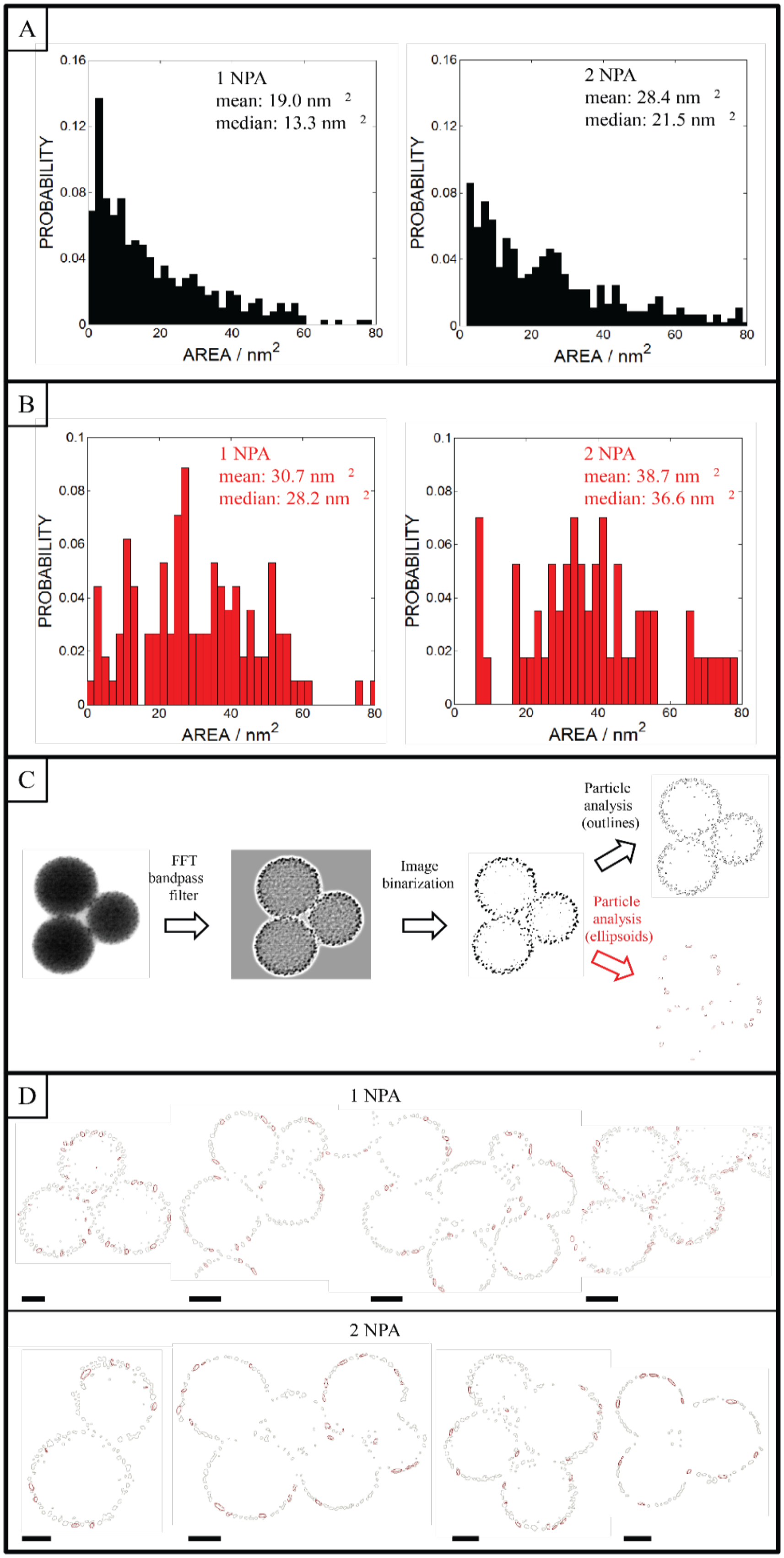
A
1 NPA
mean: 19.0 nm 2
median: 13.3 nm 2
PROBABILITY
0.16
0.12
0.08
0.04
0
0
20
40
60
80
AREA / nm2
2 NPA
mean: 28.4 nm 2
median: 21.5 nm 2
B
1 NPA
mean: 30.7 nm 2
median: 28.2 nm 2
0.1
0.08
0.06
0.04
0.02
2 NPA
mean: 38.7 nm 2
median: 36.6 nm 2
C
FFT bandpass filter
Image binarization
Particle analysis (outlines)
Particle analysis (ellipsoids)
D
1 NPA
2 NPA

Figure E4. Particle size analysis. Panels A and B show the particle area distributions based on the combination of all the STEM data presented in Figure S3 and Figure 3 of the main text. Panel A presents particle size analysis based on the outlines of the nanoparticles and nanoparticle clusters in the micrographs. Panel B shows the analysis based on the ellipsoids with aspect ratio ranging from 1.7:1 to 2.5:1. The aspect ratio was chosen in order to concentrate on the two nanoparticle clusters and nanoparticle dyads (of expected ~ 2:1 dimensions ratio). The protocol of the images processing for the particle size analysis is presented in Panel C and it contains FFT bandpass filtering followed by data binarization (transforming from grayscale to black and white image) prior to the particle size analysis. All the image processing steps were performed using ImageJ software. Panel 4 shows the outlines of the nanoparticles and their clusters that contributed to the distributions shown in Panel A (grey lines) and the ellipsoids (shown in red) contributing to the distributions shown in Panel B.

E2: One Nanoparticle Assembly Removal

To ensure that the electrostatic assembly process was not destroying the nanoparticle, the nanoparticle was removed from the SiO_2 template and the photoluminescence decay was monitored. In order to do the removal, the nanoparticle assembly was prepared in a high ionic strength solution (NaCl, I=250 mM). The SiO_2 bead was etched by placing the 1NPA assembly in a 5% sodium hydroxide (NaOH) solution for 15 minutes at 40℃ while stirring vigorously. The sample was then run through an ultracentrifugation cell and the filtrate was collected (i.e., anything that was not microbead). Then the filtrate was concentrated down using a regenerated cellulose membrane centrifugal filter with a 10,000 molecular weight cut-off (Millipore) to remove excess solvent. The photoluminescence decay of the nanoparticle that was removed from the microbead (green) behaved identically to the nanoparticle prior to assembly formation (red).

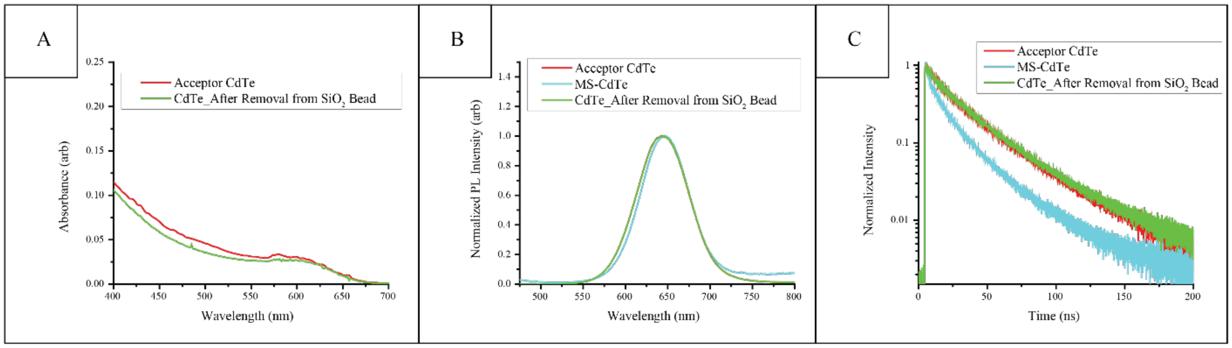

Figure E5. Absorbance of nanoparticle before and after removal from the SiO_2 bead (A). Steady state fluorescence spectra of collected nanoparticle free in solution (red), nanoparticle bound to the microbead (cyan) and nanoparticle after removal from bead (green) Ex: 440 nm, 0.7 x 0.7 nm slits, 0.1 s integration time (B). Photoluminescence decay of nanoparticle free in solution (red), nanoparticle bound to the microbead (cyan) and nanoparticle after removal from bead (green) Ex: 440 nm, 32 ps integration time, 1MHz repetition rate.

E3: Electrochemistry

Electrochemical measurements were performed on CA-CdTe to ensure that the electric field generated from the charges on the microbeads did not change the electronic state energies of the nanoparticle by a significant amount. Figure E6 shows voltammetry measurements of 4.1 nm CA-CdTe nanoparticles in solution (black) and assembled on the microbead (red). A voltammogram of the microbeads without any nanoparticles was used to background subtract the CdTe-MB assembly. The onset energy (Blue dashed line), corresponding to the valence band maximum of the nanoparticle, was found to occur at the same potential for both the free nanoparticle in solution and the nanoparticle assembled onto the template. The valence band maximum corresponds to an energy of -5.0 eV in good agreement with that reported by Jasieniak et al.[3] The oxidation peak at 0.2 V may arise from surface state defects on the nanoparticle. The electrochemical measurements were performed using a hexanethiol passivated Au ball working electrode, 3M KCL AglAgCl reference electrode (CHInstruments), and a platinum auxiliary electrode. The supporting electrolyte used during the experiment was a 0.1 M KCl pH 7 solution.

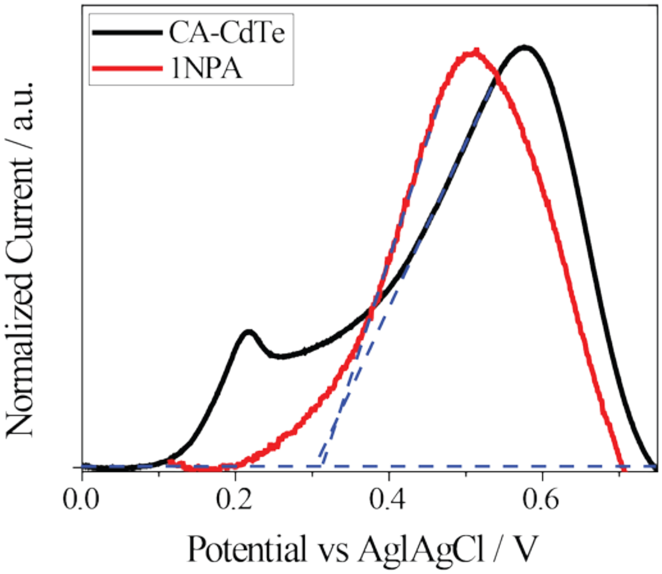

Figure E6. Shows voltammetry measurements of 4.1 nm CA-CdTe in solution (black) and assembled onto the microbeads (red). The blue dashed lines correspond to the valence band maximum of CdTe and indicate that the microbeads do not greatly change the electronic states of the nanoparticles

E4. Fluorescence Decays and Distribution Fitting of Energy and Electron Transfer Assemblies

The figure shown below (Figure E7) is a sample of the photoluminescence decays and distribution fitting for 2NPA assemblies. In one case the systems were modeled such that energy transfer was favored (black, red) and in the other case electron transfer was favored (green, blue). In order to ensure energy transfer was favored a larger bandgap CA-CdTe nanoparticle was synthesized. Because of the difference in size, the decays of the two nanoparticles free in solution are not identical. The 2NPA assembly in the electron transfer case (blue) is more significantly quenched than the 2NPA assembly in the energy transfer case (red). The free nanoparticles have a broad distribution with a low amplitude thus they are barely distinguishable from the baseline in Figure E7B.

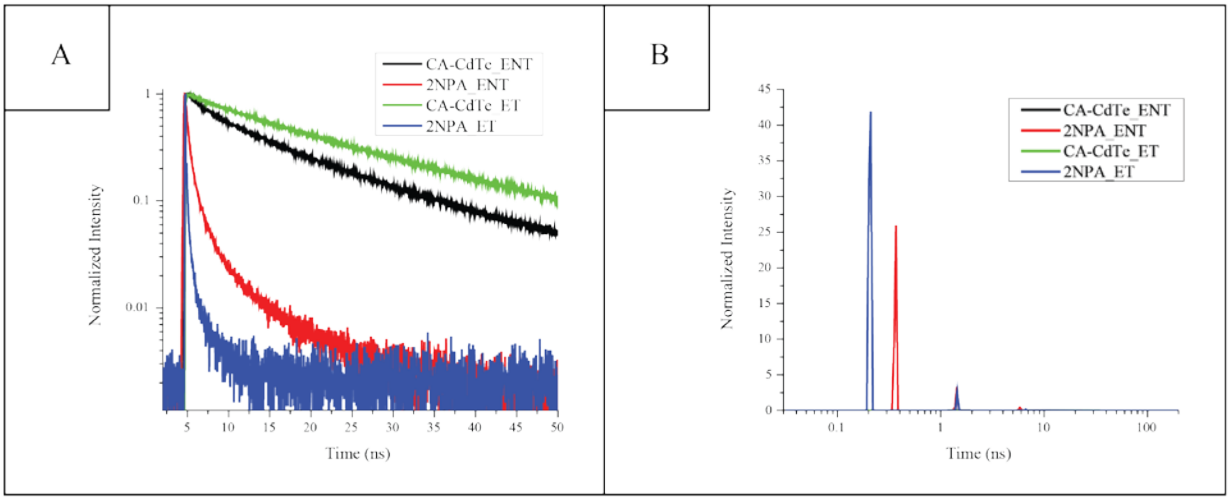

Figure E7. Photoluminescence decays are shown in panel A and the lifetime distribution fitting results are shown in panel B; for the CA-CdTe free in solution (black, green), the 2NPA (red, blue). The case which facilities electron transfer is indicated by ET (green, blue) and the case which facilitates energy transfer is indicated by ENT (red, black).

E5: FRET Efficiency and R_0

In addition to confirming the presence of two nanoparticles attached to a template, it is important to confirm that these particles interact. As an initial study, we used Förster resonance energy transfer (FRET) to assess the proximity of the nanoparticles on the microsphere. The Förster distance (R_0), which is defined as the distance at which energy transfer is 50% efficient, may be calculated by:[4]

$$R_0 = 0.211\left(\kappa^2 \eta^{-4} Q_D J(\lambda)\right)^{1/6} \qquad \textbf{Equation E1}$$

in which κ is the orientation factor related to dipole-dipole interactions between the donor and acceptor molecule (κ^2=2/3 for random orientations), η is the refractive index which was assumed to be 2, Q_D is the quantum yield of the donor, and $J(\lambda)$ is the overlap integral between the emission spectrum of the donor and the absorption spectrum of the acceptor. The overlap is given by:

$$J(\lambda) = \frac{\int_0^\infty F_D(\lambda)\varepsilon_A(\lambda)\lambda^4 d\lambda}{\int_0^\infty F_D\,(\lambda) d\lambda}$$ **Equation E2**

where F_D is the donor's emission spectrum, ε_A is the acceptor's extinction coefficient, and λ is the wavelength in nanometers. Given this relationship, the Förster distance can be calculated. It should be noted that the energy transfer probability will increase as the R_0 increases. To calculate the efficiency of energy transfer Equation E3 is used where r is the distance separating the two NCs.

$$E = \frac{1}{1 + \left(\frac{r}{R_0}\right)^6}$$ **Equation E3**

The FRET efficiency for this two nanoparticle system is approximately 100% as evidence by the spectral overlap of the donor (CA CdTe) emission and the acceptor (TGA CdTe) absorption, the type one heterojunction which promotes energy transfer. The R_0 value calculated for this system is 50 Å. The observation that the energy transfer does not change over our value of 6 Å, implies that the nanoparticles are within a few nanometers of each other.

E6: Fitting Protocol

The electron transfer rate (k_{et}) was determined by comparing the Type I system, which does not promote electron transfer, with the Type II system, which does promote electron transfer. The difference between these photoluminescence decays yields the k_{et}. Because the long-lived lifetime components are small in amplitude and do not shift significantly between the Type I and Type II cases in our system, it was assumed that they do not play an integral role in the k_{et}. In order to confirm that the long lived lifetime components do not play a large role in the analysis, the average lifetime of the decay was compared to the short time constant of each decay, both Type I and Type II (Figure E8).

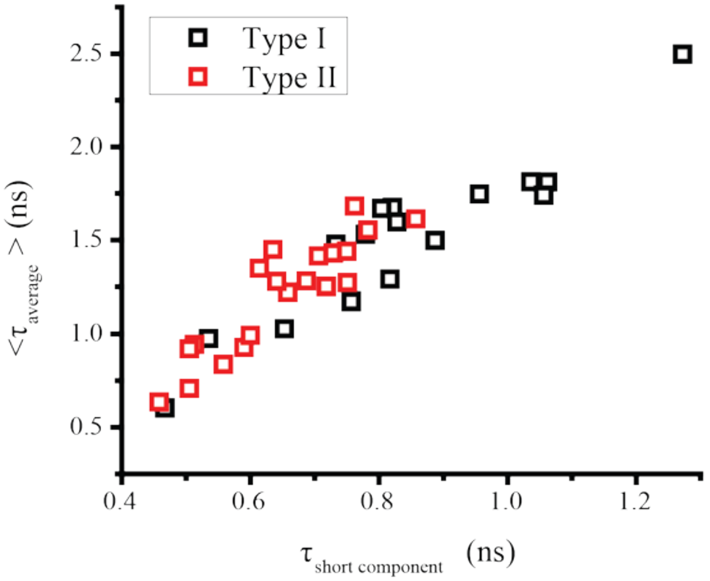

Figure E8. Plot comparing the average lifetime of each decay with the short time constant of each decay for both Type I systems (black) and Type II systems (red).

It is evident that there is a correlation between the length of the short time constant and the average lifetime of the decay. Thus, while neglecting the longer time constants may affect the exact magnitude calculated for the electron transfer rate, the trends that are found in this study are consistent.

Quantum dot photoluminescence decays are frequently fit using a distribution of lifetime components. However, to ensure that the method of fitting did not skew the calculated electron transfer rates, short lifetime components were compared for two fitting methods: a sum of exponentials and a distribution of lifetime components (Figure E9).

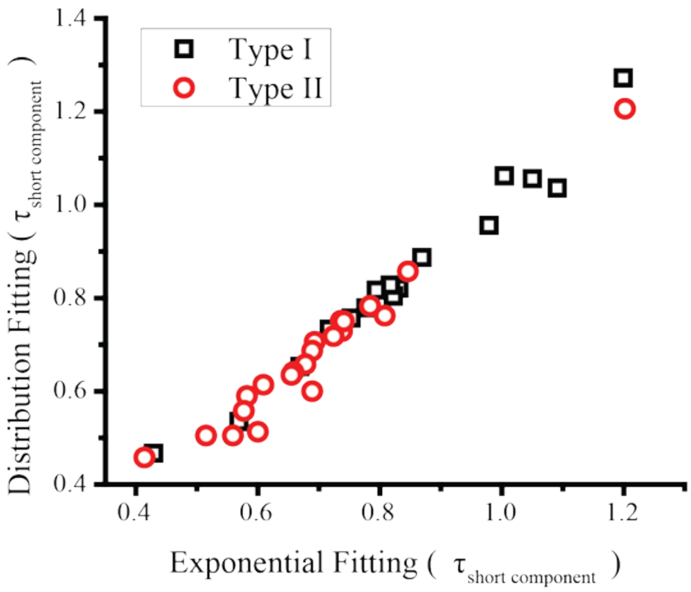

Figure E9. Plot comparing the short lifetime components of each decay that were fit by two different methods for both Type I systems (black) and Type II systems (red).

It is evident that the short lifetime component does not change drastically with the method of fitting, as the slope for both the Type I and Type II systems are nearly one. Thus, fitting the nanoparticle assembly decays as a distribution of lifetime components is adequate.

In addition to the details described above a few other careful considerations were taken. Another control, a dendrimer, was utilized. The dendrimer is negatively charged, is terminated with carboxylic acid units, is of similar size, and does not absorb in the regime that was studied. The carboxylic acid functional group allowed it to be covalently linked to the donor nanoparticle, and its lack of absorbance indicates that energy transfer should not be feasible. Electron transfer was also not favorable and a similar control was utilized for CdSe-CdTe aggregates in Wu et. al.[29]**Error! Bookmark not defined.** It was found that the dendrimer control mimics the results found for he Type I TGA-CdSe system, however, it fails to do so for the longer ligands studied. Because the microbead interacts with the donor nanoparticle as a result of the quenching observed when the donor is removed from the surface of the microbead, by introducing more methylene groups (ie. increasing the distance between the nanoparticle and the microbead), the quenching effect is changed. Thus, designing a Type I system accounts for all of the potential pathways, aside from electron transfer, that may take place.

E7: Bessel Function Analysis

The general compact form for the semi-classical Marcus equation is listed below (Equation E4) and it is derived in full in the work by J. Jortner.[5]

$$k_{ET} = \frac{2\pi}{\hbar^2 \omega_S} |V|^2 exp(-S)\, exp\big(-S_S(2\tilde{\nu}_S + 1) - S(2\tilde{\nu} + 1)\big)$$
$$\sum_{m=0}^{\infty} \left(\frac{\tilde{\nu}_S + 1}{\tilde{\nu}_S}\right)^{\left({}^{p(m)}/_{2}\right)} I_{|p(m)|}\sqrt{2S_S[\tilde{\nu}_S(\tilde{\nu}_S + 1)]}\left(\frac{\tilde{\nu} + 1}{\tilde{\nu}}\right)^{\left({}^{m}/_{2}\right)} I_{|m|}\sqrt{2S[\tilde{\nu}(\tilde{\nu} + 1)]}$$

Equation E4

where ω is the frequency of the longitudinal optical phonon (207 cm^{-1}), S is the Huang-Rhys factor, $\tilde{\nu}$ is defined as $\left[\exp\left(\frac{\hbar\omega_l}{kT}\right) - 1\right]^{-1}$, $p(m)$ is defined as $\frac{(\Delta_r G - m\hbar\omega_C)}{\hbar\omega_S}$, and $I_{|m|}$ is the Bessel function. The equation listed in the manuscript, Equation E3, is simply one limit, in the case of high temperature. However, for the the limit of the intermediate temperature regime $kT \approx \hbar\omega_l$, Equation E5 is obtained[5]

$$k_{ET} = \frac{2\pi}{\hbar} |V|^2 \frac{1}{\sqrt{2\pi S\hbar\omega kT}} exp(-S)$$
$$\sum_{m=0}^{\infty} \left[\exp\left(\frac{-(\Delta_r G(-S\hbar\omega - m\hbar\omega)^2}{4S\hbar\omega kT}\right) + 3\exp\left(\frac{-(\Delta_r G - S\hbar\omega - m\hbar\omega)^2}{4S\hbar\omega kT}\right)\right]\left(\frac{\tilde{\nu} + 1}{\tilde{\nu}}\right)^{\left({}^{m}/_{2}\right)}$$
$$I_{|m|}\sqrt{S[\tilde{\nu}(\tilde{\nu} + 1)]}$$

Equation E5

If the value for S was kept consistent between the high temperature and intermediate temperature systems and only the electronic coupling was allowed to be a floating variable, the shape of the fit remained nearly identical and the electronic coupling was found to be 0.4 cm^{-1}. This indicates that while the magnitude of the electronic coupling may vary between these models, the simpler semi-classical Marcus equation provides clear insight on the interactions in this semiconductor nanoparticle system.

E8: Confirmation of Covalently Bound Nanoparticle Aggregates

Control experiments were completed to ensure that the nanoparticles were covalently linked through an amide bond (described in the literature),[6-8] as opposed to electrostatically linked, which is necessary for the understanding of the distance dependent study. This procedure was adapted from Wu et. al.[5] which described methods for monitoring the interaction of electrostatic donor-acceptor nanoparticle aggregates in solution. The nanoparticle aggregates studied were of a molar ratio of 1 donor to 5 acceptor nanoparticles. The electrostatic and covalent systems were placed in nearly identical conditions. Both systems stirred in phosphate buffered saline (PBS) buffer at pH 7 for 15 hours in the dark under argon. The covalently bound system was prepared as described above with the addition of the catalyst EDC and sulfo-NHS. The donor nanoparticle was quenched in the presence of the acceptor in both the electrostatic and covalently bound systems (red) (Figure E10 Panel A). These data indicate that the donor nanoparticle interacted with the acceptor. Note that in the case of the covalently bound system the donor emission is more efficiently quenched than in the electrostatic case. The donor nanoparticle only was studied under identical conditions, including in the presence of EDC, and there was no change in the emission intensity.

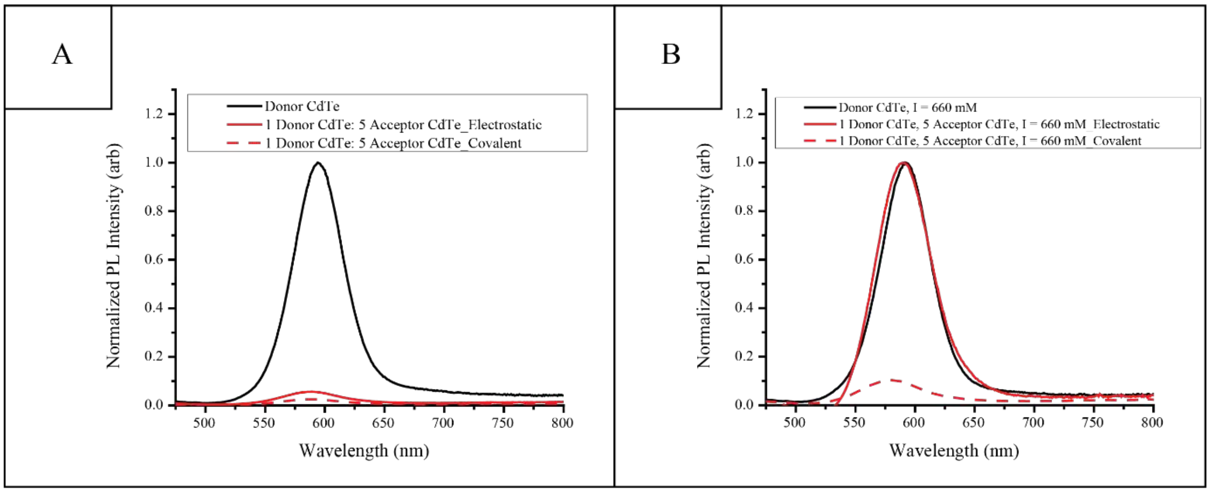

Figure E10. Steady state fluorescence spectra of collected of the donor CdTe (black) with no acceptor in solution along with a ratio of 1 Donor: 5 Acceptor CdTe systems either bound electrostatically (red, solid line) or covalently (red, dashed line) Ex: 440 nm, 0.7 x 0.7 nm slits, 0.1 s integration time (A). Steady state fluorescence spectra of donor CdTe (black) in high ionic strength solution and electrostatic aggregates (red) and covalent aggregates (red dash) in high ionic strength solution (B).

It has been shown that in electrostatically bound nanoparticle aggregates an increase in the ionic strength will dissociate the aggregates and increase the emission intensity coming from the donor nanoparticle.[9] Thus, the donor only, as well as the electrostatically and covalently bound systems, were placed in a solution of high ionic strength (I=660 mM). Sodium chloride (NaCl) was added to the aggregate system and stirred for 10 minutes. In the electrostatic assembly the fluorescence intensity recovered to have the same intensity as the donor only system (see Figure E10 Panel B). However, in the covalently bound case, while the fluorescence intensity did recover slightly, the overall emission was still significantly quenched. This indicates two important points: 1) The bond between the covalently bound aggregate system is significantly stronger than the electrostatically bound aggregate system and 2) The covalently bound aggregate system may have some electrostatic interactions, but the interaction is not dominant. This, along with the supporting literature, confirms that an amide bond covalently linking these nanoparticle aggregates is formed.

REFERENCES

(1) You, J.; Dou, L.; Yoshimura, K.; Takehito, K.; Ohya, K.; Moriarty, T.; Emery, K.; Chen, C.; Gao, J.; Gang, L.; Yang, Y.; A polymer tandem solar cell with 10.6% power conversion efficiency. *Nat. Commun.*, **2013**, 4, 1446.

(2) Rasband, W.S., ImageJ, U. S. National Institutes of Health, Bethesda, Maryland, USA, http://imagej.nih.gov/ij/, **1997-2016**.

(3) Jasieniak, J.; Califano, M.; Watkins, S. E.; Size Dependent Valence and Conduction Band-Edge Energies of Semiconductor Nanocrystals. *ACS Nano*, **2011**, 5, 5888.

(4) Lakowicz, J. R. *Principles of Fluorescence Spectroscopy*, 3rd ed. Springer: **2006**; p. 1-61, 97-155, 331-382, 443-475.

(5) Jortner, J.; Temperature dependent activation energy for electron transfer between biological molecules. *J. Chem. Phys*., **1976**, 64, 4860.

(6) Bartczak, B. and Kanaras, A. G.; Preparation of Peptide-Functionalized Gold Nanoparticles Using One Pot EDC/Sulfo-NHS Coupling. *Langmuir*. **2011**, 27, 10119.

(7) Sellers, D. G.; Button, A. A.; Nasca, J. N.; Wolfe, G. E.; Chauhan S.;Watson, D. F.; Excited-State Charge Transfer within Covalently Linked Quantum Dot Heterostructures. *J. Phys. Chem. C*, **2015**, 119, 27737.

(8) Osovsky, R.; Shavel, A.; Gaponik, N.; Amirav, L.; Eychmuller, A.; Weller, H.; Lifshitz, E.; Electrostatic and Covalent Interactions in CdTe Nanocrystalline Assemblies. *J. Phys. Chem. B*, **2005**, 109, 20244.

(9) Wu, M.; Mukherjee, P.; Lamont, D. N.; Waldeck, D. H.; Electron Transfer and Fluorescence Quenching of Nanoparticle Assemblies. *J. Phys. Chem. C*, **2010**, 114, 5751.